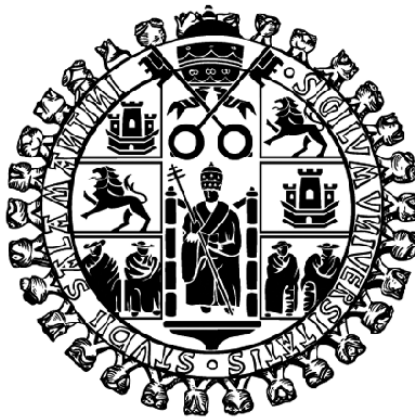# Progress in the conceptual design of future gamma-tracking arrays with imaging capabilities. Lifetime measurement in neutron-rich nuclei in the region of the double magic ^{78}Ni with the AGATA demonstrator

María Doncel Monasterio

Departamento de Física Fundamental, USAL

Tesis doctoral, marzo de 2012

Directores: Begoña Quintana Arnés y Andrés Gadea Raga

La ignorancia es la felicidad

Contents

Introduction

The work developed in this P.h.D thesis is related to different topics currently under study in the frame of γ-spectroscopy with tracking detectors for nuclear structure research.

The first part is devoted to the developments and improvements on the capabilities of highly segmented Ge detectors based on the tracking and imaging concepts when used in γ spectroscopy systems. The work has been mainly focused on the new Ge detection system proposed for the DESPEC experiment at the GSI facility and on the developments in several tracking/imaging codes both for this future array as well as for the present highly efficient tracking array, AGATA. The second one, corresponds to the measurement performed in June 2010 at the Laboratori Nazionali di Legnaro (LNL): *Lifetime measurement in neutron-rich Ni, Cu and Zn isotopes* (M. Doncel, E. Sahin and A. Goergen). This measurement constitutes one of the first experiments performed at the LNL with the AGATA Demonstrator. In particular, it has been the first time the AGATA Demonstrator has been coupled to the differential plunger setup as well as to the PRISMA spectrometer to perform a lifetime measurement through the Recoil Distance Doppler Shift Method.

Its contents have been structured in four chapters and some conclusions. Chapter 1 contains a brief summary of the HPGe detectors evolution as well as the achievements on nuclear structure studies associated to this evolution. A detailed explanation of the nowadays best high resolution gamma ray spectroscopy system, AGATA, closes this chapter.

The study of the best performance for the Ge array proposed for the DESPEC experiment through Monte Carlo simulations is described in Chapter 2. Firstly the optimization of the technical proposal has been done. Once it has been optimized, the study of the more suitable configuration, in terms of peak efficiency and P/T ratio, has been performed. Finally, the proposed setup is shown.

Chapter 3 is devoted to the developments of several algorithms for highly segmented Ge arrays. In particular, a background-suppression algorithm have been developed for the AGATA array, whose objective is to discriminate the origin of the γ rays by means of tracking back the γ rays coming from different positions. This algorithm has been also optimized for the particular conditions of the DESPEC experiment and it has been applied to the Ge proposed setup for the experiment. Finally, a Compton imaging algorithm for γ-ray tracking HPGe detectors has been developed for the unique experimental conditions of the DESPEC experiment, trying to reconstruct the γ path inside the detector and identify the γ-ray emitting source position in the focal plane.

The lifetime measurement performed at the LNL is described in Chapter 4. The aim of the experiment has been to determine the lifetime of the excited states in ^{71}Cu through the

Recoil Distance Doppler Shift Method (RDDS) using the AGATA Demonstrator coupled to the plunger setup and to the PRISMA spectrometer. The RDDS method and the devices used for the measurement are firstly described. Then the data analysis is explained and, finally, the obtained results are shown.

Chapter 1

Large scale instrumentation for γ ray spectroscopy

1.1 Introduction to the high resolution γ-ray spectroscopy

The nucleus is a unique strongly interacting quantum mechanical system. Consisting of a few up to a few hundred nucleons, its structure combines the macroscopic features expected of nuclear matter in a bulk form with the microscopic properties associated with the motion of a finite number of fermions in a potential. It represents a self-bound, complex system, which displays a rich variety of excitation modes governed by the interplay of nucleons in individual orbits and by their collective behavior. Understanding nuclear excitations is one of the principal goals of nuclear structure studies. A tool to investigate nuclear structure under extreme conditions is the high resolution γ-ray spectroscopy. The study of the γ-decay properties of the atomic nucleus has provided a wealth information on the behavior of such a system, for example, under the influence of high temperatures, high spin or large deformations as well as for extreme isospin values and of the total nuclear mass.

The de-excitation of nuclei that are created in a nuclear reaction in a state of finite excitation energy, temperature and spin to the ground state is characterized by the emission of a certain number of γ rays. The information about how the nuclear structure changes during the decay while the nucleus loses energy and angular momentum is obtained by investigating the properties of these excited states, such as their energy, emission sequence and time relationship as well as their electro-magnetic properties, through the measurement of the γ-rays emitted. New challenges for nuclear spectroscopy are imminent nowadays when high intensity radioactive ion beams (RIB) are emerging in a wide energy range: from the Coulomb energy regime, typical for the European ISOL facilities as SPIRAL2 and HIE ISOLDE, to the intermediate and relativistic energy regimes of fragmentation facilities, such as SIS/Super-FRS and, in particular, the new international facility FAIR. In the Coulomb energy regime, classical reaction types as transfer, deep-inelastic or compound reactions become available for few species with intensities comparable to those of today's stable beams. At intermediate energies, i.e., between 50 and 200 MeV/u, Coulomb excitation can be employed to populate low-spin states of new far-from-the-stability-line nuclei: depending on the available beam energy,

highly excited states up to the giant resonances can be reached. At higher energies, secondary fragmentation becomes a powerful tool to create very exotic fragments that are excited to relatively high spins; i.e., in violent collisions, spins of more than $30\hbar$ can be reached [1]. Finally, at relativistic energies, the rarest species, those close to the drip lines, can be studied using decay spectroscopy after implantation.

Exotic beams allow approaching and mapping the drip-line regions in order to answer the open questions in nuclear structure physics and to explore nuclear stability at the very limits. Nuclei far from stability allow amplifying and isolating particular aspects of the nuclear interaction and dynamics and may favor the occurrence of new symmetries. First and foremost, high-resolution γ-spectroscopic studies will open up unique possibilities allowing a very rich physics program to be addressed that covers the full range of topics in which the nuclear physics community is currently interested. The investigation of exotic nuclei will be aiming at essentially all nuclear degrees of freedom, such as (i) proton-rich nuclei at and beyond the proton drip line and the extension of the N=Z line, (ii) neutron-rich nuclei towards the drip line in medium heavy elements and (iii) the heaviest elements towards new super-heavy elements. The internal degrees of freedom of nuclei will be exploited by investigating (i) ultra-high spin states produced in extremely cold reactions, (ii) meta-stable states at high spins and at very large deformation, (iii) multi-phonon giant resonances as well as other high-temperature phenomena, such as quantum chaos.

A sizeable part of the present knowledge of exotic nuclei comes from γ spectroscopy. Although the study of the exotic nuclei is not the main reason for the development of γ-detection systems, due to their good resolution and peak efficiency, they are suitable for that. The quality of these systems related to nuclear spectroscopy is evaluated by the resolving power (R) which is estimated by: the relation between the peak area to the total spectrum area (P/T), the separation in γ energy of a certain cascade (SE_γ) and the effective energy resolution of the detector measured as the FWHM (ΔE_γ). The equation is as follows:

$$R = 0.76 \frac{SE_\gamma}{\Delta E_\gamma} P/T \qquad (1.1)$$

where the factor 0.76 is related to the fraction of the Gaussian peak taken into account for setting the coincidences.

The inception of the high resolution γ-ray spectroscopy started with the development of Ge semiconductor detectors [2]. Actually, good energy resolution, less than 1 keV at 120 keV and about 2 keV at 1 MeV, can be obtained with this kind of detectors. The fast progress of nuclear structure physics in the early 1970's was clearly related to the advent of the Ge(Li) detector. Along the sixties and the seventies, Ge(Li) detectors were used in coincidence experiments studying nuclei populated in the decay of long-lived isotopes as well as nuclei populated by fusion–evaporation reactions at particle accelerators. For the first time, the efficiency and the energy resolution of a detector was good enough to filter cascades of γ rays out of the complex in-beam spectra and to establish detailed level schemes. An example of the new physics achievable with these systems was the discovery of back-bending, the alignment of pairs of particles in time-reversed orbits, by A. Johnson et al. in 1971, showing the validity of the collective rotational model [3]. This was identified in a γ–γ coincidence experiment with two small Ge(Li) detectors. It

was now possible to determine both, spins of excited states from the angular distribution
or correlation of γ rays and their parity from the measurement of the linear polarization
of the γ rays. From eighties these detectors were replaced by the High Purity Ge detectors
(HPGe) with better energy resolution and without the need to keep them permanently
cold.

The main drawback of Ge detectors is the limited volume of the crystals that causes a
low P/T value due to the scape of γ rays out of the crystal as a consequence of a Compton
interaction. The continuum background observed in γ spectra is due to the radioactivity
present in the detector and surrounding environment, to the cosmic radiation but mainly
at high γ energies to the Compton interaction of non-fully absorbed γ rays in the crystal
coming from the source. In the last years, a substantial improvement in γ-spectroscopy
systems based on high resolution HPGe detectors has been achieved. Besides the increase
of the crystal volume obtained from the improvements in the Ge crystal growing technique,
a new technology based on Compton-suppressed HPGe detectors, in which anti-Compton
detectors are surrounding the Ge ones, was developed (Fig. 1.1) [4]. The objective was to
improve the sensitivity by increasing the P/T ratio. In this way, events not fully absorbed
in the Ge detector have a high probability to be detected in the anti-Compton detector
and consequently can be rejected. With this method a P/T of 50% can be obtained.
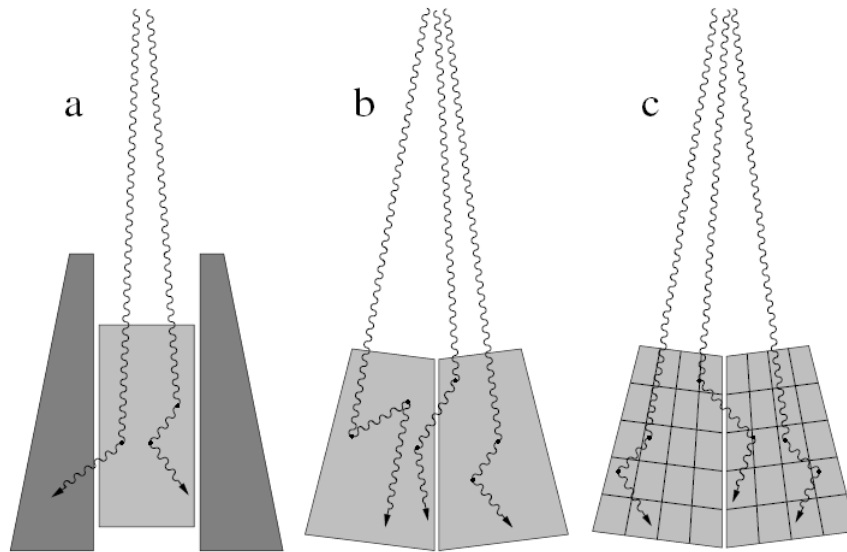
Figure 1.1: a) Anti-Compton detector surrounding the Ge detector with the aim of
suppress the partially absorbed events in the spectra; b) detector composed by different Ge
crystals that allows to add the signals; c) segmented detector that allows the reconstruction
of the individual trajectory of γ rays [5].

The material employed for the development of anti-Compton (AC) shields has to be
selected in order to guarantee the maximum reduction of the background radiation. The
first AC detectors were based on the NaI(Tl) scintillator. From middle of eighties other
scintillator materials have been used, in particular, the so-called BGO ($Bi_4Ge_3O_{12}$). Due
to its higher density and its higher mean Z value, it is up to 3 times more efficient per
unit length than NaI.

The first arrays made up of escape-suppressed Ge detectors were TESSA (The Escape Suppressed Spectrometer Array) [6–8] and HERA (High Energy Resolution Array) [9]. TESSA was developed in 1980 in Riso (Denmark) and was composed by five Ge(Li) detectors surrounded by coaxial NaI(Tl) detectors. HERA was developed also at the beginning of eighties in the Lawrence Berkeley National Laboratory (LBNL), but for this array already n-type Ge detectors were used and the anti-Compton detectors were made of BGO instead of NaI(Tl) as in TESSA. The high efficiency obtained with this system, about 1.5% at 1.3 MeV, made possible to measure γ-γ-γ coincidences for the first time. With these arrays P/T ratios around 60% are obtained compared to the 20% of the unshielded detector. The solid angle covered by Ge in these systems is limited and, therefore, the peak efficiency. Other arrays were built in the 1980's, all using BGO suppression shields and between twelve and thirty n-type Ge detectors of 25%–35% relative efficiency. All these arrays had some specific improvement in technology and were adapted to the specific scientific interest of the collaborations devoted to built them. In particular, TESSA3, which became well-known for the discovery of superdeformation in ^{152}Dy [10], consisted of sixteen Ge detectors with its respective BGO shields.

In the second half of the 1980's the nuclear physics community started to plan the next generation of γ-ray arrays. The goal was a 4π array of escape-suppressed Ge detectors covering as large solid angle as possible to maximize efficiency. Projects based on this idea were GASP [11, 12] in Italy, EUROGAM [13, 14] and EUROBALL [15–17] as European collaborations and GAMMASPHERE [18] in USA. GASP was the first 4π detector developed in Europe, specifically in the Laboratori Nazionali di Legnaro (INFN, Italy), in 1992 and it is still in operation. Different configurations can be arranged for the array depending on the experiment to perform. The configuration I is based on a polyhedron with one hundred and twenty two faces of which forty are used for the HPGe detectors, twenty eight in the so-called "hexagonal" positions and twelve in the "pentagonal" ones, two are devoted to the beam pipe and the remaining eighty are used for the BGO detectors inner ball. Instead of the eighty BGO detectors, a Pb shield made of two hemispheres smaller in diameter (19 cm) having the same symmetry as the inner ball and playing a collimator role is inserted in the Configuration II (Fig. 1.2). In such a replacement, the Compton suppressed Ge detectors are moved nearer to the target reducing the target-detector distance from 27 cm to about 20 cm for the twenty eight detectors in the hexagonal positions and from 27 cm to 24 cm for the twelve in pentagonal ones. As a result of this geometry, the total photopeak efficiency at 1.33 MeV is almost doubled: from a standard value of 3%, obtained with configuration I, up to 5.8% which is preferred for the most of the spectroscopic studies needing a large collected statistic. The gain in efficiency comes with a reduction of the resolving power (R) due to the large Doppler broadening of the lines caused by the increased solid angle of the Ge detectors. Therefore, in experimental situations where a reduced resolving power is acceptable (e.g low recoil velocities), configuration II can be an acceptable compromise. This is the case both when measuring lifetimes, either with the Doppler Shift Attenuation Method (DSAM) [19–21] or with the Recoil Distance Plunger Technique [19, 22], and in Transient Field g-factor measurements, where the precision of the measurement is determined mainly by the collected statistic. Nowadays GASP is still working coupled with ancillary detectors as ISIS [23] or the neutron n-ring system [24]. With the latter, innovative results have been obtained recently as the the identification of excited states in ^{91}Rh by Margineau et al. [25].

Figure 1.2: Configuration II of GASP.

The largest Compton-suppressed Ge arrays built are EUROBALL and GAMMAS-PHERE. GAMMASPHERE was developed in 1987 at the LBNL (USA). It is made up by one hundred-ten hexagonal Ge detectors to achieve the spherical shape. With its configuration 95% of the solid angle is covered of which 46% corresponds to Ge detectors, obtaining P/T values of 68%. Important features of the system are the high symmetry of the system around the target, like GASP, and the fact that in its last version of 1993, seventy of the one hundred-ten crystals were longitudinal-electrically segmented improving the energy resolution from 5.5 keV to 3.9 keV at a recoil velocity of 2%. Exciting new results have been found for the structure of nuclei at the proton drip-line with this system, for instance, in the study of the proton decay of ^{141}Ho [26]. Nearly all of the known proton emitters decay from spherical nuclei. The proton decay of ^{141}Ho is thought to be one of the few examples of proton decay from a deformed nucleus [27].

The segmentation of the electric contact in the Ge crystals, introduced firstly in the GAMMASPHERE array, provides an improvement on the resolution power, as the granularity rises and, therefore, the capability to solve multiple interactions in the same detector. However, the main advantage of the electric segmentation is related to the energy resolution because the opening angle of the detector considered for the Doppler broadening correction decreases and, as a consequence, the photon energy can be more accurately determined. As mentioned above, the FWHM of a γ line of energy 1.3 MeV measured with a Ge detector is $\Delta E \sim 2$ keV but in most in-beam experiments the line width is broadened due to the Doppler effect. The sign of the Doppler effect in the spectra is double. From one side, the E_0 energy of a photon which is emitted from a residual nucleus moving with velocity v and detected at an angle θ with respect to the beam axis is Doppler-shifted and is given by:

$$E_\gamma = E_0(1 + \frac{v}{c}cos\theta) \tag{1.2}$$

where E_γ is the measured energy and c the light velocity (Fig. 1.3). It should be noticed that this relation is valid for low velocities, thus $\beta < 1$.

From the other side, besides the Doppler shift, due to the finite opening angle $\Delta\theta$ of the detector which results in an uncertainty in the real value of θ, the Doppler effect also results in a broadening of the spectral γ line of:

$$\Delta E_\gamma = E_0\frac{v}{c}sin\theta\Delta\theta \tag{1.3}$$

The Doppler shift can be corrected by knowing θ when either the emitted nucleus or the projectile is detected by a sensible position detector. The precision which the direction of the emitted γ ray can be obtained with depends on how the interaction position inside the detector is known. In conventional systems, where the maximum information is the position of the hit detector, θ is calculated as the angle between the emitted nucleus and the direction defined by the emitter point and the center of the detector opening window, taking as uncertainty the detector opening angle $\Delta\theta$ seen from the emitter point (Fig. 1.3). The broadening is reduced with the segmentation due to the decrease of the opening angle. For instance, for 1 MeV γ rays emitted by nuclei moving with v/c $\sim$ 5%, detected by a 5 cm radius detector placed at 20 cm and with 90$^{\text{o}}$ respect to the nucleus velocity vector, the Doppler broadening is about 25 keV to be compared with the 2 keV intrinsic resolution. Other effects which contribute to the broadening of a γ line are the angular spread of the recoiling nuclei in the target and the variation of the velocity of the recoils.
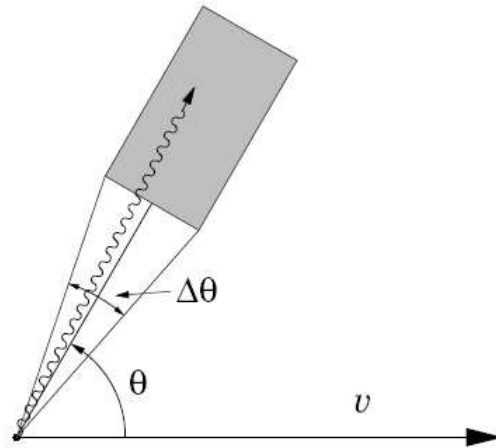

Figure 1.3: The Doppler shift depends on the detection angle (θ) and the Doppler broadening is related to the opening angle ($\Delta\theta$).

In Europe, as an alternative approach to the segmentation concept, the evolution of high resolution detector techniques in order to increase the granularity was achieved mainly

by using composite detectors, i.e, detectors composed by several crystals packed in the same cryostat, making feasible all the crystals to work as a single detector. In this way, adding the interactions happened in all crystals placed in the same cryostat, the probability to detect the γ-energy full absorption is incremented, decreasing the background and increasing the P/T ratio. Two types of composite detectors were developed: Clover detectors composed by four crystals [28] and Cluster detectors by seven detectors [29,30]. Within the EUROBALL developments, several arrays have been built in Europe with these composite detectors. The first array was EUROGAM II, formed by two rings made up by twelve Clover detectors, placed in the beam direction, and thirty individual detectors from EUROGAM I in the forward and backward directions. The peak efficiency increased from 5.6%, obtained with EUROGAM I, to 8.1% at 1.3 MeV. The next step came with EUROBALL III developed by an European collaboration in 1997. It was composed by EUROGAM II plus fifteen cluster detectors. This system, initially installed at LNL, was moved to IReS Strasbourg, where two hundred and ten BGO detectors in a spherical configuration were added, which gave rise to what is currently known as EUROBALL IV (Fig. 1.4). By grouping the inner ball detectors, both Ge detectors and BGO elements, into one hundred-sixty four subgroups of equal efficiency and solid angle, an excellent performance for the determination of the total γ-ray energy and γ multiplicity was achieved.
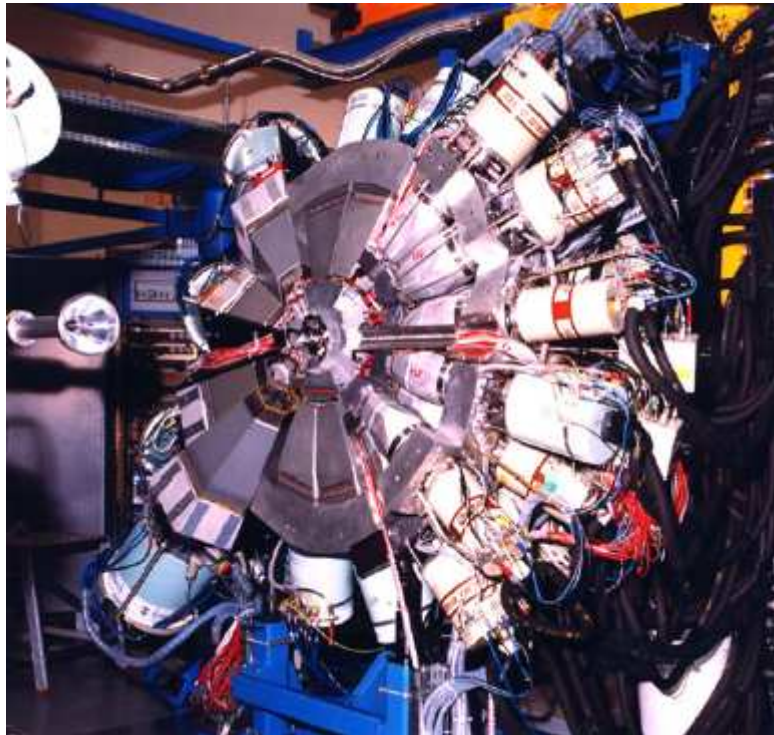

Figure 1.4: EUROBALL IV.

After the successful implementation of encapsulated crystals in the EUROBALL clusters, several arrays have benefit from this technique. The encapsulation provides electric isolation. It also makes independent the vacuum of the detector from the cryostat vac-

uum that contains the cold part of the preamplifier needed close to the crystal to reduce the crosstalk and to avoid electronic oscillations in the preamplifier. Besides, it has to be taken into account that Ge detectors are damaged by the neutron flux in "in-beam" experiments. Fast neutrons, emitted in most of the nuclear reactions, impinge in the detector, disturbing the atoms in the lattice and moving them away from their initial positions in the crystallographic net which creates charge traps. As a consequence, the charge collection in γ events is spoiled and, therefore, the energy resolution of the system. In order to recover the original characteristic of the detector is required a thermal treatment, called annealing, in which the crystals are heated close to 100^0 for a long period. The encapsulation facilitates this process for complex detectors making viable the use of clusterization.

Between EUROBALL IV and GAMMASPHERE there are many similarities. Both systems are based on a spherical configuration, BGO detectors are used as anti-Compton suppressors and peak efficiency is close to 10% for both. The differences between them, related to design and configuration mainly, provides them of different measurement capabilities. For instance, the main advantage of GAMMASPHERE is the high symmetry of the system, doing data analysis easier. EUROBALL IV has higher efficiency for high-energy γ rays due to the cluster detectors and better sensitivity for polarization measurements due to the Clover detectors, as the polarization is obtained in terms of the Compton asymmetry between 0^0 and 90^0. Clover detectors, formed by four crystals in a square configuration, are ideal detectors for this kind of measurement. Nevertheless, although Cluster and Clover detectors increase the resolution power and the efficiency of the system, they work under certain constrains. They, and in general, any composite detector, suffer from a certain drawback: the so-called "summing effect" when two γ rays interacting in the same crystal are detected as only one with energy equal to the addition of both energies. However, with their advantages and drawbacks, GAMMASPHERE and EUROBALL are the summit of 4π arrays based on escape-suppressed Ge detectors.

The dawn of the last millennium saw the birth of the first-generation radioactive beam facilities. These facilities, very challenging at this time, had very limited beam intensities. In case of the facilities based on ISOL technique, experiments were performed with nuclear reactions as Coulomb excitation or transfer reactions with inverse kinematics where the multiplicity of γ rays is really low. The radioactive beam intensity is low about $10^3 - 10^5$ particles per second and the velocity of the reaction products is high. So, this kind of experiments requires high efficiency and high granularity to increase the energy resolution after Doppler correction. To achieve this requirements, compact detection systems based on electrically segmented Ge detector technology have been developed. Examples of such a systems are, in Europe, EXOGAM [31, 32] and MINIBALL [33, 34] and, as it has aforementioned, the last version of GAMMASPHERE at the United States. EXOGAM was built to perform experiments for the SPIRAL project (Radioactive Ions Production and on-Line Acceleration System) [35] in GANIL (Grand Accélérateur National d'Ions Lourds) [36]. It consists on sixteen Clover detectors, each of them composed by four Ge crystals 60 mm diameter and 70 mm length, electrically segmented in the azimuthal direction in four equal segments. The Clover detectors are placed at 11 cm from the target and the efficiency at 1.3 MeV is about 20% for low multiplicity. MINIBALL was developed to perform experiments at REX-ISOLDE (Radioactive beam EXperiment at ISOLDE) [37] at CERN, as a collaboration between Germany and Belgium. Forty encapsulated Ge detectors, grouped in eight cryostats with three detectors and four cryostats with four detectors, electrically segmented in six segments, make up the system. A digital processing

of the preamplifier signals was used for the first time for MINIBALL. This treatment allows to analyze the shape of the electric pulses and opens the possibility to determine the interaction position of the γ ray in the crystal. The second generation of radioactive ion beams facilities, now under construction, involves a major challenge in the γ-ray spectroscopy instrumentation. The γ-ray tracking concept, has been extended by the EU and USA communities in the last two decades as a brilliant solution to the instrumental necessities of these new facilities.

1.2 Gamma-tracking arrays

The second generation of radioactive ion beam facilities which will be operative in few years will open possibilities to study new regions of the nuclear chart. Exotic nuclei will be produced in these facilities, most of them in small quantity, because the farther the nucleus is from the stability line the lower the production cross section is. Therefore, new developments on detection systems are needed in order to improve the sensitivity by increasing P/T values and efficiency. Additionally, high granularity is required to avoid the system to get blind during the beam flash. To respond to these requirements, a new generation of γ-ray detectors based on Pulse Shape Analysis (PSA) and tracking is currently being developed. Four-π solid angle geometry arrays will be suitable to profit about this technique since anti-Compton detectors are not needed and the spectroscopic system efficiency will be higher as most of the solid angle will be covered by Ge. In these new arrays currently in development, the target will be surrounded from one hundred to two hundred position sensitive Ge detectors, in such a way, that more than 80% of the solid angle will be covered by Ge. Using digital electronics and the PSA technique it is possible, as it is explained below, to determine energy, position and time of each γ-ray interaction and, therefore, to determine the path inside the detector.

The studies needed to determine the feasibility of both high segmentation of Ge detectors and reconstruction of the photon path, not only to a conceptual level but also to a technical level, started in Europe with the italian project so-called MARS [38, 39], which was incorporated later to the European network *Developing of Gamma-ray Tracking Arrays*. In this project a highly segmented prototype was built. It was composed by a coaxial crystal 90 mm length and 72 mm diameter. The external contact was electrically segmented in twenty-five segments: six angular sections, four transversal sections and one additional segment 10 mm diameter placed in the center of the frontal face. The good results obtained in position resolution performance [40] were the starting point to the AGATA project (Advanced Gamma Tracking Array), a 4π highly segmented Ge tracking array for γ spectroscopy. However, the first conceptual design study for applying γ-ray tracking to a proposed major new detector for nuclear structure physics studies was done at Lawrence Berkeley National Laboratory (LBNL) in 1994 in which arose the project to build an array named GRETA (Gamma-Ray Energy Tracking Array)) [41]. The current design of GRETA is based upon a geodesic configuration, consisting of one hundred and twenty hexagons arranged in a close-packed 4π geometry. GRETA will comprise a total of forty cluster modules. GRETINA is the first phase of a staged approach to GRETA. GRETINA will have thirty highly-segmented coaxial germanium crystals and is 1/4 of the full GRETA. The European equivalent for the development of an array of HPGe detectors based on the techniques of γ-ray tracking and PSA is AGATA [42–44]. It will

be suitable for nuclear structure studies at the planned European radioactive ion beam and high-intensity stable beam facilities.

In these new tracking arrays the Ge crystal contacts are longitudinally and transversally segmented, while the aforementioned arrays (EXOGAM, MINIBALL) have detectors segmented only in one direction. As a consequence of the two dimension segmentation, the position of the interaction points can be determined inside the crystal thanks to the position dependence of the Ge electric signal produced. With the interaction points it is possible to reconstruct the single γ-ray tracks and therefore, to reject those corresponding to not fully absorbed γ rays.

1.2.1   PSA techniques

To determine the interaction position, digital electronics and pulse shape analysis techniques (PSA) are needed. Digital electronics allows for the complete signal digitization instead of the analogue treatment of the signal that includes integration of the charge, generation of a voltage pulse and measurement of the maximum signal amplitude to obtain the energy as in conventional systems. PSA techniques have been developed to determine not only the energy deposited but also time and position for each interaction inside the detector with high precision. To obtain accurately the interaction position in three dimensions, a detailed understanding of the signal shape versus interaction position is necessary. PSA techniques have to take into account not only the real signal but also the induced ones in the neighboring segments (mirror signals). As it will be shown, by a comparison between calculated and experimental signals it is possible to get the position interaction with high accuracy. To use pulse shape analysis to determine interaction position is, however, not unique for tracking arrays like AGATA or GRETA. This is for example done also in MINIBALL, where the azimuthal position is obtained by comparing the amplitudes of the mirror charges [45]. The radial position is obtained from the shape of the signal of the hit segment. This is good enough to correct for Doppler effects, but it does not give the z coordinate needed to do γ-ray tracking.

To determine the position in three dimensions accurately, an exhaustive understanding of the signal shape is needed. A signal is shaped when electrons and holes are collected on the electrodes producing induced charges of opposite sign. Induced signals are not only produced in the segments where interactions have taken place, but transient signals in the neighboring segments as well. The difference between both signals is that the signal obtained in the hit segment is a net-charge signal with a non-vanishing integrated current, while on the transient signals the integral of the current over the collecting time is zero. The analysis of both net charge signals and transient signals enables us to determine the position of the interactions with a higher resolution than the segment size which is about few millimeters. For coaxial detectors, the radial position is derived from the charge collection time, named drift time, which depends on the distance to the electrode, and the integral of the current gives the charge which provides the energy measurement. The azimuthal position of the main interaction within a segment is extracted from the amplitudes of the mirror charges induced in the neighboring segments. The amplitude of the mirror charge signal depends both on the distance of the main interaction to the neighboring segments and on its radial position. Mirror charge signals in a n-type Ge detector are positive for interactions close to the core where mainly holes are moving and negative for interactions in the outer part of the detector where the net-charge signal

is dominated by the collection of electrons. Fig. 1.5 shows an example of pulse shapes measured on an AGATA detector with a collimated ^{137}Cs source. Three different events in which a photon is fully absorbed in segment F4 are shown: events a, b and c are depicted in green, blue and red, respectively. In segment F4 the net signal is shown, but in the other segments transient signals are observed. As events a and b are close to the core, the mirror signals in the neighboring segments are positive while for event c, they are negative. As an example we consider what happens in event c: the interaction has hit the segment F4 close to A4, so the amplitude in A4 is larger than in E4. To extract the height in which the interaction has happened, F3 and F5 segments are considered. The amplitude of the mirror signal in segment F5 is larger than in segment F3 so the interaction takes place closer to segment F5 [46].
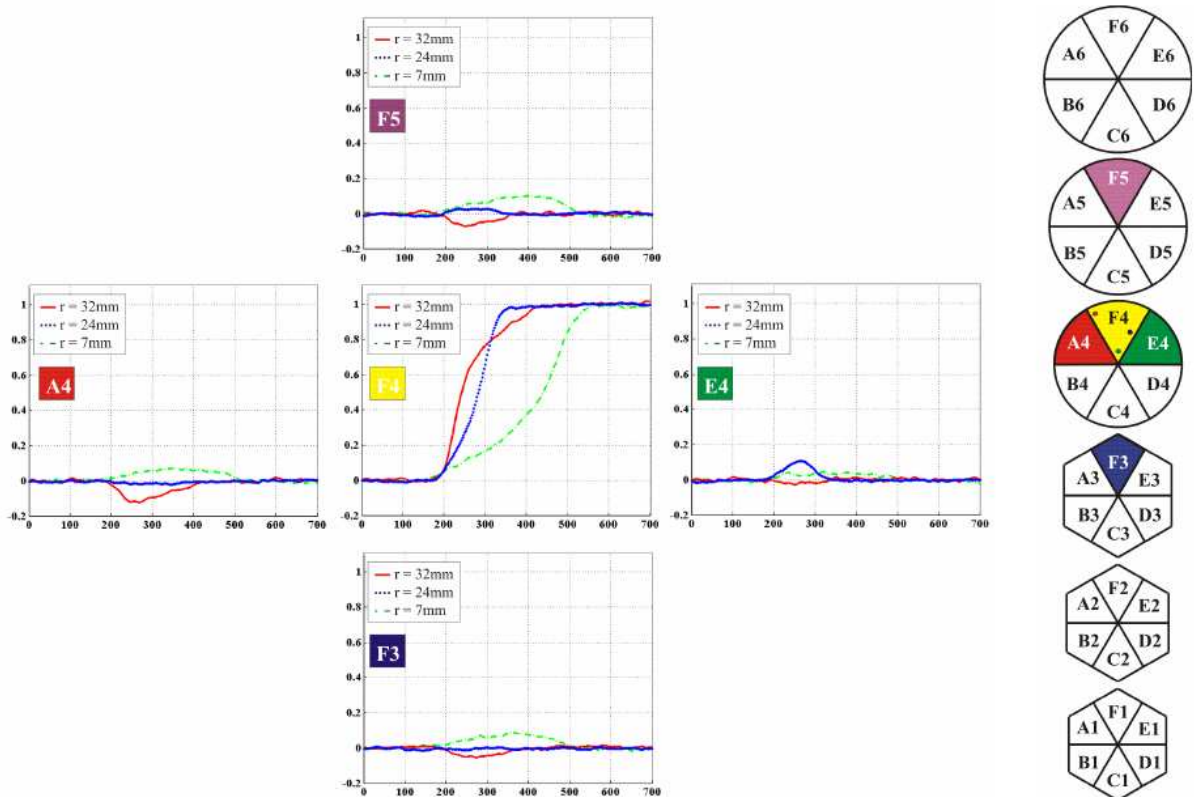
Figure 1.5: Net core and transient segment signals shaped in an AGATA detector when a γ ray is fully absorbed in segment F4. In green, blue and red are shown events a, b and c, respectively. The position is extracted from the net signal in F4 segment as well as from the amplitude and sign of the induced signals in the neighboring segments.

PSA algorithms work performing a comparison between the measured signals and a signal data base. The data-base can be obtained through Pulse Shape simulation algorithms. Many codes have been developed, as the MGS code (Multi Geometry Simulation) [53] developed at Strasbourg (IRes), used by the AGATA collaboration. It calculates the signal shapes in points belonging to a cubic lattice having 2 mm step. The calculations so made are really fast but not very accurate due to the simplicity of

the code which does not take into account the implementation of the inhomogeneities in the impurity concentration and in the charge mobility. In order to improve the simulated pulse data base, the crystals are scanned using radioactive sources. This method has been employed in Liverpool and in Cologne [51, 52]. It gives a very precise pulse shape information, despite of being a really slow process. To avoid the need of using simulations and to improve the timing, new instrumentation is now being developed, like the SAlamanca Lyso-based Scanning Array (SALSA) [54]. It performs the electrical signal characterization through imaging techniques, obtaining experimental data much faster than conventional scanning tables [55].

Different PSA algorithms have been developed by the AGATA collaboration. Actually, one of the most simple implementations is being used, the so-called Adaptive Grid Search algorithm (AGS), where the sampled pulse shapes are quickly compared to a database of pulse shapes for different interaction positions [47]. The algorithm was originally developed and tested on the experimental data from an "in-beam" experiment with MARS, the italian γ-tracking prototype [48–50]. The position calculation is based on the comparison between both measured transient and net signals and calculated signals from a fine grid of points in the crystal. The algorithm used for the comparison between the experimental and calculated signals is done to be independent on the interaction position. Therefore, no requirements about the geometry of the grid simulated basis used is needed. The signal comparison is done evaluating the following figure of merit (FOM):

$$FOM = \sum_{j \in NS} \sum_{i=T_0}^{T_{end}} (S_{ij}^m - S_{ij}^c)^p \tag{1.4}$$

where S_{ij}^m and S_{ij}^c are the measured and calculated signals respectively. The indexes j and i stand, respectively, for the segment index and sampled time.

The algorithm evaluates the FOM over all the calculated points belonging to the real segment and the smallest value identifies the coordinates of the interaction point. The FOM defined in this way becomes a metric for positive values of p, in particular for $p = 2$ is the Euclidean metric. All the parameters in the algorithm have been optimized in order to minimize the energy resolution, measured as FWHM after Doppler correction.

This algorithm shows some limitations as it searches only for one interaction point per segment. When there are more than one, it takes all interactions in the same segment as one placed in the center of gravity with energy equal to the sum of the individual energy depositions. Therefore, about 30% of statistic is lost in the experimental conditions because there is no possibility to identify those events. For events with more than one segment fired, a hit pattern deduced from geometrical considerations is established in order to avoid the interference in transient signals due to other interactions. For each net charge found all neighboring segments are considered when there is not another net signal on them. The best results are obtained taking into account neighboring segments where an overlapping of transient signals of two interactions is found. If these events are discarded a worsen energy resolution is found. An example of this pattern is showed in Fig. 1.6. The signals registered from both the central contact and the net-charge segment are not considered for the analysis since their inclusion in the FOM calculation results in a worsening of the energy resolution.
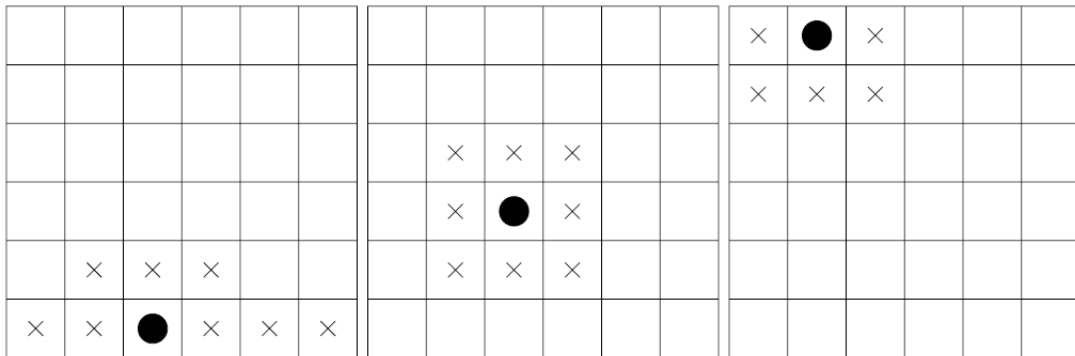
Figure 1.6: Pattern of one of the PSA algorithms developed for AGATA: the Adaptive Grid Search. Black points are the segments where the net charges are produced and with X are shown the neighboring segments.

In Fig. 1.7 is shown a comparison between the simulated and experimental data for an AGATA detector. An energy of 791 keV has been deposited in segment B4. In black are plotted the measured signals and in red the simulated ones. Different positions are compared in order to extract the interaction position, and the one in which both datasets are more compatible is assumed to be the real interaction point [56].

1.2.2 Gamma-ray tracking methods

We need to mention that in a large part of the energy range of interest in nuclear physics, the most probable interaction is the Compton scattering. When followed by a photoelectric in the last interaction point, the photon is fully absorbed. Conventional γ spectroscopy builds spectra from the deposited energy by the γ ray in the active volume of the detector. However, γ-ray tracking involves to build spectra from the reconstructed energy of the γ ray by means of disentangling all the interaction points which belongs to the same event and, later, determining the emission energy and the direction of the fully absorbed γ ray [57]. This concept needs of detecting all interaction points of the scattered γ rays into the active Ge crystal to combine them in order to find the right sequence which provides the initial energy of the photons (Fig. 1.8). The interaction points belonging to a particular γ ray are identified simply by their position and energy, being possible to determine when a γ ray has been fully absorbed. Events where their γ-ray energy is partially absorbed can be rejected decreasing the background and improving the P/T ratio. With this method it is also possible to avoid the problem of random and coincidence summing because the full γ-ray energy is obtained by summing only the interactions belonging to the track of this photon.

The position of the two first interactions allows to determine the emission angle of the γ ray from the source with respect to the detector where has impinged, which is particularly important when detecting radiation emitted by fast moving nuclei after a reaction since it determines the extent of the energy spread arising from the Doppler shift. Tracking will be able to determine this position with much better accuracy (about 2 mm FWHM) than existing detectors due to the high accuracy obtained by PSA. In addition, the location of the first and the second interaction points gives the scattering angle, by
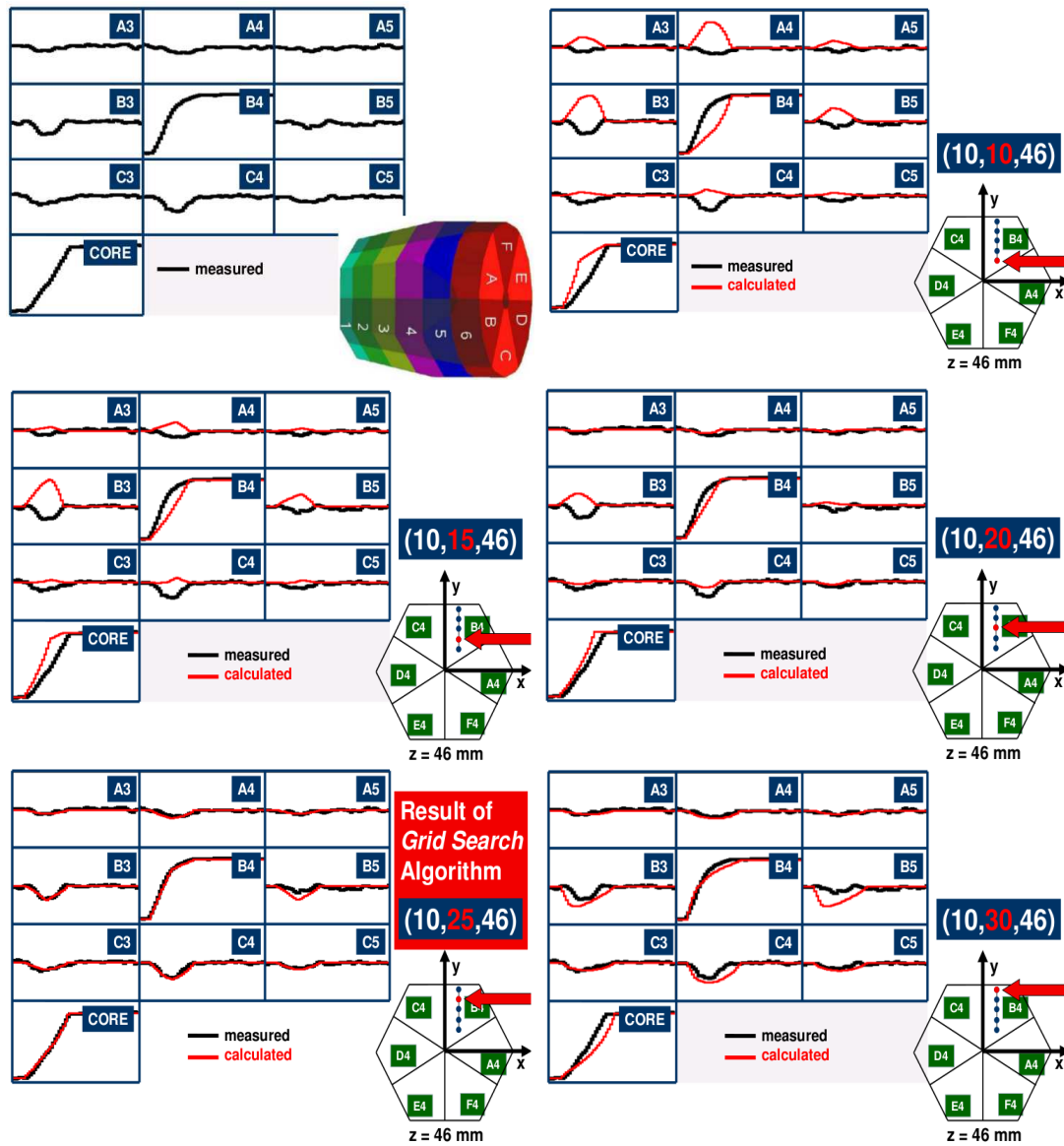
Figure 1.7: Comparison between the simulated and experimental data for an interaction of 791 keV in segment B4 of an AGATA detector. Black and red lines correspond to measured and calculated signals, respectively. After the matching the corresponding interaction position is obtained as (10,25,46).

the Klein-Nishina formula, which provides information about the linear polarization of photons. This information is essential to determine the parity of nuclear levels.

The fundamentals of the tracking algorithms are the electromagnetic radiation interactions with matter in the energy range interesting for nuclear spectroscopy, from 10 keV to 10 MeV (Fig. 1.9). The interaction mechanisms of photons in a solid state detector are restricted to photoelectric absorption, Compton scattering, electron-positron pair production and Rayleigh scattering. The relevance of each interaction mechanism
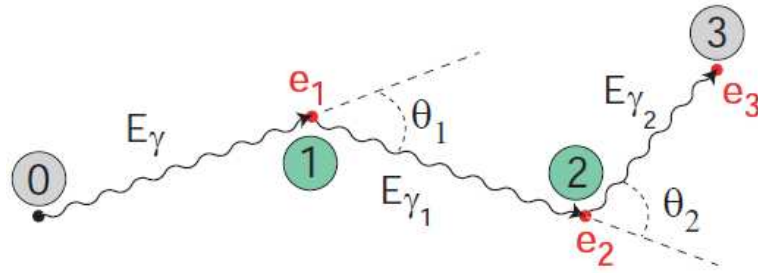
Figure 1.8: Path of the γ ray inside the detector reconstructed by tracking.

as a function of the energy is shown in Fig. 1.10. The mean free path of the photon inside the material can be estimated in this way by the relation between the γ-ray energy and the probability of interaction. The main interaction process in Ge for low energy ($E < 150$ keV) is the photoelectric absorption. As it can be seen in Fig. 1.10, γ rays with energy between 150 keV and 8 MeV are mainly interacting by a Compton scattering sequence and finally, they can be completely absorbed in the detector by a photoelectric interaction, if most of their energy has been lost in these sequence. Interaction position and energy are parameters which are known from pulse shape analysis of the signals corresponding to each interaction and both provide us a well defined relation between the scattering angle and the energy deposited through the Compton scattering, as seen as follows:

Figure 1.9: Interaction mechanism of photons with matter exploited by tracking algorithms.

$$E_{\gamma}^{'} = \frac{E_{\gamma}}{1 + \frac{E_{\gamma}}{m_0 c^2}(1 - cos\theta)} \tag{1.5}$$

This relation is valid for all the Compton interactions taking place in the sequence until the γ ray is fully absorbed by a photoelectric interaction or escapes out of the detector.

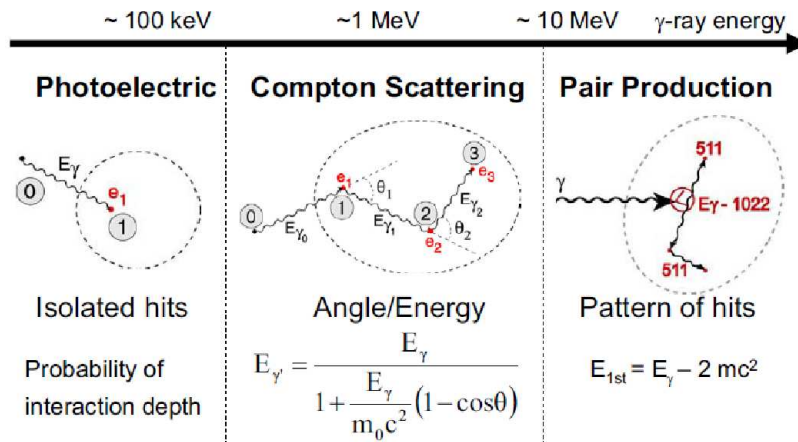Over few MeV, pair production becomes a significant process. In this process, for not too energetic γ rays, the total energy of the photon minus the $2mc^2$ needed to create the electron-positron pair are assumed by tracking algorithms to be deposited in the first interaction point. Regarding the Rayleigh scattering, this is not considered in most of tracking algorithms as there is no energy deposition. However, although its cross section is only significant for low energies, it should be included in the calculations because the direction of the γ ray is modified in the process.
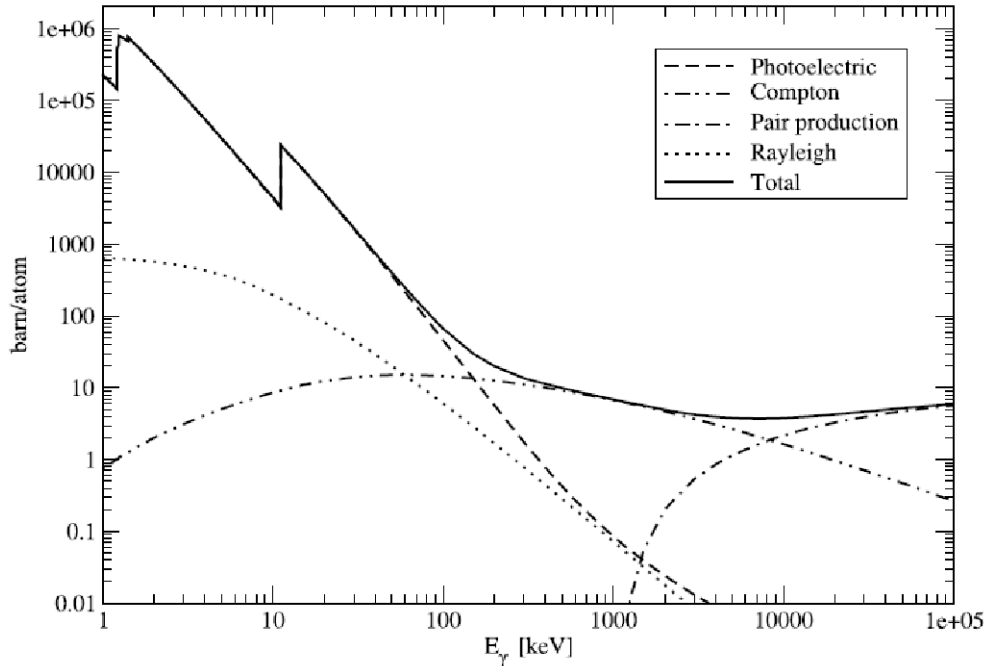
Figure 1.10: Interaction cross sections for a γ-ray in germanium [58].

The performance of the tracking codes depends strongly on the precision of the spatial determination of the interaction points of the scattered γ rays and, consequently, on the quality and reliability of the PSA technique. Different codes have been developed by the AGATA collaboration depending on the initial approach carried out to build the tracks: Back-tracking and forward-tracking algorithms. Back-tracking starts with the reconstruction of the interaction sequence taking as the initial point the last interaction. It is assumed that a photoelectric absorption has taken place and then it goes back trying to reconstruct the path of the γ ray until the initial source is reached. Codes based on this idea have been developed by J. Van der Marel [59] and by L. Michelina [60]. Conversely, forward-tracking codes make a clusterization of the interaction points according to their relative angular separation in order to assign each cluster to a given γ ray. The starting point is the emitting source and then the algorithm follows all the interactions until the photon is fully absorbed in the detector. This approach has been followed in the MARS Gamma Tracking code (MGT) done by D. Bazzacco [61], or in the Orsay Forward Tracking code (OFT) developed by A. Lopez Martens [62]. However, another approaches have also been tried like the fuzzy and the probabilistic codes.

A comparison between the backward-tracking and forward-tracking methods has been performed using the same Monte Carlo simulated data in order to clarify which is the best approach for the tracking code [63]. The forward-tracking algorithm has shown to be more efficient and to give a better P/T value than the back-tracking algorithm for all incident γ-ray energies and for all event multiplicities, except in the case of high-multiplicity rotational cascades in which the forward-tracking algorithm looses efficiency at low energy because of summing. Once here, the AGATA collaboration has been decided to use this kind of approach. MGT and OFT are very similar. The main differences between them are related to the thresholds considered for the different process: OFT considers photoelectric effect till 600 keV while MGT takes it into account till 1 MeV. MGT has better capabilities than OFT related to peak efficiency and P/T but it is less sensible to the emission point, therefore it cannot be used to perform background rejection. Currently, the OFT is being used by the collaboration, but still efforts are ongoing to improve the performances of the code.

Let us describe a typical forward algorithm in deep. The structure of these algorithms is the following:

- clusterization process

- reconstruction of the trajectories

- validation by means of a figure of merit

For the clusterization, two criteria are used: the Link and the Leader algorithms. In the first one, all the interaction points with an angular distance among them lower than a fixed value belong to the same cluster. In the second approach, the angular distance is evaluated respect to a reference interaction point. The Link algorithm gives better results for the efficiency and the P/T ratio for low multiplicity events but with high multiplicity the Leader algorithm shows a better response. Once the clusterization is done, the interaction points are randomly ordered in a scattering sequence having as starting point the position of the source. The energy of each γ ray, before each interaction, is calculated by adding the energies of the clustered points which is true only when the photon is fully absorbed. A complex figure of merit is used to evaluate the success of the process which includes weighting factors for the number of interaction points in the sequence, for the clusterization algorithm used and for the spatial isolation of the cluster related to other interaction points. The figure of merit also considers different contributions of the interactions related to their position in the sequence, as the energy deposited in the last interactions is lower and, therefore, the uncertainty in the position resolution is higher. In case of photoelectric interaction, the cluster contains only one interaction point and it should be distinguished from events in which the photon interacts once escapes from the detector. The figure of merit is calculated in terms of the mean free path of γ rays in Ge detectors and of the photoelectric probability. When a cluster of energy higher than 1,022 keV is found, the algorithm checks if there is any point belonging to the cluster with energy $E = E_0 - 1,022$ and if there are two sub-clusters inside with energy equal to 511 keV. If both conditions are fulfilled, a pair production event is assumed and a new figure of merit is calculated.

The values obtained with this figure of merit are compared with a threshold to determine whether the events have been well reconstructed or whether they should be rejected. The performance of the algorithm depends on the chosen values for the threshold. If low values are chosen, it can be assured that only good events have been reconstructed,

but also good events having high uncertainties on position and energy can be rejected as they give high values for the figure of merit. On the other hand, if high values are considered for the threshold, bad events can be considered as good ones, so a compromise between these values has to be adopted. Finally, the algorithm tries to recover some of the wrongly identified clusters. For example, one type of incorrectly identified cluster comes from a single γ ray being separated into two clusters. This γ ray can be correctly identified by tracking putting together all pairs of bad clusters. When the result gives a small χ^2, the γ ray is recovered by adding the two clusters. The clusters which do not satisfy any of the above criteria are rejected.

1.3   The Advanced GAmma Tracking Array (AGATA)

The Advanced GAmma Tracking Array, referred to by AGATA, is a highly segmented γ-spectroscopy system developed by an European collaboration [42–44]. The project was proposed in 1996 and after 12 years, the first commissioning tests were performed successfully at the LNL (Italy).

The design goals for the array have been the following:

- efficiency larger than 40% for events with γ-ray multiplicity 1 and larger than 25% for multiplicity 30;

- peak-to-total ratio around 60% for multiplicity 1;

- high granularity to minimize the probability of multiple hits in the same segment even for high γ-multiplicity events and to improve the Doppler correction.

- position resolution better than 5 mm FWHM for the single interaction point;

- capability to run at high counting rates up to 50 kHz for each germanium detector, either because of high radioactivity or because of high beam intensities;

- large free space to host ancillary detectors.

- capability to measure accurately the angular distribution and polarization of γ rays which is provided by the tracking process.

1.3.1   Setup design

Several options for the design of the spectrometer have been investigated by the collaboration, always having in mind a close-packed 4π geometry. The final design has been chosen using a Monte Carlo code based on GEANT4 which simulates the interaction of γ rays in the detector and allows inclusion of realistic shapes and passive materials [61]. The chosen geometry, shown in Fig. 1.11, is based on tiling the sphere with one hundred and eighty hexagons. The one hundred and eighty crystals are grouped into sixty identical triple clusters; each of them with three Ge detectors. In this configuration three slightly different shapes are required to maximize the solid angle coverage (blue, green and red crystals). The main characteristics of the geometry are summarized in Table 1.1.

As it has been discussed previously, in order to exploit PSA techniques achieving high position accuracy as required for γ tracking, the HPGe crystals should be highly
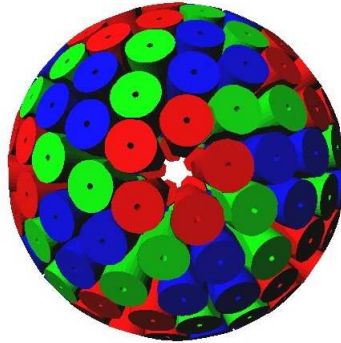
Figure 1.11: Geometrical configuration of the AGATA spectrometer obtained by Monte Carlo simulations. Green, blue and red colors correspond to the three different crystal shapes.

Table 1.1: Characteristics of the geometry of the AGATA array [43].

Number of crystals shapes	3
Number of clusters	60
Solid angle coverage (%)	82
Mass Ge (Kg)	362
Crystal face to center distance (cm)	23.1
Number of electronic channels	6660

segmented. A 36-fold segmentation with the outer contact divided into six azimuthal and six longitudinal segments which provide thirty six electronically independent outputs, plus the one from the core has been chosen for the coaxial Ge crystals in order to get a precision of few millimeters. The crystals have a length of 9 cm and an initial diameter before shaping of 8 cm. In order to fit into the 4π ball, the cylindrical crystals are tapered to form a hexagonal geometry at the front of the crystal with an approximated 8° tapering angle. A schematic view of the capsule is shown in Fig. 1.12. The detectors are located inside a 0.5 mm thick aluminum housing, with an internal distance between the crystal surface and the aluminum of 0.5 mm, instead of the 5 mm distance used in conventional detectors, such as EUROBALL or MINIBALL. In this way, the detector vacuum is separated from the cryostat vacuum and the capsules can be packed in a common cryostat Fig. 1.13.

The first stage of AGATA, the so-called "The Demonstrator", is currently working at LNL (INFN, Italy) (Fig. 1.14). It consists on a sub-array of five triple cluster modules, therefore with fifteen capsules. It is powerful by itself comprising the detectors, the electronics, the acquisition system an all associated infrastructure developed for the full AGATA. At the AGATA detector-to-target distance of 23.5 cm, which corresponds to the nominal position, the Demonstrator has an efficiency of 3% at 1.3 MeV for multiplicity 1 and 2% for multiplicity 30.
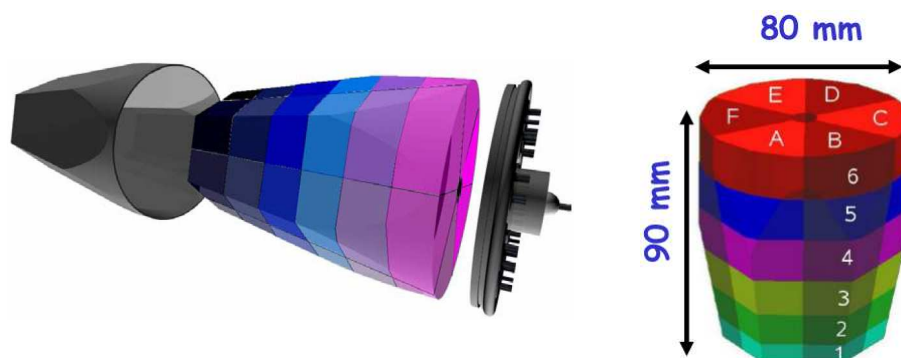
Figure 1.12: Schematic draw of an AGATA capsule with its segmentation.
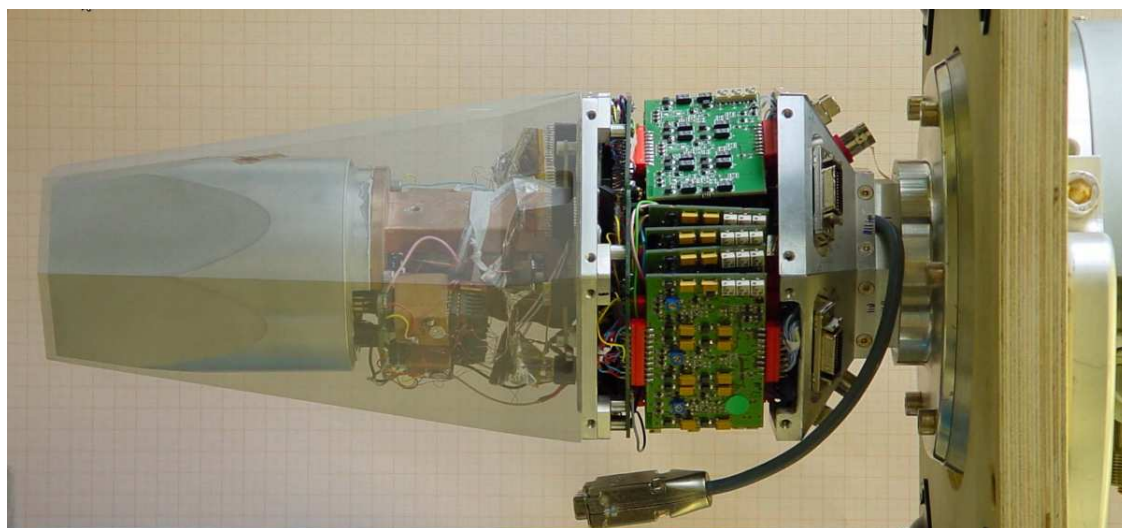
Figure 1.13: Detailed view of the AGATA capsule with its preamplifier.

1.3.2   Data acquisition system and electronics

The AGATA array requires a significant development in digital electronics and the associated data acquisition system to process the signals from the Ge detectors. The full system has to deal with 6600 channels and a possible rate up to 50 kHz for each detector. This causes an extremely high data flux which is too large to be stored and which has, therefore, to be analyzed in real time in order to extract the useful physical information. This is done by the Data Acquisition System (DAQ) shown in Fig. 1.15 [44, 64].

The whole set of thirty seven charge pulses from each detector in the array have to be digitized and stored. The electronics principle of AGATA is to sample these outputs with fast ADC's to preserve the full signal information in a clean environment so that accurate energy, time and position can be extracted. From a technical point of view, the Data Acquisition System (DAQ) considers the complete array as an aggregation of individual crystals, where data are synchronously stored and time tagged by the Global Trigger

Figure 1.14: View of the current AGATA stage: The Demonstrator.

System (GTS). For this reason, the data flow for each detector starts from the digitizers for each detector channel to the PSA farm, where the position of the γ-ray interactions is estimated (Fig. 1.16).

The model for the AGATA readout, shown in Fig. 1.16, is composed by two types of trigger: a local trigger signal which generates a signal by using the central core contact of each detector and an external global trigger which ge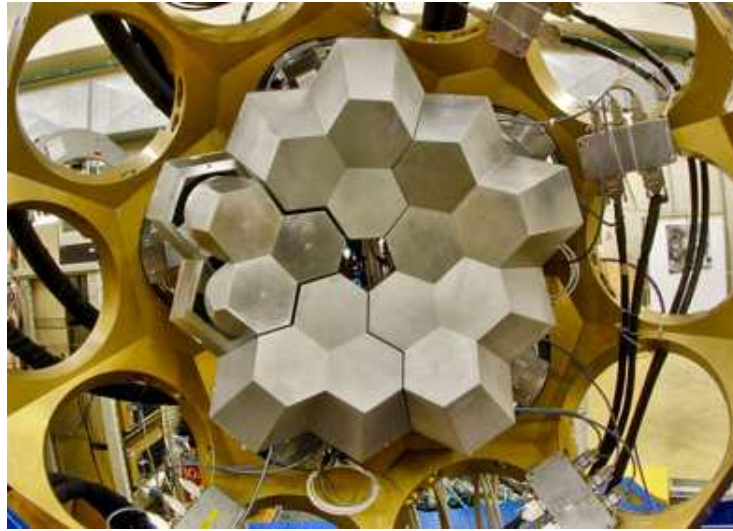nerates the validation from the central trigger processor. This processor shares a global time reference supplied by the GTS system, which is distributed through an optical fiber network.

The main components of the electronics are described in the following paragraphs. The preamplifiers are the only analog part in the whole electronics and constitutes the real front-end electronics of the apparatus. They can simultaneously read out the segment and core signals of an AGATA detector through advanced charge–sensitive resistive feedback preamplifiers. There are two parts in the preamplifier stage. The cold part is located close to the detector electrodes, at cryogenic temperatures, where a Field Effect Transistor (FET) coupled with both a capacitor and a feedback resistor performs the first amplification avoiding most of the inter-channel crosstalk. The warm part is out of the cryostat, at room temperature, where the signal coming from the cold part is aconditionated to be sent to the digitizer stage. After the preamplifiers, the digitizers are the first digital electronics in the data flow and the last ones before leaving the experimental room. They needs to be placed at a maximum distance of 5 meters to the detectors. Their task is to digitize the preamplifier signals at 100 MHz with 14 bit ADC's and to send them through an optical link, by groups of six, to the preprocessing cards. Each digitizer, using custom mechanics in a water-cooled standalone box, needs eight cards: six for segments, one for core and one for power supply. The preprocessing system performs digital signal processing to extract the useful information for each detected signal, i. e. energy, time and a selection of the signals of interest made up by the segments where the interaction has taken place. To be able to perform the requested operation in real time, which means to analyze a sample every 10 ns, the signal-processing algorithms are implemented
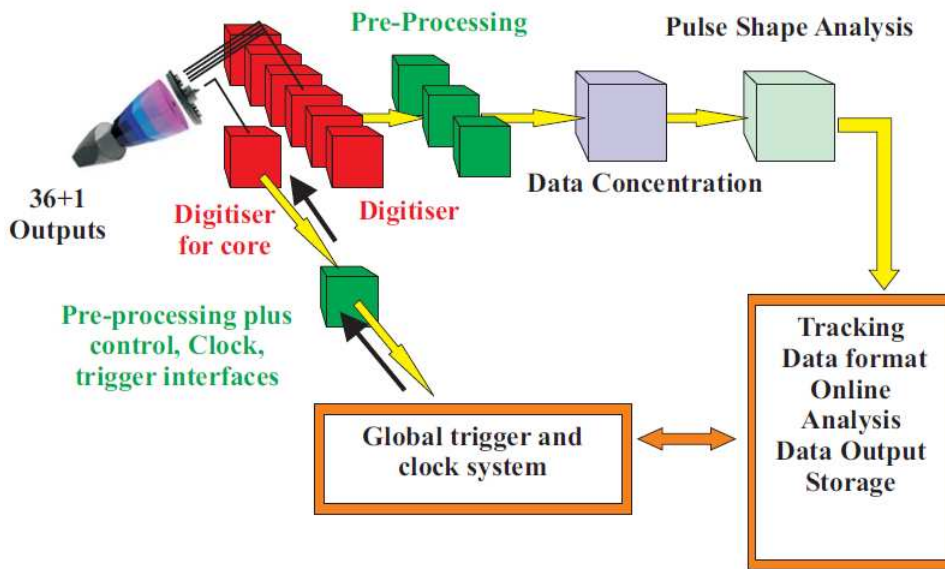
Figure 1.15: Schematic view of the DAQ of AGATA.

into powerful highly-parallel FPGA's (Field Programmable Gate Array). These cards transmit their outputs to the pulse processing part of the system which consists on a farm of computers, where PSA is done.

In the AGATA scheme, the ancillary detectors can use a similar digital electronics but can also use a classical VME-based analogue DAQ. In this case, the time correlation to the AGATA detectors is performed by a dedicated VME module, called AGAVA, which interfaces to the GTS system by reading its clock and time stamp, then by sending local trigger requests and finally getting the corresponding validations.
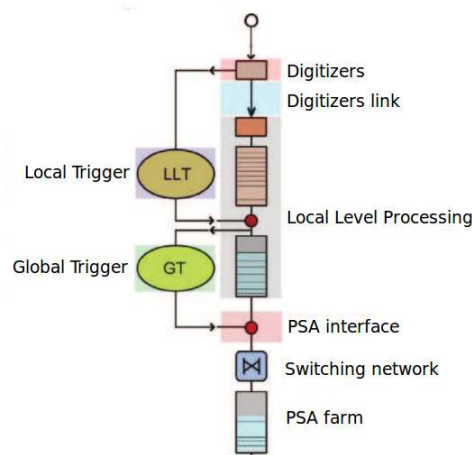
Figure 1.16: Data flow for the AGATA readout.

Chapter 2

Conceptual design of a Ge array with imaging capabilities for DESPEC

2.1 The NUSTAR-FAIR facility

NUSTAR acronyms of NUclear Structure, Astrophysics and Reactions [65] is part of the Facility for Antiproton and Ion Research (FAIR) [66] devoted to Nuclear Physics experiments to be performed with the exotic beams produced with the Super-FRS fragment separator, which constitutes one of the pillars of the FAIR scientific program. NUSTAR is composed by several projects which cover the fundamental aspects arisen nowadays on the nuclear structure investigation. The two parts of NUSTAR that are relevant for this work are the experiments HISPEC, from HIgh-Resolution In-flight SPECtroscopy [67,68], and DESPEC, from DEcay SPECtroscopy [68]. Before going into a detailed description of the experimental requirements of these sub-projects, a short description of the core instrument of NUSTAR, which is the fragment separator Super-FRS, is necessary.

The Super-FRS is a large-acceptance superconducting fragment separator [69]. It will be the most powerful in-flight separator for exotic nuclei at relativistic energies. Rare isotopes of all elements up to uranium can be produced with a spatial separation within some hundred nanoseconds, thus very short-lived nuclei can be studied efficiently. Comparing to the actual FRS [70], the momentum and angular acceptance have been increased, as it is shown in Table 2.1. The FRS was designed for the production and separation of projectile fragments. Transmissions from 20% to 70% are achieved depending on the mass region, but only about 1%-2% is obtained for the transmission of fission fragments. The high interest of fission fragments as radioactive secondary beams has promoted to solve this problem increasing the Super-FRS phase space. The ion-optical resolving power has been preserved to guarantee the separation quality and the momentum resolution for the spectrometer option. The separation method of the Super-FRS is based in a dipole-ΔE-dipole scheme like the present FRS [70], i.e. a two-fold magnetic rigidity analysis before and after a thick energy degrader providing spatially separated isotopic fragment beams.

Table 2.1: Momentum and angular acceptance of the FRS and Super-FRS [71].

Facility	$\Delta p/p$ (%)	$\Delta\phi_x$	$\Delta\phi_y$	Resolution
FRS ($B\rho_{max} = 18$ Tm)	±1%	± 13 mrad	± 13 mrad	1500 (20π mm mrad)
Super-FRS ($B\rho_{max} = 20$ Tm)	±2.5%	± 40 mrad	± 20 mrad	1500 (40π mm mrad)

The Super-FRS magnetic system will consist of three branches connecting different experimental areas: the Low Energy Branch, where the HISPEC and DESPEC projects will be installed; the High Energy Branch, where complete kinematic reaction studies will be performed; and the Ring Branch, where a novelty will be electron scattering from exotic nuclei in the eA collide section.

The secondary beam production in the Super-FRS will be made, as it was at FRS, through what is known as the in-flight technique [72]. It performs the separation of the reaction products taking advantage of the reaction inverse kinematics. The fragment separator acts as an spectrometer separating through magnetic fields, as well as energy degraders, to select specific isotopes depending on their magnetic rigidity and Z. Z identification is performed measuring ΔE with ionization chambers.

Since the primary beam is made of relativistic heavy ions, the radioactive ion beam production target can be relatively thick, increasing the secondary beam sensitivity. At each experiment the target thickness is determined by the energy loss, the secondary reaction, the already produced radioactive ions and the straggling within the target. This method can be employed for short lived nuclei (μs) as the time from the production to the detection stage, the TOF, is in the range of hundred of nanoseconds. The in-flight production technique allows to reach extremely exotic nuclear species. However, the drawback of the in-flight production is the high background due to the interaction of the beam ions along the fragment separator elements as well as with the elements of the own setup. One of the first experiments performed in this way was the one done by T. Symons to observe for the first time the ^{28}Ne and ^{35}Al [73]. However, the real impact of the technique arrived in 1985 with the measurements of the interaction cross sections and radii for ^{6}He and ^{11}Li, showing the existence of halo nuclei [74, 75].

Depending on the measurement itself, the Super-FRS can be set to operate in two different modes: achromatic or monochromatic mode. In the achromatic mode, the dispersion in the position is really small, but the energy dispersion is large; therefore in the focal plane different spots corresponding to different nuclei will appear. In the monochromatic mode it is just the opposite: the energy dispersion is low, so, in the focal plane, only one not well defined spot will be displayed, being the energy dispersion for a single nuclear specie quite low.

2.1.1   The HISPEC and DESPEC experiments

HISPEC is devoted to high resolution in-flight spectroscopy by means of nuclear reactions of the secondary beam with a target. At the HISPEC set-up [68] these kind of studies can be carried out with both radioactive beams of intermediate energies, as delivered by the Super-FRS, and further decelerated beams of energies around the Coulomb barrier. Single-step Coulomb excitations and fragmentation reactions at intermediate energies as

well as inelastic scattering, transfer reactions and fusion evaporation reactions at lower energies will provide information about transition probabilities, single particle spectroscopic factors, high spin states, etc. By observing the single particle and the collective vibrational or rotational character of the states, we can conclude about basic properties of a nucleus such as its shape. To achieve this objective, the best tool is the high resolution γ spectrometry with Ge detectors to measure the gamma de-excitation of the levels populated. Actually, at HISPEC the core instrument is the already described AGATA array. In addition, beam tracking and identification detectors will be placed before and downstream after the secondary target to reinforce the experimental performance: charged particle detectors, a plunger, a magnetic spectrometer and other ancillary detectors.

The DESPEC project also requires a high resolution γ-ray detector array and a substantial part of the work performed in this PhD thesis is focused to identify the best array and the best tracking technology for DESPEC. The DESPEC experiment is devoted to the investigation of the nuclear structure measuring the de-excitation transitions emitted following an isomeric or radioactive α, β or more exotic decay. Decay studies are the starting point in the investigation of exotic nuclei, since they prove the existence of the nucleus and provide information on its decay mode and lifetime. Even with a vague estimation of the lifetime of an isotope, basic information about its decay is extracted. Information of the first excited states in nuclei far from stability is frequently obtained by means of decay spectroscopy. If the number of decays is high enough, it will be possible to do precise spectroscopy and fundamental issues as isospin symmetry in mirror nuclei or Gamow-Teller quenching in beta decay can be studied. Fermi super-allowed transitions in odd-odd nuclei with N=Z will be used to investigate the unitarity of the CKM matrix of the electroweak interaction in the Standard Model. For nuclei close to the drip lines, unusual decay modes can be expected such as beta-delayed multi neutron emission, beta-delayed fission or even direct neutron or proton radioactivity. DESPEC also intends to study the de-excitations of isomeric levels with lifetimes of the order or longer than the Super-FRS TOF. In Fig. 2.1 the expected fragmentation production rates for nuclei with half-life higher than 100 ns, the Super-FRS TOF, are shown. As we can see in this figure, many exotic nuclear species far from stability will be reachable, in particular, for neutron-rich nuclei. The relative low production of some species is not an un-surmountable issue in decay spectroscopy since no secondary reactions are needed and only the implantation-survival has to be taken into account.

The activity related to the high resolution HPGe detectors at DESPEC will follow up the present RISING (Rare ISotopes INvestigation at GSI) setup [76,77] in its stopped beam configuration, meanwhile HISPEC will be the continuation to its fast beam configuration. The RISING collaboration has conducted over the last four years several campaigns of γ-spectroscopy experiments making use of the radioactive beams produced with the SIS/FRS facility at GSI, Darmstadt. The γ-ray detectors used in the RISING experiment are, for the stopped beam configuration, fifteen of the cluster Ge detectors from the EUROBALL spectrometer and, for the fast beam configuration, eight sixth-fold segmented MINIBALL triple Ge detectors in addition to the previous setup. The RISING array is, up to now, the most efficient γ-ray detector system coupled to an in-flight radioactive beam facility in the world. Efficiencies of 11% for γ rays of 1.3 MeV can be reached for the stopped beam configuration where electromagnetic decay studies of the daughter nuclei in the radioactive disintegration, including isomeric states, are performed with beam intensities well below 1 particle/s. For the fast beam configuration, designed to detect γ rays emitted
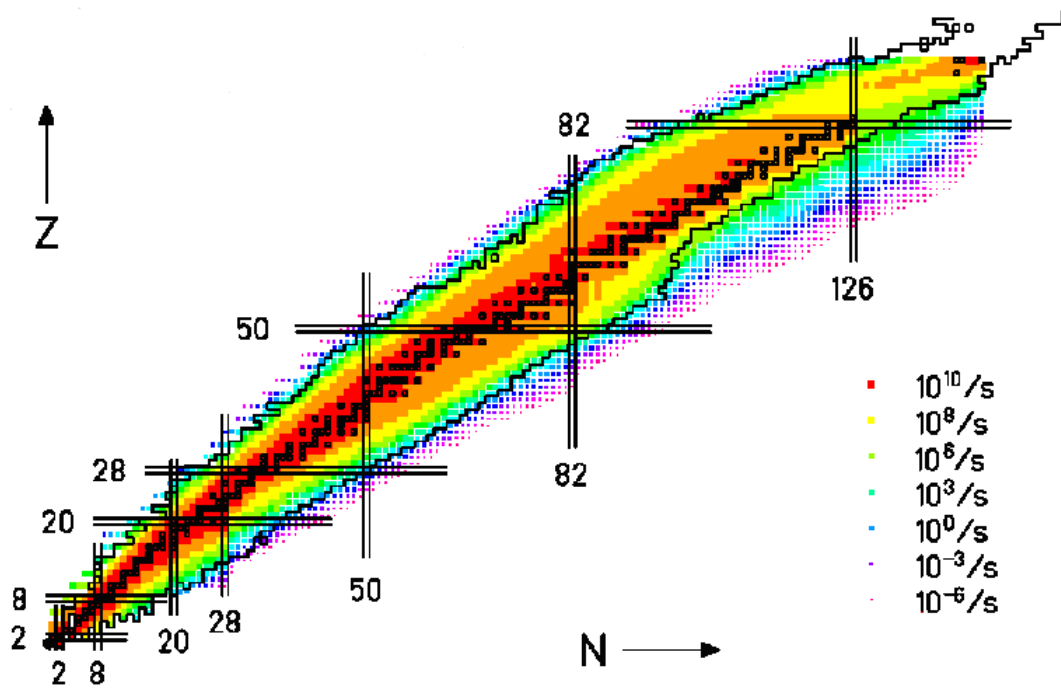
Figure 2.1: Fragmentation production rates for nuclei which half life is higher than 100 ns.

by radioactive beams moving at relativistic energies, and being excited via Coulomb excitation or via fragmentation reactions at a secondary target, efficiencies about 3% at 1.3 MeV can be obtained. In the RISING stopped beam campaign a wide range of isomeric states have been identified in, for example ^{82}Nb [78], ^{86}Tc [79] and ^{204}Pt [80]. In the fast beam configuration, intermediate energy Coulomb excitation was used to measure shape co-existence in ^{134}Ce and ^{136}Nd [81] or the reduced probability transition (B(E2: $0^+ \rightarrow 2^+$)) in the neutron-rich ^{56}Cr and ^{58}Cr [82].

Limitations imposed by the setup are related to the large Doppler effects and to the background caused by atomic processes and unwanted nuclear interactions. The main atomic radiation contributing to this background are K-and-L-shell X rays from ionized target atoms, radiative electron capture of the target electrons into the projectile K and/or L shells, primary bremsstrahlung from target electrons produced by the collisions with the projectile, secondary bremsstrahlung from energetic knock-out electrons which re-scatter in the target and/or the surrounding material [83–85]. The atomic cross-sections of all these processes depend strongly on the atomic number of projectile and target. Based on experimental results, a limitation on the energy of the incident beam of 100 A MeV has been imposed for γ rays lower than 400 keV.

The Ge array required for the DESPEC experiment needs to have high efficiency and granularity to deal with the background originated in relativistic heavy-ion reactions. Higher the granularity of the Ge array, better the resolving power, diminishing the risk for the detector to get blind by the flash of particles coming in the implantation. Moreover, the granularity is directly related to the possibility of measure isomers with short half life;

as the granularity increases, the position can be better determined and, therefore, as it will be shown later, the quality of imaging to associate the emission with the isomer also increases. Overall, the best experimental situation is obtained when the origin of the γ ray can be determined because in this case tracking can be improved. This is one of the main reason to develop a highly segmented Ge array based on planar detectors as being those with highest position resolution. The successful correlation of the implanted ion and its emission will allow to reach higher implantation rates by measuring coincidences. Besides, the emission position information will give access to the analysis of γ-ray polarization and angular correlations; without forgetting, as mentioned previously, that tracking will also contribute to the decreasing of the background values.

The initial concept for the DESPEC high resolution setup is shown in Fig. 2.2 and it is constituted by the following building blocks:

- An implantation Double Side Silicon Detector (DSSD) called AIDA (Advanced Implantation Detector Array) [86], which acts as an active stopper and whose aim is to identify the implantation position of the ions and to detect the charged signal of the decay, therefore, α, β and β^+ particles.

- the high granularity Ge detector for γ-ray spectroscopy and

- the neutron detector [87].

Besides, it is foreseen to use fast $LaBr$ detectors, a total absorption spectrometer and additional detectors for g-factor and quadrupole moment measurements.
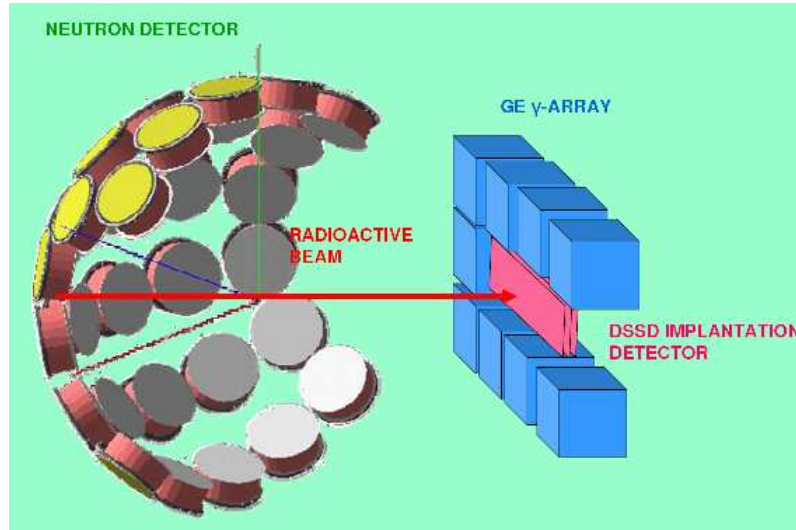
Figure 2.2: Schematic view of the main components of DESPEC [88].

The implantation of the ions in AIDA before the decay will be a common feature in most of the experiments planned for DESPEC. An important requirement for AIDA is the high pixelation, necessary to unequivocally correlate implantation signals with signals following the decay process in AIDA or any other detector of the setup. To achieve these objectives, AIDA will use large area double-sided silicon strip detectors (DSSSD) and a

specific integrated circuit (ASIC) for the analogue treatment of the signals. The Ge array, surrounding the implantation detector in a flexible geometry is the basis of this set up. In addition, the neutron detector will be placed surrounding both the Ge detector and AIDA. Complementary, g-factor and quadrupole moments measurements are expected to be performed if the final design of the Ge array does allow it.

2.2   From tracking to imaging arrays

Currently available gamma tracking algorithms developed for multidetector arrays such as AGATA [63,89] and GRETA [90,91] show a limited sensitivity to determine the origin of the radiation. Nevertheless, a condition on the γ-ray origin would help to reduce the background, specially in isomer-decay spectroscopy. For this reason, the application of Compton imaging to nuclear structure experiments is under development. The concept of Compton imaging was first introduced about 30 years ago by Todd for nuclear medicine [92] and by Schoenfelder for astrophysical applications [93]. However, only recent developments in three-dimensional position-sensitive HPGe detectors and improvements in electronics provide the basis to achieve an imaging system with high resolution γ-ray detectors [94,95]. In our case, Compton imaging serves to reconstruct the emission point of the γ rays in the implantation plane and, therefore, to identify the position of the source. For stopped beam measurements, such as isomeric decay or g-factor determinations, where the secondary beam is slowed down in an active stopper, imaging would increase the overall efficiency identifying the origin of the photons and, therefore, giving the implantation position. Then, with this technique, it is also possible to distinguish γ rays emitted by the source from those originated outside, providing a new method to reduce the experimental background which is critical in experiments with broad time conditions.

Let us shortly see the fundamentals of imaging. Let us think in a photon which enters in a detector and interacts via Compton scattering until it is finally absorbed by a photoelectric effect. Through the Compton scattering formula it is possible to calculate the angle of the incident γ ray by measuring the first and the second interaction points. Both the deposited energy in the first interaction and the energy of the incident γ ray determine the scattering angle.

$$cos\theta_c = 1 - \frac{(E_\gamma - E_\gamma')mc^2}{E_\gamma' E_\gamma} \tag{2.1}$$

If the direction of the Compton-scattered electron is not measured, it is not possible to determine the scattering plane and, therefore, it is only possible to deduce the position of the source as being within the intersection of a cone with the plane containing the source (Fig. 2.3). The symmetry axis of the cone is determined by the position of the two first interactions and the opening angle is given by the Compton scattering angle of the first interaction. By analyzing the superpositions of the cones obtained for different γ rays, the source distribution is reconstructed.

The quality of imaging with Ge detectors depends on the reduction of uncertainties induced by both the opening angle and the symmetry axis of the cone. The uncertainty due to the opening angle is caused directly by two effects: the energy resolution and the
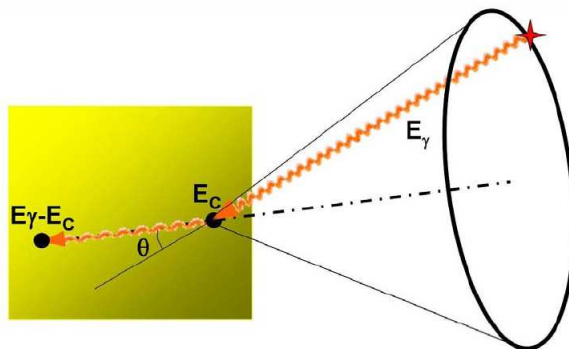
Figure 2.3: Schematic view of the imaging process.

Compton profile. The scattering angle, as it has been mentioned before, is obtained by the Klein-Nishina formula, therefore, it clearly depends on the detector energy resolution. This formula is obtained assuming that the scattered electron is free at rest but in reality it is bound and it has a finite momentum whose distribution is called Compton profile. Because of this momentum distribution, the scattered electron energy will depend not only on the scattering angle but also on the initial momentum, resulting in an inaccuracy in the γ scattering angle determination if the standard Compton formula is used. More details can be found in the work of Y. Du and collaborators [96], where it is shown that the effect of the Compton profile can be even larger than the one due to the energy resolution. On the other hand, the position resolution obtained with PSA techniques is affecting the determination of the two interaction points position and, therefore, the determination of the cone axis which indirectly also affects the angle determination.

In order to evaluate the influence of the different factors on the imaging performance with Ge coaxial detectors, a comparison of energy, position and Compton profile derived uncertainties has been made [97]. The test was performed at the Laboratori Nazionali di Legnaro using a ^{60}Co radioactive source positioned at 1 m from the AGATA prototype detector S#001. The intrinsic energy resolution of the detector is a function of the energy with the following shape:

$$FWHM = \sqrt{a + bE} \qquad (2.2)$$

assuming respectively 1.0 keV and 2.3 keV at 122 keV and 1,332 keV photon energies, respectively. Regarding position uncertainty an energy-dependent position resolution was considered which produces 5 mm FWHM for 1,332 keV photons. The contribution of the Compton profile to the overall uncertainty was taken from ref. [98]. This study concluded that the most important source of uncertainty is the position resolution, so PSA techniques are the key to do imaging.

It is well known that position resolution is considerable better in planar Ge detectors [99,100] than in coaxial ones [101]. Because of this fact, currently, tracking and imaging capabilities of planar detectors are investigated. The use of planar detectors was already explored during the preparatory phase of AGATA [102,103] but the production technology of planar detectors limited the thickness by < 2 cm. Although, nowadays, thicker

planar crystals can be produced, to achieve a good enough efficiency, these γ-tracking arrays should be built based on stacks of planar detectors, each of them with a highly pixeled electrode or with opposites electrodes pixeled in perpendicular bands. However, the main difficulty remains regarding the use of planar detectors: the guard ring on the crystal edge creates a dead layer which makes the solid angle and efficiency to depend on its thickness. Furthermore, the high pixelation leads to a large number of channels, one per electric segment.

2.3   Basic requirements of the Ge array for DESPEC

Let us fix some ideas already mentioned before starting the description of the study performed in this work to obtain the most reliable design for the DESPEC Ge array. According to the requirements of the experiment, considering the low production of the species of interest and the high background of the setup, the specifications of the Ge array for DESPEC have to fulfill what follows:

- High efficiency,

- high granularity and

- good position and energy resolution to perform tracking and imaging.

Regarding the latter, tracking is needed to improve the peak-to-total ratio by adding events corresponding to the same track. A further reduction of the background comes when tracking is able to distinguish not fully absorbed γ rays. Imaging would increase the overall efficiency of the experiment by means of helping to find the origin of the emitted γ ray in the implantation position, which also would achieve a further reduction of the background coming from external sources.

High granularity is needed in order to avoid the lost of efficiency due to the flash in the implantation reaction. This flash is related to the implantation of high energy ions in the Si-DSSD at the focal plane. When the granularity increases, the probability of measuring the γ rays emitted in the decay is higher because the signals coming from the interference of the flash can be separated from the signals of interest.

On this basis, the most suitable approach considered by the collaboration for the Ge array is based on planar detectors. The technical proposal (Fig. 2.4) for this Ge detector array [68] foresees a setup of twenty four stacks, with three planar detectors each one, placed surrounding a 24*8 cm^2 focal plane where AIDA, the Si-DSSD system, will be located. Nowadays tracking feasibility has been studied only for coaxial detectors [59, 63, 91]. Therefore, our study with planar detectors would be useful to get information about this promising application. The first stage of the study has been done through Monte Carlo simulations to get the optimum geometrical design of the setup attending to efficiencies and P/T.

2.4   MC simulations with the Geant4 toolkit

The best method to optimize the specifications regarding mainly the geometry of a γ-spectroscopy system is the Monte Carlo simulation technique. Monte Carlo (MC) methods
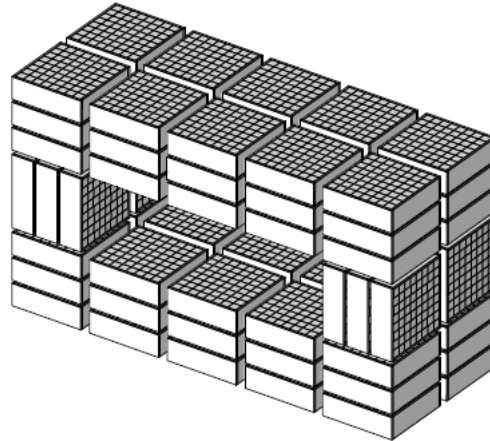
Figure 2.4: Current technical proposal for DESPEC based on planar detectors [104].

were introduced by Fermi, Ulam, Von Neuman and Metropolis during the Manhattan project in 1943 for neutron transportation calculation. The MC approach provides a method to solve probabilistic problems, where analytical calculations are very complex, in order to obtain an approximate value for the solution [105]. Therefore, this method is a good way to describe the behavior of particles because the interaction of particles with matter is governed by probability distributions. This procedure reproduces the behavior of both, systems and physics process through probability distributions of random numbers [106]. The sequence of numbers used for the calculations is not random itself because it is generated by algebraic algorithms. So MC method works with pseudo-random numbers. Nevertheless, they almost have the same properties as random numbers. The sequence can start in a specific point as well as in a random way. The first option is useful for testing the codes because in this case all calculations should give the same value. The second one is the right one to obtain the simulated results because contains the statistical fluctuations, proper of the interaction processes, which arises when the MC simulation run more than once. Otherwise, several runs make the results to improve. MC simulations are highly useful to solve problems in complex experimental conditions, for example with multiple detectors.

In a Particle and Nuclear Physics context, the MC simulation of an experiment means, by one hand, the generation of the particles produced in a reaction or in a decay and, on the other hand, the particle transportation into the matter, including the detection systems, based on the interaction probabilities in the different mediums. At present the most complete toolkit for the simulation of Nuclear and Particle Physics experiments is Geant4. GEANT, acronym of GEometry ANd Tracking, is a tool with several versions. Up to Geant3 they were developed at CERN in Fortran language. But since 1994 is being developed and maintained by an international collaboration as an extended and improved C++ version. Nowadays, Geant4 is free access and its documentation, user manual, database, etc. can be downloaded of its web page [107, 108].

The first step to perform a simulation is the implementation of the system geometry. It should be described with the dimensions, shapes and materials of which is composed, in the *DetectorConstruction* class. A complete design of the geometry can be implemented

to reproduce with high precision the detectors used for the experiment. Once the geometry is defined, the particles should be generated in a random way which involves to create an event. This is done specifying the properties and type of the particles that will be thrown by the *PrimaryGenerator* class and controlling the information at event level in the *EventAction* class. The part of the code which checks the run of all the sequences of events is the *RunAction* class. After the particle is generated, it travels through the implemented geometry until an interaction happens. The distance between two consecutive interactions is the step, the object in which the elemental information for the transport of the particle through the material is contained.

To determine which interaction takes place, different aspects are considered. First of all, Geant4 makes a classification of processes attending to the step:

- PostStep Processes: when they take place once the step has finished (i.e. Compton effect).

- AlongStep Processes: when occurring while the step is happening (i.e. Ionization).

- AtRest Processes: when taking place once the step has finished and the particle is at rest (i.e. Decay).

The processes included in the simulation, which are classified within the three types mentioned above, are chosen by the user, being possible a combination of different types; i.e. bremsstrahlung can be considered as PostStep and AlongStep. Once the processes are selected from the Geant4 package, they are available for each interaction. Two methods are applied in this case: *IsApplicable* and *GetMeanFreePath*. The first one evaluates for the generated particle what processes can be applied. When a process is accepted the second method makes the calculation of the mean free path (λ) as a function of its cross sections. The cross sections are taken from experimental databases: EADL (Evaluated Atomic Data Library) [109], EEDL (Evaluated Electrons Data Library) [110] and EPDL97 (Evaluated Photons Data Library) [111]. Geant4 chooses as right process the one with smaller λ once is weighted by using a certain random distribution. Once the process is determined, the probabilities are updated for the next interaction. At the same time the properties of the particle (kinetic energy, position and time) are also updated. For our particular case, γ rays are the initial particles. When photons interact with matter, electrons and positrons are produced having to be also considered. For our range of energy, low-energy electromagnetic processes should be used. The processes defined in the low-energy electromagnetic package are valid in a range from 250 eV to 100 GeV. Processes not defined here, as being not properly low energy processes such as electron/positron annihilation, are taken from the Standard electromagnetic package.

The processes considered in our simulations have been the following: related to γ rays, pair production, Compton scattering, photoelectric absorption and Rayleigh effect; and for light charged particles, ionization, bremsstrahlung and multiple scattering. When the light charged particle is a positron, positron-annihilation is also considered. Once the tracked particle suffers an interaction it can disappear, create a new particle or simply change its kinematic. The trajectory of the particle is followed until it disappears or becomes at rest, or keeps a small energy, below a threshold, that is considered to be absorbed in the last interaction. This lower energy limit is established in the code in terms of a length value, the step length, and converted directly to an energy value. The useful information regarding the interaction happened is generated at the step level. After each interaction

the response of the detector is obtained and information like energy deposited, position, momentum, time, secondary particles generated, etc can be extracted. The control of the information is made by the *SteppingAction* class. It is directly related to the *Hit* class, where the interactions are stored, and to the *SensitiveDetector* class, where the detector itself is declared as sensible. Regarding the visualization of the implemented geometry, as well as the physical events occurred, different displays can be used. In our particular case, the *vrml* viewer has been used.

Geant4 has been widely validated for photons and low-energy electromagnetic processes, the expected processes for DESPEC where γ rays emitted in a range from 10 keV to 10 MeV are foreseen [112–114]. Once it is assured that the results provided by Geant4 are good enough, the toolkit can be safely employed to determine the response of a Ge detection system designed for photon measurements. In our particular case, we need to perform a study which leads us to determine the more suitable characteristics of a Ge detection system made by planar detectors, placed surrounding a rectangular focal plane, to obtain maximum values for the efficiency and for the P/T ratio.

Regarding efficiency, two performance figures are of interest for each given energy, i.e. the total efficiency that gives us the number of γ rays that have interacted in the detector and the peak efficiency that corresponds to the number of γ rays completely absorbed in the detector. In both cases, values are related to the total number of γ rays emitted by the source. Besides peak efficiency, the performance of the detector is evaluated in terms of the P/T ratio, number of γ rays completely absorbed with respect to the number of γ rays detected at a certain energy which corresponds to the ratio between peak and total efficiency. Obviously the highest the performance the better the spectroscopy system. Furthermore, this parameter (P/T) is directly related to the sensitivity of the system because it shows an implicit relation between the peak and the background in the spectrum. Higher the P/T, higher the area of the peak respect to the number of total counts. A variation on this value because of the geometry means an improvement on the probability to detect γ rays completely absorbed and so a better response of the system.

2.5 Performance study of the DESPEC Ge array

The starting point of the present study is the technical proposal for the DESPEC experiment. The Ge array described in this proposal consists on a system made by twenty four stacks, each one with three Germanium Double Sided Strip detectors (Ge-DSSD's) of 72*72*22 mm^3. Therefore, in total, the complete system is composed by seventy two crystals (see Fig. 2.4). A Ge-DSSD is characterized by a large number of electronic channels because its opposite surfaces are electrically segmented. In our case, a segmentation in eight strips giving sixty-four sensitive pixels has been chosen to determine the position interaction.

The twenty four stacks are placed surrounding AIDA, the implantation detector of the experiment. AIDA is a Double Sided Stripped Silicon Detector (DSSSD) of 24*8 cm^2 area. As a first stage in the simulations, AIDA has not been considered and a vacuum focal plane, where photons coming from the decay are generated, has been implemented. Each stack is a rectangular box of an AlMgSi alloy (98% of Al, 1% of Si and 1% of Mg) with dimensions 93*101*122,5 mm^3. Inside this housing the Ge crystals are placed, each one with its own support made of the same previously defined alloy. Besides, stack housing

works also as a cryostat to keep the detectors at an optimum temperature, the one of the liquid nitrogen. The individual support of the crystals together with its inner elements are shown in Fig. 2.5. On one hand, the support (grey in the figure) is shown with the empty space needed for the Printed Circuit Boards (PCB's). On the other hand, one can see in the figure the Ge crystal in blue, some pieces to fix the crystal to the housing in dark blue, and, finally, the electronics (green area). This picture corresponds to the design in development at GSI (Germany).

For all simulations performed, the same energy range has been considered: from 100 keV to 8 MeV. In particular, photons with energies of 100 keV, 250 keV, 500 keV, 1 MeV, 2 MeV, 5 MeV and 8 MeV have been simulated. Within this range, most values of γ-ray energies produced in the experiments proposed for DESPEC are covered. A maximum energy of 8 MeV has been selected as a sensible limit for γ rays emitted following β-decay processes with the largest Q values. The simulations have been performed with multiplicity one (M = 1). Therefore one event corresponds with one γ ray at a certain energy. To obtain results with enough statistic, 100.000 events have been used by default.
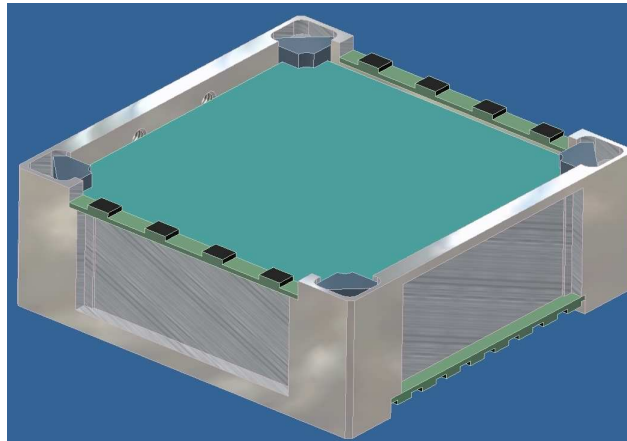

Figure 2.5: Detailed view of the Ge crystal with its support.

The first step to investigate the technical proposal performance is done studying the effect of the crystal parameters on the detector capabilities, taking as fixed parameters the guard ring of the crystals as 5 mm and the distance between crystals in one stack as 7 mm. The electric contacts, placed in the opposite surfaces of the Ge-DSSD, have been taken into account in the simulations. At present this parameter is not fixed because the contacts that will be used are not already defined. The typical Ge detector contact size is of the order of μm and so, the worst, although unrealistic, case has been simulated to check its influence in the results. Several configurations including different Al_2O_3 contact thickness, ranging from 0.1 mm to 1 mm, as well as a shield between two adjacent crystals to avoid crosstalk, were simulated. The obtained results show that the total efficiency is almost equal, about 35% at 1.3 MeV, for all studied cases; but the peak efficiency decreases from 7.5% to 5% at 1.3 MeV when the material surrounding the active Ge is increased, so the P/T ratio is also worsen going from 21% to 15% in the most unfavorable case. Therefore 0.1 mm for the Al_2O_3 contact thickness and no isolated crystals have been considered as starting point for the rest of studies.

The most important factor determining the efficiency of a system is the amount of active Ge material. Two different issues are directly contributing to the reduction of this material in Ge planar detectors. The first one is the guard ring which is produced by the segmentation made in the own crystal to avoid border effects when an electric field is applied. The thickness of the lost material, which is Ge, has been included in the simulation by a variable parameter ranging from 3 to 5 mm, although 5 mm is a more realistic value. The second effect is related to the dead layers which can be produced in the upper and lower surfaces of the Ge crystal due to the contribution of the electric contacts employed in the system design. As it has been mentioned before, the characteristics of the contacts have not been defined yet, so it is not possible to determine the amount of lost material by this effect. Nevertheless, the expected thickness of the dead layers should not be too high as nowadays most of the manufactures employs the thin contact technology, getting contacts about few μm by means of Li contacts in planar detectors.

Another important parameter affecting the performance of the array is the distance between the crystals inside each stack. With the current design, this value ranges from 7 to 10 mm: 7 mm in case all the individual housing are as close as possible and 10 mm in case of maximum separation.

To study how these two parameters: guard ring thickness and crystal-crystal distance, affect the basic capabilities of the system, simulations have been performed to calculate peak and total efficiencies, so obtaining also P/T ratios, changing their values between the limits above established. Specifically three different simulations have been performed: the first one, with 5 mm guard ring thickness and 7 mm distance (SIM1); the second one, with 3 mm thickness and 7 mm distance (SIM2); and the last one, with 5 mm thickness and 10 mm distance (SIM3). The results are shown in Table 2.2 for γ rays of 1,332 keV.

The results of these MC simulations have been used to fix optimal values in the crystal and in the cryostat because of their influence in the global performance of the full DESPEC array. From our study it could be concluded that the separation between crystals is not a critical parameter as is shown by the P/T value (Table 2.2) but guard ring thickness does it because it is directly related to the amount of active Ge and, therefore, when it decreases the capabilities of the system improve. However, the thickness has to be fixed at 5 mm because nowadays it seems the only realistic value. This parameter plays a decisive role in the design of the system and, therefore, a compromise to get the minimum value should be considered as long as the electric signal generation is not affected because of the field distortion effects in the borders.

Table 2.2: Total efficiency (ε_T), peak efficiency (ε_p) and P/T values corresponding to photons of 1,332 keV for the different configurations. SIM1 corresponds to 5 mm guard ring thickness and 7 mm distance between crystals, SIM2 is 3 mm and 7 mm and SIM3 is 5 mm and 10 mm, respectively.

Configuration	ε_T (%)	ε_p (%)	P/T (%)
SIM1	35.86	7.51	20.94
SIM2	38.77	9.40	24.24
SIM3	36.32	7.72	21.26

To determine the influence of the contact dead layer thickness on the performance of the system, simulations have been performed modifying this value from 0 to 2 mm, each 0.5 mm. As it is shown in Table 2.3, the thickness which depends on the type of contact used for the detector has a high impact in the performance of the array. As it has been mentioned above, we expect to use thin contacts, so, from now in advance their thickness has been fixed to zero in the simulations as in ideal conditions, although some material will be lost inevitably. In Fig. 2.6, one can see the peak efficiencies corresponding to the different emission points within the AIDA plane, which have been obtained with the optimized values for the technical proposal configuration.
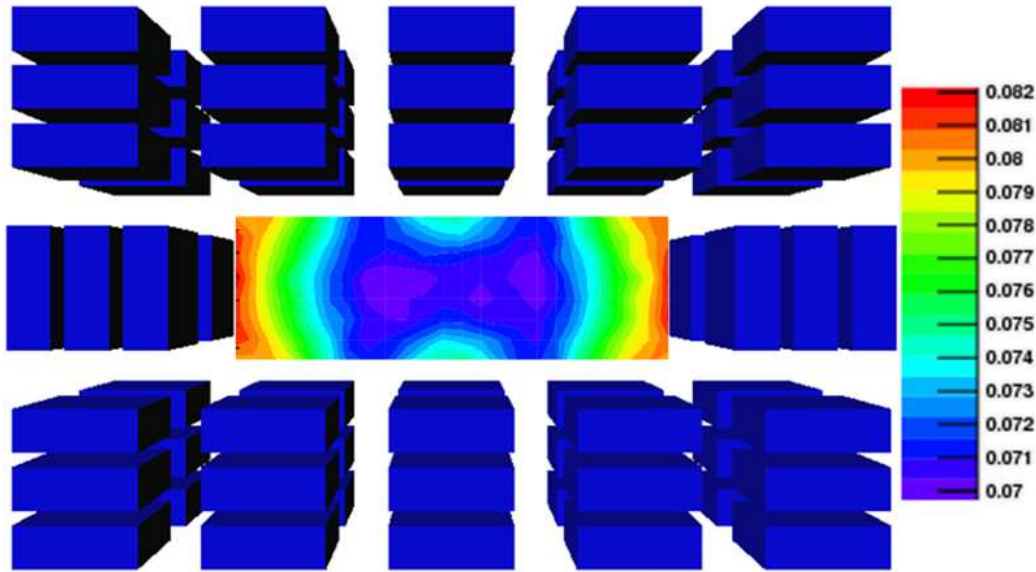

Figure 2.6: Peak efficiency (ε_p) of the technical proposal for 1,332 keV γ rays.

Once the effects of the individual stacks on the capabilities of the detection system have been studied and optimized but realistic values have been chosen, the next step is related to study different possible geometries adapted to the requirements of the γ-detection system with the ideas arisen within the DESPEC collaboration. From now on an approach to the AIDA setup has been considered. It consists on three silicon layers of 240*80*1 mm^3, separated 3 mm, placed in the center of the array. The central slide is divided in one hundred ninety two 1 cm^2 pixels and the photons are thrown from the center of each pixel so one hundred ninety two different emission positions are considered, positions which have an associate efficiency as we can see in Fig. 2.6.

In the previous simulations, it was already noticed the efficiency loss because of the use of square planar detectors due to the long distances between the crystals belonging to different stacks. Therefore, configurations with large rectangular crystals were also analyzed. Placing a long crystal instead of two squares ones makes the solid angle to increase and, what is more important, the internal hole where γ rays are more probable to be detected to be covered.

For the sake of clarity, in this new study the technical proposal has been called GEDESPEC1 and the equivalent one with rectangular crystals GEDESPEC2. Both

Table 2.3: Total efficiency (ε_T), peak efficiency (ε_p) and P/T values at 1,332 keV for different dead layer thickness.

Dead Layer thickness (mm)	ε_T (%)	ε_p (%)	P/T (%)
0.0	35.86	7.51	20.94
0.5	34.38	6.75	19.63
1.0	34.73	5.38	15.49
1.5	33.01	4.98	15.09
2.0	31.68	4.53	14.30

geometries shown in Fig. 2.7, have the same Ge volume but for GEDESPEC2 the crystals are 74*22*138 mm^3 and so, some distances have changed, as the housing or the stack dimensions. In GEDESPEC2 only twelve stacks are needed, instead of the twenty four we have in GEDESPEC1, thus the number of crystals goes from seventy two to thirty six although the amount of Ge is preserved. If we also reconsider the technical proposal geometry, it seems interesting to check the effect on the efficiency of the crystals placed in the corners of the array since they are situated further away from the emission focal plane. Therefore, two new geometries have been implemented: one with square detectors and the equivalent one with rectangular detectors both without the stacks placed in the corners: their names, GEDESPEC3 and GEDESPEC4, respectively shown in Fig. 2.8. Another alternative for the Ge system is to consider stacks made up with four rectangular Ge-DSSD instead of three: GEDESPEC5 and GEDESPEC6 without and with corners, respectively drawn in Fig. 2.9. In Table 2.4 the implemented configurations are summarized.

Because of the experiments proposed for DESPEC and the two operational modes of the Super-FRS: achromatic or monochromatic, the ion implantation in the AIDA plane will not be homogeneous. To evaluate the basic benefits for the different geometries, the most relevant parameters are the peak efficiency and the P/T ratio, therefore, mean values of these parameters ($(\overline{\varepsilon_p})$ and $(\overline{P/T})$) have been calculated in a surface of 22*6 cm^2 of the AIDA central slide since in this region ions will be implanted with higher probability (Table 2.5). Other important parameters that should be considered in the choice of the

Table 2.4: Main characteristics of the geometries under study. It should be noticed that for GEDESPEC5 and GEDESPEC6, stacks with four crystals instead of three have been used.

Configuration	Nº of stacks	Nº of crystals	Crystals type
GEDESPEC1	24	72	square
GEDESPEC2	12	36	long
GEDESPEC3	16	48	square
GEDESPEC4	8	24	long
GEDESPEC5	8	32	long
GEDESPEC6	12	48	long

Figure 2.7: Peak efficiency (ε_p) obtained for two of the implemented geometries for the DESPEC Ge array: GEDESPEC1 (up) and GEDESPEC2 (bottom) at 1,332 keV. For GEDESPEC1 one million of events have been simulated to increase statistic.

Figure 2.8: . Peak efficiency (ε_p) obtained for two of the implemented geometries for the DESPEC Ge array: GEDESPEC3 (up) and GEDESPEC4 (bottom) at 1,332 keV. For GEDESPEC3 one million of events have been simulated to increase statistic.
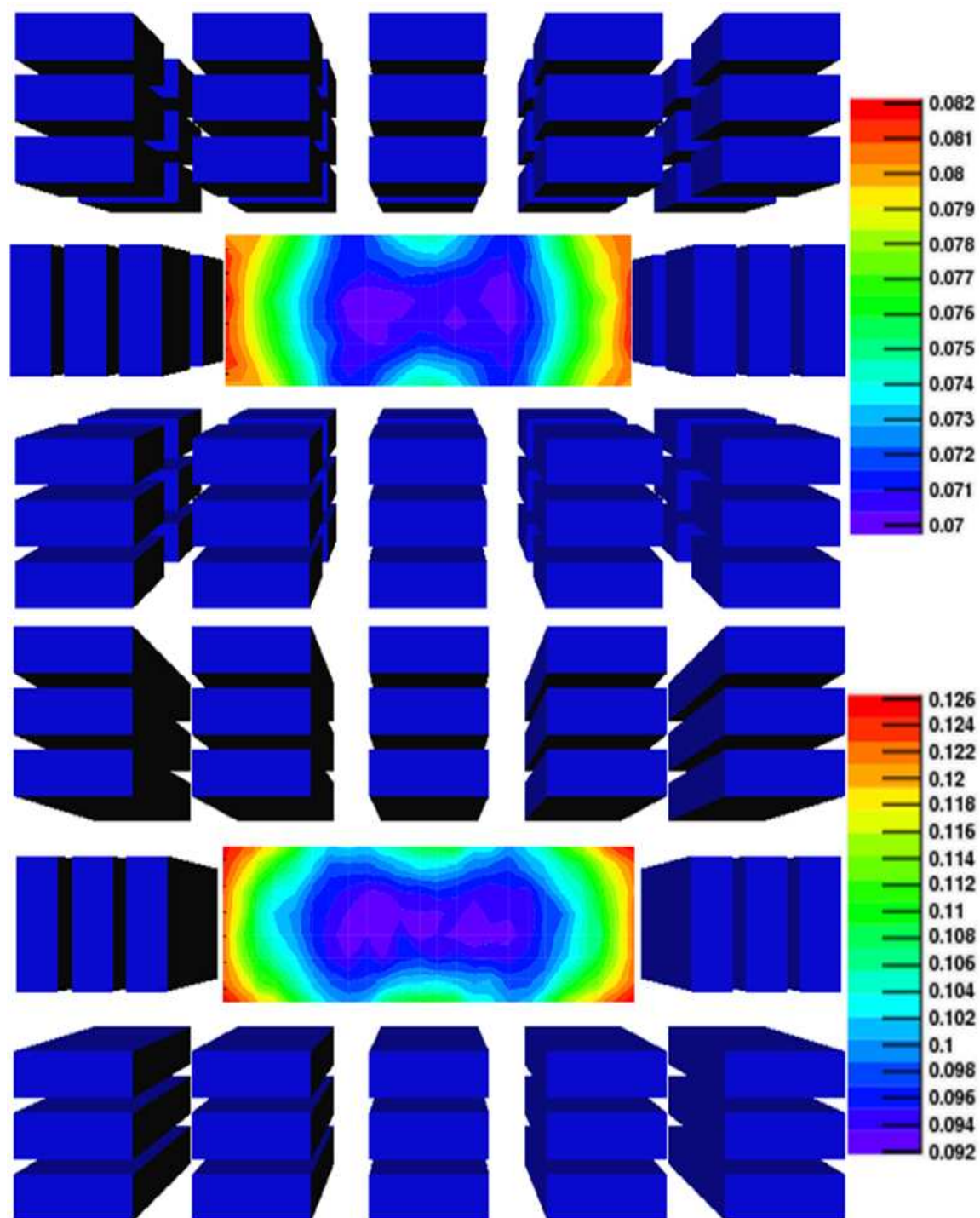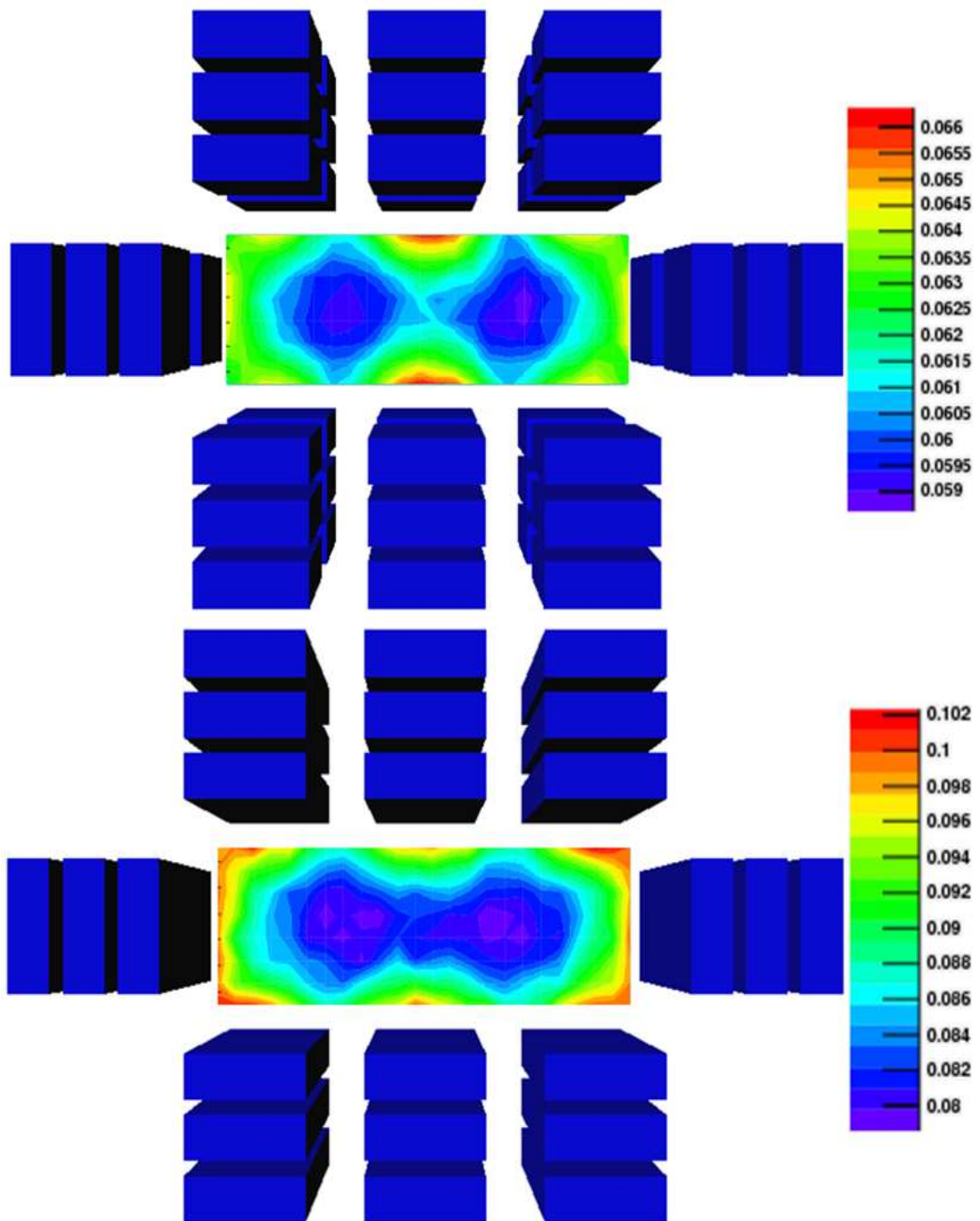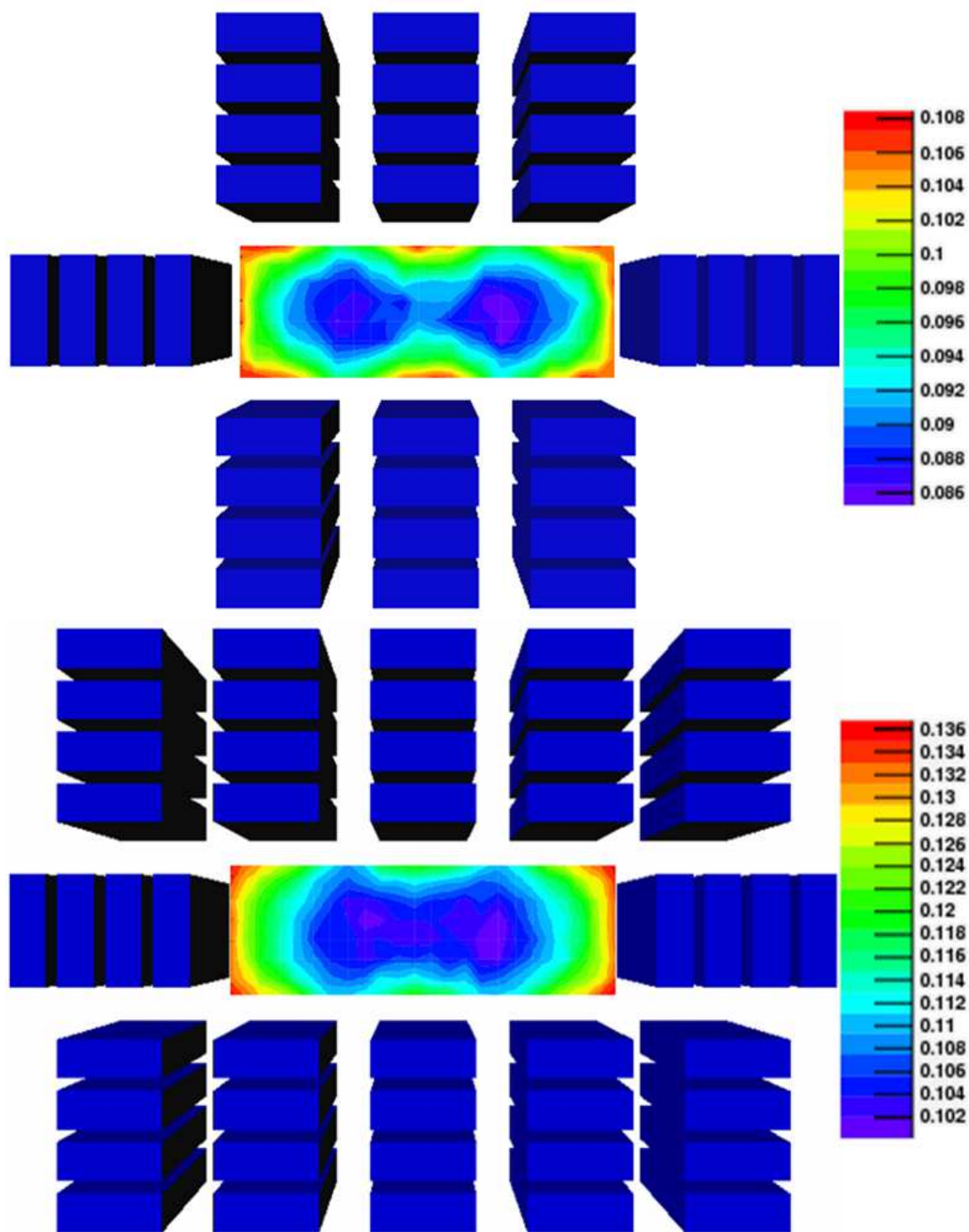
Figure 2.9: . Peak efficiency (ε_p) obtained for two of the implemented geometries for the DESPEC Ge array: GEDESPEC5 (up) and GEDESPEC6 (bottom) at 1,332 keV.

array geometry are the number of electronic channels and the amount of Ge employed in the design, because they are directly related to the cost of the system. These values are summarized in Table 2.6. In Table 2.5 it can be seen how the efficiency decreases when the γ-ray energy is increased. The probability of going through the system and escaping not depositing the total energy on the array rises when the photon energy is increased. We observe the same behavior for the P/T ratio.

Table 2.5: Peak efficiency ($\overline{\varepsilon_p}$) and P/T ($\overline{P/T}$) for the different configurations at three energies. For GEDESPEC1 and GEDESPEC3 one million of events have been simulated to increase statistic.

	E = 100 keV		E = 1,332 keV		E = 8,000 keV	
Geometry	$\overline{\varepsilon_p}$ (%)	$\overline{P/T}$ (%)	$\overline{\varepsilon_p}$ (%)	$\overline{P/T}$ (%)	$\overline{\varepsilon_p}$ (%)	$\overline{P/T}$ (%)
GEDESPEC 1	27.28	86.10	7.35	20.30	1.43	4.44
GEDESPEC 2	33.74	87.66	10.08	26.87	2.43	7.39
GEDESPEC 3	25.10	86.48	6.12	20.16	1.11	4.20
GEDESPEC 4	32.36	87.88	8.52	26.36	1.93	6.92
GEDESPEC 5	31.80	87.89	9.26	27.89	2.32	7.93
GEDESPEC 6	33.37	87.69	11.06	28.50	2.98	8.55

Table 2.6: Number of electronic channels and amount of Ge employed corresponding to the different arrays. For the geometries based on long crystals, 16*8 strips have been considered instead of the 8*8 used for the squares ones.

Geometry	Nº of electronic channels	Ge volume (cm^3)
GEDESPEC 1	1,152	8,212
GEDESPEC 2	864	7,869
GEDESPEC 3	768	5,474
GEDESPEC 4	576	5,246
GEDESPEC 5	768	6,995
GEDESPEC 6	1,152	10,784

To better understand the results obtained in Table 2.5, the 1,332 keV peak efficiency mapping for all geometries is shown in Fig. 2.7, Fig. 2.8 and Fig. 2.9. We observe how it increases as long as we move in the implantation plane from the center to the borders. This effect is due to photons emitted close to the edge because they travel less distance to get the detector being more likely to be completely absorbed. It is also caused by the fact that the active material seen by these γ rays is bigger leading to a larger solid angle coverage.

Attending peak efficiency and P/T, GEDESPEC2, GEDESPEC4 and GEDESPEC5 are the most suitable geometries, all based on rectangular crystals, independently of the active amount of Ge involved. It can be noticed how GEDESPEC1 is the three-crystal-stack geometry with higher Ge volume and number of channels and so, the most expensive.

However, its basic performance is even worse than the one of GEDESPEC4, the array in which both parameters are minimum.

The study of the feasibility of the production of long crystals was carried out meanwhile the conceptual design of the array was under development. Unfortunately technical problems were found on the production of long crystals due to their impurity gradient orientation. To get long crystals, the raw germanium crystal once grown should be cut along the axial direction; while in square crystals, the germanium is cut perpendicular to the axial axis. For square crystals the impurity gradient goes in the direction in which the electric field is applied and so, an inverse potential can be applied in the contacts to generate the depletion layer. However, for long crystals the impurities increase in the perpendicular axis in which the electric field is applied. Therefore, is not possible to polarize the crystal without losing a huge amount of dead material. Due to the technical problems emerged in the manufacturing process, it has been rejected the use of long crystals in the design of the Ge array.

2.6   Through the imaging concept with Ge-DSSD's

In the last section different configurations considered for the DESPEC Ge array have been explained. Globally, their characteristics in terms of peak efficiency and P/T have resulted to be not as good as it was expected. But we did not consider whether the different configurations studied were suitable to an imaging array or not. In Fig. 2.10 it is sketched how Compton imaging is performed in a planar detector. In this section, we intend to analyze what characteristics a system with imaging capabilities should have. The requirements that an imaging array should fulfill are the following:

- Good position resolution to determine the interaction positions with high precision,

- minimum source-Ge distance and, in case of an active implanter like AIDA, parallel surfaces between AIDA and Ge array in order to decrease the area projected by the imaging cone on AIDA, which defines the emission position,

- large separation between Ge crystals in the stacks as the distance between the interaction points of the same γ ray is a decisive parameter in the Compton angle uncertainty determination.

First requirement is fulfilled by any array made with Ge-DSSD's. However, the second one is not fulfilled by the configurations in which planar detectors surround AIDA placed perpendicularly to the implantation plane. This is the case for all the proposals studied previously. Therefore, an imaging array should have its detector windows parallel to the implantation plane. The configuration which fits better to these requirements is a wall placed in front of AIDA as seen in Fig. 2.11 because the intersection area between the cone that defines the emission point and AIDA is smaller.

Several options have been studied but all of them have the same idea behind: detector surfaces parallel to the AIDA plane. In the simulations, only the Ge crystals without cryostat have been implemented, being their dimensions the same ones as those considered previously. The guard ring thickness is 5 mm and no dead layers are considered. The separation between crystals in both the X and Y axis is 21 mm and 10 mm in the Z axis. These values have been applied to all simulated cases, the main difference between them
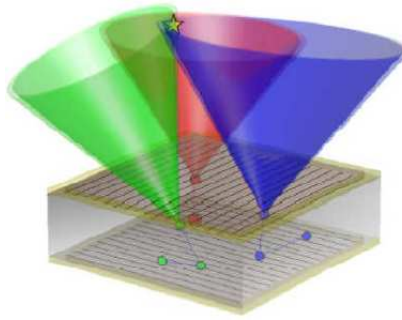
Figure 2.10: Image reconstruction on a planar detector. The points inside the planar detector, in blue, green and red, respectively correspond to different tracked γ rays. Each track through its two first interaction points defines a cone, showed in the picture in its respective color. The γ-ray origin is given by the intersection of the different cones.

is the positioning of the crystals in the different rows and how these rows are placed one with respect each other in the total array configuration, although the first row is always placed 18 mm distance to the central slide of AIDA. Besides, to perform a high quality imaging a large segmentation is needed: higher the position resolution better the imaging capabilities. Therefore, 12*12 strips instead of the 8*8 considered before, have been taking into account. As the number of crystals employed is different, the number of electronic channels and the amount of Ge employed is not the same for all the arrays.

In Fig. 2.12, Fig. 2.13 and Fig. 2.14 peak efficiencies of several of the implemented geometries corresponding to 1,332 keV γ rays are shown. The results obtained for each of them, in terms of peak efficiency, P/T, number of electronic channels and Ge volume are shown in Table 2.7. Both peak efficiency and P/T values have the same order of magnitude as the ones of the perpendicularly faced geometries. It means the basic capabilities of the system not to improve attending these parameters although we gain an imaging array. However, a main disadvantage for these configurations arises: the fact that detectors placed after the beam line will be not working properly due to the high beam intensity going through AIDA. These detectors will receive a large amount of background radiation that might make them inactive and, superfluous for the array. Therefore, some empty space should be left in front of AIDA and, consequently, the peak efficiency and the P/T will decrease as the detectors replaced by the holes have a high influence in the performance of the system.

Summarizing all the results obtained in the MC simulations of all the configurations made up by realistic planar detectors, efficiency values between 5% and 11% and P/T values between 18% and 36% could be reached. The highest efficiencies and P/T correspond to arrays with an inaccessible number of detectors or with the currently technically unfeasible long planar detectors, which shows that with a proposal based only on planar detectors is not possible to get a Ge array with a basic performance substantially better than the one of the conventional RISING array, with about 11% efficiency for the stopped beam configuration. Even if imaging could be performed with these setups, the low values obtained for efficiency and P/T makes senseless to achieve this capability. Therefore, new ideas have been explored for the conceptual design of the DESPEC γ-ray array taking the advantage of the large-efficiency AGATA array.
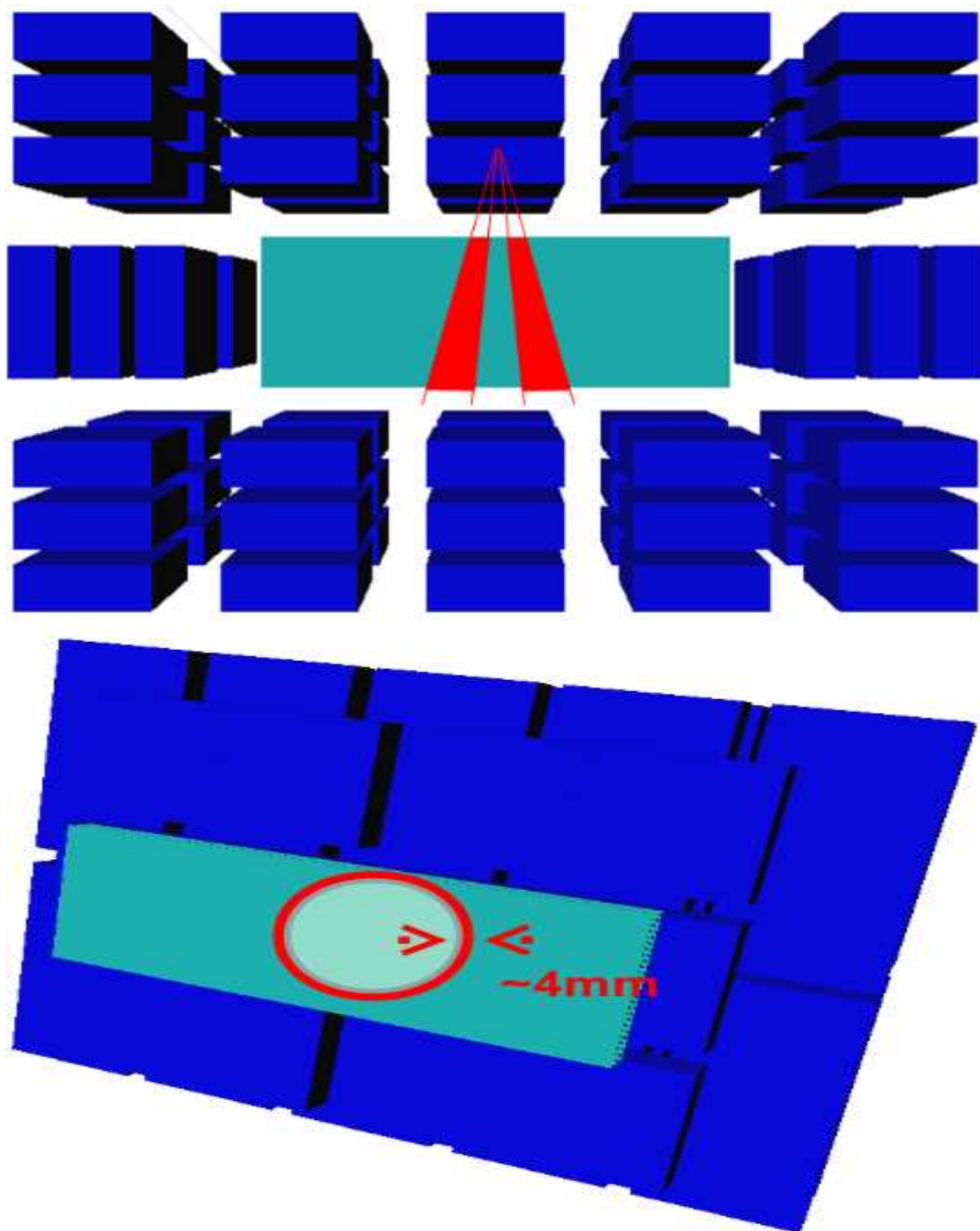
Figure 2.11: Comparison between the intersected areas by the expanded cone and the implantation plane in AIDA for both types of geometries. For the technical proposal, in the best conditions, the intersection is about 15% of the area, while in the wall geometries, in unfavorable conditions, this value is about 5%.
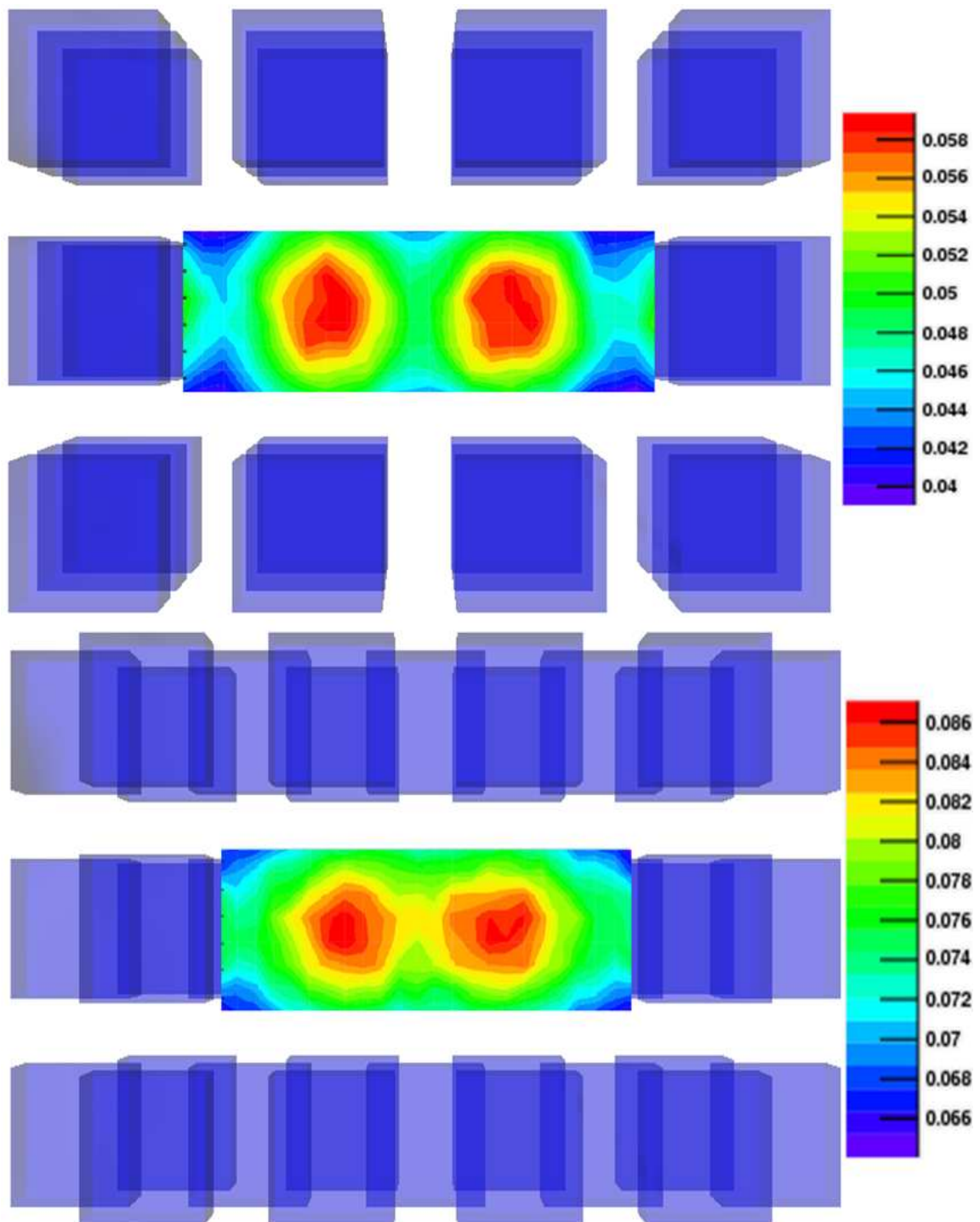
Figure 2.12: Peak efficiency (ε_p) at 1,332 keV for different implemented wall geometries of the Ge array for DESPEC.
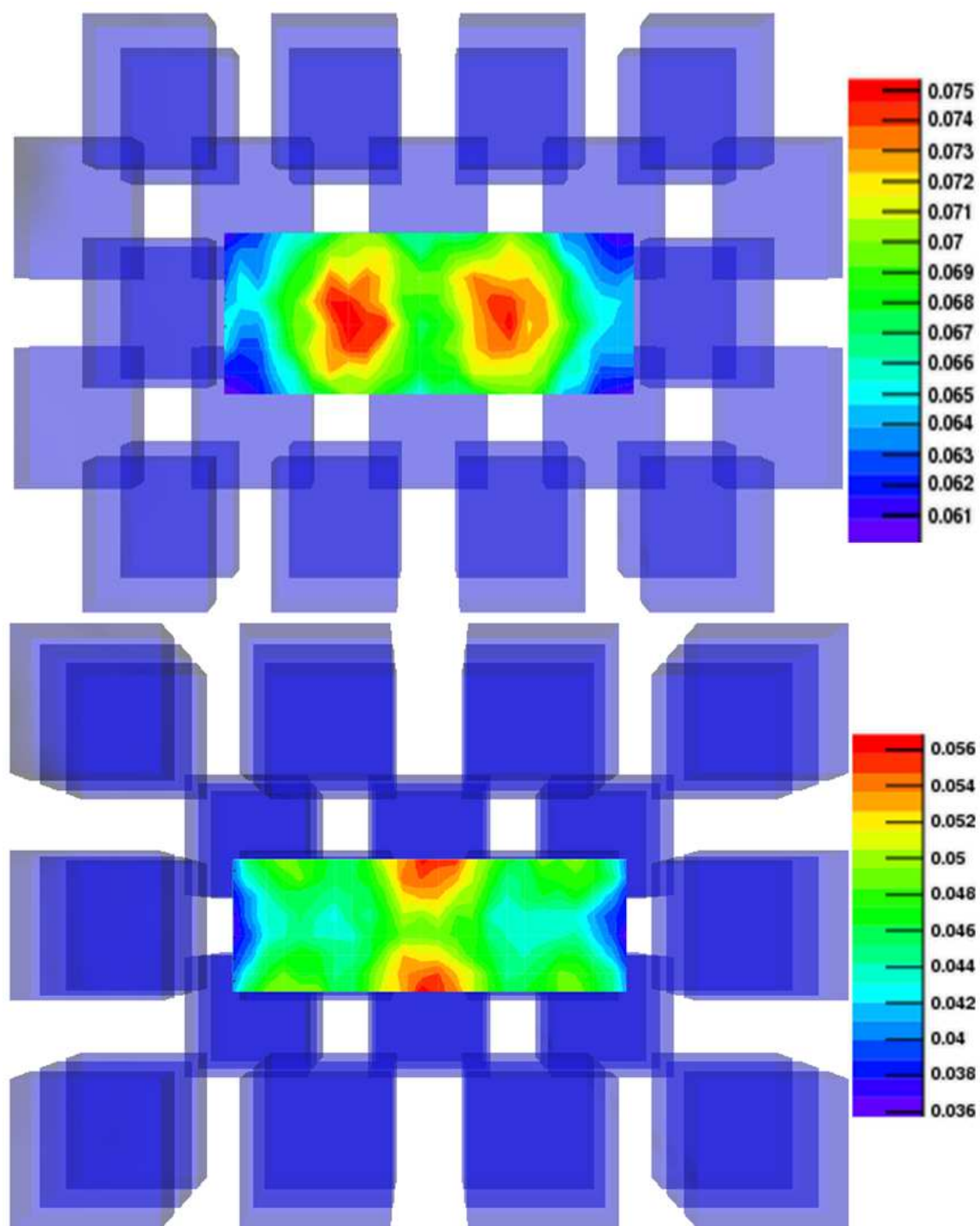
Figure 2.13: Peak efficiency (ε_p) at 1,332 keV for different implemented wall geometries of the Ge array for DESPEC.
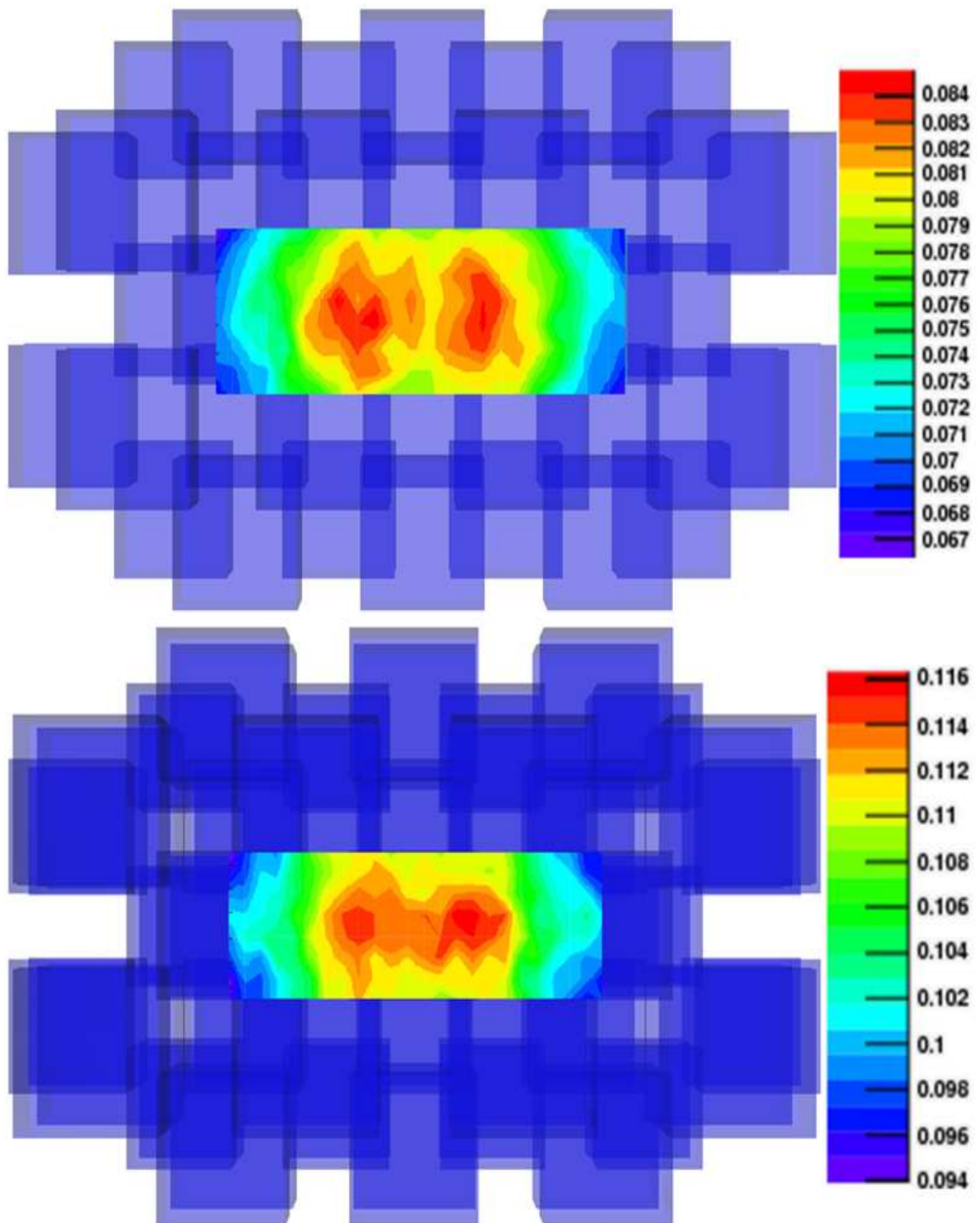
Figure 2.14: Peak efficiency (ε_p) at 1,332 keV for different implemented wall geometries of the Ge array for DESPEC.

Table 2.7: Peak efficiency (ε_p) and P/T ratio for 1.332 keV γ rays, number of crystals and number of electronic channels considering 12*12 strips instead of the 8*8 for the wall configurations. It is also given the amount of Ge involved in the different configurations.

| Geometry	ε_p (%)	P/T (%)	Nº crystals	Nº channels	Ge volume (cm^3)
WALL 1	5,11	18,94	36	864	4.106
WALL 2	7,92	28,95	39	936	4.448
WALL 3	6,91	26,56	34	816	3.878
WALL 4	4,65	18,79	54	1.872	6.159
WALL 5	7,85	29,05	39	936	4.448
WALL 6	10,80	36,14	78	1.872	8.896

2.7 Towards the telescope system: Ge-DSSD shell + AGATA

It has just been shown that an array based on planar detectors does not fulfill the capabilities needed for a Ge array for the DESPEC experiment. Now, with the idea of optimizing human and financial resources, a new configuration has been investigated involving AGATA, the tracking array up to now with better capabilities. AGATA, as it has been explained, is a Ge gamma array based on the tracking concept. AGATA is though to be shares among the main laboratories in Europe with radioactive beam facilities. It has been planned to be in SPIRAL2 at Ganil, in FAIR at GSI and at the LNL. Therefore, it could be available for the DESPEC experiment. When coupled with Ge-DSSD's we could gain a γ-ray telescope, providing the highly efficient AGATA with imaging capabilities (Fig. 2.15). Therefore, the objective is to exploit the high efficiency of AGATA, about 40% at 1.3 MeV, and the high position resolution of planar detectors, about 1-2 mm [99, 100] versus the 5 mm for the coaxial detectors of AGATA [101].

To check the maximum capabilities that could be obtained with a full 4π array of DSSD's and AGATA coaxial detectors, an ideal case has been implemented. It consists on two shells of 2 and 9 cm thickness, the narrower one imitating the DSSD shell and the wider one as AGATA (Fig. 2.16). The DSSD shell is centered at 12 cm of the origin of the system, so its face is at 11 cm and the rear at 13 cm, while the AGATA shell window is located at 24 cm. The MC results obtained for three different energies: 100, 661 and 1,332 keV are given in Table 2.8.

To analyze the effect of each shell in efficiency and P/T ratio for every energy, we select the MC events to calculate: the global values for the whole system, referred to as AGATA + Ge-DSSD; the values corresponding to events with interactions just in AGATA, referred to as AGATA; as the previous one but for interactions only in the Ge-DSSD shell, referred to as Ge-DSSD; and, finally, aiming to isolate the most favorable cases for imaging, the values obtained when only the first interaction happens in the Ge-DSSD shell, referred to as AGATA + Ge-DSSD-1

At low energies, all events fully deposit their energy in the detectors, either in the AGATA shell or in the Ge-DSSD shell or in the complete system, even for events having
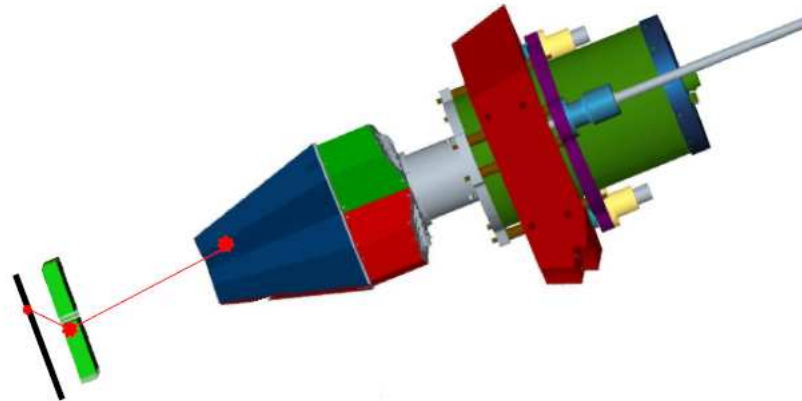
Figure 2.15: The Ge imaging telescope concept based on coupling an AGATA capsule to a Ge-DSSD.

only the first interaction in the Ge-DSSD shell. At 661 keV if only the Ge-DSSD shell is considered, a 52% of events suffer some interaction although just a 24% is completely absorbed. Peak efficiency corresponding to AGATA events is higher, about 86%. If the array is composed by both systems this value rises to 92% while if only events having the first interaction in the Ge-DSSD shell are considered, the peak efficiency decreases to about 33% although the P/T ratio goes to 98%. At 1,332 keV, when going from the composed system taking into account all events to consider only those events in which

Figure 2.16: Ideal implementation of AGATA coupled to a set of Ge-DSSD. In blue, the AGATA shell and in purple the Ge-DSSD shell. The inner part of both shells is depicted in red. In green the trajectories of some photons of 1,332 keV thrown from the center of the system.

Table 2.8: Peak efficiency (ε_p), total efficiency (ε_T) and P/T ratio at different energies for the different implemented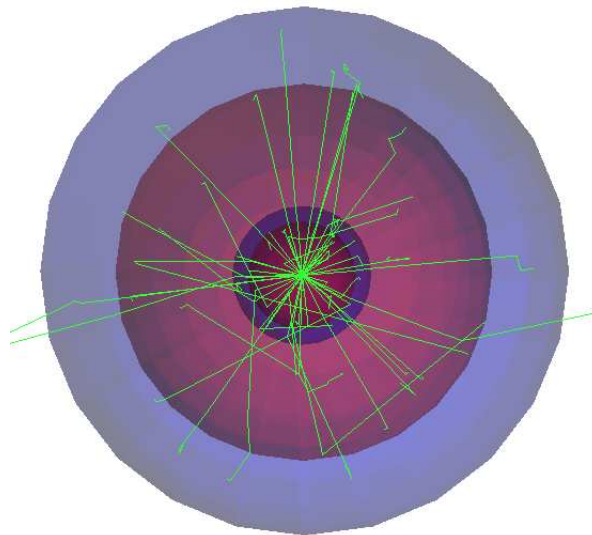 arrays. AGATA + Ge-DSSD corresponds to the complete system, AGATA to the shell imitating AGATA; Ge-DSSD to the shell simulating Ge-DSSD, and AGATA + Ge-DSSD-1 to the full array but only events having the first interaction in Ge-DSSD have been selected for the analysis. Ten million events have been considered to increase statistic.

Geometry	Energy (keV)	ε_p (%)	ε_T (%)	P/T (%)
AGATA + Ge-DSSD		100	100	100
AGATA	100	100	100	100
Ge-DSSD		99	99	99
AGATA + Ge-DSSD-1		99	99	100
AGATA + Ge-DSSD		92	98	93
AGATA	661	86	96	90
Ge-DSSD		24	52	46
AGATA + Ge-DSSD-1		33	34	98
AGATA + Ge-DSSD		79	94	83
AGATA	1,332	71	91	78
Ge-DSSD		14	41	33
AGATA + Ge-DSSD-1		19	20	93

we are interested, the peak and the total efficiencies decrease but the P/T value raises. Therefore, if imaging constrains are applied, efficiency is lost but we gain in terms of P/T and so, for experiments where the statistic is good enough, imaging can involve an additional capability for the system.

It should be noticed that this implementation corresponds to maximum values obtainable for two Ge shells. However, the real configuration, that will be available in few years, will not include the 4π AGATA array and it should benefit of the advantages of the planar detectors which are now being developed in the frame of the DESPEC collaboration.

The configuration approved to be installed in GSI is the so-called S2' configuration consisting on ten triple clusters and five double clusters covering a 1π solid angle [115]. With the idea of profit about planar detectors, one configuration has been proposed to the collaboration for the DESPEC experiment. A modified version of the AGATA code described in [61] with a detailed geometrical implementation of the S2' configuration has been implemented in the simulations. A set of six planar HPGe detectors of 70*70*20 mm^3 (Ge-DESPEC) placed between AIDA and the AGATA detectors has been added to the aforementioned configuration. In the geometry implementation, a 1 mm thick aluminum housing surrounds each planar crystal, which in its turn has a 5 mm width guard ring. Therefore, the active area remains 60*60*20 mm^3. AGATA detectors are located at the nominal position of 23 cm from the target. However the planar array is placed as close as possible to the emitting source, at 12 cm of the implantation plane, but always inside the solid angle covered by the AGATA detectors. This is done for the first interaction to have a higher probability to occur in one of the planar detectors. In Fig. 2.17 the peak efficiency obtained for 1,332 keV γ rays for the most feasible configuration on this context

is shown.

Peak efficiency (7,3%) as well as P/T (44%) obtained are almost the same as the ones obtained with the S2' configuration without the Ge-DSSD. In Fig. 2.18 the peak efficiency for both configurations is shown. The picture on the left shows the value for the S2' configuration (AGATA) and the one on the right side shows the value for S2' configuration with the set of planars (AGATA+Ge-DSSD). Therefore, in terms of these parameters is not worth to use a complementary array of planars coupled to AGATA. The main advantage of this setup is obtained in terms of imaging: if the first interaction takes place in the Ge-DSSD, as it has better position resolution than AGATA, an improvement of the quality of imaging can be achieved.

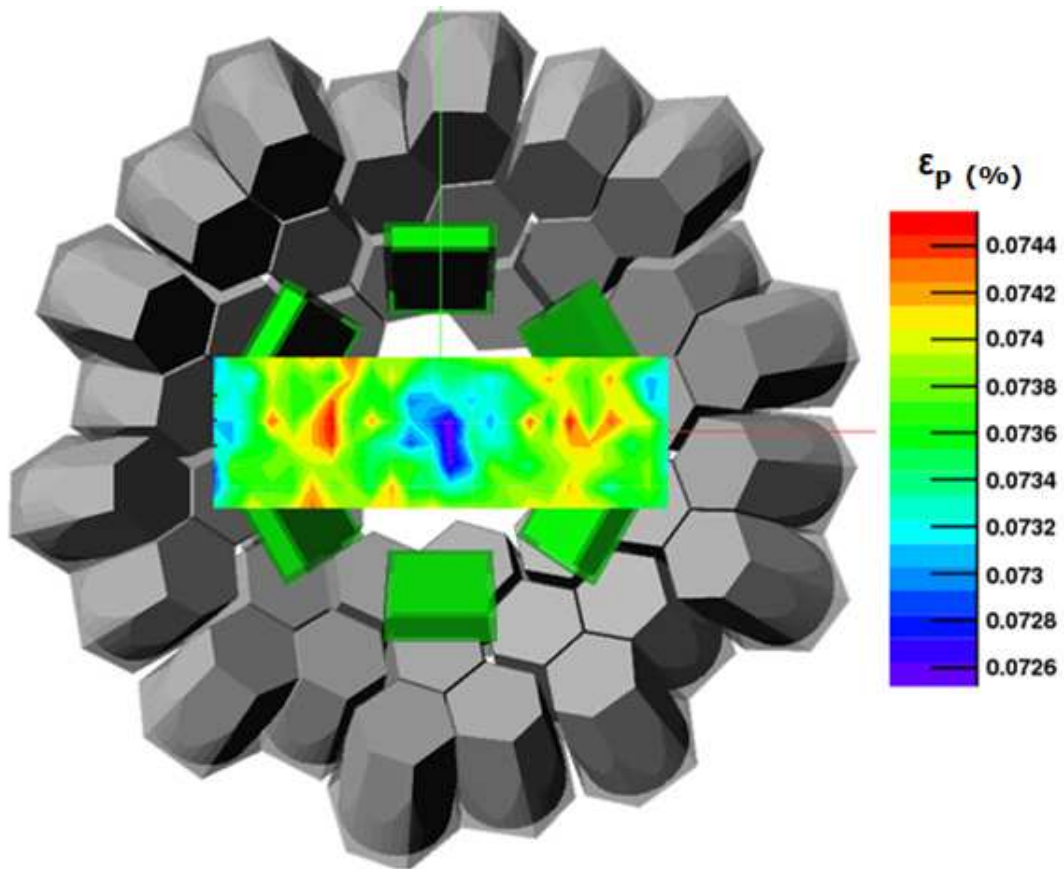Figure 2.17: Peak efficiency (ε_p) for the configuration based on AGATA S2'configuration + Ge-DSSD. In orange and green the X and Y axis, respectively. Ten million events have been considered to increase statistic.
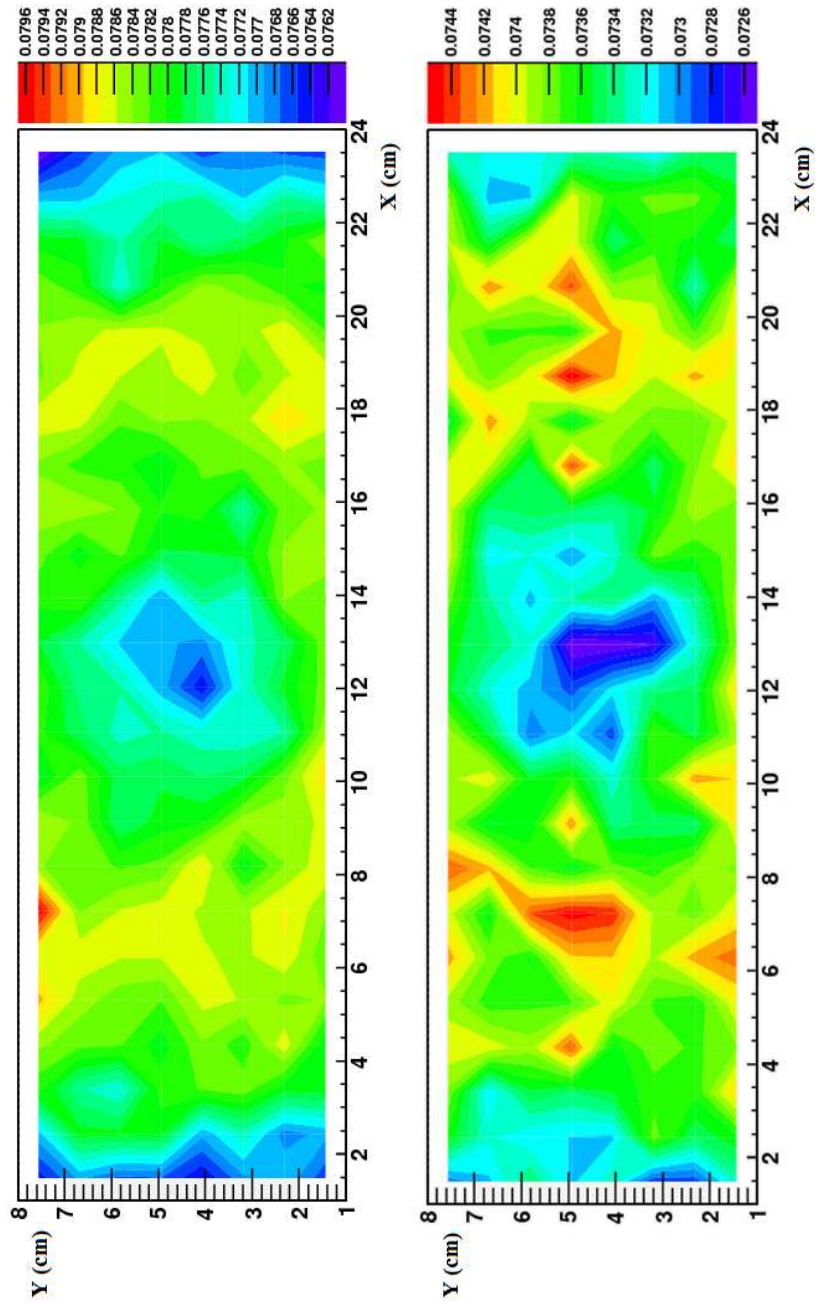
Figure 2.18: Peak efficiency (ε_p) for the S2' configuration (up) and S2' + Ge-DSSD (bottom) for γ rays of 1,332 keV. Ten million events have been considered to increase statistic.

Chapter 3

Towards the full exploitation of γ-ray tracking capabilities through the use of imaging algorithms

3.1 Background suppression algorithm for the AGATA array

As we explained in Chapter 1, in RIB facilities beam intensities will be orders of magnitude lower than those reached on the existing stable beam facilities. As a consequence, experiments will be performed with high background levels coming from both, the cocktail of nuclear species reaching the secondary target and the partial decay of the secondary beam. In case of in-flight production, nuclei of interest are produced by secondary beams with v/c up to 50% obtained by projectile fragmentation so the lower intensities are expected (a few pps for the most exotic species). An example of what is currently known is offered by the RISING device, installed at the focal plane of the FRagment Separator (FRS) at GSI. A detailed study of the radiation components in the target area [76] showed that background sources are either the beam dump or the implantation detector, but also the decays occurring at a distance between 1 and 4 m upstream from the target which are likely originated in the FRS tracking detectors and degraders.

A way to reduce the background is the use of very narrow time gates [76]. But to have a sizeable effect, a FWHM time resolution of the order of 1 ns would be required for the detectors. Unfortunately, this resolution is far exceeding what is currently achievable with a conventional large-volume germanium detector. However, the use of segmented-contact germanium detectors could lead to a significant background reduction. Currently efforts are ongoing in order to: improve the timing properties of germanium detectors with the use of pulse shape analysis [116]; discriminate gammas from neutrons, which constitute another important background contribution [117, 118]; and use optimized electronics, as the fast-reset preamplifiers, to avoid long dead times due to signal saturation produced by the high-energy-charged-particle background [119]. In this context, an additional technique aiming to improve the response function with the objective to reduce the background relies on the capability of γ tracking to provide partial information of the incoming direction of the γ rays, thus allowing a reduction of the $\gamma-$ray background coming from sources with different

origin as the target. To quantify the imaging capabilities for the AGATA array, which will be used for the HISPEC experiment, we have developed a background suppression algorithm based on the Compton scattering formula [120]. Its objective is to discriminate the origin of the γ rays on an event-by-event basis, tracking back the γ rays coming from different positions and assigning them to specific emitting locations. The algorithm has been tested with experimental data from a measurement performed at the Laboratori Nazionali di Legnaro (LNL), using an AGATA 36-fold-segmented symmetric germanium detector prototype. This is the first time that the background reduction capability of AGATA detectors has been investigated experimentally. Besides, MC simulations have been made to check the performance of the algorithm under ideal conditions.

3.1.1 Algorithm implementation

As mentioned above, in setups as RISING, the three main sources of background are the fragment separator detectors and degraders which are placed upstream, the target in the center of the setup and either the beam dump or the implantation/tracking detector for the reaction products after the target. In order to emulate in a simplified way the experimental conditions, in the algorithm implementation three sources placed around an AGATA detector prototype have been considered, trying to reproduce the incoming direction of the radiation in an in-beam experiment from target, beam dump and beam line. The algorithm has been implemented trying to take maximum advantage of this particular geometry.

The algorithm performs a comparison between the scattering angle of the γ ray in the first interaction as it is obtained from the kinematics of the Compton scattering (θ_C) and the angle estimated from geometrical considerations (θ_G). Considering the three positions of the sources, the three values of θ_G are obtained for each interaction point. The Compton angle (θ_C) is calculated using a simple probabilistic tracking, i.e. assuming that the first interaction recorded is a Compton scattering and that the γ ray is fully absorbed in the detector. The scattering angle can be calculated with the Compton scattering formula as follows:

$$cos\theta_C = 1 - \frac{(E_\gamma - E_\gamma^{'})mc^2}{E_\gamma^{'} E_\gamma} \tag{3.1}$$

where E_γ, the initial energy of the γ ray, and $E_\gamma^{'}$, the energy after the scattering, are known.

The difference between both angles $|\Delta\theta| = \theta_G - \theta_C$ is evaluated for the three sources and the γ ray is assigned to the source giving the smaller difference. In this way, three spectra are obtained, each of them incremented when the γ ray is assigned to the corresponding source.

As explained in Chapter 2, the two first interaction points of a γ ray emitted by a given source defines a cone. From a qualitative study (Fig. 3.1), it can be seen that the uncertainty in the cone axis is given by the following relation:

$$\delta\theta_p^2 \simeq (\delta r_1^2/\Delta r)^2 + (\delta r_2^2/\Delta r)^2 \implies \delta\theta_p \simeq \frac{\sqrt{(\delta r_1^2 + \delta r_2^2)}}{\Delta r} \tag{3.2}$$

under the approximation $\delta r << \Delta r * sen\theta$, where δr_1 and δr_2 are the uncertainties in the position resolution of the first and the second interaction points respectively, and Δr is the distance between the two interaction points [97].
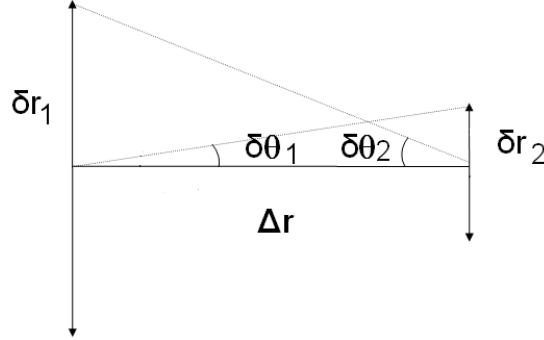

Figure 3.1: Schematic picture to show the dependence of the cone axis uncertainty $(\delta\theta_p)$ on the position resolution uncertainties of the two interaction points $(\delta r_1$ and $\delta r_2)$.

Therefore, for a given position resolution, the distance between interactions becomes the most important parameter. To ensure a good enough resolution on the scattering angle, we used a threshold (d_{min}) on this parameter to select the events. As a consequence, all events with distances between interactions lower than d_{min} are disregarded in the analysis.

An extra condition on the maximum deviation allowed for the Compton angle with respect to the geometrical scattering angle, defined as $\Delta\theta$, has been used to further improve the background suppression capability. For this purpose, it has been defined a simple empirical angular acceptance, A_θ, using the position resolution and the distance between the interaction points. $|\Delta\theta|$ has to be less than the angular acceptance (A_θ) given by

$$A_\theta = arctg(\frac{2FWHM}{|\overrightarrow{\Delta r}|}) \tag{3.3}$$

where Δr is the distance between the interaction points, $FWHM$ is the full width at half maximum in position resolution and the factor 2 comes from the optimization of the algorithm. A good assumption for $FWHM$ is 5 mm as reported in [101].

It has been determined that approximately 70% of the correct events will give an angular difference $|\Delta\theta|$ within the limits defined by this A_θ empirical acceptance. In Fig. 3.2 a schematic view of the algorithm is shown.

3.1.2 Experimental details

The measurements used to check the algorithm have been made with one of the single symmetric AGATA crystal prototype, the so-called S#001 equipped with charge-sensitive fast preamplifiers (Fig. 3.3). This crystal has the outer contact segmented in thirty-six segments. The thirty-seven signals, thirty-six from the segments and one from the central contact, were acquired using CAEN model N1728A digitizer cards with 14 bits resolution and 100 MHz sampling rate. These NIM-standard digitizer modules directly

calculate the amplitude, therefore the absorbed γ-ray energy of the input signal through a moving window deconvolution algorithm [121] running on the on-board FPGA, providing also the data corresponding to the sampled pulses. Proper synchronization of the thirty-seven channels is fundamental considering the subsequent analysis to be performed. A common clock was distributed in a daisy-like chain to all of the modules, while the trigger signal, which was generated by a leading edge discriminator sensing the central contact of the AGATA detector, was distributed through a star connection. Each module was independently read out, the full event being reconstructed off-line by exploiting the time stamp information. In order to limit the rate of data transferred, only the first 200 samples were read out for each channel together with the energy value internally calculated, as explained above.

Sources of ^{60}Co emitting photons at 1,173 keV and 1,333 keV, ^{137}Cs with a γ ray at 662 keV and ^{152}Eu with γ-ray emissions at 122 keV, 244 keV, 344 keV and 1,408 keV, have been used for the test measurement. As said above, the positions of the sources have been chosen to roughly reproduce the incoming direction of the radiation from target, beam dump and beam line in an in-beam experiment. Considering a Cartesian coordinate system in the center of the frontal face of the crystal, with the Z axis pointing to the center of the detector, the position coordinates in mm for the three different sources are the following: ^{60}Co (807, 586, 68); ^{137}Cs (-147, 147, -978) and ^{152}Eu (-816, -567, -104). The raw spectrum obtained considering only events having two interaction points inside the detector is shown in Fig. 3.4.
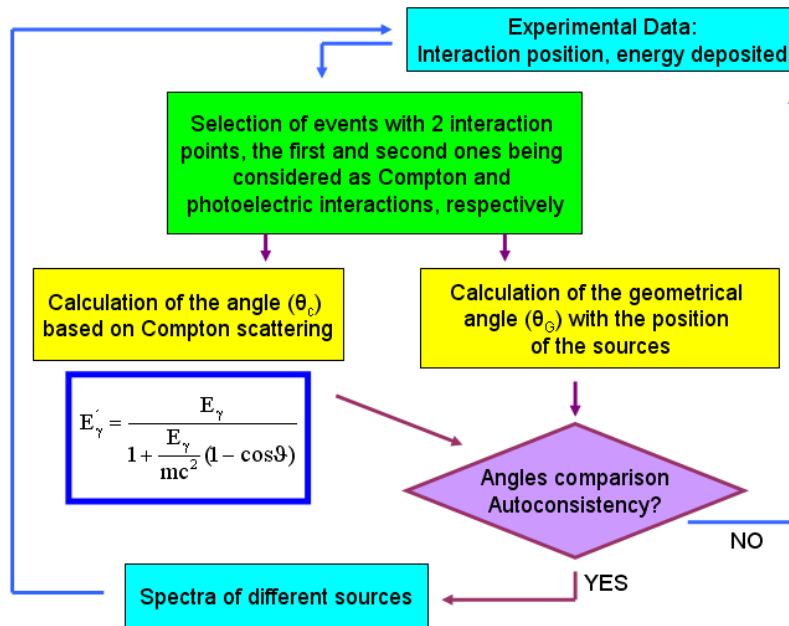
Figure 3.2: Outline of the algorithm implementation.
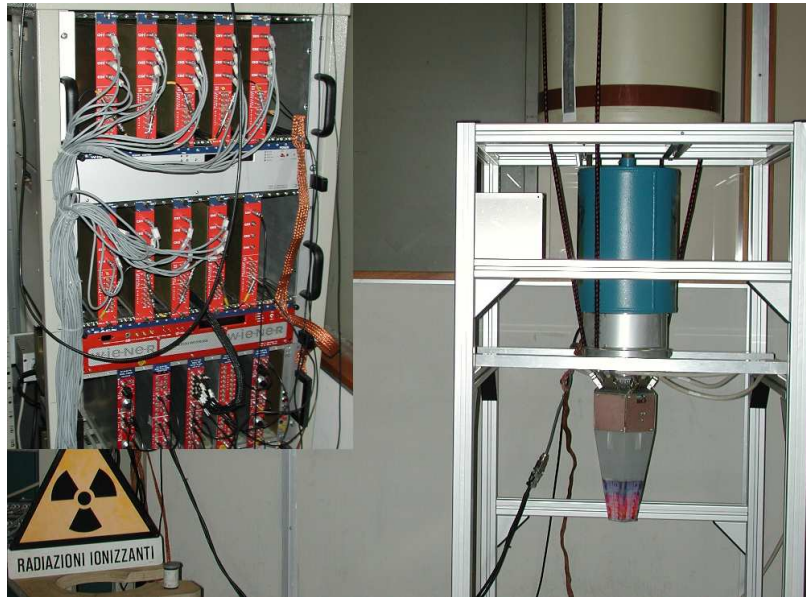
Figure 3.3: Experimental setup.
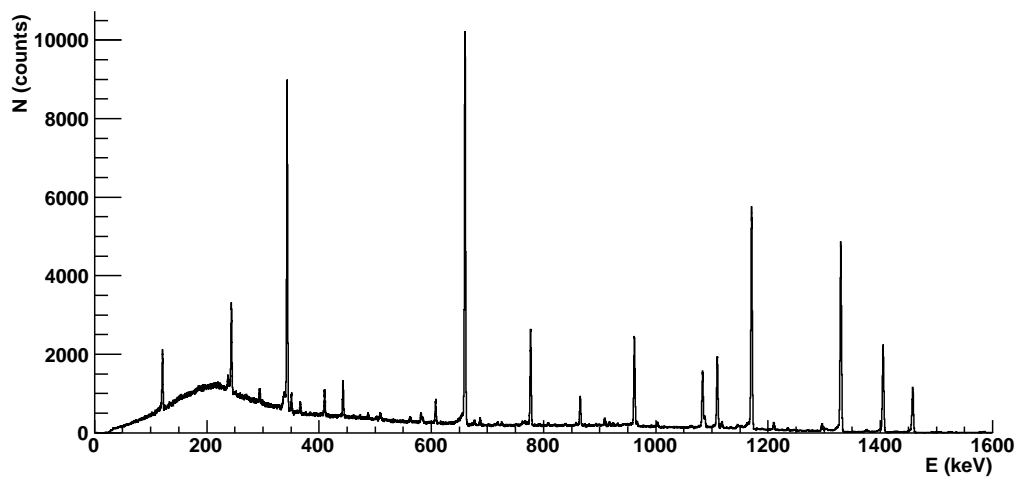
Figure 3.4: Raw spectrum considering only events having two interaction points.

In order to obtain the position of the interactions the analysis of the pulse shapes was performed using the Adaptive Grid Search PSA algorithm [47] mentioned in Chapter 1.

3.1.3 Monte Carlo simulations

Monte Carlo simulations have been performed, using the AGATA code described in [61], with a detailed geometrical implementation of the AGATA symmetric capsule. The simulated events consist on monochromatic photons at the characteristic energies of the

sources employed in the experimental test. Photons are emitted from the corresponding source positions in order to mimic the experimental setup (Fig. 3.5).

The simulation provides the single interaction points inside the AGATA detector given with arbitrary precision in energy and position, i.e, the finite resolution of the detectors is not taken into account. Hence the simulated data have been twice processed, firstly by smearing the values given by the MC simulation according to the detector energy resolution. Secondly, for the data to be comparable to the experimental ones, a packing and another smearing have been performed to simulate the effect of PSA. As the used PSA algorithm works for only one interaction per segment, the simulated energy deposits were packed to their center of gravity calculated by weighting the individual positions with the energy deposited in each interaction. Once the interaction point is defined, a smearing in the position resolution of FWHM of 5 mm with a Gaussian distribution is applied. The simulated data has been exactly analyzed with the same procedure used for the experimental one.
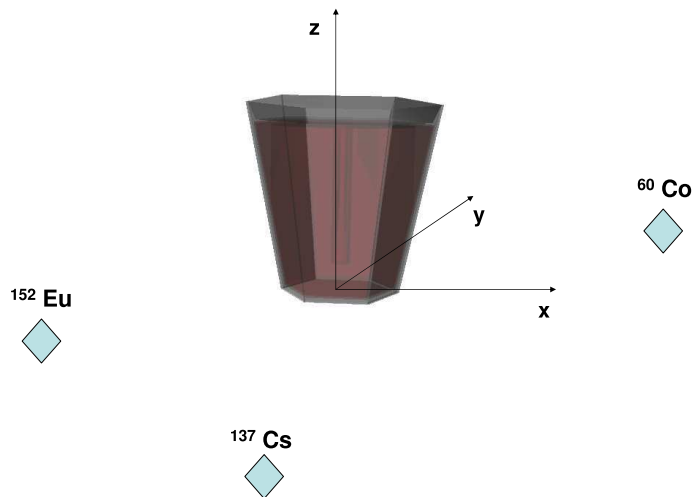
Figure 3.5: Geometrical description of the position of the sources with respect to the detector. The crystal is 80 mm diameter and 90 mm length. The sources are placed around the detector at approximately 1 m distance. For pictorial needs the scale is not respected.

3.1.4   Results and discussion

It is important to notice that the functionality of a single segmented AGATA detector cannot be directly scaled to the full tracking array, mainly because the typical γ-ray energies seldom release the full energy in the volume of a single crystal.

A fundamental parameter for the imaging analysis is the minimum distance requested between interaction (d_{min}) as the average distance between interactions bears severe differences in its value when evaluated for a cluster of several AGATA capsules. However, in the present work, it has been decided to perform the imaging analysis in the conditions expected for a real full tracking array by means of requesting an average distance corresponding to the most probable distance between interactions in the full array. Distances larger than 2 cm correspond to about 70% of the total events for 1-MeV γ rays in

the full AGATA, and when larger than 1 cm about 90% of the events are embraced in the above mentioned conditions. Concerning the multiplicity of the interactions, although not representing a handicap in a real tracking array, the reason to limit our test to γ tracks of two interactions has been to simplify the signal decomposition in the Pulse Shape Analysis process. Monte Carlo simulations for the full AGATA shows that 95% of photopeak events have more than two interactions and reduces to 82% if all events are included. If only events with two interactions are considered, the values go to about 25%. Therefore, the procedures described in this work have a wide applicability for AGATA detectors.

Previously to obtain the results which provides some insight in the imaging capabilities of a single AGATA capsule, we have studied the influence of the two most relevant parameters: d_{min}, the minimum distance between two interactions, and A_θ, the angular acceptance. The value of d_{min} has been optimized using the variational method where several values of the minimum distance between interactions have been selected. These values are $d_{min} = 0$, 1, 2 and 4 cm. For each value, the algorithm selects the events corresponding to the three possible source origins, giving as result three different spectra. We should remember that in each position a different source is placed. Therefore, in these spectra the emissions coming from the source placed in the corresponding position should be enhanced with respect to the other ones.

In Fig. 3.6 the ratios between the number of reconstructed events assigned to ^{60}Co, ^{137}Cs and ^{152}Eu positions, related to the total number of reconstructed events are shown as a function of d_{min}. The picture makes clear how the assignment of the events to the right source position raises up when the distance between the interaction points increases. However, relative peak efficiencies calculated with respect to the number of reconstructed events drop as the distance increases, going down from 75% for $d_{min} = 1$ cm, to 40% for $d_{min} = 2$ cm and 6% for $d_{min} = 4$ cm. As a compromise between this selectivity parameter and the efficiency, a value of $d_{min} = 2$ cm has been selected in the following. With this threshold the number of events correctly assigned to the source is about 50% of the total reconstructed events, while the ratio of events wrongly assigned to this source is about 25% for each one of the other two sources.

In order to evaluate the effect of the angular acceptance, A_θ, the results obtained with and without considering A_θ in the analysis of the experimental data are compared. The ratios between the number of correctly assigned events and the number of total assigned events are shown in Fig. 3.7 for the positions corresponding to the ^{60}Co, ^{137}Cs and ^{152}Eu sources. Overall, the ratio of well-assigned γ rays is slightly higher when imposing an upper limit to $\Delta\theta$, increasing an amount ranging from 1 to 4%. It is also observed as correspondingly the assigned background simultaneously decreases.

The spectra for ^{60}Co, ^{137}Cs and ^{152}Eu positions obtained from the experimental data once the algorithm optimization has been accomplished are drawn in Fig. 3.8 where one can observe that the peaks shaped by the emissions of the source placed in the position corresponding to the reconstructed spectrum are enhanced with respect to those of the raw spectrum. With the analysis performed by the algorithm a sizeable background reduction is achieved. In Table 3.1 it can be seen how the P/T ratio shows an enhancement factor of about 3.5 in the peaks of the spectrum corresponding to the source with the associated emission.
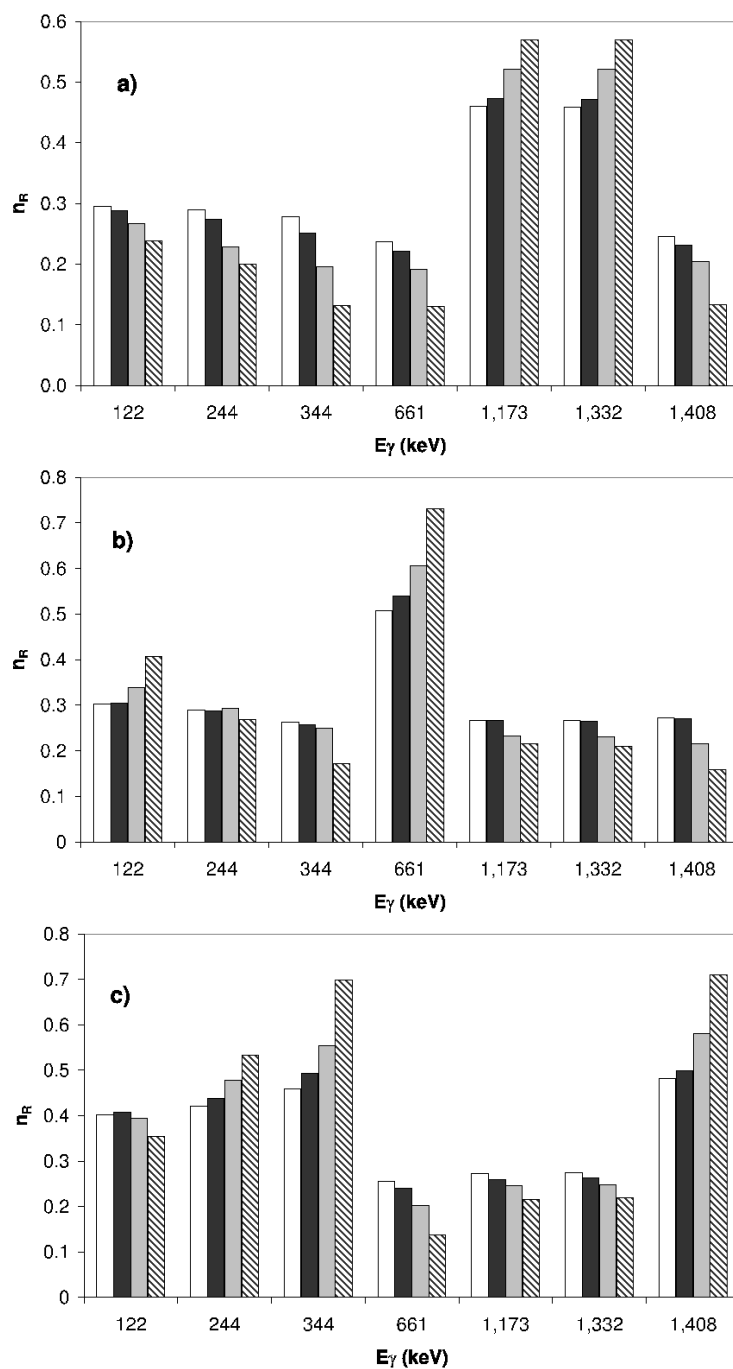
Figure 3.6: a) Ratio of reconstructed events for the main γ-ray lines with respect to the total number of reconstructed events (n_R) for different values of d_{min} assigned to the ^{60}Co position. White, black, grey and ruled bars correspond to a d_{min} of 0, 1, 2 and 4 cm, respectively. In b) and c) the same ratio is shown but for the ^{137}Cs and ^{152}Eu positions, respectively.
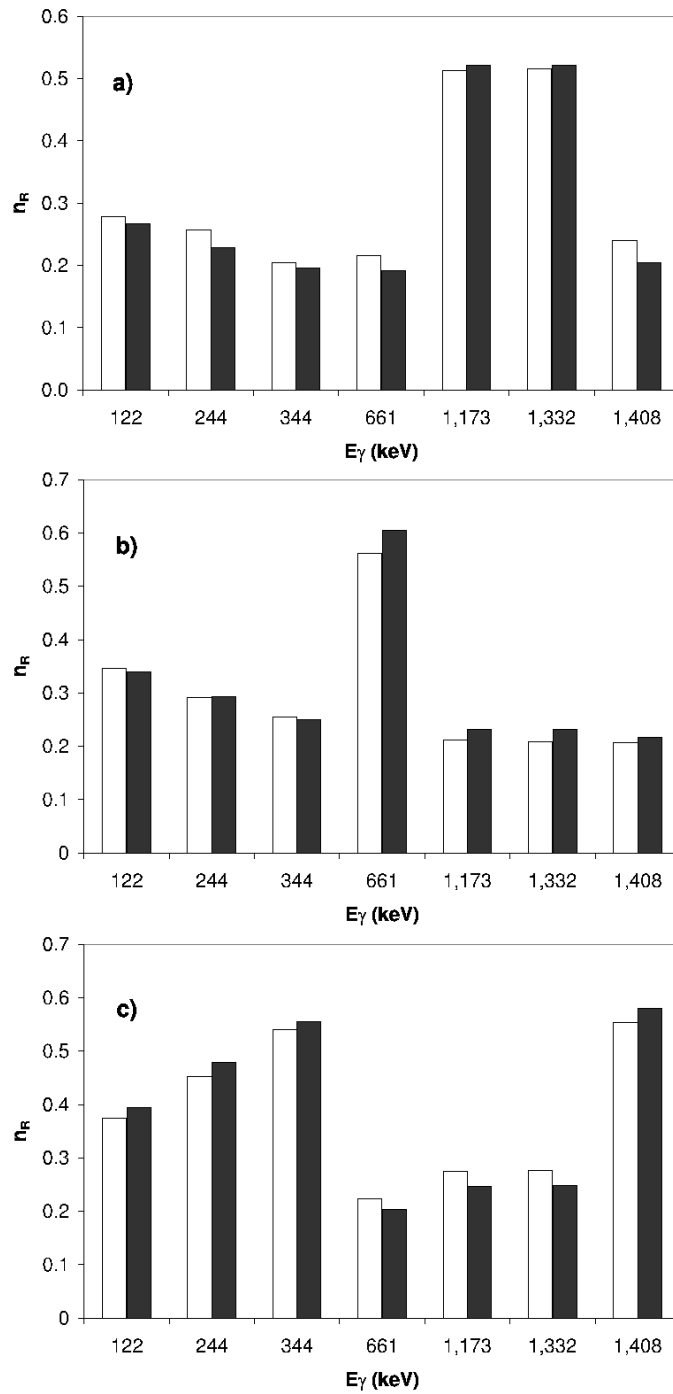
Figure 3.7: a) Ratio of reconstructed events for the main γ-ray lines with respect to the total number of reconstructed events (n_R), with (black bars) and without (white bars) A_θ in the analysis for the position corresponding to ^{60}Co. In b) and c) the same ratio is shown but for the ^{137}Cs and ^{152}Eu positions, respectively.

Figure 3.8: Spectra of the γ radiation assigned to each source position using the background suppression algorithm. The spectrum in the top is incremented if the event is assigned to the ^{60}Co position; the central one corresponds to ^{137}Cs and the one in the bottom to ^{152}Eu.

Table 3.1: P/T ratio for the total, ^{60}Co, ^{137}Cs and ^{152}Eu spectra.

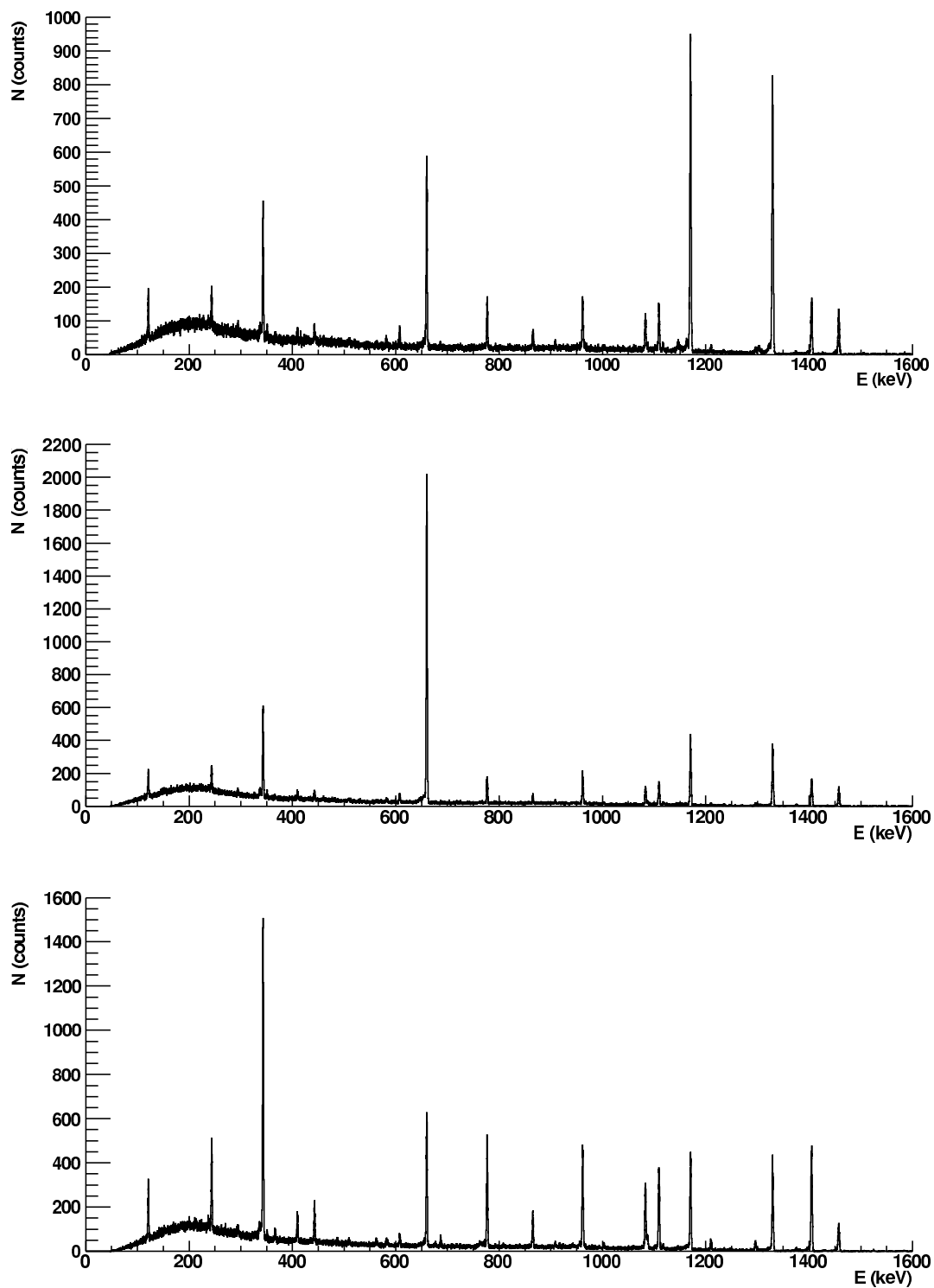| E(keV)	Total (%)	^{60}Co (%)	^{137}Cs (%)	^{152}Eu (%)
244	1.51	1.34	1.72	**2.28**
344	2.64	2.64	3.39	**6.10**
662	2.59	3.20	**10.13**	2.76
1,173	1.64	**5.33**	2.37	2.04
1,333	1.42	**4.69**	2.08	1.81
1,408	0.67	0.91	0.97	**2.11**

Finally, it is meaningful to mention that the ratios of well-reconstructed events with respect to the total reconstructed events in experimental spectra are about 80% of the simulated ones. This means that there are still effects on the real data which are not reproduced by the simulation.

3.2 Background-suppression algorithm for the composed system based on Ge-DSSD + AGATA

As it has been discussed in Chapter 2, we have investigated a possible configuration for the Ge array of the DESPEC experiment based on the coupling of the AGATA array and a set of planar detectors. For the composed system to profit of both, the high efficiency of the AGATA setup and the high position resolution of planar detectors.

As position resolution is directly related to the electric signal production, planar detectors have better response than the quasi-coaxial ones. Electric signals from planars are better understood than the ones from coaxial detectors since the former ones are generated by a simpler electric field generated between the contacts placed in the opposite surfaces of the crystal. For quasi-coaxial detectors, whose geometry is cylindrical, the inner contact is placed along the axis, and the outer one, on the surface of the detector; so the electric field cannot be uniform due to the geometry itself (Fig. 3.9). Besides, the crystal lattice influences also the electric response of Ge detectors. Drift velocities are not identical for the three crystallographic directions being their maximum relative difference of 1.3. Planar detectors are usually cut in a way that the $< 001 >$ direction is parallel to the applied electric field. However, in coaxial detectors the charge motion can occur in any direction with respect to the crystallographic axis, most of the time radially, resulting in different velocities and, therefore, in a deviation between the electric field direction and the charge drift velocity vector. Nowadays, as already mentioned, standard values for the position resolution is, for AGATA detectors, about 5 mm [101] and 1-2 mm for planar detectors [99, 100].
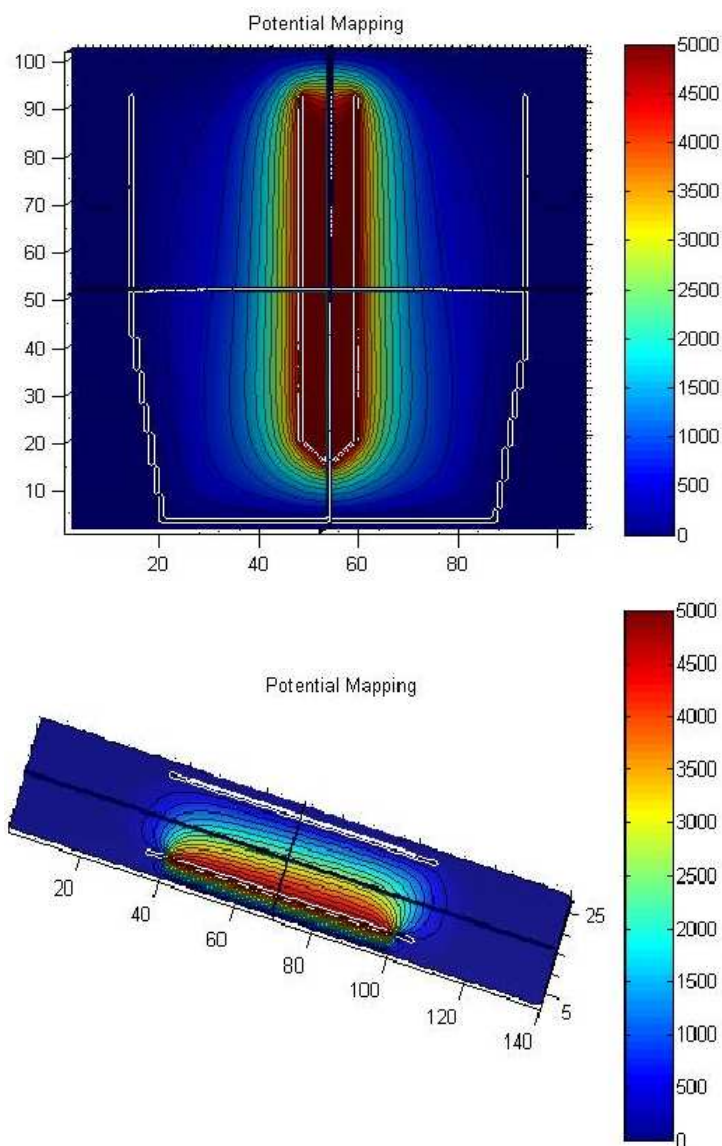
Figure 3.9: Top and bottom pictures show, respectively, the potential mapping for an AGATA detector and for a planar detector (in volts). The pictures have been obtained with the MGS code described in Chapter 1.

It has been previously shown that with the coupled system, the peak efficiency is almost the same that the one obtained only with the 1π S2' configuration, about 7%. Therefore, in terms of efficiency, the addition of an inner array of planar detectors is not significant. This combined system is only meaningful if it provides better imaging capability. At this point an improvement in the Doppler correction as well as a significant reduction of the Compton background is expected if the first interaction takes place in planar detectors.

To study the performance of the combined Ge array in terms of imaging, the background algorithm developed for AGATA, described in the previous section, has been applied [122]. The main objective of the study is to characterize the capabilities to

discriminate between γ sources placed at different locations of the system made up of a set of planar Ge detectors in a daisy configuration and AGATA detectors in their next configuration, the so-called S2': a semi-spherical distribution covering a 1π solid angle which will be running at GSI for 2012 and 2013. As the full system is not currently available, this study will be done through MC simulations.

3.2.1 Method

The Monte Carlo implementation of the setup has been already described in Chapter 2 but for the sake of clarity the simulated setup is shown again (Fig. 3.10). The geometry implemented was the 1π S2' AGATA configuration coupled to six planar Ge detectors. AGATA detectors were placed at their nominal position, 23 cm from the target, and the planar array was placed at approximately 12 cm of the implantation plane, inside the solid angle covered by AGATA detectors. Planar detector dimensions were 70*70*20 mm^3 but due to the 5 mm guard ring thickness, the active area remained 60*60*20 mm^3.
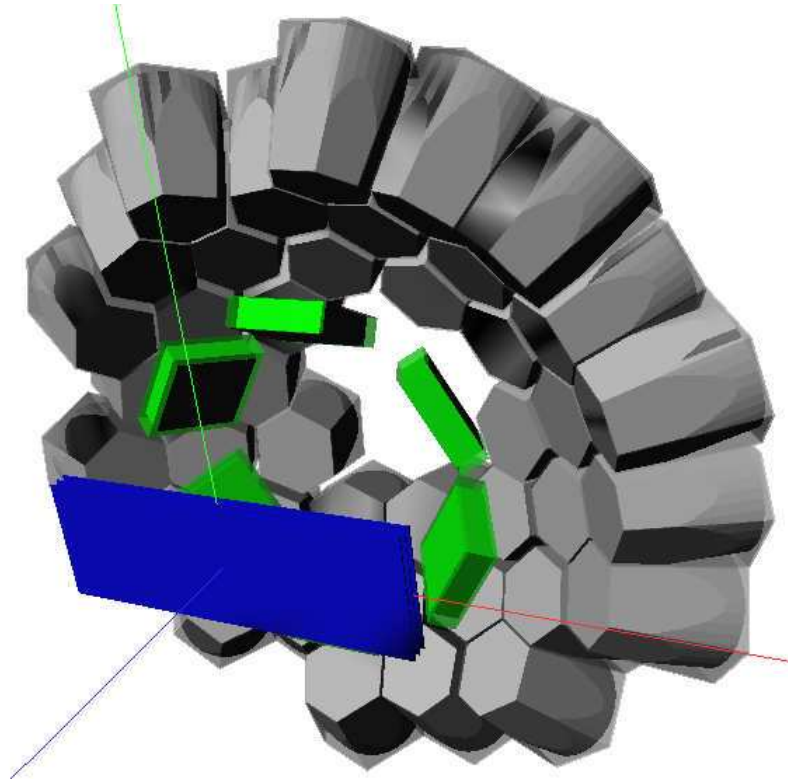
Figure 3.10: MC implementation of the system composed by the implantation detector AIDA, the set of planar detectors and AGATA in the S2' configuration. Red, green and blue correspond to X, Y and Z axis, respectively.

Point sources of ^{60}Co with emission energies of 1,173 and 1,333 keV, ^{137}Cs with its γ emission at 662 keV and ^{152}Eu emitting at 244, 344 and 1,408 keV, are placed in the same plane as AIDA with coordinates (15,0,0), (0,0,0) and (0,15,0) cm, respectively. The simulated events are simply monochromatic photons at the γ energies of the sources

emitted from the different source positions.

The simulated data have been pre-processed to emulate the experimental ones. The procedure followed has been already described in the previous study involving only AGATA, but now we take 1 mm FWHM for the position resolution of the planar detectors. The pre-processed data become the input of the background-suppression algorithm, a modified version of the one specifically developed for the coaxial detectors of AGATA, which is based on the Compton formula. In the data processing, only events with two interactions are taken into account reducing the possible events to the following three: coaxial-coaxial events (CC), planar-planar events (PP) and planar-coaxial events or vice versa (PC). With respect to the free parameters of the algorithm, d_{min} is set to 1 cm to increase statistic and A_θ is evaluated with a FWHM of 5 mm for the coaxial detectors and 1 mm for the planar ones.

3.2.2   Analysis and results

The background-suppression algorithm adapted to the DESPEC experiment also assigns the events to one of the gamma sources during the reconstruction process, being its output a spectrum for each source. The efficiency after Compton reconstruction is about 35%, CC events representing 33% and PP and CP ones about 1% each one. The results are summarized in Table 3.2 where it can be seen how the number of events correctly reconstructed is higher for PC events than for CC or PP ones. This is mainly due to the fact that all the events consisting of one interaction in a planar detector and another one in an AGATA detector always satisfy the condition on the minimum distance between interactions imposed by the algorithm.

Table 3.2: Ratio (%) for the main γ-ray lines of reconstructed peak events assigned to the correct source with respect to the total number of reconstructed peak events in all the source spectra for the different cases considered in the study. PC column corresponds to events having one interaction in a planar detector and the other in an AGATA detector; PP and CC columns, to events having both interactions in planar or AGATA detectors, respectively; and the Total column to all cases considered together.

Source	E(keV)	Total	PC	PP	CC
^{60}Co	1,173	60	**81**	73	59
	1,333	62	**83**	79	61
^{137}Cs	662	53	**80**	69	51
^{152}Eu	244	62	74	**78**	60
	344	60	**77**	74	58
	1,408	63	**85**	81	62

The use of our algorithm results in an enhancement of the P/T ratio. An improvement between 2 and 3% is obtained in the ^{60}Co, ^{137}Cs and ^{152}Eu spectra with respect to the raw data. In Table 3.3, P/T results for every source spectrum are given attending to the different kind of events. It is clear how the P/T ratio is better in the case of PC events for all energies, except for the 244 keV emission line of the ^{152}Eu source. This is because the lower the energy the higher the probability of having two interactions at short distances, as happened for PP events. In Fig. 3.11, Fig. 3.12 and Fig. 3.13 the ^{60}Co, ^{137}Cs and ^{152}Eu source spectra obtained for CC and PC events are shown, respectively. It can be observed a better source identification of the PC events with respect to the CC ones but with the drawback of the worse statistic since most events are CC ones. Therefore, an array composed of AGATA and planar detectors presents better capabilities for imaging purposes due to the better position resolution of planar detectors.
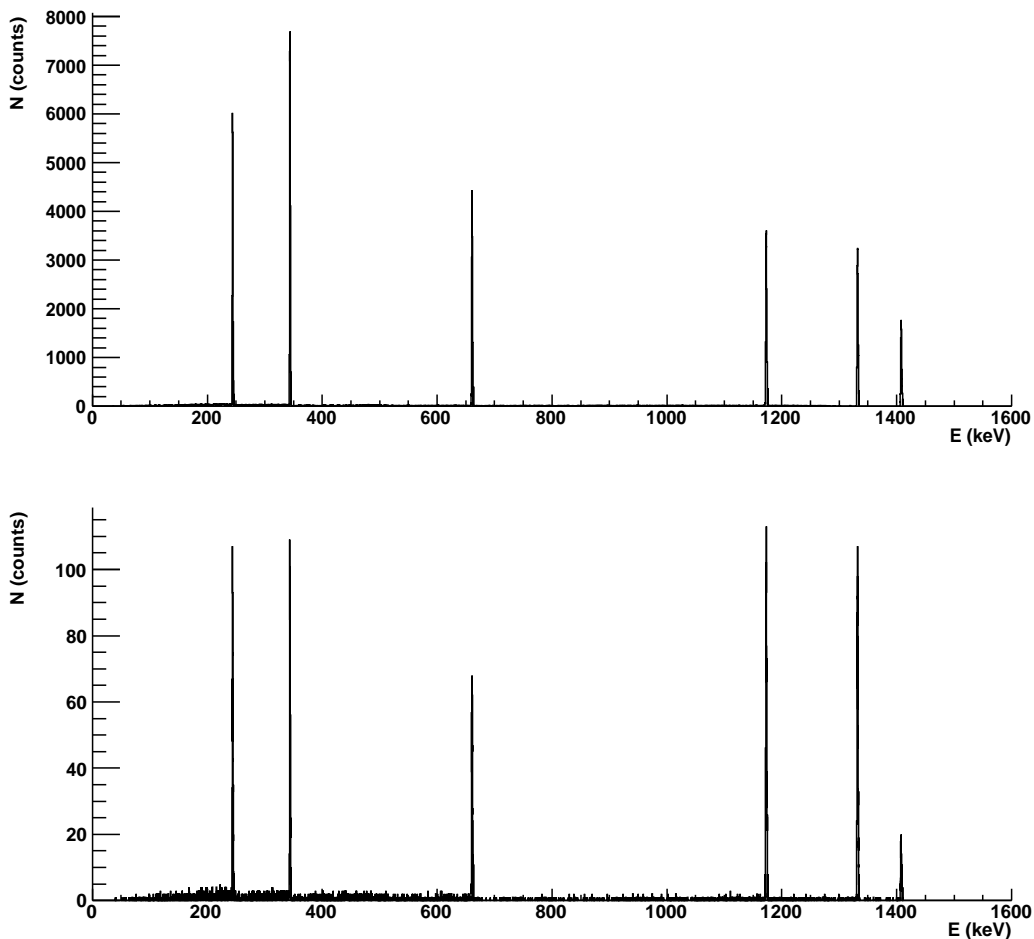
Figure 3.11: Spectra of the γ radiation assigned to the ^{60}Co source for CC events (top) and for PC events (bottom).
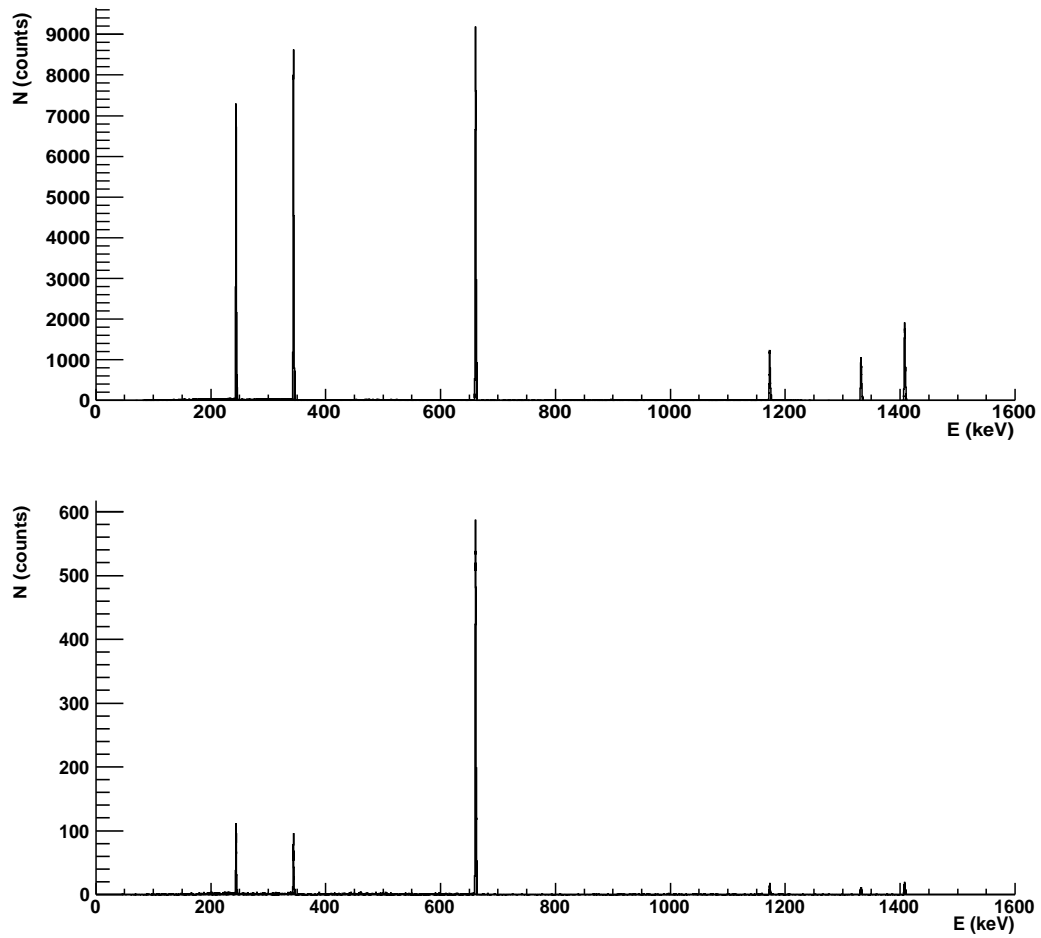
Figure 3.12: Spectra of the γ radiation assigned to the ^{137}Cs source for CC events (top) and for PC events (bottom).

Table 3.3: P/T ratio (%) for the ^{60}Co, ^{137}Cs and ^{152}Eu spectra for the different cases. PC, PP, CC and Total columns have the same meaning as in Table 3.2.

Source	E(keV)	Total	PC	PP	CC
^{60}Co	1,173	13	**18**	10	13
	1,332	11	**16**	8	11
^{137}Cs	661	27	**60**	45	26
^{152}Eu	244	30	34	**40**	30
	344	33	**38**	34	33
	1,408	12	**13**	6	12
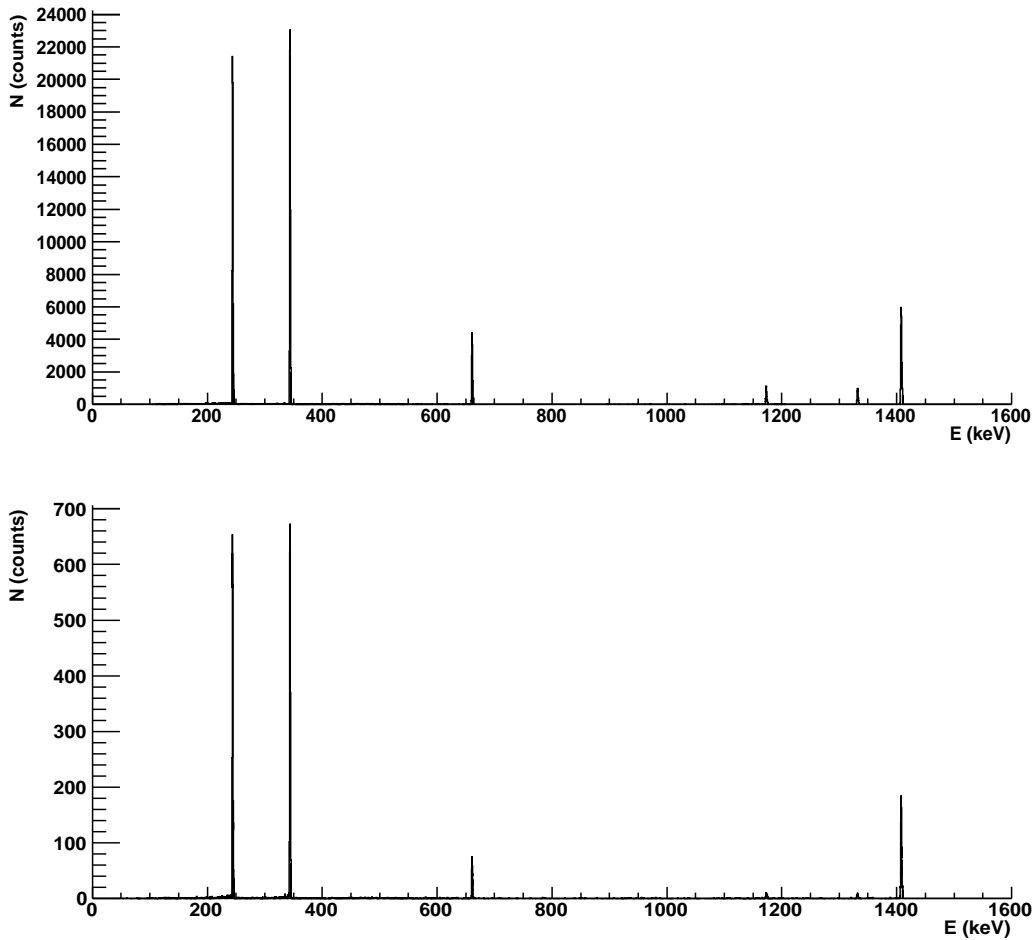
Figure 3.13: Spectra of the γ radiation assigned to the ^{152}Eu source for CC events (top) and for PC events (bottom).

3.3 A new Compton imaging algorithm to study the capabilities of the Ge array for DESPEC

We intend to go a step further of the background-suppression algorithm willing to propose a new Compton imaging algorithm which affords the determination of the γ-ray origin in a probabilistic way. As it has been explained in Chapter 1, current tracking algorithms are mainly based on statistical methods, using a clusterization process through different algorithms to group the interaction points in the detector. All of them have the same constraints with events of one interaction, because it is not possible to distinguish those photons that have been completely absorbed in the detector through a photoelectric interaction from those which have interacted through an unique Compton scattering and, therefore, contributing to the background. In these codes, the γ track is disentangled by using a figure of merit weighted by different factors as the energy deposited in the interaction, the number of reconstructed points or the clusterization process used.

In this context, we have developed a new Compton imaging algorithm for γ-ray tracking HPGe detectors for the unique experimental conditions of the DESPEC experiment [68]. The objective is to reconstruct the γ path inside the detector correctly identifying the positions in the sequence of interactions that takes place inside the detector. The purpose of Compton imaging is to identify the γ-ray emitting source position in the focal plane. In doing so, imaging increases the overall efficiency providing the implantation position which makes possible to identify the γ-ray origin in the isomeric experiments. With this technique it is also possible to distinguish photons emitted by the source from those originated outside the focal plane, providing a method to reduce the spectral background.

The tracking process is performed through a back-tracking method, assuming that the photon is completely absorbed in the detector and, therefore, taking the last interaction as a photoelectric one which will be the starting point for the reconstruction process. The main differences respect to previous algorithms are: first, the consideration of all possible combinations for the interactions to reconstruct the γ path instead of using a clusterization process and, second, the fact that the reconstruction process is based on the Compton probability instead of the direct application of the Compton scattering formula. The pair production process is not included in the implementation, neither events having only one interaction point.

As it has been explained in the previous section, the performance of the Ge array for the DESPEC experiment in terms of imaging is under study. To evaluate the performance of the algorithm we have studied the imaging capabilities of the geometry composed by a set of Ge Double Side Strip Detectors (Ge-DSSD's) coupled to AGATA which is described in detail in Chapter 2. To test the algorithm, Monte Carlo simulations of the ideal array, consisting in two shells have been used (Fig. 2.16). The algorithm's purpose is to reconstruct those events having the first interaction in the Ge-DSSD shell to get ride of its 1-2 mm position resolution in comparison with the 5 mm one of coaxial detectors.

3.3.1   The imaging algorithm

Our algorithm works in an iterative way. It means the algorithm to search for all possible tracks considering all combinations of the interaction points. To disentangle the tracks from the interaction positions given by the PSA, the algorithm proceeds following a backtracking method. From the pool of the interaction points, it takes one interaction position as the last one for the trial track assuming as hypothesis that the photon is completely absorbed and, therefore, that the last interaction is a photoelectric interaction characterized by its mean free path (λ). Then, the traveled distance in Ge between this point and all possible second interactions is calculated. This parameter is called effective distance because it is not the geometrical distance between the positions of both interactions. This effective distance calculated for each pair is compared with the mean free path and those points that verify: $d_{ef} < 3\lambda$ are considered as candidates to be the second interaction point in the backtracked sequence. To select one among all points that have satisfied the criterion, the total Compton cross section is calculated for the couple formed by the first interaction, actually the last one in the track, and each possible second one as follows:

$$\sigma_t = 2\pi r_0^2 \left[\frac{1+\alpha}{\alpha^2} \left[\frac{2(1+\alpha)}{1+2\alpha} - \frac{ln(1+2\alpha)}{\alpha} \right] + \frac{ln(1+2\alpha)}{2\alpha} - \frac{1+3\alpha}{(1+2\alpha)^2} \right] \qquad (3.4)$$

being $\alpha = \frac{E_0(keV)}{511}$ and r_0 the classical electron radius ($r_0 = 2.818$ fm).

The pair with the maximum value of the cross section is selected as the most probable and, therefore, the second interaction point is chosen. The same procedure is followed for all the sequence in the event until a track is obtained although the mean free path is calculated assuming a Compton interaction. The track finishes when there is not any point verifying the condition on λ. A schematic view of the algorithm implementation is shown in Fig. 3.14.
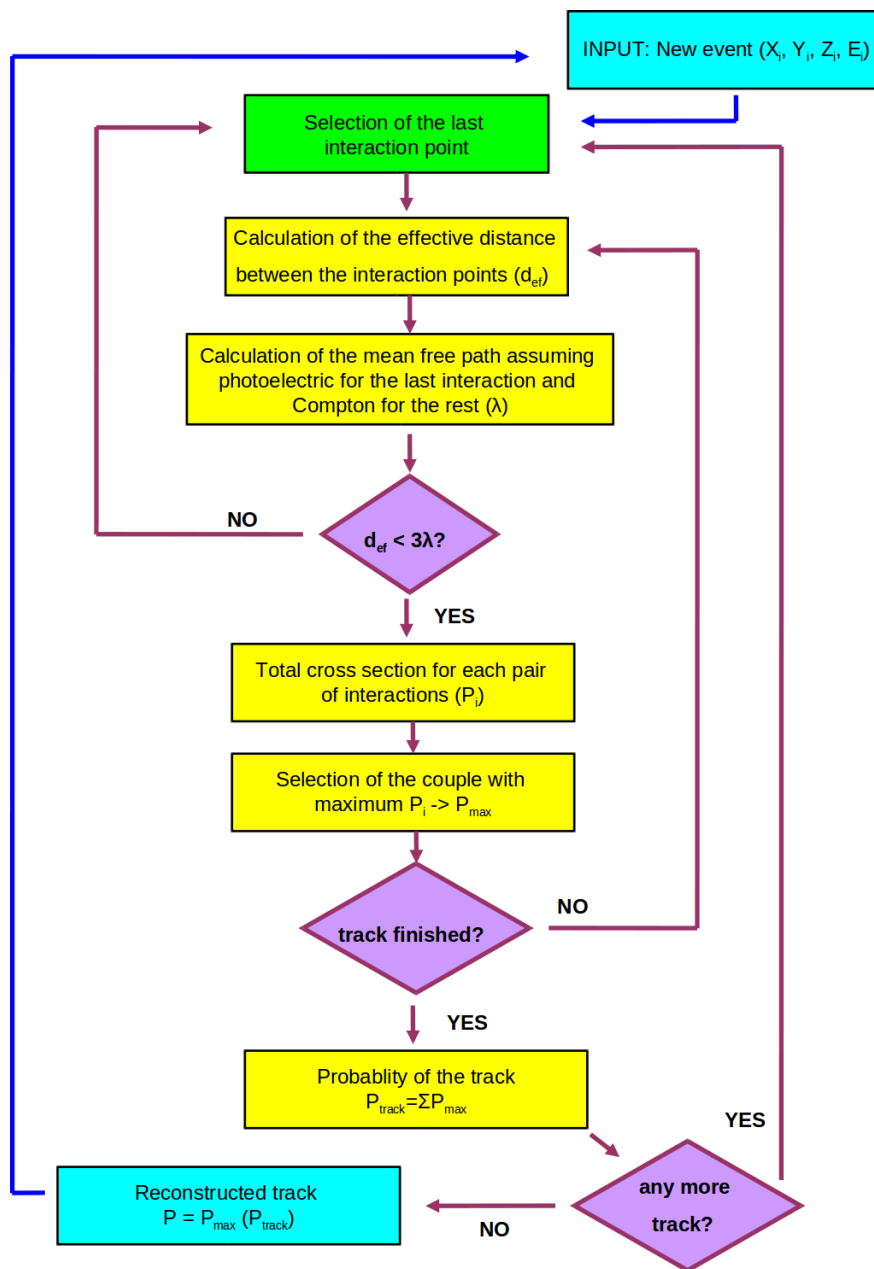

Figure 3.14: Outline of the algorithm implementation.

The mean free path is calculated through the attenuation coefficient: either of Compton scattering or of photoelectric interaction if the last interaction is involved in the pair.

$$\lambda = \frac{1}{\tau} \tag{3.5}$$

The attenuation coefficient is obtained through the differential cross sections for the different processes as:

$$\tau_i = \frac{\sigma_i N_{Avog} \rho_0}{M} \tag{3.6}$$

where $\sigma_i = \sigma_c$ or σ_p is the differential cross section for Compton or photoelectric effects respectively, N_{Avog} is the Avogadro number, M is the atomic mass of the material and ρ_0 is the material density ($\rho_0 = 5.323 \ g/cm^3$ for Ge). The cross section data have been taken from the Evaluated Photons Data Library [111]. The values for the energies of interest can be obtained interpolating linearly from this library.

Once the path in Ge of the γ ray is determined, with the two first interaction points, imaging can be performed. The line defined by these two points gives us the axis of the imaging cone while the incident direction is obtained from the Compton angle defined by the first interaction. The emission position will be obtained superimposing all cones corresponding to events of the same total deposited energy obtaining a well-defined spot in the focal plane. This performance will be included in future developments of the code.

3.3.2   Monte Carlo simulations

The Monte Carlo simulations performed to test the imaging algorithm have been made with the Geant4 tool. The geometry implementation of the ideal system consists, as it has been mentioned in Chapter 2, of two Ge shells of 2 and 9 cm thickness, imitating the Ge-DSSD shell and AGATA, respectively (Fig. 2.16). The shells are placed concentricly: the planar one goes from 11 to 13 cm and the coaxial one from 24 to 33 cm with respect to the geometrical centre. Monoenergetic gammas of 1,333 keV and 662 keV thrown from the centre of reference have been used for the analysis. Only the information on the gamma interactions has been considered in the simulation output. Therefore, data corresponding to secondary particles, provided also by Geant4, have been skipped. Actually, in real experiments only the interaction positions of γ rays in Ge can be obtained through PSA techniques altough they are a consequence of the absorption position spread of secondary particles. However, we have checked by simulations that the spot size is some orders of magnitude smaller than the position resolution of the detectors. Finally, the analysis has been restricted to multiplicity one although in future implementations it is expected to work with higher values.

As it has been explained in previous sections, to get a response of the detector comparable to the experimental results a pre-processing data is needed. Therefore, both packing and smearing processes have been applied to the simulated data, taking into account 5 mm FWHM for the position resolution of the detectors. The pre-processed data become the input of the Compton imaging algorithm.

3.3.3 Results and discussion

Due to the ideal geometry implementation for the data analysis, both peak and total efficiencies obtained with the simulation are unrealistic but they are useful to compare ideal performances among different setup proposals. In this respect, the efficiency values obtained are clearly higher than those obtained for the designs based only in planar detectors. The values are shown in Table 4.2.

In Table 3.5 the ratio of events having one, two, three and four or more interactions with respect to the total number of events, after the pre-processing, for the γ-ray emission lines of the sources is shown. It is clear that after the processing, most of the events consists of one or two interaction points. As the algorithm does not consider those events having only one interaction point, the reconstruction process is reduced to about 50% of the simulated events. The results obtained once the algorithm is applied are summarized in Table 3.6, where the ratio between the number of well reconstructed events having one, two, three and four or more interactions and the total number of events with the same number of interactions is shown. From these data it can be said that the algorithm works quite well when the track consists of two points: almost 95% of events are well reconstructed whereas only about 50% of events having more than two interactions are well reconstructed. In Table 3.7 are shown the same ratios but considering only those events having the first interaction point in the Ge-DSSD shell. These events should be obtained with better position resolution and, therefore, they are better candidates to provide an accurate imaging analysis. A sizeable number of well reconstructed tracks fulfills this condition. Therefore, in principle, this geometry is suitable for imaging purposes.

An improvement in terms of P/T values is obtained when the imaging algorithm is applied (see Table 3.8). It means our algorithm works rejecting mostly not completely absorbed events, those which contribute to the background, and reconstructing those tracks belonging to photons which have deposited all their energy inside the detector.

In Fig. 3.15 the spectra of the different sources are displayed. In green, red and blue colours are shown respectively, the output of the MC simulation, the spectra when all well reconstructed events are considered and the spectra if only well reconstructed events having the first interaction in the Ge-DSSD shell are considered. The reduction in the continous background is achieved mainly at low energies although is substantial in the whole energy range.

Table 3.4: Simulated peak (ε_p) and total (ε_T) efficiencies for the two energies studied corresponding to emission lines of ^{60}Co and ^{137}Cs sources. One million of events have been simulated to have a good enough statistic.

Source	E (keV)	$\varepsilon_T(\%)$	$\varepsilon_p(\%)$
^{60}Co	1,333	94.5	77.6
^{137}Cs	662	97.8	90.2

Table 3.5: Ratio (%) of events having one (Ev_1), two (Ev_2), three (Ev_3) and four or more interactions (Ev_4), respectively, with respect to the total number of events for the main γ-ray emission lines of a ^{60}Co and a ^{137}Cs sources.

Source	E (keV)	Ev_1	Ev_2	Ev_3	Ev_4
^{60}Co	1,333	49.9	41.8	7.6	0.7
^{137}Cs	662	53.9	38.3	7.5	0.3

Table 3.6: Ratio (%) of well reconstructed events having two (N_2), three (N_3) and four or more interactions (N_4), respectively, with respect to the total number of events with the same number of interactions at 1,333 and 662 keV.

Source	E(keV)	N_2	N_3	N_4
^{60}Co	1,333	97.0	54.2	57.1
^{137}Cs	662	96.3	50.0	50.0

Table 3.7: Ratio (%) of properly reconstructed events of two (N_2p), three (N_3p) and four or more interactions (N_4p), respectively, with respect to the total number of events with the same number of interactions when the first interaction is in the Ge-DSSD shell.

Source	E(keV)	N_2p	N_3p	N_4p
^{60}Co	1,333	63.3	47.2	57.1
^{137}Cs	662	73.0	38.9	50.0

Table 3.8: P/T values obtained with the simulated data after pre-processing (MC), with the data obtained from the algorithm considering all reconstructed events (AR) and considering only reconstructed events having the first interaction in the Ge-DSSD shell (PR).

P/T (%)				
Source	E(keV)	MC	AR	PR
^{60}Co	1,333	82	91	94
^{137}Cs	662	92	97	94

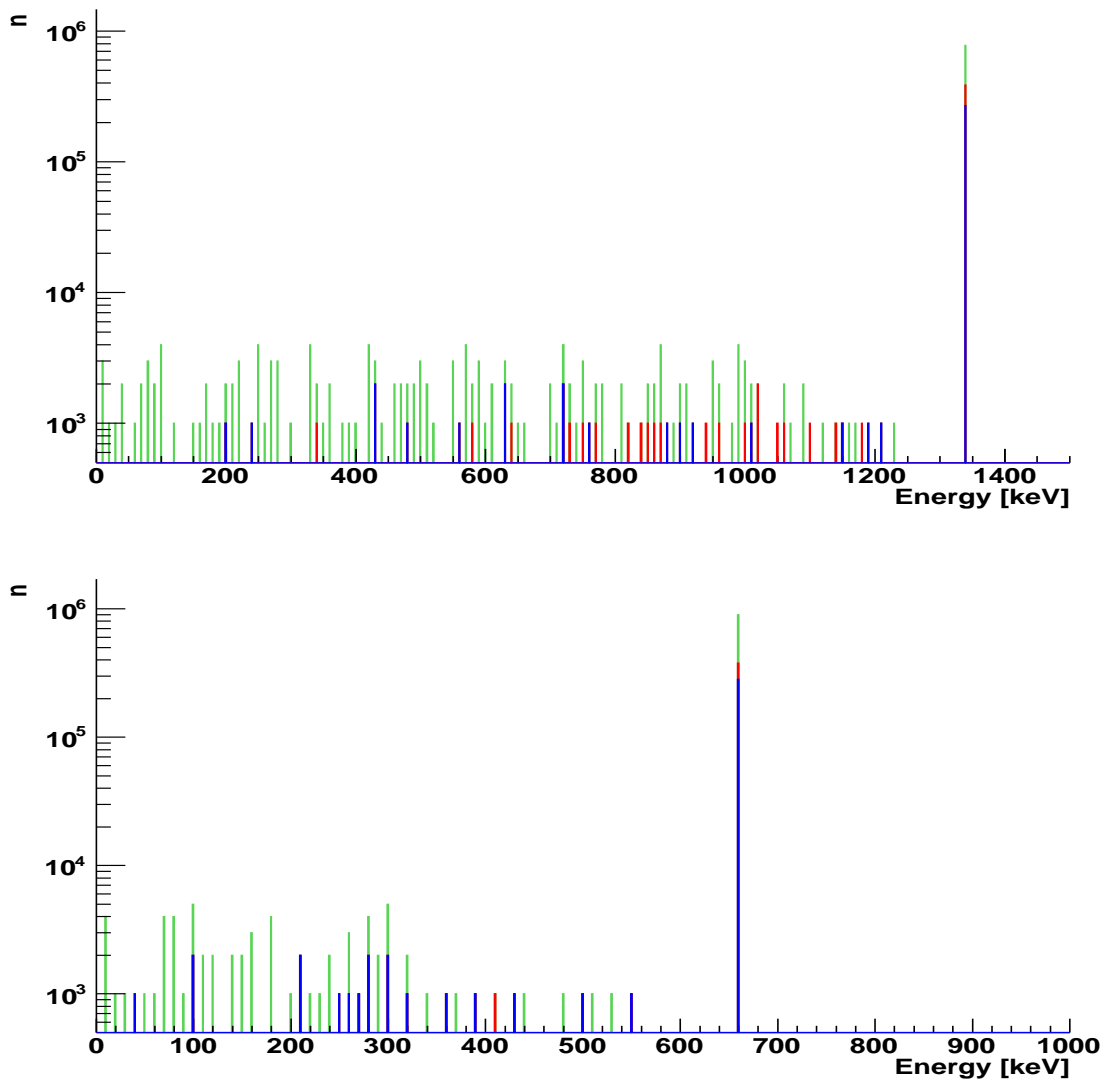Figure 3.15: Spectra obtained for the 1,333 keV γ-emission line of ^{60}Co (top) and for the 662 keV γ-ray of ^{137}Cs (bottom). Green, red and blue correspond, respectively to: the output of the MC simulation, the spectra of well reconstructed events and the spectra of well reconstructed events if only those which have the first interaction in the Ge-DSSD shell are considered.

Chapter 4

Lifetime measurement of neutron-rich nuclei in the region of the double magic ^{78}Ni with the γ-tracking AGATA demonstrator.

4.1 Introduction

The "Magic Number" is probably the most fundamental concept governing the structure of the atomic nucleus at low excitation energy. The incept of the nuclear shell model was triggered by the identification by Goeppert-Mayer and Jensen of the magic numbers and their origin [123]. Since then, the nuclear structure studies have followed and advanced on the ground of the shell model. For long time, these studies have been performed for stable nuclei or nuclei close to the stability line. For those nuclei the magic numbers suggested by Goeppert-Mayer and Jensen are valid and, therefore, the shell structure can be well understood in terms of the harmonic oscillator potential with a spin-orbit interaction. As we move away for the beta-stability line, the nucleon-nucleon residual interaction plays an important role modifying the known shell structure for stable nuclei.

The exotic nuclei provide unusual opportunities for testing models of nuclear structure that have been proposed and optimized for nuclei in, or near, the stability valley. The lightest neutron-rich exotic nuclei are especially relevant due to the large isospin values reachable within the boundaries of the neutron drip line. Neutron-rich nuclei are as well of extreme relevance for the stellar nucleosynthesis. In particular, nuclei in the intermediate mass region, close to ^{78}Ni, play an important role in the nucleosynthesis via r-process.

In 1975, the first indication of an anomalous ordering of the single particle levels, on exotic isotopes of Li and Na, was obtained through mass measurements performed by C. Thibault and R. Klapisch and collaborators. For ^{11}Li a binding energy of 170 ± 80 keV was found, when this isotope had been predicted to be unbound. Furthermore, it was noted that ^{31}Na and ^{32}Na were considerably more bound than predicted theoretically considering a N=20 shell closure [124, 125]. This re-ordering of the shell structure was suggested to be originated by deformation. The ^{31}Na and ^{32}Na binding energies were reproduced through Hartree-Fock calculations considering the promotion of neutrons from

Lifetime measurement of neutron-rich nuclei in the region of the double magic ^{78}Ni with the γ-tracking AGATA demonstrator.

78

$d_{3/2}$ to the $f_{7/2}$ intruder orbit (the $f_{7/2}$ orbit is called an intruder orbit because it belongs to the next major shell) [126]. The occupation of intruder orbits was very surprising, since N = 20 was believed to be a magic number and no excitations across the shell gap should be present at low excitation energies. Later, mass measurements were extended to Mg isotopes and it was found that both ^{31}Mg and ^{32}Mg were as well far more bound than expected. These studies were repeated and extended with different techniques (for recent tabulated values see [127]). In the cases of Ne, Na and Mg isotopes around N = 20 even most improved models assuming a closed sd shell cannot reproduce the experimental binding energies, although they are successful in other cases. Moreover, nuclei with the same number of neutrons, but more protons do not exhibit such shell changes. The initial idea that the deformation induces a re-ordering of the orbital inverting the single particle energies, gave rise to the name of "island of inversion" for this particular region.

Recent theoretical calculations [128–130] and experimental results have indicated that magic numbers can change depending on where they lie on the nuclear chart due to the residual nucleon-nucleon interaction thus implicating a more local applicability of the concept. In particular, due to the residual tensor interaction ($\sigma\tau$).

To understand the underlying single-particle properties of a nucleus and, therefore, the shell evolution we can make use of the effective (spherical) single-particle energies (ESPE's), evaluated as a measurement of mean effects on a nucleon in a specified single-particle orbit from the other nucleons. The ESPE of an occupied orbit is defined to be the separation energy of this orbit with opposite sign (the separation energy is the minimum energy needed to take out a nucleon from its orbit). The ESPE of an unoccupied orbit is defined as the binding energy gained by putting a proton/neutron into this orbit with the opposite sign. The ESPE of an orbit j varies as an orbit j' is filled. If this energy change becomes sufficiently significant, the shell gap can disappear due to the reduction of the spin–orbit splitting. The tensor component of the residual interaction is the main responsible of this energy modifications and it is expected to depend strongly on the filling of the orbitals near the Fermi surface.

The nature of the monopole part of the tensor interaction is such that an attraction (repulsion) is expected for orbitals with anti-parallel (parallel) spin configuration [131]. Fig. 4.1 a) shows a nucleon on j=l-1/2 ($j_<$) which is interacting with another on j'=l+1/2 ($j'_>$). Due to the high relative momentum between them, the spatial wave function of their relative motion is narrowly distributed in the direction of the orbital motion. The spins of the two nucleons are parallel in this case, giving rise to basically S=1. The ellipse in Fig. 4.1 a) represents such relative-motion wave function being spread more along the total spin S=1. The same mechanism holds for two nucleons in $j_>$ and $j'_<$ (or vice versa). On the other hand, as in Fig. 4.1 b), the tensor force produces a repulsive effect for two nucleons in $j_>$ and $j'_>$ (or vice versa) because the wave function of the relative motion is stretched in the direction of the orbital motion.

The single-particle energy of an orbit j is given by its kinetic energy and the effects from the inert core (closed shell) on the orbit j. As some nucleons are added to another orbit j', the single-particle energy of the orbit j is changed (Fig. 4.2). The nucleons on j' can generate various many-body states, but we are interested in monopole effects independent of details of such many-body states. The two-body matrix element of the interaction depends on the total angular momentum (J) of the two interacting nucleons in orbits j and j'. Since we are investigating a mean effect, this J-dependence is averaged out with a weight factor $(2J + 1)$ and only diagonal matrix elements are taken. Since the

angular correlation is taken away, two nucleons can be at any magnetic sub-state, yielding the same binding energy. The monopole component of the tensor interaction is thus given by the matrix element [129] and references therein:

$$V_{j,j'}^T = \frac{\sum_J (2J+1)\langle jj'|V|jj'\rangle_{JT}}{\sum_J (2J+1)} \tag{4.1}$$

where $\langle jj'|V|jj'\rangle_{JT}$ stands for the matrix element of a state where two nucleons are coupled to an angular momentum J and an isospin T.
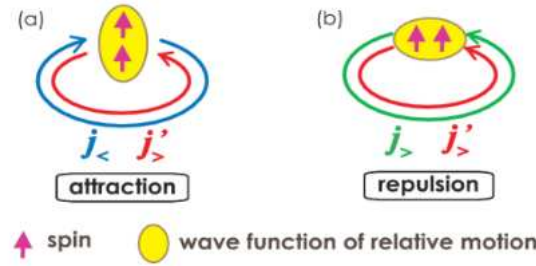

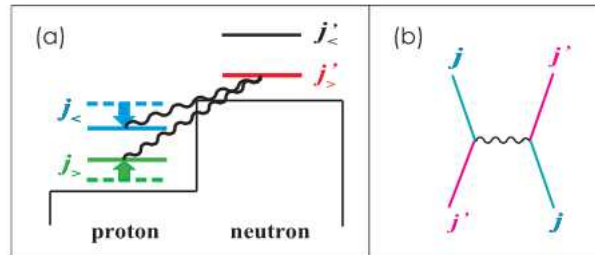Figure 4.1: Dependence of the tensor component with the orbital filling. Taken from [129].

Figure 4.2: a) Schematic picture of the monopole interaction produced by the tensor force between a proton in $j_{>,<}=l\pm 1/2$ and a neutron in $j'_{>,<}=l'\pm 1/2$. b) Exchange processes contributing to the monopole interaction of the tensor force. Taken from [129].

Therefore, in evaluating the effects of the monopole interaction in a system with many valence nucleons, only the number of nucleons in each orbit matters. This implies that the effect can be accumulated and, therefore, it becomes larger as the orbit occupation increases. Different regions of the nuclear chart where nuclei have large neutron excess, have been studied in the context of the shell evolution as the p-shell and sd-shell [131]. In this work, we are interested in the neutron-rich isotopes around the double magic nucleus ^{78}Ni involving the fp-shell.

4.2   Towards ^{78}Ni

The region of neutron-rich nuclei around Z=28 (Ni) is of particular interest for understanding the evolution of the shell structure for nuclei with large neutron excess.

In fact nucleus ^{78}Ni is, as far as we know, the bound double magic nucleus with the highest neutron-proton ratio ($N/P \sim 1.78$). In the neighbourhood of ^{78}Ni, the addition of neutrons to the $1g_{9/2}$ orbital changes the relative energies of the proton $2p_{3/2}$, $2p_{1/2}$ and $1f_{5/2}$ orbitals due to the strongly attractive proton-neutron spin-flip interaction. In particular, it is predicted that the Z=28 gap for protons in the fp-shell becomes smaller moving from ^{68}Ni to ^{78}Ni as a result of the attraction between the proton $f_{5/2}$ and the neutron $g_{9/2}$ orbits and repulsion between the proton $f_{7/2}$ and neutron $g_{9/2}$ configurations, thus modifying or even inverting the effective single particle states [129–132].

In Fig. 4.3 the ESPE's predicted within the shell-model calculations with the GXPF1 effective interaction [133], with the changes due to the tensor force in the proton fp-shell as neutrons occupy the $1g_{9/2}$ orbit going from ^{68}Ni (N=40) to ^{78}Ni (N=50) are shown. The proton $1f_{5/2}$ is pulled down while the $1f_{7/2}$ is lifted up, as N increases. Thus the Z=28 gap becomes smaller as approaching to ^{78}Ni and the sequence of the orbits is quite different when comparing ^{68}Ni to ^{78}Ni [134].
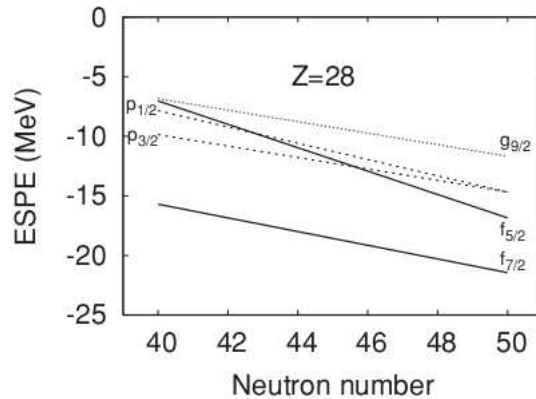

Figure 4.3: Proton ESPE's predicted by the shell model with the GXPF1 effective interaction in Ni isotopes as a function of N.

The tensor component of the residual interaction is predicted to affect the transition matrix elements. In particular to drive the $B(E2 : 2^+ \rightarrow 0^+)$ matrix elements of the Ni isotopes towards large values when approaching ^{78}Ni. The $B(E2 : 2^+ \rightarrow 0^+)$ values for the Ni isotopes have been measured up to ^{70}Ni where a large E2 strength of $B(E2 : 2^+ \rightarrow 0^+) = 860(140)e^2fm^4$ has been found [135]. Such a large transition probability has been attributed to the effect of the large core polarization caused by the strong spin-isospin interaction when the number of neutrons in the $g_{9/2}$ orbital increases [135]. The increase of the core polarization results in an enhancement of the $B(E2 : 2^+ \rightarrow 0^+)$ corresponding to an enhancement of the nuclear collectivity.

It is worth to mention the unexpected behaviour found for the ^{68}Ni isotope having N=40. Its large 2^+ excitation energy $E(2^+) = 2.033$ MeV, measured by Broda [137], together with the value for the reduced transition probability measured through Coulomb excitation by Sorlin [136], $B(E2 : 2^+ \rightarrow 0^+) \sim 260(60)e^2fm^4$ is really slow compared with the values of the neighbouring nuclei as ^{66}Ni about $620(100)e^2fm^4$, points to a possible N=40 shell gap pointing to a double magic character for the ^{68}Ni nucleus. However, this gap gets reduced (or even disappears) when protons are removed from ^{68}Ni. The

nucleus ^{66}Fe, with only two protons less, shows a sudden change in nuclear structure with an increased collectivity manifested via its low-lying 2^+ state. Along the iron chain, indications for a collective behaviour come from the systematics of the 2^+ states [138] as well as from the recent measurement of the $B(E2)$ values in ^{64,66}Fe [140, 178]. The evolution of the $B(E2)$ values in iron isotopes points to a sudden increase of collectivity when approaching N=40. Another case where the N=40 sub-shell closure could be in principle explored is the ^{80}Zr nucleus (N=40, Z=40) as for protons the Z=40 sub-shell closure has been clearly demonstrated in the ^{90}Zr nucleus [141]. However, the ^{80}Zr nucleus has been found to be strongly deformed and does not show any trace of shell closure [142]. Therefore, the sub-shell closure in N=40 seems to be a local phenomena in the ^{68}Ni nucleus [143].

In Fig. 4.4 the experimental $B(E2 : 2^+ \rightarrow 0^+)$ values for the Ni isotopes are reported together with different theoretical predictions. The N=40 shell closure clearly appears as a local minimum of the electromagnetic transition rates for ^{68}Ni, in very good agreement with the local maximum observed for the 2^+ excitation energy. A similar behaviour is expected for the N=50 ^{78}Ni. Between these two shell closures, the occupancy of the $\nu g_{9/2}$ orbital is predicted to produce a region of higher collectivity enhanced by the core polarization mechanism. Transition probabilities are therefore expected to be large, of the order of $B(E2 : 2^+ \rightarrow 0^+) \sim 1000 e^2 fm^4$ [144, 145], as indicated already by the measured $B(E2)$ in ^{70}Ni [144]. Note the good agreement obtained between the experimental value and the SM calculations reported in Fig. 4.4 obtained only if an unrealistically high value of the neutron polarization charge of $e_n = 1.5e$ is assumed. The reproduction of the experimental data is already lost for $e_n = 1.0e$ [145] giving a trend basically similar to other theoretical descriptions (shown in the figure).
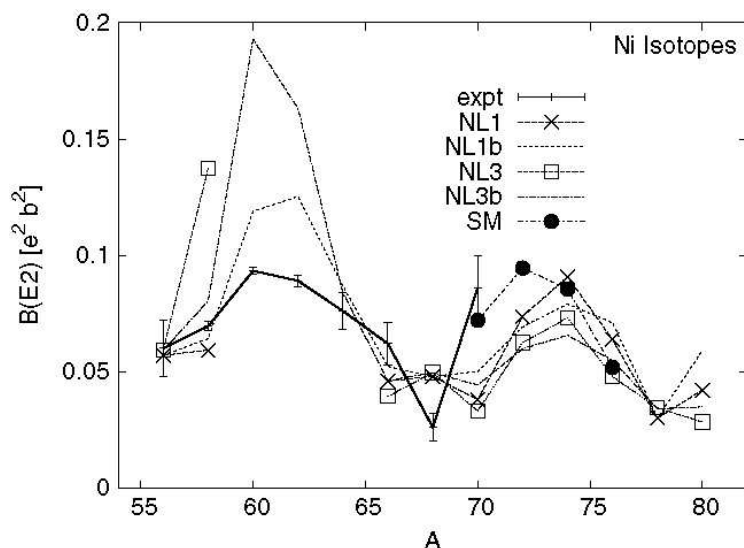

Figure 4.4: $B(E2 : 2^+ \rightarrow 0^+)$ values in the Ni isotopes. Taken from [144].

4.2.1 The Cu isotopes

Neutron-rich Cu isotopes, having one proton outside the Z=28 shell, are also good probes of the single particle structure in the region of ^{78}Ni. The characterization of their excited states allows searching for possible shell modifications due to the tensor interaction mentioned above. Shell-model calculations including the effect of the tensor force predict a lowering of the $\pi f_{5/2}$ state causing an inversion of the $\pi f_{5/2}$-$\pi p_{3/2}$ effective single particle states around ^{75}Cu which has been recently confirmed by nuclear spin and magnetic moment measurements performed at the ISOLDE facility [146]. In these measurement the spin of the ground state of ^{75}Cu has been identified as $I=5/2$ (Fig. 4.5).

β-decay and Coulomb excitation studies have provided detailed information on the excited states of the neutron-rich Cu isotopes up to A=73 [147–149] providing several candidates for states of mainly single particle character $\pi f_{5/2}$, $\pi f_{7/2}$ and $\pi p_{1/2}$ (Fig. 4.6). In particular, in Ref. [149] the single-particle nature of the $I^\pi=5/2^-$ state for ^{71,73}Cu isotopes has been confirmed through the measurement of the reduced transition probabilities by Coulomb excitation (Table 4.1). In the same work, the $I^\pi=1/2^-$ states have been identified as low-lying collective states, while $I^\pi=7/2^-$ ones as particle-core states following identical behaviour in their (A-1) Ni neighbour nuclei (Fig. 4.7)
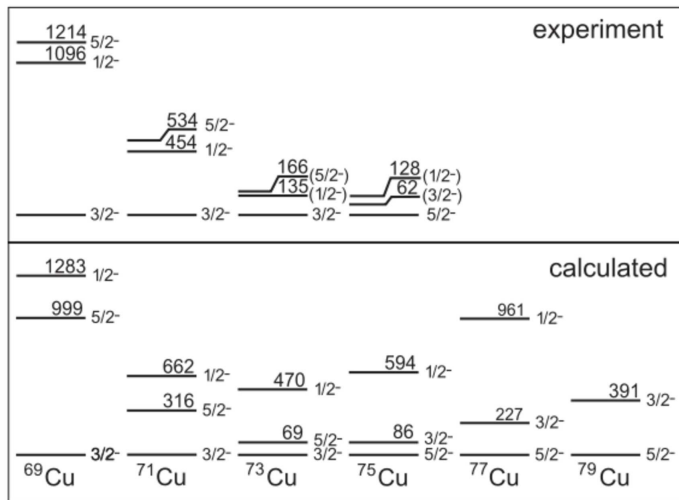

Figure 4.5: Energy of the lowest levels from experiment compared to large-scale shell-model calculations. See [146] and references therein.

Table 4.1: $BE(2)$ experimental values (W.u.) compared with the results of the large scale shell-model calculations(SM). The shell-model $BE(2)$ values were calculated with the effective charges $e_\pi = 1.5e$, $e_\nu = 0.5e$.

	^{71}Cu		^{73}Cu	
	exp (W.u.)	SM (W.u.)	exp (W.u.)	SM (W.u.)
$B(E2 : 1/2^- \rightarrow 3/2^-)$	20.4(22)	7.3	23.1(21)	7.5
$B(E2 : 5/2^- \rightarrow 3/2^-)$	3.9(5)	1.7	4.4(5)	1.3
$B(E2 : 7/2^- \rightarrow 3/2^-)$	10.7(12)	1.5	14.9(18)	2.3

The present experimental work aims to determine the collective or single particle character of the $I^\pi = 7/2^-$ states in n-rich Cu isotopes and in particular in ^{71}Cu where lies at 981 keV excitation energy. From the shell-model calculations three different configurations can give rise to the $7/2^-$ states:
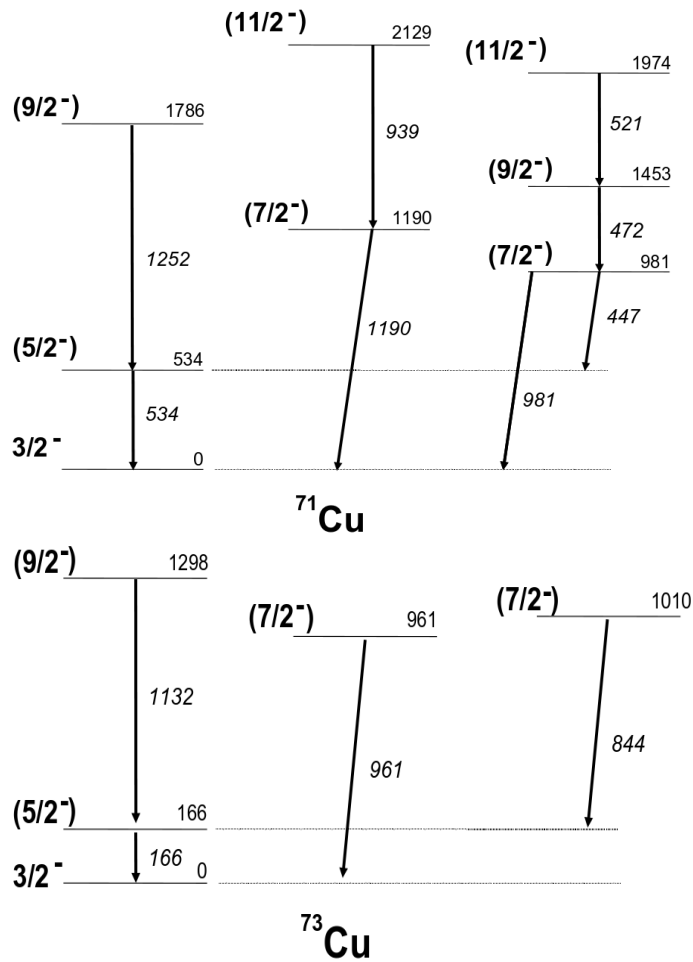

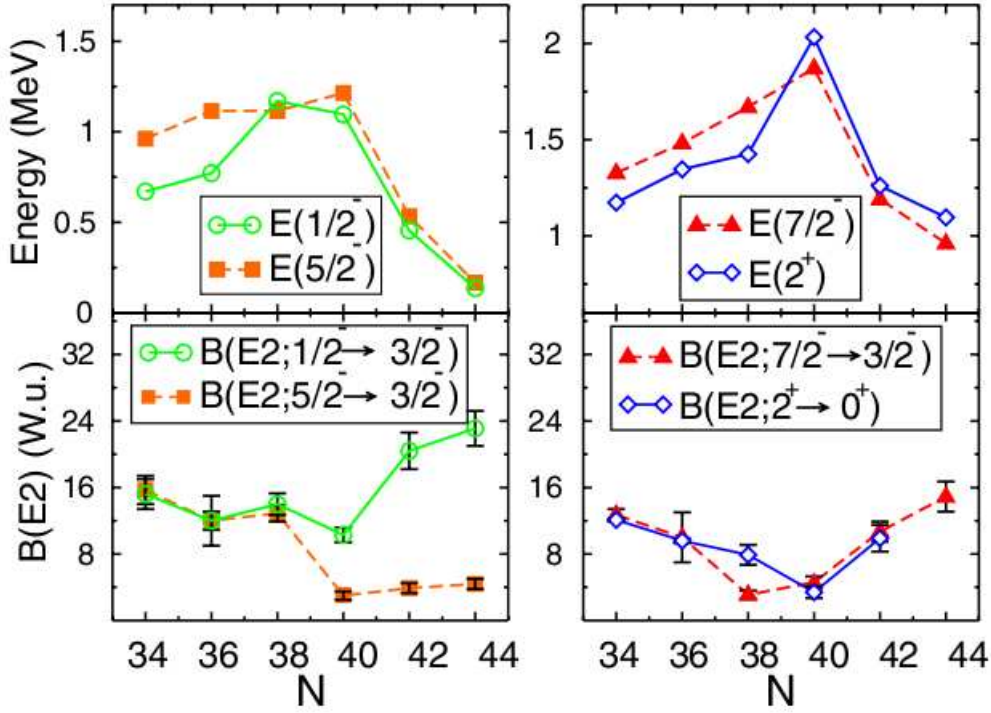Figure 4.6: Low-lying excited levels in ^{71}Cu and ^{73}Cu isotopes.

Figure 4.7: Top: Systematics of the energies of the $1/2^-$, $5/2^-$, and core-coupled $7/2^-$ states in the odd ^{63,73}Cu along with the 2^+ levels in the ^{63,73}Ni. Bottom: Experimental $B(E2)$ values in odd ^{63,73}Cu and ^{62,70}Ni. The lines connect the experimental points for the states of same spin but do not imply that the structure remains the same. Taken from [149].

- either a coupling of the single-particle configuration of $\pi p_{3/2}$ to the 2^+ core excitation leading to the $7/2^-$ $[\pi p_{3/2} \otimes 2^+]$ levels,

- or similarly, a coupling of the single-particle configuration of $\pi f_{5/2}$ to the 2^+ core excitation leading to the $7/2^-$ and $9/2^-$ $[\pi f_{5/2} \otimes 2^+]$ levels,

- or finally, the excitation of one proton hole into the $\pi f_{7/2}$ orbit, which results with the $7/2^-$ $[\pi f_{7/2}^{-1}]$ level.

The characterization of such states and, in particular, the identification of the $\pi f_{7/2}^{-1}$ particle-hole excitations across the Z=28 shell will provide essential information on the shell gap size and, therefore, on the evolution of the aforementioned Z=28 energy gap. The knowledge of the electromagnetic transition matrix elements de-exciting such states, obtained through lifetime measurements and the comparison with shell-model calculations will also contribute to the shell gap determination.

The estimated values for the lifetimes obtained considering the reduced probability transitions measured by Stefanescu and collaborators are shown in Table 4.2. The estimation has been done assuming a single particle configuration for the $I^\pi = 7/2^-$ state ($B(E2) = 4$ W.u) and a collective character for the $I^\pi = 9/2^-$ state ($B(E2) = 11$ W.u) [149] using the following relation taken from [150]:

Table 4.2: Expected lifetime values for the $I^\pi = 7/2^-$ and $I^\pi = 9/2^-$ states in ^{71,73}Cu calculated taking the $B(E2)$ values obtained by Stefanescu et al [149].

Nucleus	E_γ (keV)	$I_i^\pi \to I_f^\pi$	$B(E2)$ (W.u.)	τ (ps)
^{71}Cu	1,251	$9/2^- \to 5/2^-$	11	1.4
	981	$7/2^- \to 3/2^-$	4	12.9
^{73}Cu	1,132	$9/2^- \to 5/2^-$	15	1.6
	844	$7/2^- \to 5/2^-$	4	26.4

$$T(E2) = 1.22 * 10^9 E^5 B(E2\downarrow) \tag{4.2}$$

where T(E2)=$1/\tau$ (s^{-1}) is the transition probability, E (MeV) is the energy of the γ transition and B(E2) is the reduced transition probability (e^2fm^4)

4.3 Structure studies on neutron-rich nuclei in a stable-beam facility: Multi nucleon transfer reactions

Multi-nucleon transfer reactions with heavy ions have demonstrated to be a very useful tool to populate neutron-rich nuclei. This has been shown in different measurements, for example, the one performed by D. Mengoni and collaborators to measure the lifetimes of low-lying excited states of the neutron-rich ^{44,46}Ar nuclei [151], or the one in which the identification of gamma energies up to A=75 for neutron-rich Cu isotopes has been performed [152]. In our particular case, i.e. excited states in Cu isotopes with relatively high spin, it is feasible to use this reaction mechanism for the nuclei production. In the following paragraphs a brief introduction to heavy-ion nuclear reactions mechanism, at energies close to the Coulomb barrier, is given, with a more detailed description of multi-nucleon transfer reactions, since it has been the reaction mechanism employed in our experiment.

A simple classification scheme of processes taking place when two heavy nuclei collide at energies above the Coulomb barrier is shown in Fig. 4.8 [153]. In the most peripheral collisions, shown on the top, quasi-elastic reactions take place and the two weakly excited final nuclei are identical or very similar to the initial target and beam nuclei. The processes include Coulomb excitation, nuclear inelastic scattering and few nucleon transfer reactions populating a small number of selected states which decay by single gamma transitions or low multiplicity gamma cascades. In central collisions shown below, the fusion reaction produces the compound nucleus with high angular momentum and well-defined high excitation energy released by subsequent evaporation of particles and high multiplicity cascades of gamma rays. At extreme values of angular momentum the compound nucleus cannot sustain the rotation and undergoes fission. This fusion–fission reaction produces two fragments broadly distributed around the symmetric splitting of the mass of the compound nucleus. As both primary fragments are highly excited the secondary particle evaporation is followed by gamma emission.

The deep-inelastic collision, shown schematically in the central panel of figure 4.8, takes place at all intermediate impact parameters between the peripheral and central collisions. During the contact of nuclear matter (interaction time about 10^{-22}s) large transfer of mass, energy and angular momentum takes place between both colliding ions. These kind of reactions, known as deep-inelastic reactions, are not completely understood because the nucleon-exchange mechanism becomes extremely complicated as the number of transferred nucleons increases.
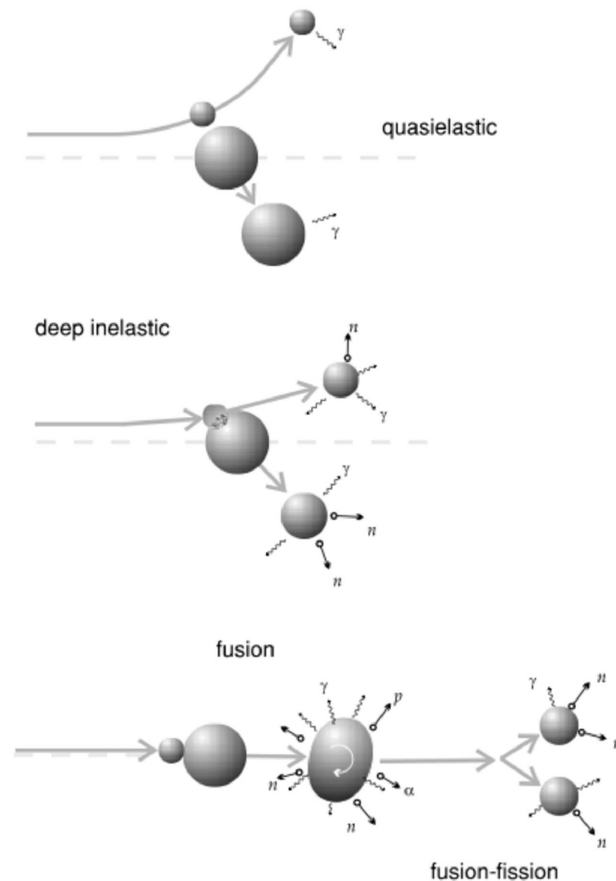
Figure 4.8: Schematic classification of reactions taking place in collisions of heavy ions at energies above the Coulomb barrier. Quasi-elastic including multi-nucleon transfer reactions and deep-inelastic collisions are called generally "Grazing reactions".

Deep-inelastic collisions tends to equilibrate the proton-neutron ratio of both reaction partners, nevertheless,this process occurs with a broad distribution centred in the equilibration line and, therefore it can populate neutron-rich nuclei, nevertheless, the largely inelastic process results on high excitation energies of the outcoming target-like and projectile-like products and frequently the products evaporate several neutrons, thus reducing the cross section for the most exotic channels. An intermediate situation is reached with the multi-nucleon transfer reactions, performed at energies around 10% to 20% above the coulomb barrier and detecting the reaction products at the grazing angle

which corresponds to the highest cross section. Therefore, is a quasi-elastic mechanism.

Recently it has been noticed that the yield of the (-2p) channels are reproduced only by using a form factor that takes into account the proton-pair transfer in addition to the classical sequential transfer, indicating that the proton pair mode may be an important degree of freedom in the transfer process leading to the population of neutron-rich nuclei. At present the pair transfer is only treated at a phenomenological level and it is difficult to relate microscopically its strength to the pair correlations in target and in projectile [154]. Therefore, these reactions are extremely important because they permit to populate, with a sizeable yield, moderately neutron-rich regions of the Segré chart that cannot be reached with fusion-evaporation reactions on stable beams and targets. For energies close to the Coulomb barrier transfer reactions play the most important role in the loss of flux from the elastic channel. At higher energies and with heavy ions, the availability of many nucleon transfer channels allows us to study the importance of particle and pair transfers and provide information on vibrational states, single particle states and their coupling, and therefore, allowing to study the shell evolution when one gradually moves away from the stability line, namely as a function of N/Z.

Some features of these reactions are:

- The collision preserves the binary character of the system. The ejectiles are similar to the initial nuclei, having exchanged a few nucleons. Therefore, it is possible to distinguish a projectile-like (or beam-like) ejectile from a target-like ejectile,

- Angular momentum is transferred from the relative orbital motion to the intrinsic spin of the two reaction products,

- The generated ejectiles de-excite primarily through evaporation of light particles such as neutrons, protons and α-particles and through γ-decay.

The cross section of multi-nucleon transfer reactions is determined by two factors: the form factor and the dynamic factor [155]. The former expresses the process dependence from the nuclear structure and, in particular, from the initial and final wave functions of the transferred nucleon. The latter comes from the reaction dynamics, and takes into account the excitation energy of reaction products. Depending on the relative relevance of these two parameters, the nucleon-transfer process happens in different regimes. If the ejectiles excitation energy is high enough (E> 20 MeV) that the transferred nucleons are in a continuum of quantum states (the density of energy levels increases with the increase of energy), the quantum-mechanical amplitude of the nucleon-exchanging process is almost only a function of the dynamic factor, and thus it does not feel the effects of nuclear structure. As a consequence, the model adopted to describe this reaction is thermodynamical, and the exchange of protons and neutrons is treated as a diffusive process. These reactions are called deep-inelastic reactions or also dumped reactions. On the contrary, if the excitation energy of ejectiles is not very high (E< 20 MeV), the picked-up or stripped nucleons are in discrete energy levels. Therefore, the process probability strongly depends on the single-particle levels of the involved nuclei, and a statistical approach is not valid. Multi-nucleon transfer reactions is the name usually employed to describe this process.

In a multi-nucleon transfer experiment it is very important to know the angle at which the reaction cross section is peaked: in fact, detectors such as those for ion identification, should be placed at this angle to reach the highest possible statistics. This angle, in the

laboratory frame, is called the grazing angle, and it indicates the direction of the ejectiles which are the products of nuclear reaction. It is thus defined as the angle θ_G at which the distance of the closest approach equals the sum of the nuclear radii, so that the two interacting nuclei are just "touching" each other.

Multi nucleon transfer reactions and deep inelastic collisions have been used successfully in the last two decades to study the structure of nuclei far from stability in the neutron-rich side of the nuclear chart. Already in the 80's M. W. Guidry et al. [156] suggested the possibility to populate high spin states in transfer reactions induced with heavy projectiles. Since then the use of these reactions in nuclear spectroscopy studies has increased, following the evolution of the gamma multidetector arrays, in some cases compiting successfully with results from first generation radioactive beam facilities. A good example are the neutron-rich nuclei around ^{68}Ni, for which investigation of the structure have revealed the quasi-doubly-magic character of N=40 Z=28 [137], and who has been investigated with both fragmentation and deep inelastic collision techniques [137,157,158]. Ancillary devices capable of identifying the reaction products or at least one of them, were already used in early works: PPAC counters in kinematic coincidences [159–161] or Si telescopes to identify the light fragment [162]. The increasing of the gamma efficiency in Compton suppressed arrays allowed to apply techniques purely based on the detection of gamma-gamma coincidences between unknown transitions from the neutron-rich nucleus and known ones from the reaction partner. The method was first used by R.Broda et al. [163] and since then it has been successfully applied up to the present days. The increasing interest for going further away from the stability for neutron-rich medium mass or heavy nuclei, has created the necessity of new techniques to univocally assign the gamma transitions to the product of interest.

A sizeable step forward in instrumentation to perform structure studies using multi-nucleon reaction was based on the coupling of a large acceptance magnetic spectrometer to a high efficiency and high resolution Ge detector array for gamma spectroscopy. Magnetic spectrometers have played an important role in the study of transfer reactions, as they provide a complete identification of the reaction products and allow the extraction of differential and total cross sections. Such instruments, coupled to modern arrays for gamma detection, allow to investigate structure properties of nuclei at the limit of the present production capabilities. This is the case of the AGATA-PRISMA setup employed in this work, at the INFN National Laboratory of Legnaro (Italy). Multi-nucleon transfer reactions have been widely used at LNL in order to complement the nuclear structure information on neutron-rich nuclei, especially for high spin states.

Cross sections: the GRAZING code

The calculated cross sections have been obtained by using the semiclassical model GRAZING [164, 165]. This model calculates the evolution of the reaction by taking into account, besides the relative motion variables, the intrinsic degrees of freedom of projectile and target. These are the isoscalar surface modes and the single-nucleon transfer channels. The multinucleon transfer channels are described via a multistep mechanism. The relative motion of the system is calculated in a nuclear plus Coulomb field where for the nuclear part the empirical potential based on the Wood-Saxon of [166] has been used. The excitation of the intrinsic degrees of freedom is obtained by employing the well-known form factors for the collective surface vibrations and the one-particle

transfer channels [167, 168]. The model takes into account in a simple way the effect of neutron evaporation. The predictions from the semi-classical GRAZING model have been successfully tested against more complex DWBA calculations and also compared to a number of experimental data. In particular it has been already successfully applied in the comparison of different multinucleon transfer data [154, 169] and, recently, of fusion excitation functions and barrier distributions [170].

The cross sections calculated obtained with the GRAZING model and the experimental values obtained in the present measurement are shown in Fig. 4.9. As it can be seen in the figure the predicted cross section values are in good agreement for the elastic channel (^{76}Ge) but as far as we move to more neutron stripping channels the calculation get worse because of the neutron evaporation process in GRAZING is only included in a first approximation and, therefore, cross sections are not well reproduced for these channels.
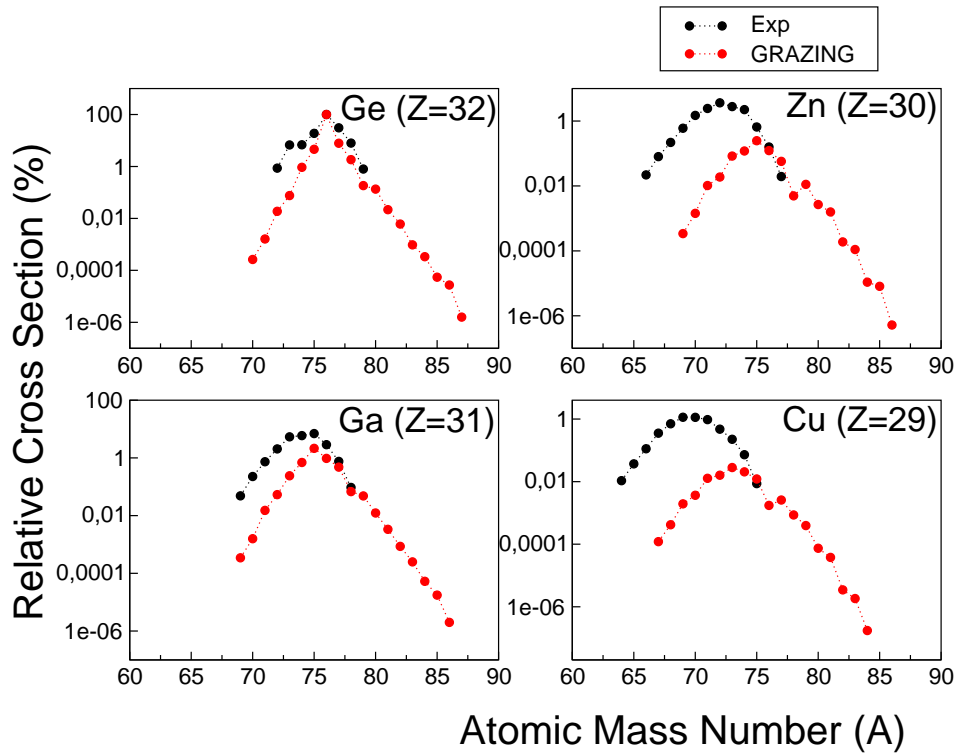
Figure 4.9: Theoretical and measured cross sections in the present experiment.

4.4 Recoil Distance Doppler Shift Method (RDDS) for Lifetime measurements

The current spectroscopic data for Cu isotopes are very scarce. Therefore, information on energies of excited states and on transition strengths is really important to understand the role of the $\nu g_{9/2}$ orbital for the development of the collectivity. The measurement of the reduced transition probability (B(E2)), obtained trough the direct measurement of the transition lifetime (eq.4.2), can provide spectroscopic information as its value is directly related to the enhancement of the collectivity. Presently, most of the B(E2) information

Lifetime measurement of neutron-rich nuclei in the region of the double magic ^{78}Ni with the γ-tracking AGATA demonstrator.

90

available, in the region under study, corresponds to indirect measurements obtained using low energy (safe) and relativistic Coulomb excitation in radioactive beam facilities or direct measurements using fusion-evaporation reactions when possible [140, 171–173]. In the last decades, mainly after the incept of the high-resolution gamma spectroscopy technology, a variety of techniques in order to measure lifetimes in different time ranges for in-beam experiments have been developed (Fig. 4.10). For example, the Recoil Shadow Anisotropy Method (RSAM) is used for identifying isomers in the nanosecond range and measuring their lifetimes [19]. The Doppler Shift Attenuation Method (DSAM) is used for lifetime measurements in the femtosecond range. It is based on the analysis of the detected energy distribution of the emitted γ rays during the slowing down process of an excited recoiling nucleus. Energetic ions come to rest typically in about 1 ps inside a solid material, therefore, from the line-shape of their emitted γ rays, with and attenuated Doppler-shift, lifetime values from tens of femtoseconds to few picoseconds can be evaluated [19–21]

Techniques for lifetime measurements

GRID: Gamma ray induced Doppler broadening
DSAM: Doppler shift attenuation method
RFD: Recoil straggling method
RDDS: Recoil distance Doppler shift method
RSAM: Recoil shadow anisotropy method
FEST: Fast electronic scintillation method
NFR: Nuclear resonance fluorescence
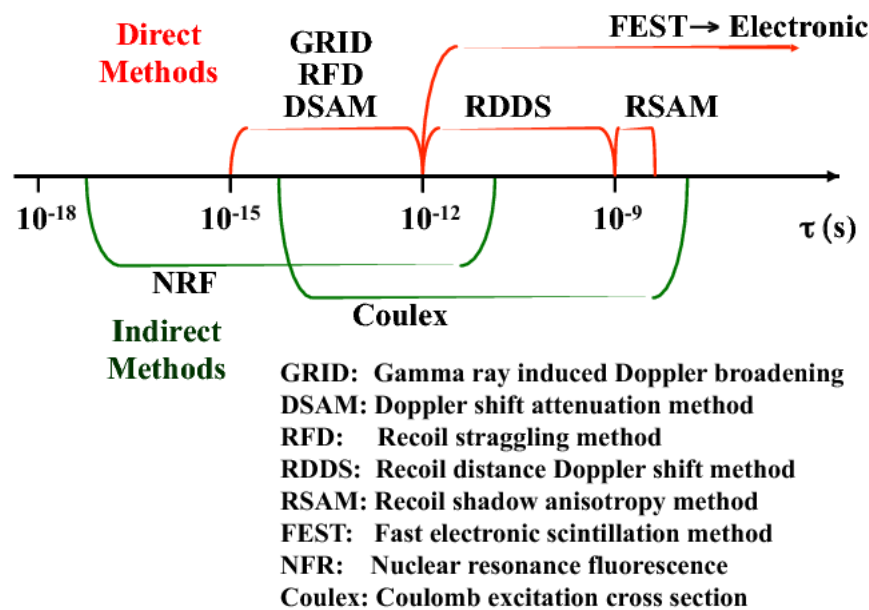Coulex: Coulomb excitation cross section

Figure 4.10: Techniques developed for the lifetime determination in different time ranges.

In our case, the lifetime of the excited states of interest is expected to be of the order of several picoseconds and we have resorted to the Recoil Distance Doppler Shift method (RDDS) [19, 22]. This method has been widely used for the determination of lifetimes in several regions of the Segré chart. Some examples are the determination of the 8_1^+ and 10_1^+ excited states of ^{120}Xe [174], or the one performed by A. Dewald and collaborators [175], in which the lifetimes of two superdeformed states in ^{192}Hg were measured using the GASP setup at the LNL. A differential version of the technique was developed for grazing Reactions, i.e. for Ge arrays coupled to magnetic spectrometers,

and commissioned with the ^{64}Ni (400 MeV) + ^{208}Pb reaction for the first time in a CLARA-PRISMA campaign at the LNL in collaboration with the IKP University of Cologne group [176]. Afterwards, successful measurements have been performed with this method, i.e, the one performed by J.J. Valiente-Dobón and collaborators, to determine the lifetime of the neutron-rich ^{50}Ca and ^{51}Sc isotopes [177] or the lifetime determination of the low-lying excited states of the neutron-rich ^{44,46}Ar performed by D. Mengoni and collaborators [151]. Later, the technique was used with the EXOGAM-VAMOS setup to measure the lifetime of the 2^+ states in ^{62}Fe and ^{64}Fe [178]. Another example is the determination of the lifetime of the $9/2_1^-$ and the $3/2_1^-$ states in ^{63}Co and the $9/2_1^-$ state in ^{63}Co [179]. In this work, we have used for the first time this technique with the AGATA Demonstrator coupled to the PRISMA spectrometer and the Cologne plunger. The main improvements with respect to previous experiments, are coming from AGATA detector. As it has been shown before, AGATA is a position sensitive detector and, therefore, a better Doppler correction with respect to conventional arrays can be done. Additionally the higher efficiency and counting rate capability for γ-ray detection of the AGATA Demonstrator further improve the measurement.

Conceptually, the differential RDDS method [19, 22] consists of a thin target at a fixed position and an energy degrader to change the velocity of the incoming ions. The γ rays, measured with a gamma-ray spectrometer (in our case AGATA Demonstrator), are emitted by ions, whose mass, atomic number and velocity are measured in a magnetic spectrometer (PRISMA). The method requires measuring the intensity of the γ rays emitted before or/and after the degrader by the beam-like products, as a function of the target-degrader distance. Since the Doppler correction is done with the information provided by PRISMA, different Doppler shifts are originated depending on where the γ-ray emission takes place, as the ion velocity distribution after passing the degrader is peaked at lower values than the initial one due to the energy loss. This results on each γ transition producing two peaks corresponding to the two recoiling velocities (Fig. 4.11). The degrader thickness should be large enough to assure that the energy shift between the two peaks is higher than the energy resolution of AGATA detectors ($\sim$ 2.4 keV at 1.3 MeV and larger in in-beam measurements). The fit of relative intensities of the two peaks, as a function of the target-degrader distance, allows to determine the lifetime of the state of interest.

One of the limitations of the RDDS method is due to the so-called side feeding of an excited level after the reaction. If the feeding process is not well determined, for example due to feeding, of our levels of interest, by unobserved transitions, unrealistic lifetime values may be obtained. The advantage of using the differential RDDS technique in a setup with a magnetic spectrometer like PRISMA is that information on the contribution of side feeding can be obtained. In grazing reactions the excitation energy of the partners can be estimated measuring the kinetic energy loss of one of the partners (TKEL). The magnetic spectrometer allows to gate in the kinetic energy loss and therefore to set limits on the excitation energy of the reaction products.

Velocity distribution of the recoiling nuclei

The energy of the emitted γ rays before and after the degrader (E_{bef} and E_{aft}, respectively) can be obtained through the Doppler relation for small velocities ($\beta < 1$):
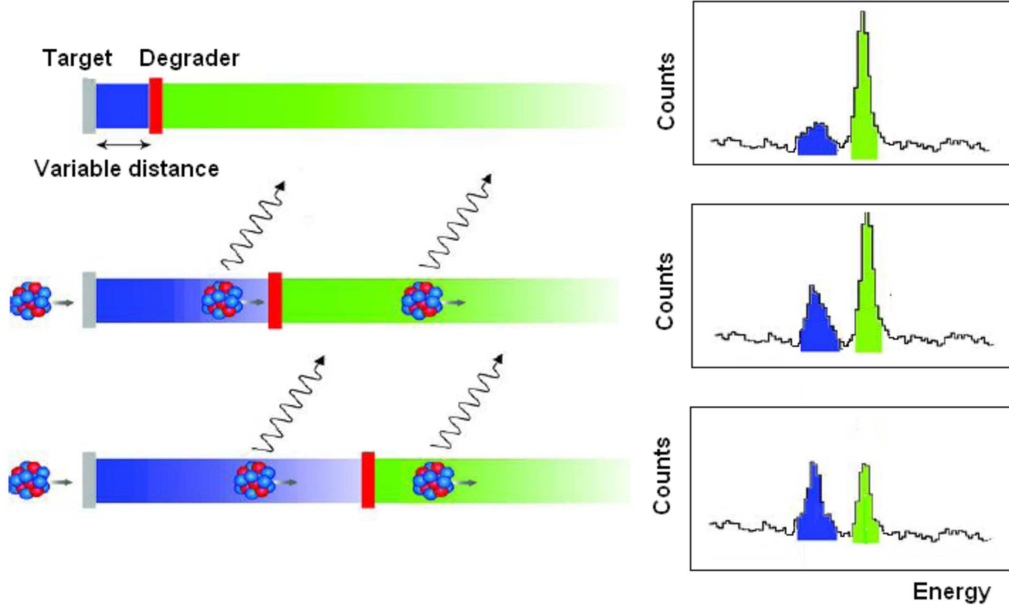
Figure 4.11: Principle of the RDDS method. γ rays emitted after and before the degrader feel different Doppler shifts due to the different velocity distributions of the emitting nuclei, so they appear at different energies in the gamma spectra.

$$E_{bef} = E_0(1 + \beta_{bef}cos\theta)E_{aft} = E_0(1 + \beta_{aft}cos\theta) \tag{4.3}$$

where E_0 is the correct energy for the γ transition, θ is the angle between the emitting nucleus and its corresponding γ ray and β_{bef} and β_{aft} are the velocity distributions before and after the degrader, respectively.

With PRISMA is possible to obtain the velocity distribution of the ions that have passed the degrader (β_{aft}). Therefore, the right Doppler correction is obtained for γ rays emitted after the ions passing the degrader and, thus, this transitions appear like a peak at the correct energy in the spectra (unshifted peak), while ions decaying before the degrader give a lower energy peak wrongly Doppler corrected with β_{aft} (shifted peak). The wrongly-corrected γ rays appear on the γ spectra in a shifted peak, with an energy:

$$E_0^{shifted} = E_{bef}(1 + \beta_{aft}cos\theta) \tag{4.4}$$

Once the ion velocity distribution after the degrader (β_{aft}) is determined, the average velocity before the degrader (β_{bef}) can be obtained substituting E_{bef} from the eq.4.3 and re-arranging the resulting equation:

$$\frac{E_0^{shifted} - E_0}{E_0} = (\beta_{bef} - \beta_{aft})cos\theta \tag{4.5}$$

The Doppler correction of the emitted γ rays is performed on an event-by-event basis, giving a better resolution for the corresponding peak (FWHM$\sim$ 3.5 keV) than the one obtained for the shifted component (FWHM$\sim$ 6 keV).

Radioactive decay of excited nuclei. Lifetime determination

The time evolution of nuclide concentrations undergoing a linear decay chain is a probabilistic process, governed by a set of first-order differential equations, called Bateman equations. If N_1 radioactive nuclei are present at time t, the number of decays for a certain state is given by:

$$\frac{dN_1}{dt} = -\lambda_1 N_1 \tag{4.6}$$

where λ_1 is the decay constant and N_1 is the population of the state. The solution comes as a typical exponential law:

$$dN_1(t) = N_o e^{-\lambda_1 t} \tag{4.7}$$

When a radioactive nucleus (1) decays with decay constant λ_1 to nucleus (2), the differential relation for the last one becomes:

$$\frac{dN_2}{dt} = \lambda_1 N_1 - \lambda_2 N_2 \tag{4.8}$$

And successively, for the ith nucleus:

$$\frac{dN_i}{dt} = \lambda_{i-1} N_{i-1} - \lambda_i N_i \qquad (i = 2, n) \tag{4.9}$$

where λ_i is the decay constant of ith nuclide and N_i is given by the initial population of the state.

Solving the equations, with the initial population for the excited state considered as initial conditions, the lifetime can be calculated as the inverse of the decay constant ($\tau = 1/\lambda$). Therefore, the number of decays after an before the degrader can be expressed in terms of this radioactive decay equations as follows:

$$I_u(t) = N_0 e^{(\frac{-d}{v\tau})} \qquad I_s(t) = N_0 - N_0 e^{(\frac{-d}{v\tau})} \tag{4.10}$$

$I_u(t)$ and $I_s(t)$ are the intensity of the peaks after ($I_u(t)$) and before ($I_s(t)$) the degrader respectively, obtained by calculating the area of the peaks through a Gaussian fit. To obtain an independent value of the number of nuclei produced in the reaction, the ratio R is defined as:

Lifetime measurement of neutron-rich nuclei in the region of the double magic ^{78}Ni with the γ-tracking AGATA demonstrator.

94

$$R = \frac{I_u}{I_u + I_s} = \frac{N_0 e^{\left(\frac{-d}{v\tau}\right)}}{N_0} = e^{\left(\frac{-d}{\beta c\tau}\right)} \tag{4.11}$$

With this relation is possible to extract the lifetime of the excited state as a function of the distance between target and degrader. Nevertheless, often the error of the determined lifetime is sizeable since both peaks shifted and unshifted are used in the normalization. The use of a Ion tracking Spectrometer, as PRISMA, where the mass and Z is determined in an event-by-event basis, allows a new approach to determine the lifetime, using only one of the peaks, the shifted or the unshifted one. In this case the normalization is done considering the number of nuclei populated in the reaction and detected in PRISMA (N_0). To our knowledge this is the first time that such technique is used. In this case the R ratio mentioned before is obtained as:

$$R = \frac{I_u}{N_0} = e^{\left(\frac{-d}{\beta C\tau}\right)} \tag{4.12}$$

$$R = \frac{I_s}{N_0} = 1 - e^{\left(\frac{-d}{\beta C\tau}\right)} \tag{4.13}$$

if the unshifted and shifted peak are used, respectively.

The main difference between both methods is that meanwhile, in the first one, the intensity of both peaks has to be measured, in the second one, the determination is done in terms of only one of the measured peaks. This approach can provide information about the lifetime of the excited state in measurements where the statistics is not high, like the present case, and, therefore, depending on the value of the lifetime (short or long) one of the peaks can not be accurately determined. It has to be noticed that the exploitation of the approach through the shifted peak can be employed only when the lifetime we are interested in is expected to be short because as we move to higher values the information contained in the shifted peak is lost as most of the ions decay when moving after the degrader.

The distance that should be considered for the lifetime determination is not corresponding to the distance between the target and the degrader, because as it will be shown later, the plunger was tilded 10° with respect to the Z axis in the experimental setup (Fig. 4.13). So an effective distance has to be considered (d'):

$$d' = \frac{D + d}{cos\theta} \tag{4.14}$$

where D is the real distance between target and degrader, d is the degrader thickness and θ is the angle between the optical PRISMA axis and the target angle. Besides, the offset of the target (different for each measured distance) should be considered. The distances considered for the analysis are summarized in Table 4.3.

4.5 Experimental details

As it has been mentioned above, it is possible to populate neutron-rich nuclei, like the Cu isotopes we are interested in, through multi-nucleon transfer reactions. Due to the low-cross sections involved in this reaction mechanism, high efficiency and very selective detection systems are required. The AGATA detector coupled to the PRISMA spectrometer (see Fig. 4.12) is presently the best setup for the measurement as it allows to detect the beam-like reaction products and their corresponding γ rays with high sensitivity.

A multi-nucleon transfer reaction with a ^{76}Ge beam of 577 MeV energy impinging on a ^{238}U target of 1.5 mg/cm^2 together with a 1.4 mg/cm^2 thick Ta backing has been used to populate the excited states of the nuclei of interest. The backing is needed in order to perform the stretching of the U target, i.e, to achieve a smooth surface. The target was mounted in front of a Nb degrader foil of 4.17 mg/cm^2 thickness in a compact Plunger device, designed and built by the IKP University of Cologne. The Plunger device has been placed in the geometrical centre of the reaction chamber of the AGATA-PRISMA setup. Due to mechanical constraints, it could not be placed perpendicular to the optical axis of the spectrometer, so it is tilted by 10$^{\text{o}}$ with respect to the optical axis of PRISMA (Fig. 4.13). The projectile-like reaction products are detected and identified in the magnetic spectrometer PRISMA, which was positioned at 55$^{\text{o}}$ with respect to the beam axis, i.e, at the grazing angle. With PRISMA the mass, atomic number and velocity of the different ions are identified providing a clean selectivity of the different channels. Emitted gamma rays were detected with the AGATA Demonstrator located at backward angles sensitive to their Doppler shift. Only four of the five clusters were available for the experiment. Therefore the efficiency of the system was 3.2% at 1,332 keV.

The beam energy is selected taking into account several issues. The first one and more important is the reactions dynamics. In order to produce, with high yield, nuclei far from stability avoiding the excessive evaporation of neutrons, the multi-nucleon transfer should be the dominating grazing channel, therefore, is advisable to use beam energies up to about 20 to 30% above the coulomb barrier, for most combinations of projectile and target. The coulomb barrier in our case is about 400 MeV. Besides to be reachable by the tandem-ALPI accelerator complex, the beam energy should be adjusted as well, accordingly to the target-degrader thickness, to have sufficient energy on the reaction product to have a good Z resolution with PRISMA. Ions should arrive, as we will discuss later, in the ionization chamber with a higher energy than the Bragg peak within the second section. Therefore, the target should be thin enough to keep a sufficient energy of the reaction

Table 4.3: Target-degrader distance (D), corresponding effective distance (d') and final distance.

D (μm)	d' (μm)	d_f (μm)
100	106.42	112.01
200	207.96	211.97
500	512.59	512.00
1000	1020.30	1012.01
1900	1934.19	1912.00

**Lifetime measurement of neutron-rich nuclei in the region of the double
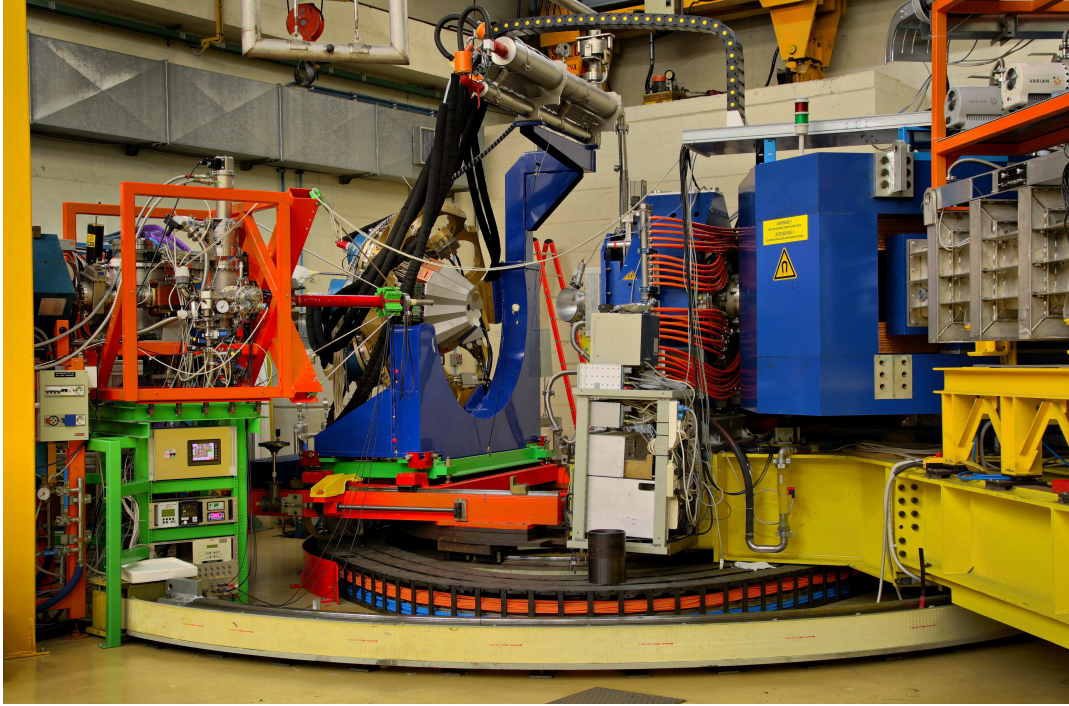magic ^{78}Ni with the γ-tracking AGATA demonstrator.**

96

Figure 4.12: PRISMA spectrometer coupled to AGATA Demonstrator at the LNL.

products. However, it should be noticed that the yield of the reaction, is directly related
to the target thickness, so a compromise should be found. For the degrader, only the
energy losses have to be considered attending to the minimum separation between the
shifted and unshifted peaks to perform a good lifetime determination in the analysis.

Table 4.4 shows the energy of the beam and the recoils at the different stages of the
target-degrader system. The values were obtained with the Stopp code [180], that is
an implementation of the semi-empirical stopping power formulas by J. Ziegler and co-
workers [181]. The kinematics of the reaction has been calculated for the several cases
using the Reaction code [180]. The projectile-like reaction partners exit the target foil with
an average energy of 375 MeV (4.93 MeV/u) and a velocity of 31 μm /ps ($\beta \sim 10.5\%$).
The Nb foil degrades the energy of the ions to 250 MeV (3.3 MeV/u) and results in an
average velocity of 26 μm /ps ($\beta \sim 8.6\%$). With this degrader thickness, the difference in
velocity is large enough to distinguish γ rays emitted before and after the degrader foil by
their different Doppler shifts if an AGATA resolution of 2 keV for 500 keV and a minimum
requirement of 2*FWHM for an acceptable separation between both peaks are assumed
($\Delta E = 4 \, \text{keV} = 0.8\%$). Assuming a minimum angle value of 120$^{\text{o}}$ between PRISMA and
AGATA, through eq. 4.5 we obtain the following value for the energy resolution:

$$\Delta v/c = 1.9\% \implies \Delta E = 4.75 \, \text{keV} = 0.95\% \tag{4.15}$$

Therefore, the degrader thickness is enough to provide the required energy separation
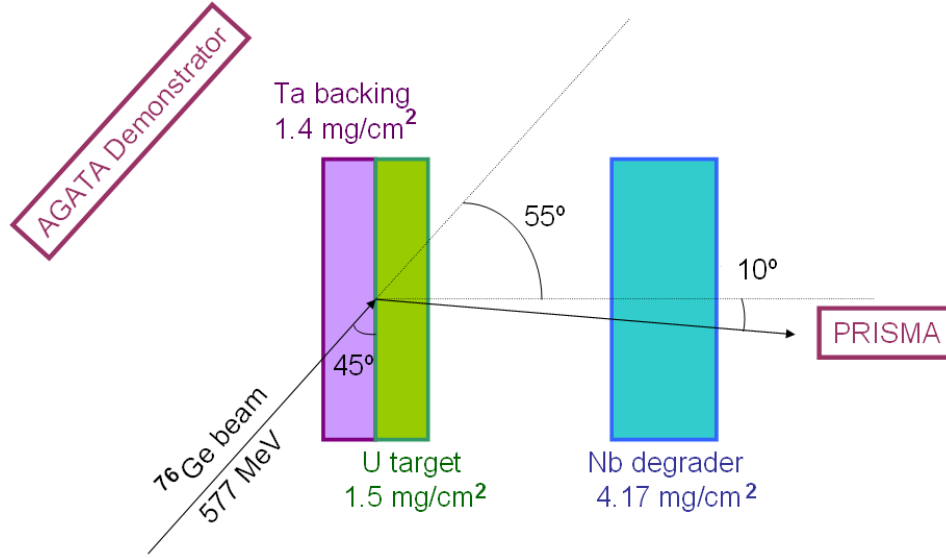between the shifted and unshifted peaks.

Figure 4.13: Schematic view of the setup. The ^{76}Ge beam impinges on the ^{238}U target together with the Ta backing. The projectile-like reaction partners exit the target going trough the Nb degrader and entering in the PRISMA spectrometer. The γ rays are identified in the AGATA Demonstrator.
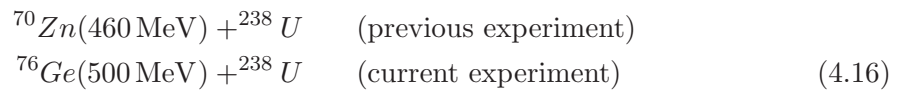
Table 4.4: Calculated ^{76}Ge beam energies at the different stages of the setup and average projectile-like energies after target and degrader, respectively (see Fig. 4.13).

ALPI	After Ta	Centre target	End target	projectile-like	after degrader
577 MeV	547 MeV	532 MeV	518 MeV	375 MeV	250 MeV

In order to cover a range from approximately 2 to 30 ps, the range of expected lifetimes of our isotopes, measurements have been performed for five different target-degrader distances: 100 μm, 200 μm, 500 μm, 1000 μm and 1900 μm.

Cross section estimates

The GRAZING code was used for the cross section estimation [182]. However to better estimate the yield of the different nuclei of interest a comparison with a previous experiment performed at LNL was done. The reactions to be compared are:

$$^{70}Zn(460\,\text{MeV}) +^{238} U \qquad \text{(previous experiment)}$$
$$^{76}Ge(500\,\text{MeV}) +^{238} U \qquad \text{(current experiment)} \qquad (4.16)$$

The comparison can be done as the Q value for both reactions is about the same order and the isotopes we are interested in are, in both cases, the same proton stripping

and neutron striping or pickup channels. The exit channels of interest in our particular case are Ni, Cu and Zn isotopes meanwhile in the previous experiment were Fe, Co and Ni (Table 4.6). To prove that the scaling can be performed, the Q values for the different channels in both reactions are shown in Table 4.5. The gain factor between both experiments was calculated to be about a factor of 1.6 (Table 4.7). The beam was reduced with respect to the previous experiment, giving a reduction factor of 0.7, the target thickness gives a factor of 1.5 as in this case the thickness was a little bit thicker than in the previous one; and finally the larger efficiency of the AGATA Demonstrator with respect to CLARA gives another factor of 1.5. Table 4.6 shows the estimated number of counts for Ni, Cu and Zn isotopes for the present experiment and their corresponding channels for the previous experiment.

Table 4.5: Q values of the proton stripping and neutron striping or pickup channels for the previous experiment (^{70}Zn + ^{238}U) and for the present one (^{76}Ge + ^{238}U) to be compared.

Reaction	Exit channels	Q value (MeV)
^{70}Zn + ^{238}U	^{66}Fe $\rightarrow (-4p)$	-26.73
	^{65}Co $\rightarrow (-3p, -2n)$	-20.26
	^{67}Co $\rightarrow (-3p)$	-19.86
	^{70}Ni $\rightarrow (-2p, +2n)$	-8.93
^{76}Ge + ^{238}U	^{72}Ni $\rightarrow (-4p)$	-26.03
	^{71}Cu $\rightarrow (-3p, -2n)$	-20.31
	^{73}Cu $\rightarrow (-3p)$	-19.68
	^{76}Zn $\rightarrow (-2p, +2n)$	-10.02

Table 4.6: Cross sections and number of counts obtained in the ^{70}Zn (460 MeV) + ^{238}U experiment performed at LNL used for the comparison with the current experiment, ^{76}Ge (500 MeV) + ^{238}U. Expected cross sections obtained with the GRAZING code and estimated number of counts for Ni, Cu and Zn isotopes for the present experiment.

Reaction	Exit channels	Grazing cross sections (μb)	Counts E_γ (keV)
^{70}Zn + ^{238}U	^{66}Fe $\rightarrow (-4p)$	100	$E_\gamma(574 keV) = 80$
	^{65}Co $\rightarrow (-3p, -2n)$	360	$E_\gamma(1480 keV) = 700$
	^{67}Co $\rightarrow (-3p)$	790	$E_\gamma(1610 keV) = 200$
	^{70}Ni $\rightarrow (-2p, +2n)$	1000	$E_\gamma(1257 keV) = 300$
^{76}Ge + ^{238}U	^{72}Ni $\rightarrow (-4p)$	100	$E_\gamma(1096 keV) = 80$
	^{71}Cu $\rightarrow (-3p, -2n)$	340	$E_\gamma(981 keV) = 1200$
	^{73}Cu $\rightarrow (-3p)$	750	$E_\gamma(844 keV) = 300$
	^{76}Zn $\rightarrow (-2p, +2n)$	1500	$E_\gamma(574 keV) = 470$

In the following sections, the instruments employed in the experiment: the PRISMA spectrometer, the differential Plunger and the AGATA Demonstrator are briefly described.

Table 4.7: Gain factor estimation between the ^{76}Ge (500 MeV) + ^{238}U and the ^{70}Zn (460 MeV) + ^{238}U experiments.

	^{70}Zn + ^{238}U	^{76}Ge + ^{238}U	Gain
Beam time	7 days	14 days	2
Beam Intensity	2 pnA	2pnA	1
Target thickness	1 mg/cm^2	2 mg/cm^2	2
Efficiency at 1 MeV	(CLARA) 2.6%	(AD) 6%	2

4.5.1 The PRISMA Spectrometer

PRISMA [183,184] is a large acceptance magnetic spectrometer, which has been designed for the identification of the reaction products of heavy-ion collisions with E = 5-20 MeV/A of the XTU Tandem-ALPI-PIAVE complex accelerator at LNL. It allows us to completely identify the reaction products in atomic and mass numbers, Z and A, and to measure their velocities.

The most interesting features of PRISMA are its very large solid angle and momentum acceptance, good mass resolution via TOF measurement; energy resolution, Z resolving power and capability of rotation around the target in a wide angular range from -30° to 140°. The above performance figures are achieved by software reconstruction of the ion tracks using the position, time and energy signals from the entrance and focal-plane detectors. In Table 4.8 the main characteristics of the spectrometer are summarized. Its large angular acceptance is obtained using large optical elements which are a quadrupole and a dipole magnet. Optical aberrations from these magnets are corrected via software reconstruction of the ion tracks which provides a very good momentum resolution. Position and angle measurements, for trajectory reconstruction, as well as energy and time of flight (TOF) measurements, for ion identification, are performed by the PRISMA detectors. The detectors of the spectrometer consists of an entrance detector based on micro-channel plates (MCP) and of the focal plane detectors which consist of a MWPPAC (Multi-Ware Parallel Plate Avalanche Counters) and an ionization chamber (IC) placed at the end of the spectrometer. The ion flight average distance from the entrance detector (MCP) to the MWPPAC focal plane detector is about 6.5 m. Timing signals needed in order to measure the TOF are taken from the MCP and the PPAC detectors, both with good time resolution. Then, considering an average velocity of about 10% of the speed of light, a window of 200 to 400 ns is optimal to measure the time of flight. A simple scheme of the spectrometer is shown in Fig. 4.14. In the following a detailed description of the different elements and detectors of PRISMA will be given.

Quadrupole magnet

The quadrupole magnet is used to focus the ions in the vertical direction. It is placed 25 cm away from the entrance detector position. It has an aperture diameter of 32 cm and a length of 42 cm.

Close to the entrance of the magnet, there is a mirror plate to limit the fringing field effect (magnetic field extended over the geometrical limits of the magnet). For the analysis

of the experimental data the fringing field is not considered and an effective length of 51 cm is used instead of the real length giving a rather good approximation of the real field. Detailed characteristics of the quadrupole are given in Table 4.9.
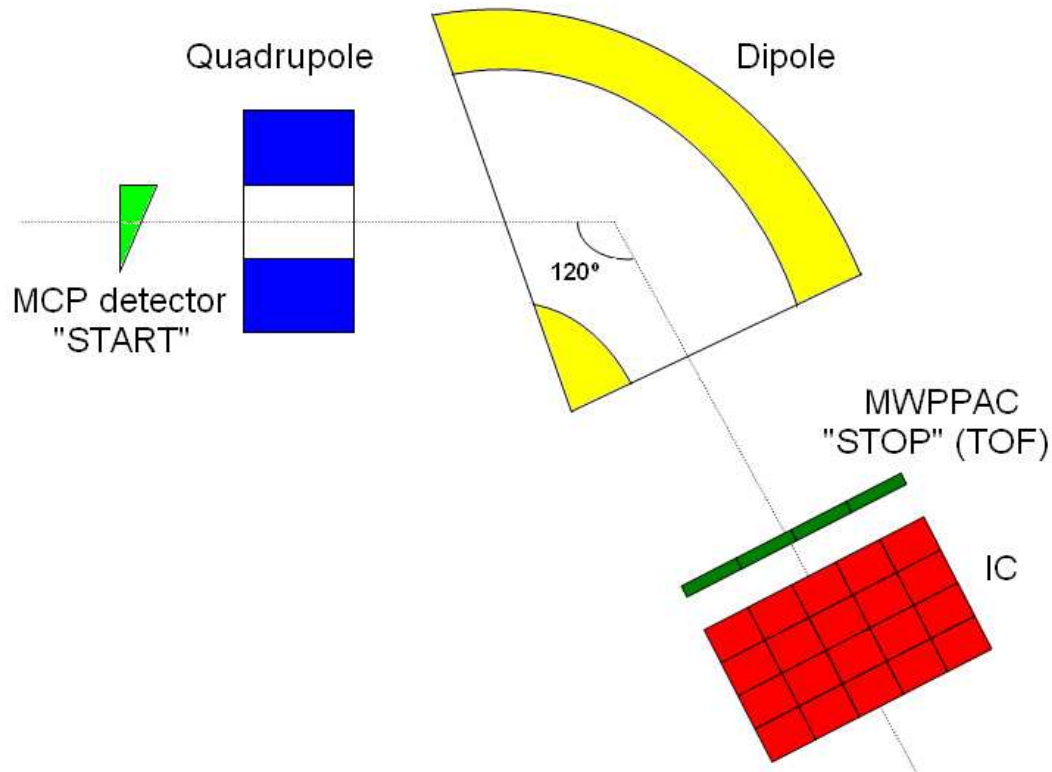

Figure 4.14: Schematic view of the PRISMA spectrometer.

Table 4.8: Performances and characteristics of the magnetic spectrometer PRISMA.

Solid angle	80 msr
Energy acceptance	$\pm 20\%$
Momentum acceptance	$\pm 10\%$
Energy resolution	up to 1/1000
Z resolution	$\sim 1/60$
A resolution	$\sim 1/200$
Counting rate capability	up to 50-100 KHz sec^{-1}

Table 4.9: Characteristic features of the PRISMA quadrupole.

Maximum field gradient (G)	5.3 T/m
Maximum pole tip field (B_0)	0.848 T
Effective length (L_{eff})	51 cm
Aperture diameter (d)	32 cm

Dipole magnet

The quadrupole singlet is followed by a large dipole magnet, placed 60 cm downstream of the quadrupole, which purpose is to act as an analyzer deflecting the ion path in trajectories depending on their magnetic rigidity. The bending angle of this magnet is 60º and the bending radius (ρ_0), corresponding to a trajectory lying on the optical axis, is 1.2 m. Since the maximum reachable field value is Bmax = 1 T, the maximum magnetic rigidity is $Bmax(\rho_0) = 1.2$ Tm. The entrance and exit surfaces form an angle of -20º and 5º, respectively, with respect to the optical axis. The pole gap for the magnet is 20 cm and the frontal size of the entrance and exit windows are 1000 mm wide. In Table 4.10 the main characteristics are summarized.

Table 4.10: Characteristic features of the PRISMA dipole.

Maximum field (B)	1.0 T/m
Bending radius (ρ_0)	1.2 m
Bending angle (ϕ)	60º
Entrance angle	-20º
Exit angle	5º
Pole gap	20 cm

Micro-Channel Plate entrance detector (MCP)

The entrance detector consists of a matched pair of 80*100 mm^2 area Multi-Channel Plates (MCP) in chevron configuration and a position sensitive anode [185]. It provides geometrical information, the positions on the X and Y axis, and a time signal. It is placed at an angle of 135º with respect to the optical axis of the spectrometer to cover all the solid angle of PRISMA at a distance of 250 mm from the target. The ions pass by a carbon foil generating secondary electrons which are accelerated towards an anode by an electric field. A weak coaxial magnetic field is used to improve the position resolution. The anode is made of two orthogonal delay lines, on the horizontal and vertical axis respectively, which provide information on the position of the ions by calculating the difference in arrival time of the signals at the two ends of each delay line. The fast time cathode signal is used as a START for TOF measurements between the MCP and the MWPPAC detectors. The intrinsic time resolution of the MCP detector is about 250-300 ps and its efficiency for heavy ions is close to 100%. In Fig. 4.15 a scheme of the setup and a MCP detector picture

are shown.

Figure 4.15: Schematic view of the setup with the reaction chamber and the MCP (left) and the MCP detector alone (right).

Multi-Wire Parallel Plate Avalanche Counter focal plane detector (MWPPAC)

The focal plane detector is an array of ten Multiwire Parallel Plate Avalanche Counters (MWPPAC) placed 323 cm downstream of the dipole exit [186]. A view of the detector is shown in Fig. 4.16. It consists of a three-electrode structure: a central cathode used for the time signal and two orthogonal wire planes used to determine the horizontal and vertical positions, with a total active area of 1000*130 mm^2. The X position sensitive anode is divided into 10 sections; each one is made of 100 wires (20 μ m diameter) with 1 mm spacing. The cathode consists of 10 sections, like in the X wire plane, with 330 wires for each section (20 μ m diameter), separated 0.3 mm, with a total of 3300 wires. A fast time signal is provided by each section of the cathode used as a STOP signal for TOF measurements performed between the MCP and the MWPPAC detectors. The Y position sensitive anode is composed of 130 wires (20 μ m diameter) with 2 mm wire separation, shorted two by two in the delay-line side. The position resolution on the horizontal axis is 1 mm, while on the vertical axis is 2 mm. The position information from MWPPAC is obtained using delay-line method: An induced signal propagates on the delay-line in both directions towards the ends of each independent section. The relative delay between two signals is proportional to the position of the incoming ion. The array provides in total thirty two signals:

- ten time signals one for each cathode section,

- twenty X position signals one for each extreme of the X delay line for each section,

- two Y position signal one for each extreme of the Y delay line.

The detector operates with Isobuthane ($C_4 H_{10}$) at a working pressure of about 7-8 mbar.

Ionization Chamber (IC)

The focal plane MWPPAC detector is followed by an ionization chamber (IC), which is used to measure the energy loss of the ions in the gas [186]. In this way with the energy
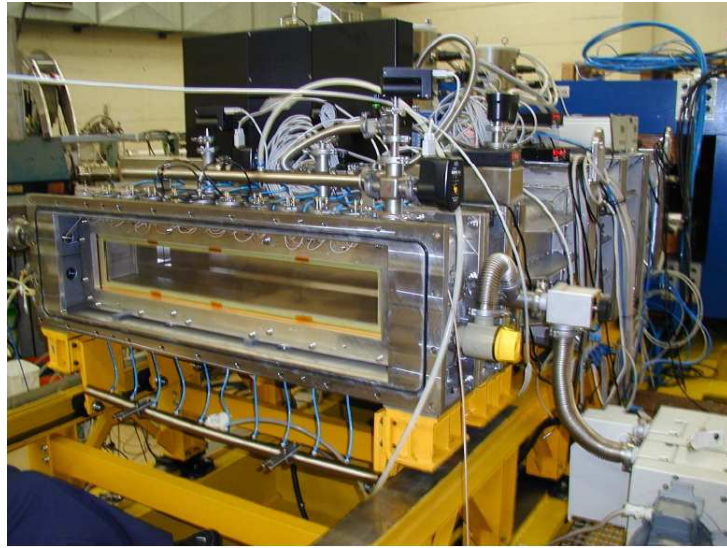
Figure 4.16: Picture of the MWPPAC detector and the pumping system.

loss, using the $\Delta E/E$ technique, it is possible to determine the atomic number Z of the ion. The detector covers a large area of the focal plane with 1200 mm long on the horizontal axis, 130 mm wide on the vertical axis and 1000 mm wide in depth (Fig. 4.17). The large dimensions of the IC allow to stop all ions inside the chamber and, therefore, to have a long range for the incoming nuclei. In this way, a good resolution on the atomic number (Z) can be obtained ($\Delta Z/Z \sim 1/70$). The IC is divided in ten equal sections in the x axis, corresponding to the MWPPAC sections, in a way that all ions coming from MWPPAC can enter directly in the active area of the chamber, and in four equal sections in depth. This depth segmentation allows to measure the energy loss in each section and so, to define the sum of the energy lost in the four sections as the total energy (E). ΔE is defined as the energy loss in the two first sections (like in our case) or only in the first one depending on the ions to be stopped. For too slow ions only one section is used to obtain a good $\Delta E - E$ telescope to determine Z. Additional sections are placed on both sides of the chamber (side sections) to act as a veto for ions with a highly bent trajectory which are not losing all their energy on the active volume. The detector is filled with Methane (CH_4) or Carbon Tetrafluoride (CF_4), methane in our case, depending on the pressure and stopping power required for the ions. The pressure ranges from a few tenths of mbar to hundred mbar.

4.5.2   The Differential Plunger

The differential Plunger is a target-degrader complex device, provided by the University of Cologne, built to measure lifetimes of excited sates in nuclei populated by multi-nucleon transfer and deep-inelastic reactions at grazing angles, ranging from 0.5 to 500 ps for $\beta \sim 10\%$ [187, 188]. The main improvement respect to the previous Cologne plunger devices is related to the optimization of the design performed for grazing reactions. In multi-nucleon transfer and deep-inelastic reactions the recoiling nuclei of interest leave the target in a direction which is normally different from the direction of the incident beam,

Lifetime measurement of neutron-rich nuclei in the region of the double magic ^{78}Ni with the γ-tracking AGATA demonstrator.
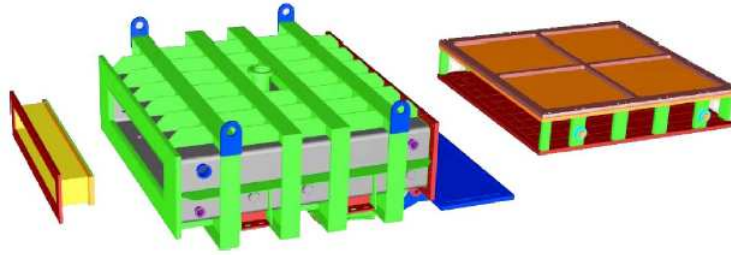
104

Figure 4.17: Schematic view of the ionization chamber.

given by the grazing angle. The plunger should be placed in this direction and, therefore, a design that enables a rotation of the device with respect to the beam axis has been done (Fig. 4.18). Assuming a 3 mm diameter for the beam, focused in the centre of the target, a maximum angle of $55^{\underline{o}}$ with an accuracy of $0.5^{\underline{o}}$, respect to the beam axis, the system can be turned. It consists of a target and a degrader foils placed in their respective frames, conical one for the target and flat for the degrader with a distance ring made of tantalum located in between. Both foils should be stretched to get uniform surfaces and to avoid changes in the fixed distance due to the heating of the foils when the beam hits them. The target cone together with the distance ring are pressed into the degrader foil to stretch it while the target should be stretched before it is glued on its frame.
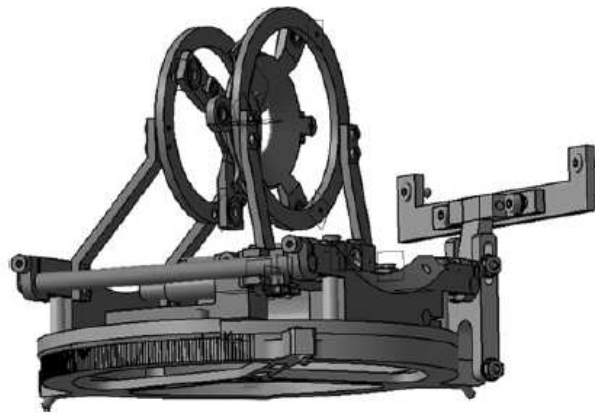

Figure 4.18: Drawing of the plunger device with its supporting structure used for the present measurement.

The target foil is fixed to the plunger while the degrader one is displaced with a piezoelectric motor. Besides, an inductive transducer, which measures the position of the degrader, in a range of up to 5 mm, with an accuracy of up to 0.01 μm is integrated. As for Doppler correction detectors placed at $90^{\underline{o}}$ are not useful (no Doppler correction can be performed at these angles), all the mechanical components have been mounted inside the target chamber close to the foils under $90^{\underline{o}}$. This is different from the concept followed for the standard Cologne-coincidence-plunger [189], where most of these components are located in a separate housing up-stream of the target chamber in order to minimize the

Table 4.11: Specifications of the differential plunger for grazing reactions.

Target-degrader separation	0-10 mm
Precision of the target-degrader distance (piezoelectric motor)	0.1 μm
Inductive transducer resolution	0.01 μm (0-40) μm range
	0.1 μm (0-200) μm range
	1 μm (0-5) mm range
Maximum rotation around the beam axis	$(55 \pm 0.5)^{\text{o}}$

amount of dead material between the target and the germanium detectors. However, for the present setup, no special considerations on this issue are needed since AGATA is placed at backwards angles covering from about 135° to 170°. In Table 4.11 the main characteristics of the differential plunger are summarized.

In the present experiment, the plunger setup includes a target of 1.5 mg/cm^2 of enriched ^{238}U evaporated onto a 1.4 mg/cm^2 Tantalum support to allow the stretching of the target, and a thick 4.17 mg/cm^2 Nb foil used as an energy degrader. Different distances, ranging from 100 μm to 1900 μm, were measured during the experiment by using the piezoelectric displacement motor and a high accuracy distance sensor which ensures a separation accuracy of about 1% between the target and degrader. In Fig. 4.19 is shown the differential plunger device standalone and placed inside the scattering chamber in the experimental setup.
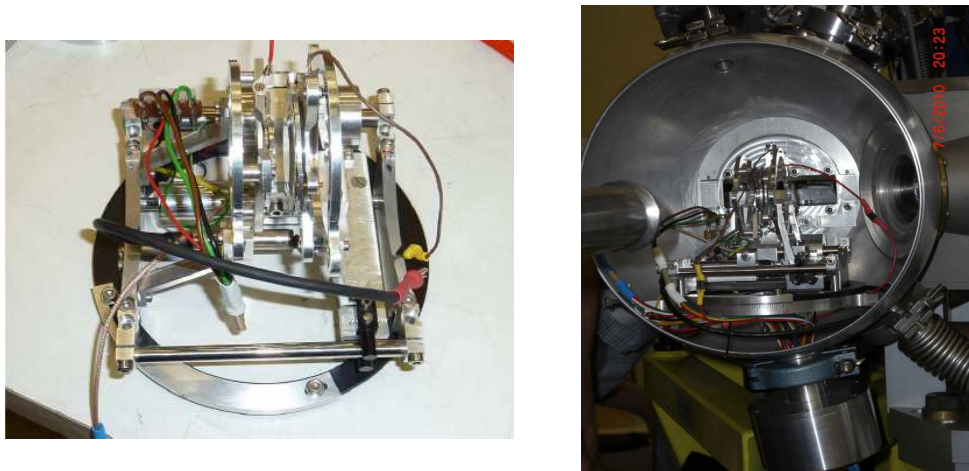

Figure 4.19: Picture of the plunger device before mounting and the device placed inside the reaction chamber for the present measurement.

4.5.3   The AGATA Demonstrator

As it has been explained before, the first implementation of the AGATA array is the AGATA Demonstrator [188] (Fig. 1.14). It is composed by five clusters (15 detectors), but for the present measurement only four of the five clusters (i.e. 80% of the efficiency) were available. It was located at 18.1 cm to the target foil while the nominal distance for the Demonstrator is 23.5 cm. The energy and efficiency calibrations were performed with an ^{152}Eu source placed in the centre of the reaction chamber (target position) using the so-called Radware approximation.

As aforementioned, through PSA techniques, it is possible to get the interaction points inside the detector with high accuracy. In this measurement the grid search algorithm, explained in Chapter 1, has been used. An example, to show the amount of information that can be obtained from PSA techniques, is presented in Fig. 4.20 and Fig. 4.21, where the statistics for the interaction points inside the detector is displayed. Figure 4.20 shows the interaction points inside the six sections of the 1B crystal, going from the bottom (left) to the top of the crystal (right). Figure 4.21 shows the bottom and the lateral view of the crystal if a cut in the X axis is done. It can be seen how the statistics decreases as we move from the the centre to the borders of the crystal as well as when moving to the higher sections of the crystal in the Z axis. In Fig. 4.22 some of the problems detected with the online PSA are shown. Figure 4.22 (left) shows the fifth section of the 2G crystal, where the A5 segment was missing (in blue); and in Fig. 4.22 (right) the fourth section of the 4B where a noisy segment (D4 in red) was found. These problems were solved in the off-line analysis, replaying the data and, therefore, improving the determination accuracy. Once the PSA is done, tracking can be performed and the interaction sequence inside the detector is determined. Figure 4.23 shows the first reconstructed interaction point for each event inside the demonstrator This information will be used for the Doppler correction.
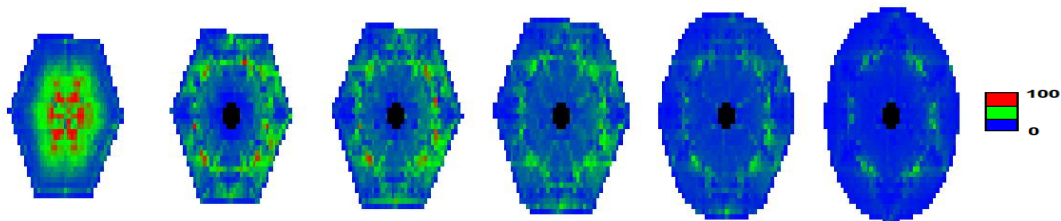

Figure 4.20: Interaction points in the six cuts corresponding to the transversal segmented sections in the 1B AGATA detector.
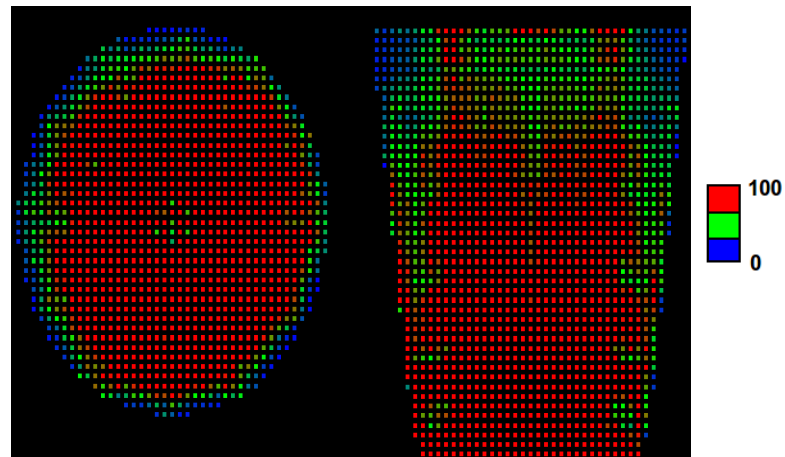
Figure 4.21: Different views of the interaction points in the 1B AGATA detector. a) corresponds to the bottom view and b) to the lateral side.
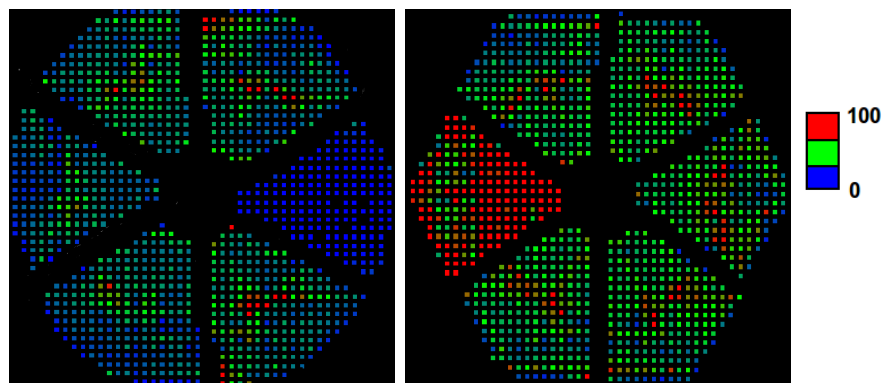

Figure 4.22: (left) View of the fifth section of the 2G crystal where segment A5 is missing (in blue); (right) View of the fourth section of the 4B crystal where it is shown the noisy segment D4 (in red).
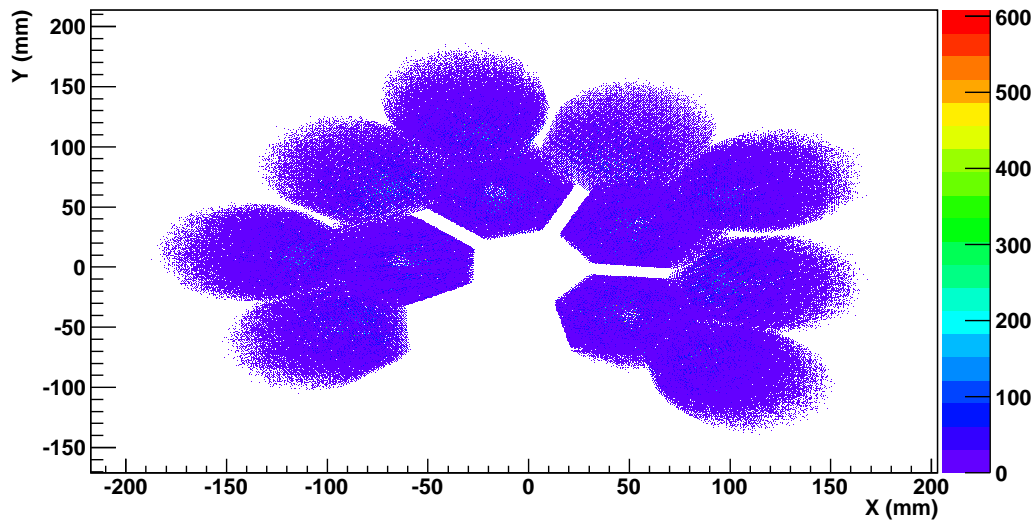
Figure 4.23: First interaction position in the laboratory frame of the γ rays within the AGATA Demonstrator that in the present experiment consists of four triple AGATA cluster detectors. The first interaction points will be used for the Doppler correction.

4.6   Data Analysis

The analysis procedure of the AGATA-PRISMA data is done in two steps; first the calibration of the detectors of PRISMA and the trajectory reconstruction of the ions in the spectrometer. This will provide the mass number (A), the atomic number (Z) and the velocity vector (β). Secondly, it will be performed the Doppler correction for γ rays, in coincidence with the projectile-like ions on an event-by-event basis, taking the information of the recoil velocity vector (β) determined by the reconstruction of the ion trajectories. Once the γ rays have been univocaly identified for a given A, Z and β, the γ spectra of the isotopes of interest is ready to perform the lifetime analysis. The data analysis has been performed using the GammaWare code [190].

The first and probably most important step in the reconstruction of the trajectories and the determination of Z and mass A is the calibration of the PRISMA detectors. In this section it will be discussed i) the calibrations of the entrance and of the focal plane detectors of the PRISMA spectrometer, ii) the procedure used for the trajectory reconstruction and the identification of the ions and iii) the final procedure to obtain the γ spectra.

MCP signal processing

The MCP detector has to be calibrated in order to determine the ion entrance positions to the spectrometer. The calibration is only performed for ions arriving at the focal plane of PRISMA. Figure 4.24 shows the mask used for the calibration where the five calibration points are highlighted. The two shadows correspond to two alignment tips that are placed within the quadrupole and dipole of PRISMA. The electric field used to accelerate the secondary electrons from the carbon foil to the MCP plates produces a distortion that

should be also corrected. In order to reach the maximum position resolution, a magnetic field, coaxial to the electron paths, is use to "spiralize" the trajectories and therefore to minimize the dispersion. The coordinates for the corrected points are shown in Table 4.12. The raw and calibrated data matrix are shown in Fig. 4.25. Once the calibration is done, X and Y position coordinates are converted to the ion entrance angles in the AGATA-PRISMA reference frame.
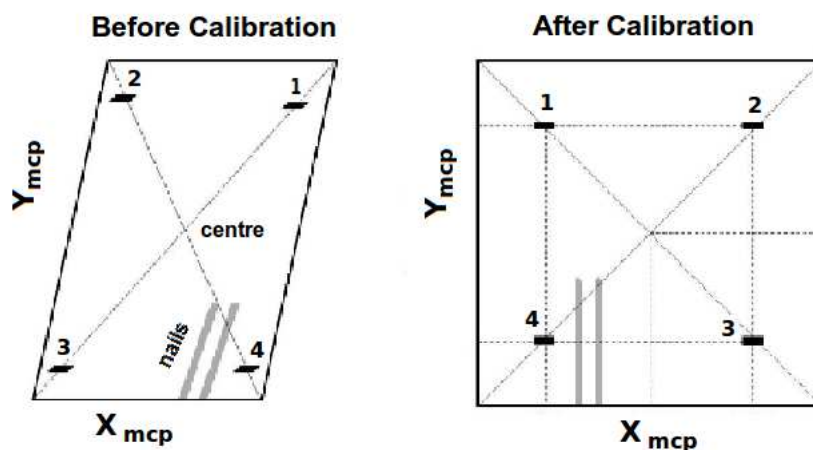

Figure 4.24: (left) Uncalibrated MCP; (right) calibrated MCP. The five calibration points have to be placed in their respective coordinates (Table 4.12).

Table 4.12: Coordinate positions of the reference points for the MCP calibration.

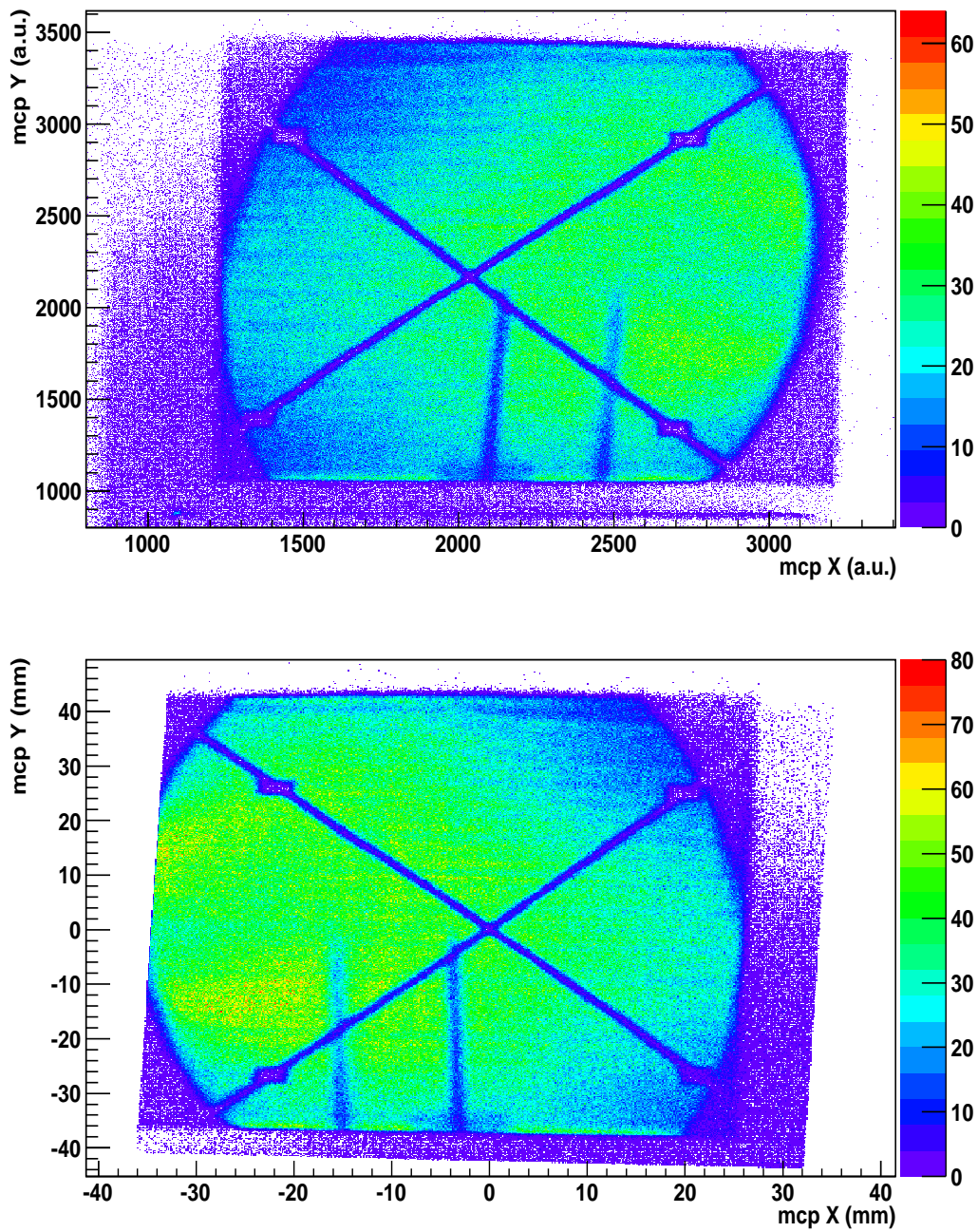| Point	X (mm)	Y (mm)
Centre	0	0
1	21.5	26.5
2	21.5	-26.5
3	-21.5	-26.5
4	-21.5	26.5

Figure 4.25: Uncalibrated MCP detector (top) and the calibrated MCP (bottom). The calculated MCP coordinates are given in the AGATA-PRISMA reference frame.

Focal plane detector (MWPPAC): X coordinate calibration

The MWPPAC detector at the focal plane gives six raw signals:

- two signals for the horizontal position (left and right),

- two signals for the vertical position (up and down),

- one signal for the time of flight (TOF),

- one amplitude signal from the cathode.

The MWPPAC detector is divided into ten sections on the X-plane giving us position and time signals individually. The horizontal position, the cathode and the TOF signals are registered for each of the sections, while the vertical position signal is common to all the sections.

When an ion enters the detector, it interacts with one of the ten sections producing two signals, called X_{left} and X_{right}, from the left and right edges of the corresponding section delay line. The position information is extracted by measuring the delay-time difference between them ($X_{fp} = X_{right} - X_{left}$). The signals are then calibrated using three reference points (the two extremes at 0 and 10 cm respectively, and a central wire). The vertical position is only used to center the trajectory but is not used for the reconstruction process. Therefore, no calibration has been done for the Y-plane. It may happen that one of the two horizontal position signals is missing. To recover events with only one position signal (right or left), normally related with extreme position in the MWPPAC section, it is possible to use as reference the cathode signal, which replaces the missing signal in the expression $X_{fp} = X_{right} - X_{left}$, that becomes, $X_c = X_{right/left} - X_{cathode}$ if the left/right signal is missing. The procedure requires a calibration curve between the coordinates X_{fp} and X_c in order to get the right reconstruction of the position for the incomplete events. In order to avoid background signals from the cathode a polygonal gate on the matrix $X_{right} + X_{left}$ vs. $X_{cathode}$ is required. The cathode signal is the trigger of the PRISMA Spectrometer. This condition is shown in Fig. 4.26.

Focal plane detector (MWPPAC): TOF calibration

The TOF measurement is fundamental in an ion-tracking spectrometer, it is the main ingredient determining the mass of the ion since required for the calculation of their absolute velocity values. This velocity is necessary for the ion mass determination and the Doppler correction of the γ-ray energies measured in AGATA. The TOF signal in PRISMA is measured as the time difference between the MCP detector (START) and the MWPPAC cathode signal (STOP). This measurement only provides relative TOF and to obtained absolute values is necessary first the TOF to be calibrated in ns. Different TOF offsets have to be considered for all the ten sections (see Fig. 4.27). However, this process does not give the absolute TOF and a fine tuning of the TOF signals is needed. This is done using the Doppler corrected γ-ray spectra measured in AGATA. The TOF tuning is done modifying a global offset until the main peaks in the gamma spectrum (inelastic excitation of the beam ion) show the proper position in energy and the smallest FWHM.
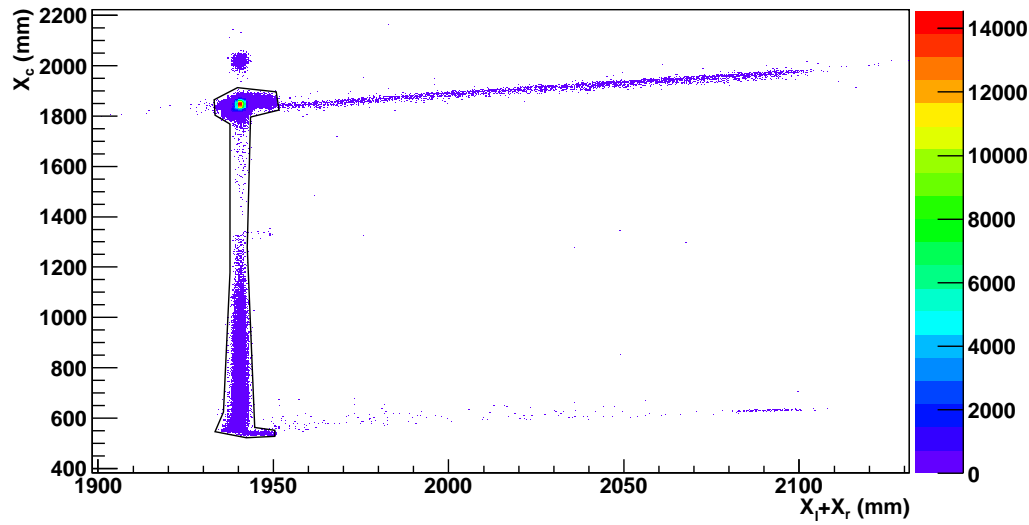
**Lifetime measurement of neutron-rich nuclei in the region of the double
magic ^{78}Ni with the γ-tracking AGATA demonstrator.**

112

Figure 4.26: MWPPAC event distribution as a function of the $X_{right} + X_{left}$ (X axis) vs. X_c (Y axis) signals. It can be seen the polygonal gate used to reduce the background signals.

Trajectory Reconstruction

The identification of the ions is based on the reconstruction of their trajectories [191]. This reconstruction is done in terms of the geometrical and timing information, provided by PRISMA, and by applying the equation of motion of a charge particle in a quadrupole and dipole magnetic fields. The information provided by PRISMA for each ion is the following:

- ion position coordinates in the MCP: (X_i, Y_i),

- ion position coordinates in the focal plane (MWPPAC): (X_f, Y_f),

- Time-of-flight of the ions between the MCP entrance and the MWPPAC: TOF,

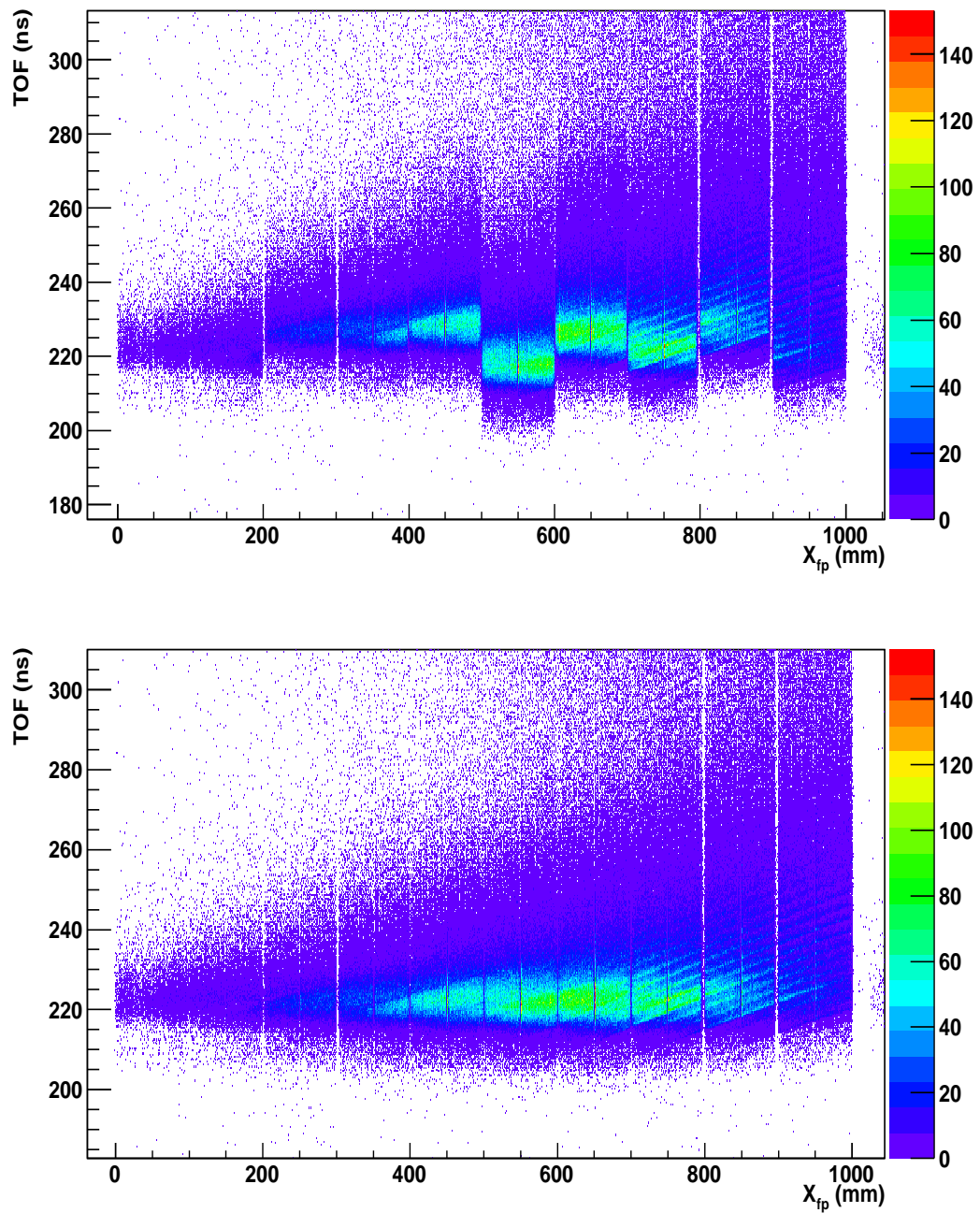- Partial and total energy loss in the IC: ΔE, E.

Figure 4.27: TOF vs. X_{fp} before the alignment of the ten sections of the MWPPAC (top) and absolute TOF vs. X_{fp} after calibration (bottom).

The trajectory reconstruction of the ions includes the determination of ion motions inside the optical elements of PRISMA, after the ions pass through the start detector. Therefore, the ion position coordinates determined from the MCP becomes the entrance position coordinates in the quadrupole. Inside the quadrupole, magnetic field charge particles are governed by the Lorentz equation:

$$\vec{F} = q\vec{v} \otimes \vec{B} \tag{4.17}$$

where F is the Lorentz force or electromagnetic force, v is the velocity of the ion and B is the quadrupole magnetic field.

Solving this equation a hyperbolic motion inside the quadrupole field is obtained, which focuses the ions in the vertical axis defocussing them on the horizontal plane. As the length of the quadrupole is a known magnitude, the coordinates of the reaction products leaving the quadrupole can be obtain. From the quadrupole to the dipole, the trajectories follow a straight line as they are supposed not to be affected by any magnetic field (ideal magnetic fields). Following the quadrupole, the ions enter inside the dipole and due to the Lorentz force their trajectories are bended with a radius R. The behaviour of an ion inside a dipole magnetic field (B_D) can be described again by the usual Lorentz force expression:

$$\frac{mv^2}{R} = q(v_\perp * B_D) \tag{4.18}$$

where q and m are the ion charge and mass, respectively, $v_\perp$ is the perpendicular component of the velocity to B_D and R is the curvature radius of the dipole.

As the radial velocity of the ions is negligible, the bending radius can be expressed in terms of the magnetic rigidity:

$$R_D = \frac{mv}{qB_D} = \frac{\rho_D}{B_D} \tag{4.19}$$

As soon as the quadrupole entrance point is known the trajectory from the quadrupole entrance to the MWPPAC is determined in terms of two parameters $R_Q = \rho_D/B_Q$ and $R_D = \rho_D/B_D$, where R_Q is the ion motion entering with a para-axial trajectory inside the quadrupole and R_D is the bending motion inside the dipole. The trajectory inside the dipole is calculated through an iterative process; $R_D = 120$ cm is assumed as the curvature radius inside the dipole, corresponding to the central trajectory, and then the magnetic rigidity is determined. Then R_Q is obtained as follows:

$$R_Q = R_D \frac{B_Q}{B_D} \tag{4.20}$$

Therefore, as the entrance of the quadrupole, the ratio B_D/B_Q and the curvature radius are known, the ion impact point in the MWPPAC is fully determined. If the calculated focal plane position does not match with the observed one (one mm difference),

the iterative process starts again with a new guess for the curvature radius till the obtained value is the correct one.

The ion trajectory is a straight line after the dipole and through the MWPPAC as the magnetic force is not affecting the ions any more. Therefore, after the trajectory reconstruction the total path of the ions inside PRISMA can be obtained. It is calculated as the contribution of different terms:

- a straight line between the target and the quadrupole entrance (L_{TQ}),

- a hyperbolic path inside the quadrupole (L_Q),

- a straight line between the quadrupole and the dipole (L_{QD}),

- a circular trajectory in the horizontal dispersion plane of the dipole (L_D),

- a straight line between the dipole and the MWPPAC (L_{DM}).

in this way:

$$L = L_{TQ} + L_Q + L_{QD} + L_D + L_{DM} \tag{4.21}$$

Once the trajectory reconstruction is done, an improvement on the TOF offset alignment can be performed. Since v = L/TOF and mv^2/R=qvB, the following expressions can be deduced:

$$TOF = \frac{m}{qB}\frac{L}{R} \qquad \frac{R}{v} = R\frac{TOF}{L} = \frac{m}{qB} \tag{4.22}$$

From the first one, the TOF offset can be adjusted since if we represent this matrix the slope corresponds to A/qB values and the average interception of these slopes gives the common TOF offset (Fig. 4.28 top). From the second expression it can be seen that different values of A/qB for the different sections of the MWPPAC give us different TOF offsets and, therefore an alignment on A/qB is equivalent to the TOF alignment. Figure 4.28 (bottom) shows the alignment on A/qB for the different sections of the MWPPAC once the TOF offset has been adjusted.
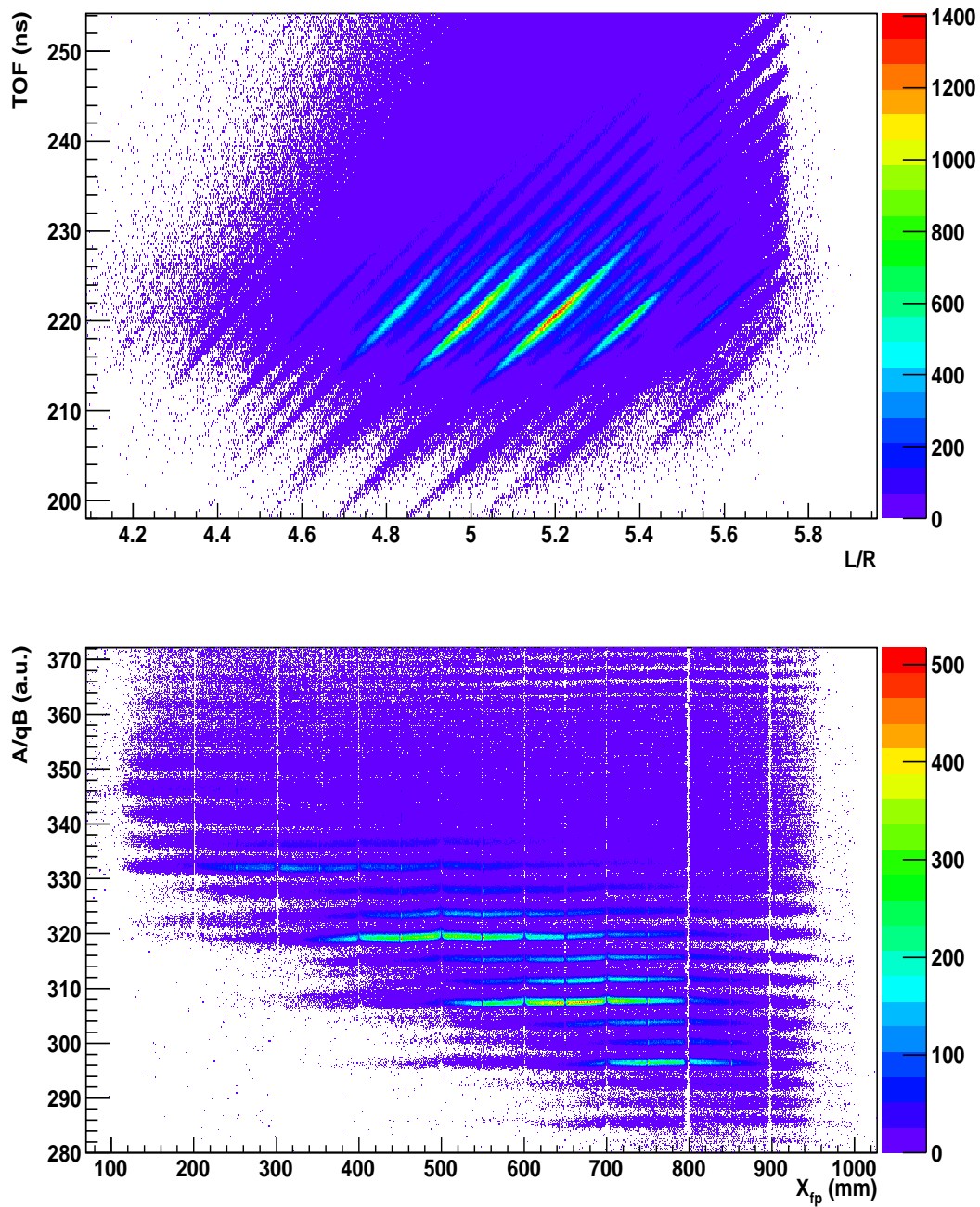
Figure 4.28: Two dimensional matrices of TOF vs. L/R for the TOF offset determination (top) and A/qB vs. X_{fp} for the A/q alignment of all sections of the MWPPAC (bottom).

Z identification

After passing the MWPPAC detector, the ions enter into the IC losing their energy by interacting with the filling gas (CH_4 in the present experiment). The conditions of the gas filling the camera are adjusted in order to assure a complete energy release for all the reaction products of interest inside the IC. The energy loss for a charge particle is given by the Bethe-Bloch formula:

$$\frac{dE}{dx} = -\frac{4\pi}{mc^2}\frac{NZ_M\rho z^2}{A\beta^2}\frac{e^2}{4\pi\varepsilon_0}ln\frac{2mc^2\beta^2}{I(1-\beta^2)} - \beta^2 \tag{4.23}$$

where Z_M, A, ρ and I are the atomic number, the mass number, the density and the mean ionization potential of the stopping material; N is the Avogadro number and Z, β and E are the atomic number, the velocity and the energy of the ion. For non relativistic particles ($\beta^2 << 1$)

$$\frac{dE}{dx} \propto \frac{mz^2}{E}ln\frac{E}{m} \tag{4.24}$$

The range of the ions inside the IC, defined as the distance travelled by a charge particle till it is stopped, can be obtained from the stopping power as follows:

$$R(T) = \int_0^T (\frac{-dE}{dx})^{-1}dx \tag{4.25}$$

Different plots can be performed in order to identify the atomic number Z in the IC. Figure 4.29 (top) shows the energy lost vs. the range of the ions (R) meanwhile the bottom shows the energy released in the two first sections (ΔE) vs. the total energy released in the IC. In both plots, well separated line structures corresponding to the beam-like reaction products can be seen. The most populated channel corresponds to Z=32 since ^{76}Ge is the beam, while the other channels, Ga (Z=31), Zn (Z=30) and Cu (Z=29) isotopes, can be identified knowing that for a fixed total energy E, the atomic number grows with ΔE and decreases with R.
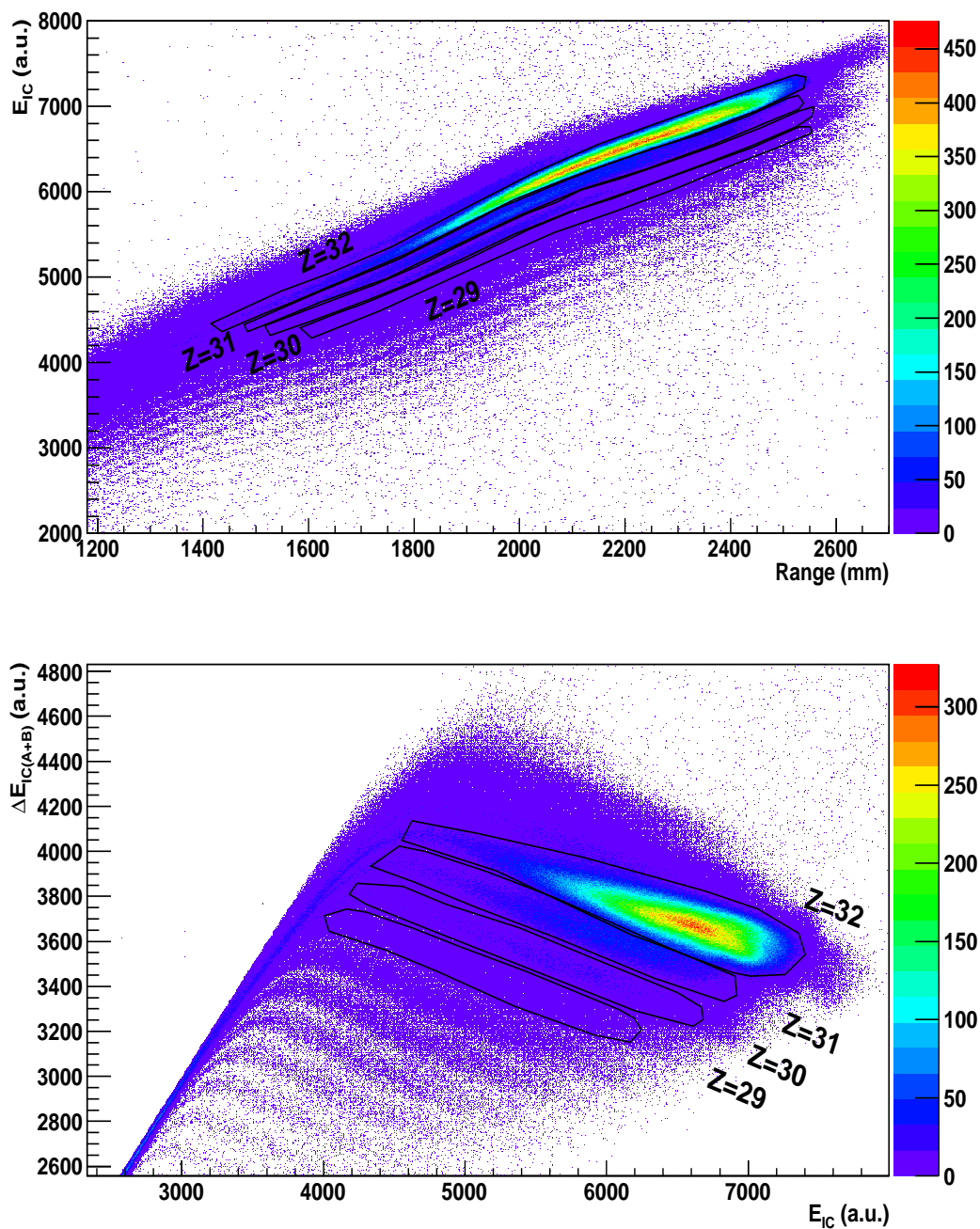
Figure 4.29: Two dimensional matrices for the Z identification of the reaction products in the IC. In the top the energy lost vs the range of the ions inside the IC is plotted and, in the bottom the energy released in the two first sections vs the total energy lost in the IC is shown.

Identification and selection of the charge states

Once all isotopes have been determined by their atomic number (Z), the charge state identification can be done. Due to the existence of several charge states, different A/q values can be obtained for each Z. The identification is based on the relation given by eq. 4.22

$$\frac{m}{q} = \frac{BR}{v}; \qquad E = \frac{mv^2}{2}; \qquad \Longrightarrow \qquad \frac{E}{v^2} = \frac{qBR}{2v} \qquad (4.26)$$

Exact values for the charge states, for each element, can be obtained through the matrix BR/v vs E/v^2 as shown in Fig. 4.30 (top). For example, the identification of the charge state values for the beam nucleus can be determined from this matrix knowing that the most intense line corresponds to the ^{76}Ge nucleus. A measured value for BR/v of 32.2 corresponds to this line and, therefore, the charge state can be determined as follows:

$$q = \frac{m}{B\frac{R}{v}} \qquad \Longrightarrow \qquad q = \frac{76}{32.2} \sim 24^+ \qquad (4.27)$$

The different lines shown in Fig. 4.30 (top) are associated to different charge states which can be calculated in the same way. In our case, charge states from 21^+ to 26^+ have been observed for ^{76}Ge. The same relations used for the identification are used to perform the charge state selection:

$$\frac{m}{q} = \frac{BR}{v}; \qquad E = \frac{mv^2}{2}; \qquad \Longrightarrow \qquad E = \frac{1}{2}qB\frac{LR}{TOF} \qquad (4.28)$$

Figure 4.30 (bottom) shows the energy lost in the IC vs $BR\beta$ matrix for each Z, used for the selection. Each line in the matrix corresponds to a different charge state value (q). The conditions on individual charge states allows to build the corresponding mass spectra (Fig. 4.31). The mass values in the spectra are assigned with respect to the most populated mass, which is the beam nucleus ^{76}Ge (Z=32; A=76). The same procedure is performed in order to identify charge states and eventually to deduce the mass spectra for the other ions. Charge states for the other Z values can be determined by comparing their traces to those of Ge element, since the same charge states of different elements should be relatively overlapped.

Lifetime measurement of neutron-rich nuclei in the region of the double magic ^{78}Ni with the γ-tracking AGATA demonstrator.
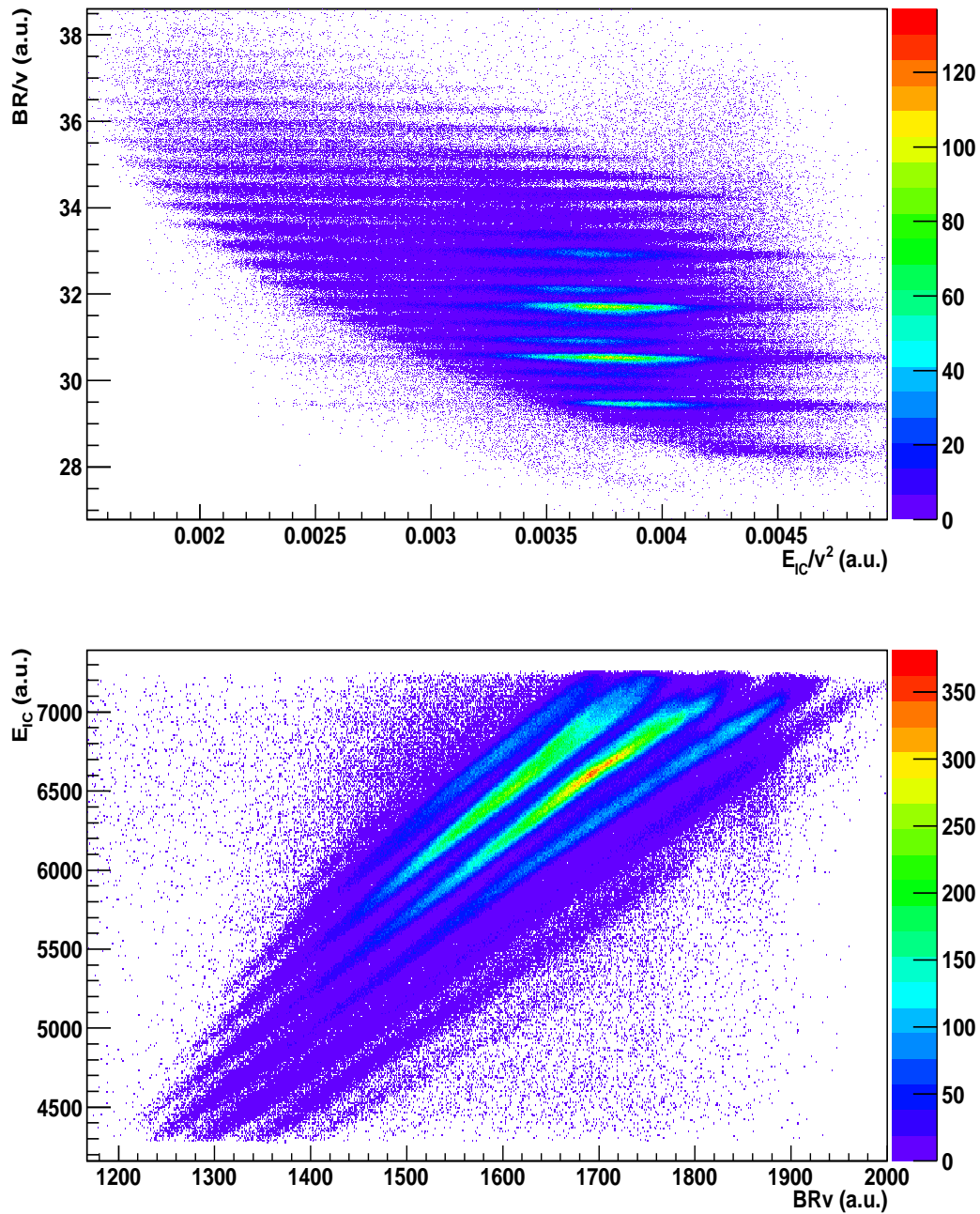
120

Figure 4.30: In the top, is plotted the BR/v vs E_{IC}/v^2 matrix to perform the charge state identification and, in the bottom, E_{IC} vs BRv matrix for each Z selection used for the identification.
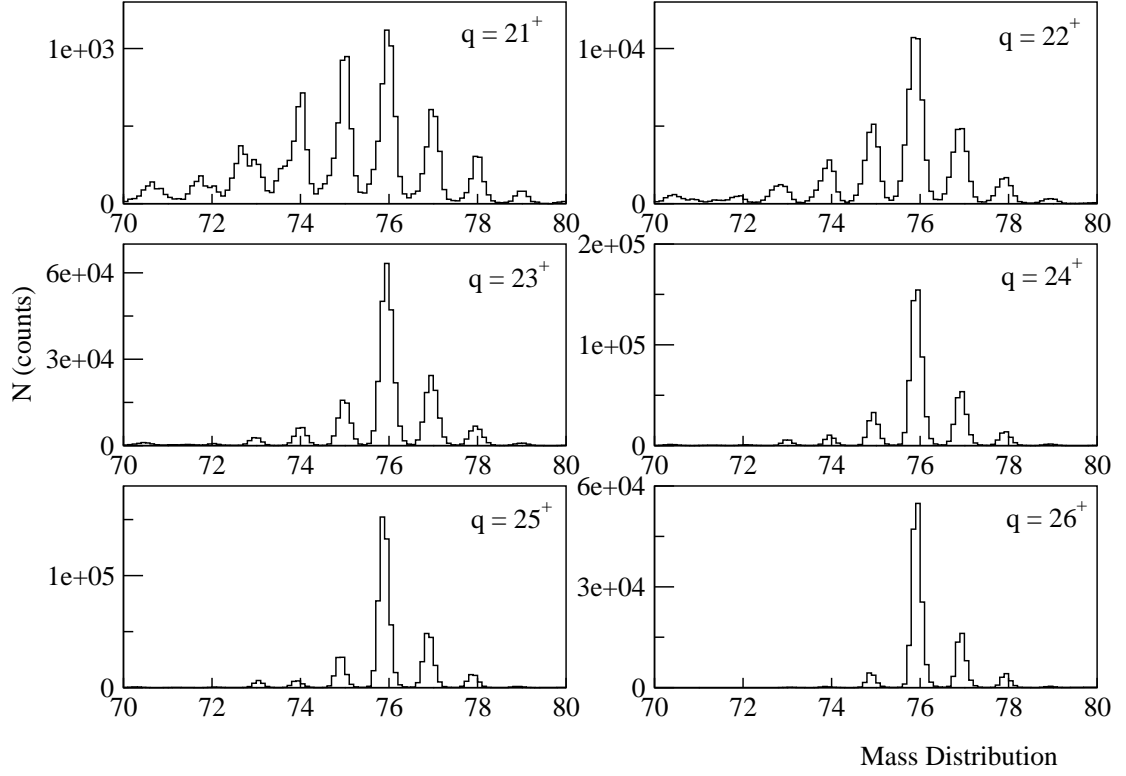
Figure 4.31: Mass spectra for the different charge states of Ge.

Doppler correction

As previously mentioned, the Doppler correction of γ rays emitted in the reaction products is performed on an event-by-event basis, taking the information from PRISMA and AGATA. Before performing the Doppler correction, the γ-ray energies from AGATA are calibrated with the standard ^{152}Eu source, then the Doppler correction is performed using the angle between the recoil velocity vector ($\vec{\beta}$) and the direction of the emitted γ rays ($\vec{\gamma}$). The angle between the detected ion (determined by the MCP start detector position) and its respective γ-ray (determined by the position of the first interaction of the γ-ray in AGATA) is calculated as follows:

$$\vec{\beta} \cdot \vec{\gamma} = |\beta||\gamma| \cos \theta \tag{4.29}$$

being $\vec{\beta}$ the position vector of the MCP and $\vec{\gamma}$ the position vector of AGATA.

Once the Doppler correction is properly performed the energy of the peaks should not display any dependency on this angle, as can be see in Fig. 4.32. The Doppler-corrected γ-ray spectrum for ^{76}Ge is shown in the Fig. 4.33.
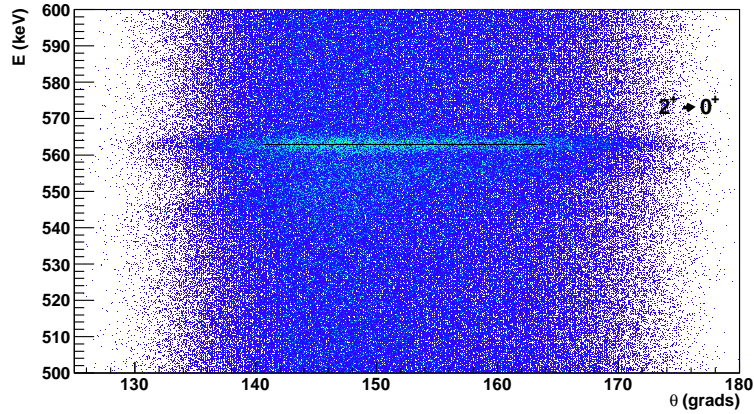
Figure 4.32: Doppler-corrected γ-ray energy of the unshifted peak of the $2^+ \rightarrow 0^+$ transition for ^{76}Ge obtained for the 200 μm statistics vs the angle between the recoil velocity vector and the direction of the emitted γ rays (θ).
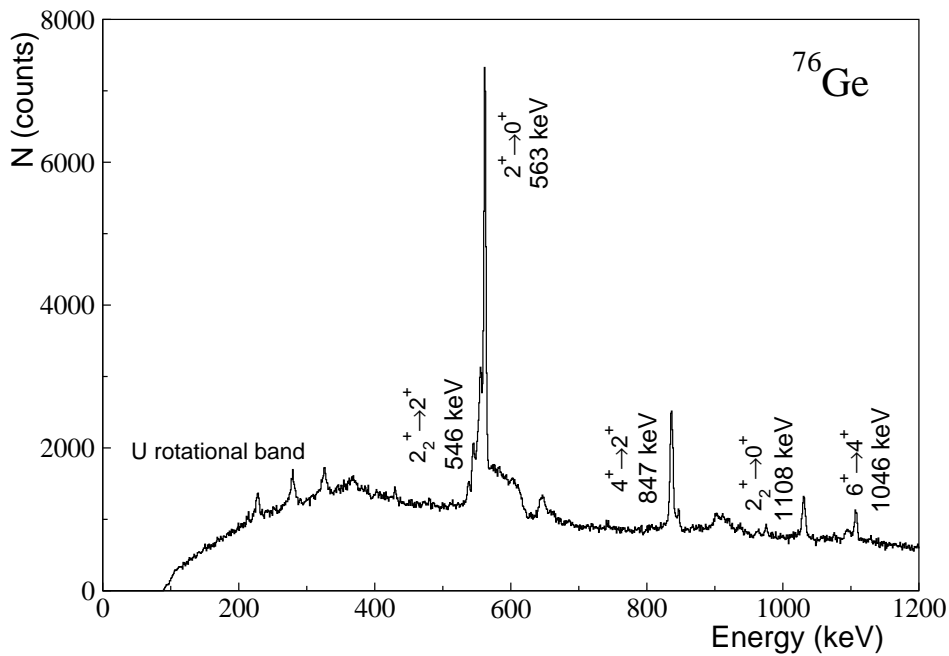

Figure 4.33: Doppler-corrected γ-ray spectrum gated for ^{76}Ge obtained for the data set corresponding to 200 μm target-degrader distance.

Mass spectra and γ-ray identification

Figure 4.34 shows the isotope yield distribution for Ge, Ga, Zn and Cu isotopes after summing all the charge states.
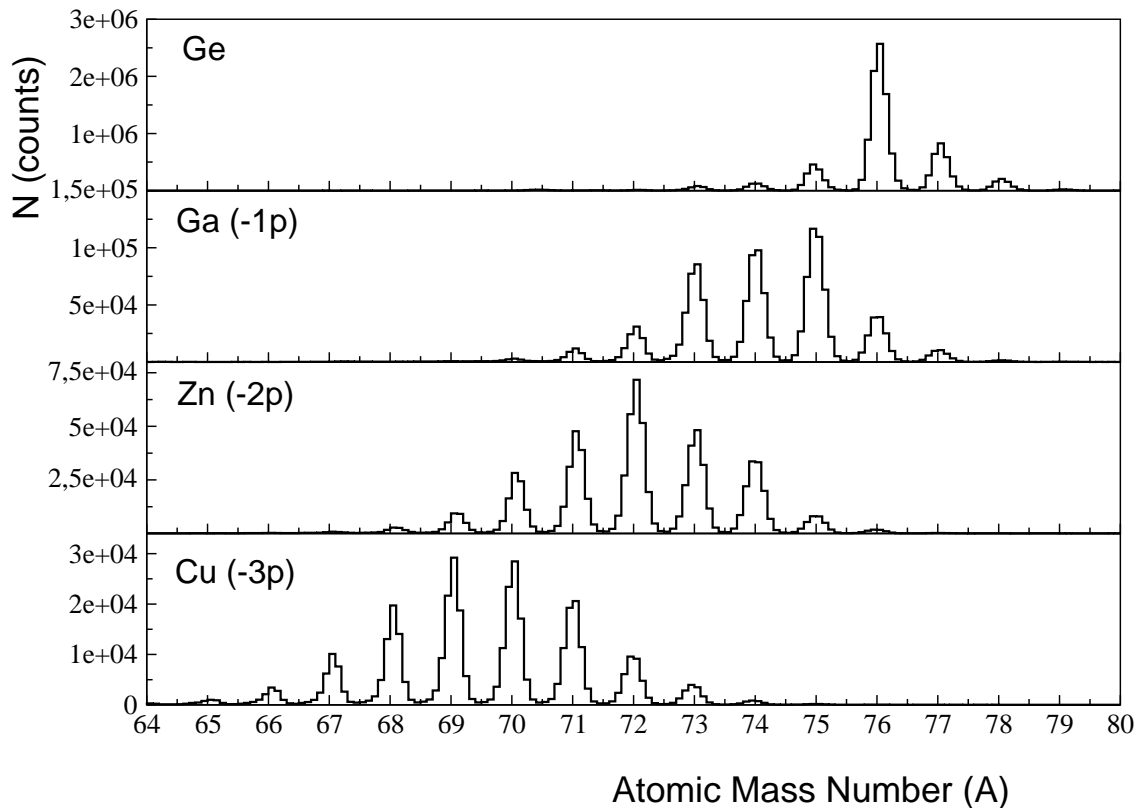

Figure 4.34: Isotope yield for Ge, Ga, Zn and Cu. The statistics shown consider all distances measured in the experiment.

While PRISMA events were always acquired, regardless the presence of an AGATA trigger, AGATA events were only acquired in coincidence with the PRISMA magnetic spectrometer, thus, all γ rays measured by AGATA were unequivocally assigned to a product nucleus. Figure 4.35 shows the coincidence time spectrum between both systems (TSDiff) obtained as the difference of the time stamp spectra between AGATA and PRISMA. It can be noticed the large background under the peak coming mainly from the random coincidences due to the high counting rates. This background can be accounted for setting gates on the coincidence spectrum shown in Fig. 4.35. During the analysis procedure, different conditions are set, on the real AGATA-PRISMA coincidence peak (continued blue lines), as well as in the random coincidence region (dashed red lines). In this way the background subtraction can be performed. Figure 4.36 shows the final γ-ray spectra for the ^{76}Ge isotope after background subtraction.

124

Lifetime measurement of neutron-rich nuclei in the region of the double magic ^{78}Ni with the γ-tracking AGATA demonstrator.
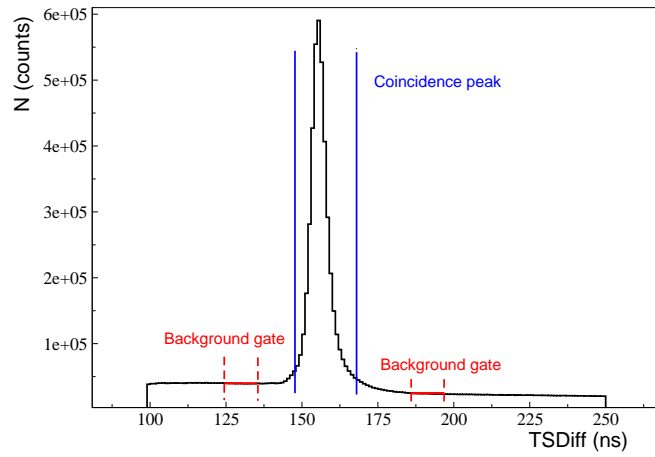

Figure 4.35: AGATA-PRISMA coincidence time spectrum. In blue it is shown the AGATA-PRISMA coincidence peak and in red the gates performed for the background subtraction.
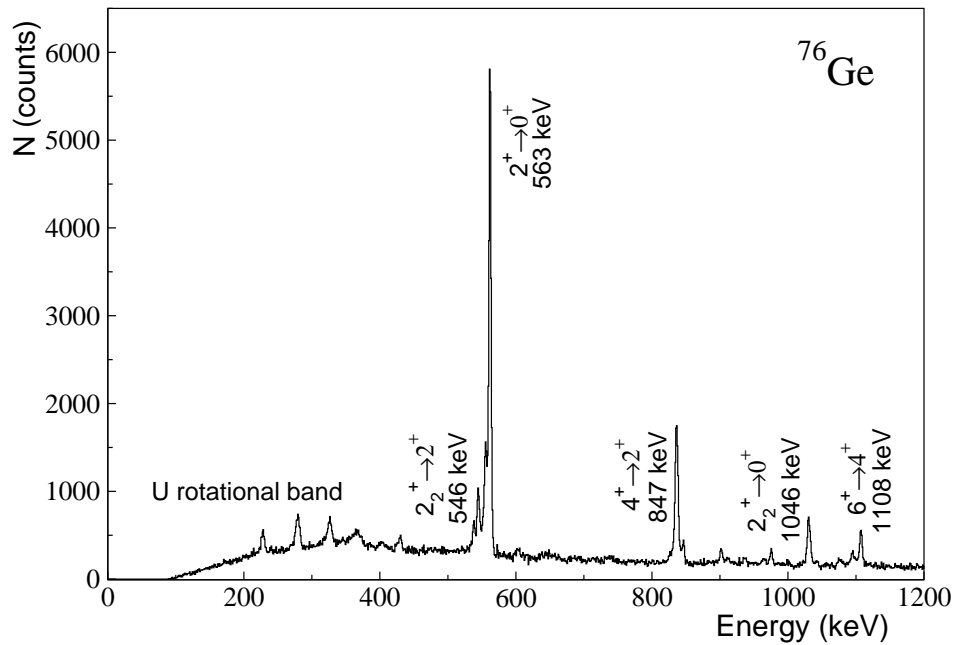

Figure 4.36: Doppler corrected gamma spectra for the ^{76}Ge isotope after background subtraction obtained for the data set corresponding to μm target-degrader distance.

4.7 Results

To determine the lifetime of the excited states of Cu isotopes we have used the RDDS method. Two different approaches have been employed to determine the lifetime of the excited states we are interested in (see section 1.4). The first one is the "conventional" one that uses for the normalization the addition of the intensities of the unshifted and shifted peaks. On the contrary, the new approach makes the normalization considering the number of nuclei populated in the reaction and detected in PRISMA. To validate the new approach, used in this work for the first time, the ^{76}Ge beam has been used (section 1.7.2). In particular, the $4^+ \to 2^+$ transition at 847 keV. Another verification of the approach has been performed for other isotope different of the elastic channel, coming from the transfer of several nucleons. The $4^+ \to 2^+$ and $2^+ \to 0^+$ transitions at 847 keV and 653 keV respectively, of the ^{72}Zn isotope have been used (section 1.7.3). Once the operation of the new approach has been sucesfully confirmed, it has been applied to the determination of the lifetime of the $7/2^-$ state at 981 keV of the ^{71}Cu isotope (section 1.7.4). However, before this, the determination of the velocity distribution, essential for the evaluation of the lifetime, will be discussed.

4.7.1 Velocity distribution

The analysis of the PRISMA data directly provides the velocity distribution of the ions after the degrader, nevertheless, as discussed in section 4.4, it is possible to obtain information on the velocity distribution before the degrader by applying eq. 4.5. Figure 4.37 shows the β distribution after the degrader and Figure. 4.38 shows the angle distribution (θ) between the MCP detector and the AGATA Demonstrator needed for the determination of the velocity distribution before the degrader. The average value of θ is 152^0.

These information together with the shifted and unshifted centroid energies ($E_0^{shifted}$, E_0) are the ingredients, according to eq. 4.5, to get information on the the beta distribution before the degrader (β_{bef}). The values involved in the determination of β_{bef} as well as the value obtained for the β_{bef} for the isotopes we are interested in are shown in Table 4.13. The uncertainty on β_{bef} has been calculated using the uncertainty propagation law but as the uncertainties on E_0 and $E_0^{shifted}$ are negligible with respect to the uncertainty on β_{aft}, the obtained values are the ones given by the FWHM of the β_{aft} distribution.

Table 4.13: Energy shift between the unshifted and shifted peak in the spectra with respect to the unshifted energy ($\Delta E/E_0$) and velocity distribution of the ions before and after the degrader, respectively, for the isotopes of interest.

Isotope	transition	Energy (keV)	$\Delta E/E_0$ (%)	β_{bef} (%)	β_{aft} (%)
^{76}Ge	$2^+ \to 0^+$	563	1.1	0.104(3)	0.091(3)
^{72}Zn	$2^+ \to 0^+$	653	1.2	0.100(5)	0.086(5)
^{71}Cu	$7/2^- \to 3/2^-$	981	0.9	0.094(5)	0.084(5)

where the energy shifts of ^{76}Ge, ^{72}Zn and ^{71}Cu have been calculated for the 563-, 653-
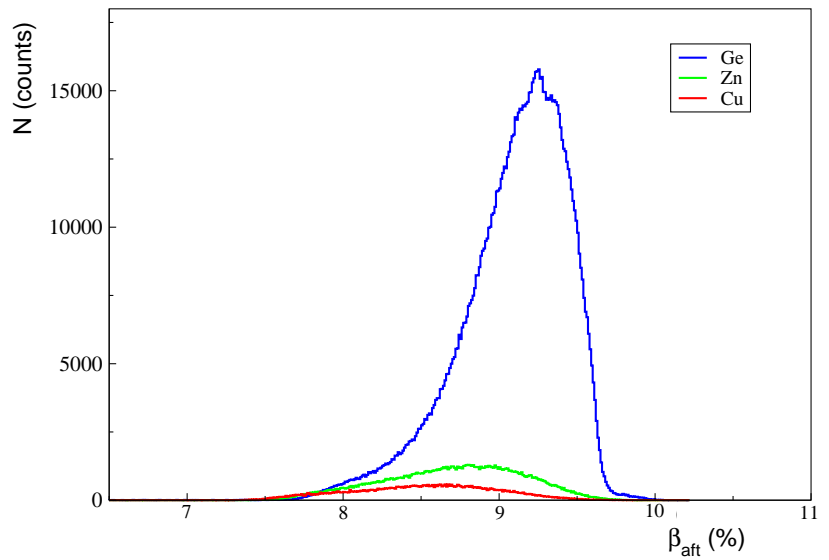
and 981-keV emission lines, respectively.

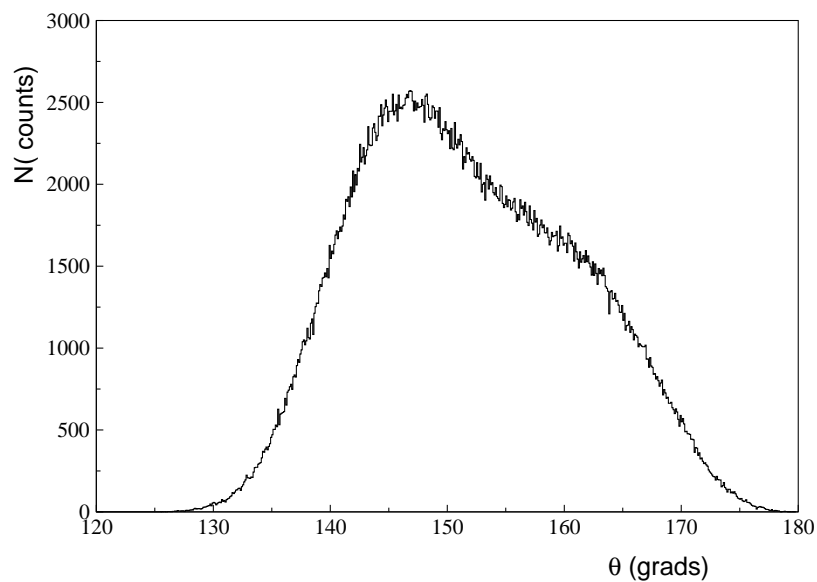Figure 4.37: Beta distribution (β_{aft}) measured in PRISMA for Ge, Zn and Cu isotopes.

Figure 4.38: Angle distribution (θ) between the MCP detector and the AGATA Demonstrator.

4.7.2 Verifying the method: Lifetime determination in the ^{76}Ge inelastic excitation.

Transitions observed in the inelastic excitation of the ^{76}Ge beam have been used to validate the new approach, to determine the lifetime of excited states, employed in the present work. In principle, the use of the inelastic excitation of the beam may be not the best way to test RDDS lifetime measurement techniques, since the inelastic excitation reaction can take place in both, the target or the degrader foils. In our particular case, the inelastic excitation cross sections for both, target and degrader, are about the same. Therefore, meanwhile the shifted peak solely corresponds to events produced in the target, the unshifted peak has the contribution of both, the excitations in the target as well as in the degrader. However, since the contribution of the excitations in the degrader, once renormalized to the number of ions, is constant for all the measurements, if the number of distances is sufficient, it is possible to account for the degrader contribution during the lifetime fit procedure.

For this test, the ^{76}Ge $4^+ \to 2^+$ transition with 847 keV energy has been chosen. Its transition lifetime is known to be 1.8(4) ps [192]. Figure 4.39 shows the Doppler corrected γ-ray spectra of ^{76}Ge, in the energy region of interest for the $4^+ \to 2^+$ transition, for the different measured distances. The calculated intensities of the unshifted and shifted peaks as well as the ratio R defined in eq. 4.11 as $I_u/(I_u + I_s)$ are shown in Table 4.14.

The second approach employs for the normalization the number of nuclei produced in the reaction and detected in PRISMA. This number is calculated selecting those events corresponding to ^{76}Ge by integrating the peak in the mass spectra. The values are shown in Table 4.15.

Table 4.14: Experimental values of the shifted peak (I_s), the unshifted peak (I_u), and R (R $= \frac{I_u}{I_u+I_s}$) as a function of the distance d_f.

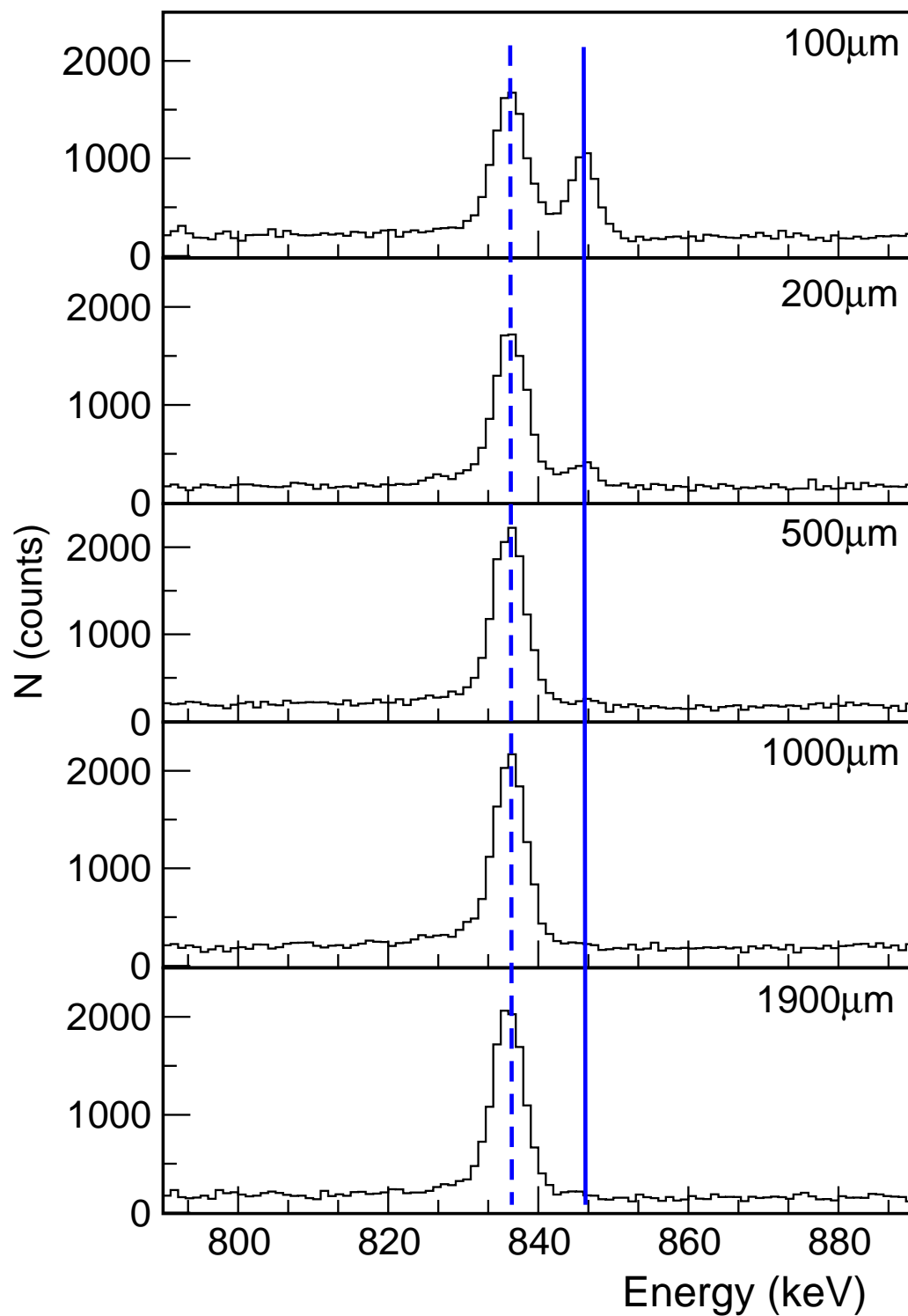| E = 847 keV $4^+ \to 2^+$				
d (μm)	d_f (μm)	I_s (counts)	I_u (counts)	R
100	112.01	7584(239)	4439(187)	0,369(28)
200	211.97	8064(225)	1131(97)	0,123(11)
500	512.00	10705(382)	245(108)	0,0224(99)
1000	1012.01	10726(519)	248(172)	0,023(16)
1900	1912.00	9750(199)	271(54)	0,0270(54)

Figure 4.39: Doppler corrected γ-ray spectra of ^{76}Ge around the $4^+ \rightarrow 2^+$ transition for the different distances. Two lines have been plotted in blue, the solid line corresponds to the unshifted peak and the dashed line to the shifted peak.

Table 4.15: Number of ^{76}Ge nuclei detected in PRISMA (N_0) for each distance (d_f).

d (μm)	d_f (μm)	N_0
100	112.01	2005818(1416)
200	211.97	1375631(1173)
500	512.00	1724937(1313)
1000	1012.01	1802040(1342)
1900	1912.00	1436109(1198)

To determine the lifetime an exponential fit has been used. n particular, for this transition, the possible known feedings from other excited states as the $0_2^+ \to 4^+$ at 501 keV ($t_{1/2} > 0.8$ ps [192]) have not been observed in the present measurement. The equation employed for the fit has been the following:

$$R(x) = A + Bexp^{(-x/C)} \tag{4.30}$$

where $C = (\beta c t_{1/2})/ln2$ being $t_{1/2}$ the half life of the excited state.

In order to check the effect of the excitation of the degrader we have performed a simulation. An arbitrary large amount of counts has been added to the area of the unshifted peak corresponding to the 100 μm target-degrader distance. An equivalent area, determined by renormalizing to the relative number of ions detected in PRISMA, has been added for the rest of target-degrade distances (Table 4.16). The selected value corresponds to about a 10% of the total number of ^{76}Ge nuclei detected in PRISMA (N_0)(see Table 4.15).

Table 4.16: Number of counts added (N_{add}) to the unshifted peak to emulate the degrader contribution for each distance.

d (μm)	d_f (μm)	I_u (counts)	N_{add}
100	112.01	4439(187)	2000
200	211.97	1131(97)	1372
500	512.00	245(108)	1720
1000	1012.01	248(172)	1797
1900	1912.00	271(54)	1432

Table 4.17 shows the value of the parameters used for the fit of the experimental data for all the approaches used in this work. The function fitted has been an exponential one defined in eq. 4.32. In the function we have used an additional parameter (A) not needed for an exponential fit. In principle, this parameter should be zero (except for the case where the shifted approach is used) but, as it is shown, it is not the case. In this parameter are included all contributions, like the contribution coming from the

degrader, that are not influencing the exponential behaviour. Therefore the lifetime can
be determined in this way as the exponential part of the function is giving the same trend
for all approaches. Figure. 4.40 shows the various fits to the exponential performed for
the different approaches.

Table 4.17: Coefficients obtained from the fit of the experimental data of the $4^+ \rightarrow 2^+$
^{76}Ge transition at 847 keV to the function $A + Bexp^{(-x/C)}$ for the different approaches.

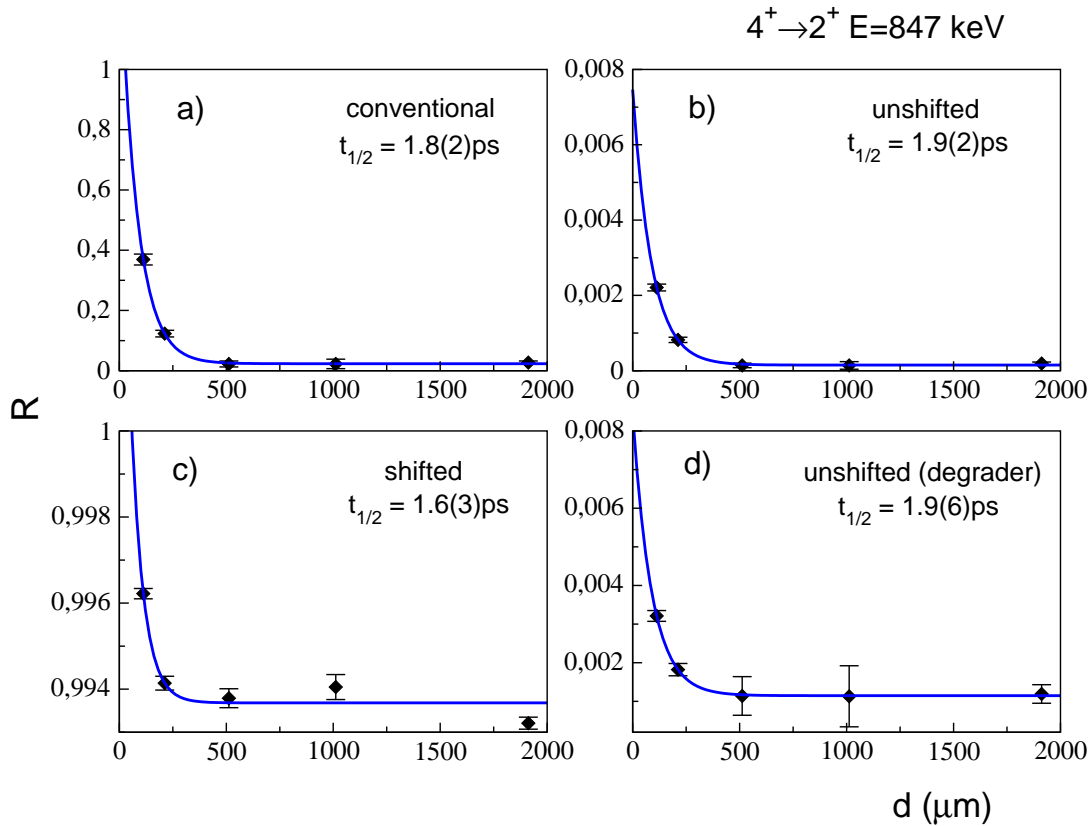| E = 847 keV $4^+ \rightarrow 2^+$ $R_1(x) = A + Bexp^{(-x/C)}$			
Method	A	B	C (μm^{-1})
conventional	$2.53(46)$ $^{-02}$	$1.48(26)$ 10^{+00}	$7.8(8)$ 10^{+01}
unshifted	$1.67(32)$ 10^{-04}	$7.7(12)$ 10^{-03}	$8.5(9)$ 10^{+01}
shifted	$9.9347(11)$ 10^{-01}	$1.37(43)$ 10^{-02}	$7.0(14)$ 10^{+01}
unshifted (degrader)	$1.17(21)$ 10^{-03}	$7.7(28)$ 10^{-03}	$8.5(26)$ 10^{+01}

Figure 4.40: Fit of the $4^+ \rightarrow 2^+$ transition at 845 keV considering the data obtained a)
when the conventional method is applied, b) when the unshifted peak is considered, c)
when the shifted peak is considered and d) when the unshifted peak and the degrader
contribution are considered.

The values obtained for the half file, the lifetime and the reduced transition probability of the $4^+ \to 2^+$ transition at 847 keV are shown in Table 4.18. The literature value is displayed together with the values obtained if the conventional normalization is considered for the calculation and if the normalization of the unshifted and shifted peak is used, referred in the table as unshifted and shifted, respectively. It is also shown the $t_{1/2}$ obtained if a fictitious contribution of the degrader is considered, referred in the table as unshifted (degrader). The agreement between the literature value and the measured values in this work allows to confirm that the new approach can be employed for the lifetime determination. Furthermore, it can be assured that the contribution of the degrader is not affecting the lifetime value of the state of interest.

Table 4.18: Half life ($t_{1/2}$), lifetime (τ) and reduced transition probability ($B(E2 \downarrow)$) for the $4^+ \to 2^+$ ^{76}Ge transition at 847 keV.

E = 847 keV $4^+ \to 2^+$			
Method	$t_{1/2}$ (ps)	τ (ps)	$B(E2 \downarrow)$ ($e^2 fm^4$)
literature	1.8(4)	2.6(6)	722(167)
conventional	1.8(2)	2.6(3)	722(83)
unshifted	1.9(2)	2.7(3)	696(77)
shifted	1.6(3)	2.3(4)	817(142)
unshifted (degrader)	1.9(6)	2.7(9)	696(232)

4.7.3 Lifetime determination for the ^{72}Zn isotope

In order to further validate the RDDS method based on the normalization to the ions detected in PRISMA (see section 4.4), the plunger analysis has been performed as well for a neutron-rich nucleus that is populated through the multi-nucleon transfer only in the reactions within the target, the ^{72}Zn nucleus. In particular, the $2^+ \to 0^+$ transition at 653 keV. The lifetime value for this transition in the literature is 13.7(17) ps [193].

This RDDS lifetime determination method requires to know the number of nuclei of interest detected in PRISMA for the normalization, in the present case, i.e. for the ^{72}Zn isotope, it has been calculated integrating directly the corresponding peak in the mass spectrum. The obtained number of ions for each target-degrader distance are indicated in Table 4.19. Figure 4.41 shows the Doppler corrected γ-ray spectra of ^{72}Zn in the energy region of interest, corresponding to the $4^+ \to 2^+$ and $2^+ \to 0^+$ transitions, and for the different distances. The area of the unshifted and shifted peaks as well as the ratio R defined in eq. 4.11 as $I_u/(I_u + I_s)$ for the $2^+ \to 0^+$ transition for the standard RDDS method and as in eq. 4.12 as $I_u/(N_0)$ for the new approach are shown in Table 4.20.
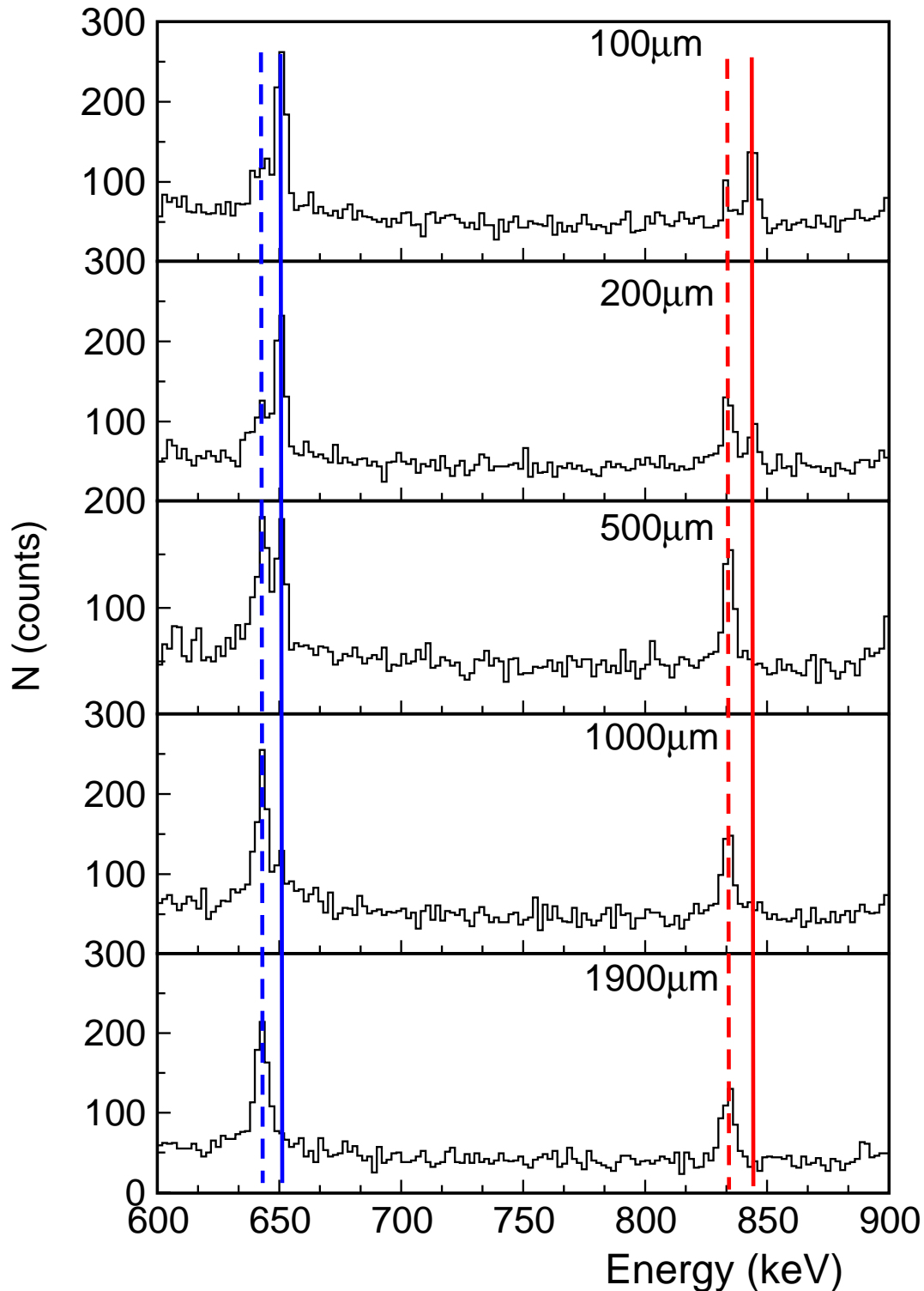
Figure 4.41: Doppler corrected γ-ray spectra for ^{72}Zn expanded to the energy region of interest, around the $2^+ \rightarrow 0^+$ and $4^+ \rightarrow 2^+$ transitions at 653 and 847 keV respectively, for the different distances. The blue and red lines correspond respectively, to the $2^+ \rightarrow 0^+$ and $4^+ \rightarrow 2^+$ transitions, the solid line plotted corresponds to the unshifted peak and the dashed line to the shifted peak.

Table 4.19: Number of ^{72}Zn nuclei detected in PRISMA (N_0) for each distance (d_f).

d (μm)	d_f (μm)	N_0
100	112.01	55454(235)
200	211.97	43401(208)
500	512.00	49351(222)
1000	1012.01	51487(227)
1900	1912.00	41625(204)

Table 4.20: Experimental values of the shifted peak areas (I_s), the unshifted peak areas (I_u) and R ($R_{conv} = \frac{I_u}{I_u+I_s}$) for the $2^+ \to 0^+$ transition, for the standard RDDS and for the new approach ($R_{new} = \frac{I_u}{N_0}$), as a function of the distance d_f.

E = 653 keV $2^+ \to 0^+$					
d (μm)	d_f (μm)	I_s (counts)	I_u (counts)	R_{conv}	R_{new}
100	112.01	141(28)	523(54)	0.79(11)	0.009(1)
200	211.97	126(10)	417(17)	0.77(4)	0.0096(4)
500	512.00	276(40)	269(37)	0.49(8)	0.0055(8)
1000	1012.01	404(50)	102(24)	0.20(5)	0.0020(5)
1900	1912.00	423(23)	28(8)	0.06(2)	0.0007(2)

Finally the determination of the lifetime is done through an exponential fit of the above mentioned ratios. Nevertheless, since it has been observed a sizeable population of the 4^+ state in this nucleus, is necessary to take into account the feeding of the 2^+ state, through the $4^+ \to 2^+$ transition with 847 keV energy. The lifetime of the 4^+ state is not well know and, therefore, the RDDS analysis for the 847 keV transition, has been performed as well. The expression employed in the fit to determine the lifetime of the 4^+ state has been the following:

$$R_1(x) = Aexp^{(-x/B)} \tag{4.31}$$

where $B = (\beta c t_{1/2})/ln2$ being $t_{1/2}$ the half life of the excited state.

The expression employed in the fit corresponding to the 2^+ state, determined using the Bateman equations [194], is the following:

$$R_2(x) = A(\frac{C}{B-C})(exp^{(-x/B)} - exp^{(-x/C)}) + Dexp^{(-x/C)} \tag{4.32}$$

where $C = (\beta c t_{1/2})/ln2$ being $t_{1/2}$ the half life of the excited state.

Figure 4.42 shows the exponential fits performed for the lifetime determination with the two RDDS approaches. As the lifetime of the $4^+ \rightarrow 2^+$ transition is very short, the longer distances are not plotted since the information of the exponential decay is coming from the shorter distances (see Figure 4.41). The values obtained for the half file, the lifetime and the reduced transition probability of the $2^+ \rightarrow 0^+$ transition at 653 keV, obtained with both RDDS approaches are summarized in Table 4.21. As for the ^{76}Ge isotope, the agreement between the known value and the lifetime obtained with both RDDS approaches let us state that the RDDS technique, using the normalization to the number of ions detected in PRISMA, is as least as good as the standard approach.
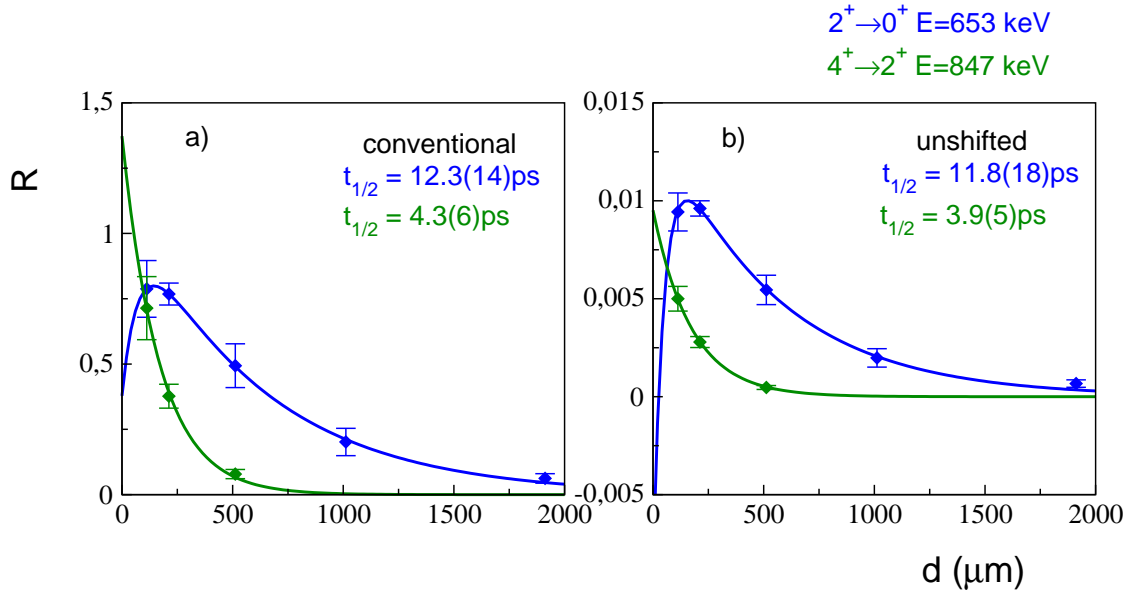

Figure 4.42: Fit of the $4^+ \rightarrow 2^+$ and $2^+ \rightarrow 0^+$ transitions with 847 keV and 653 keV respectively, considering the data obtained a) with the standard ratio for the RDDS method b) when only the unshifted peak, normalized to the number of ions detected in PRISMA, is considered.

Table 4.21: Half life ($t_{1/2}$), lifetime (τ) and reduced transition probability ($B(E2 \downarrow)$) for the $2^+ \rightarrow 0^+$ ^{72}Zn transition at 653 keV.

	E = 653 keV $2^+ \rightarrow 0^+$		
Method	$t_{1/2}$ (ps)	τ (ps)	$B(E2 \downarrow)$ ($e^2 fm^4$)
literature	13.7(17)	19.8(24)	348(42)
conventional	12.3(14)	17.1(19)	402(45)
unshifted	11.8(18)	17.0(19)	405(45)

4.7.4 Lifetime determination for the ^{71}Cu isotope

The nucleus ^{71}Cu is a neutron-rich isotope already six neutrons away from the last stable copper isotope. The accessibility to this nucleus, specially for in-beam experiments is difficult and, therefore, there is scarce knowledge about its structure. In fact, this is the first time the lifetime of the $7/2^-$ excited state, lying at 981 keV of excitation energy, has been experimentally determined.

For the lifetime analysis of the $7/2^-$ state only three target-degrader distances have been used: $100\mu m$, $200\mu m$, and $500\mu m$. The spectrum of the larger distances (1000 μm and 1900 μm) is irrelevant for the lifetime determination, as most of the information of the exponential decay is coming from the short distances. Besides, they are the plunger distances with less number of events collected, therefore, it has been decided not to include these data sets for this particular lifetime analysis. Figure 4.43 shows the spectra for the ^{71}Cu expanded in the energy region of interest and for the three relevant distances. The areas of the unshifted and shifted peaks (I_u and I_s) were calculated both with a Gaussian fit and by the integration of the counts in the peak region. The results obtained with both methods are compatible; therefore, only those coming from the integrals are reported on Table 4.22. The new approach for the RDDS fit, with the normalization to the number of ions detected in PRISMA, has been used for the lifetime determination since the statistics for the shifted peak is quite low and introduces large uncertainties. The number of ^{71}Cu nuclei detected in PRISMA for each distance is listed in Table 4.23. For this transition, the fit has been done in the same way as the $4^+ \rightarrow 2^+$ transition of the ^{76}Ge, since no feeding is expected from above, using eq. 4.32 but fixing the parameter: $A = 0$.

Table 4.22: Experimental values of the shifted peak areas (I_s), the unshifted peak areas (I_u) and R (R $= \frac{I_u}{N_0}$) for each distance d_f.

E = 981 keV $7/2^- \rightarrow 3/2^-$				
d (μm)	d_f (μm)	I_s (counts)	I_u (counts)	R
100	112.01	0(0)	41(13)	0.00244(77)
200	211.97	8(7)	30(12)	0.00225(90)
500	512.00	13(9)	15(10)	0.00102(68)

Table 4.23: Number of ^{71}Cu nuclei detected in PRISMA (N_0) for each distance.

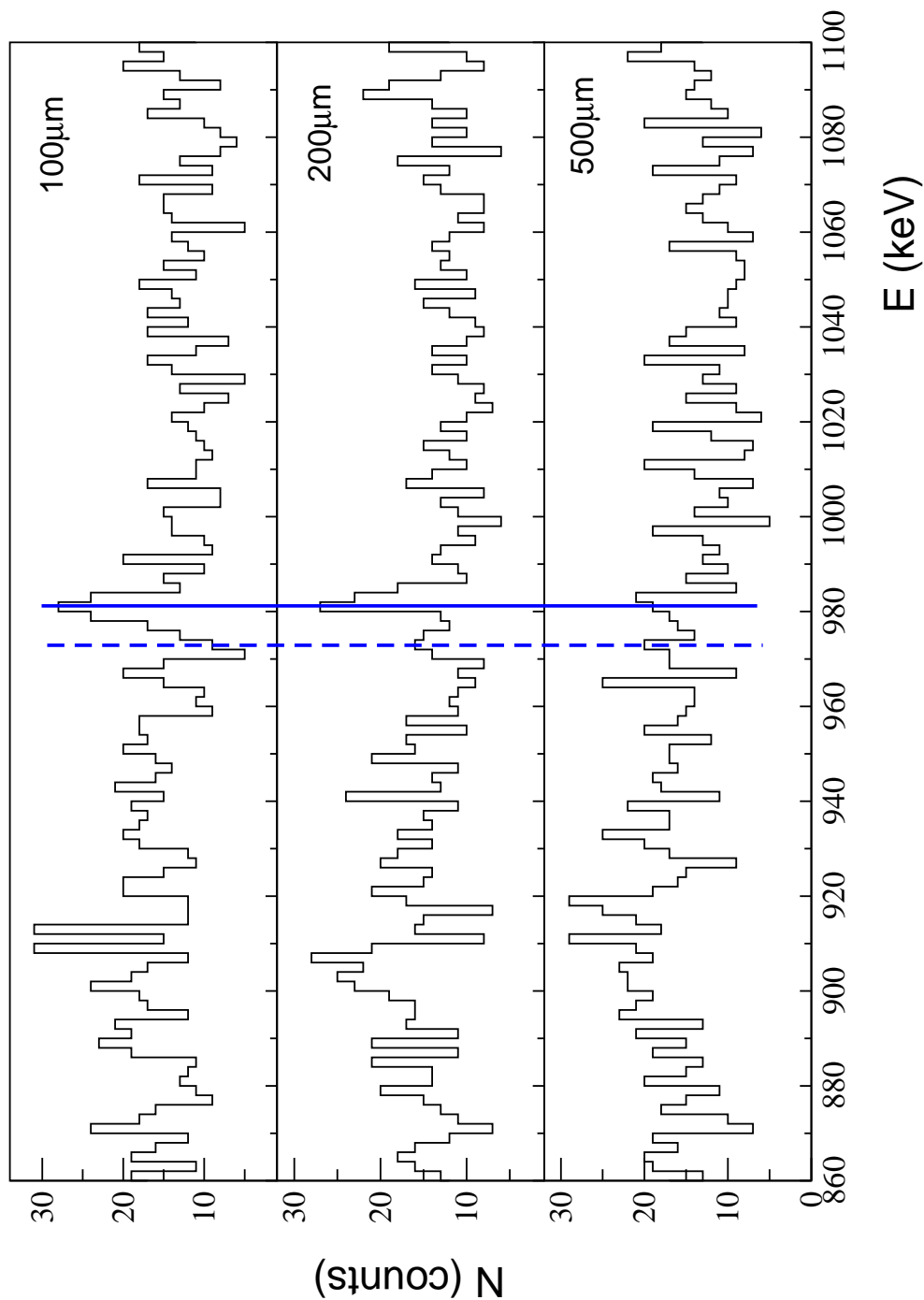| d (μm)	d_f (μm)	N_0 (counts)
100	112.01	16829(130)
200	211.97	13322(115)
500	512.00	14771(122)

Figure 4.43: Doppler corrected γ-ray spectra for ^{71}Cu expanded in the region of interest, i.e. of the $7/2^- \rightarrow 3/2^-$ transition with 981 keV for the used distances. The plotted solid line in blue marks the unshifted peak and the dashed line the shifted peak.

The obtained a value for the lifetime of the $7/2^- \to 3/2^-$ state at 981 keV for the ^{71}Cu is $\tau = 20(16)$ ps, thus with relative uncertainty of the lifetime is of 79%. The reduced transition probability obtained by using eq. 4.2 is $B(E(2 \downarrow))=45(36)$ e^2fm^4. The values are summarized in Table 4.24 and the corresponding fit is shown in Fig. 4.44.
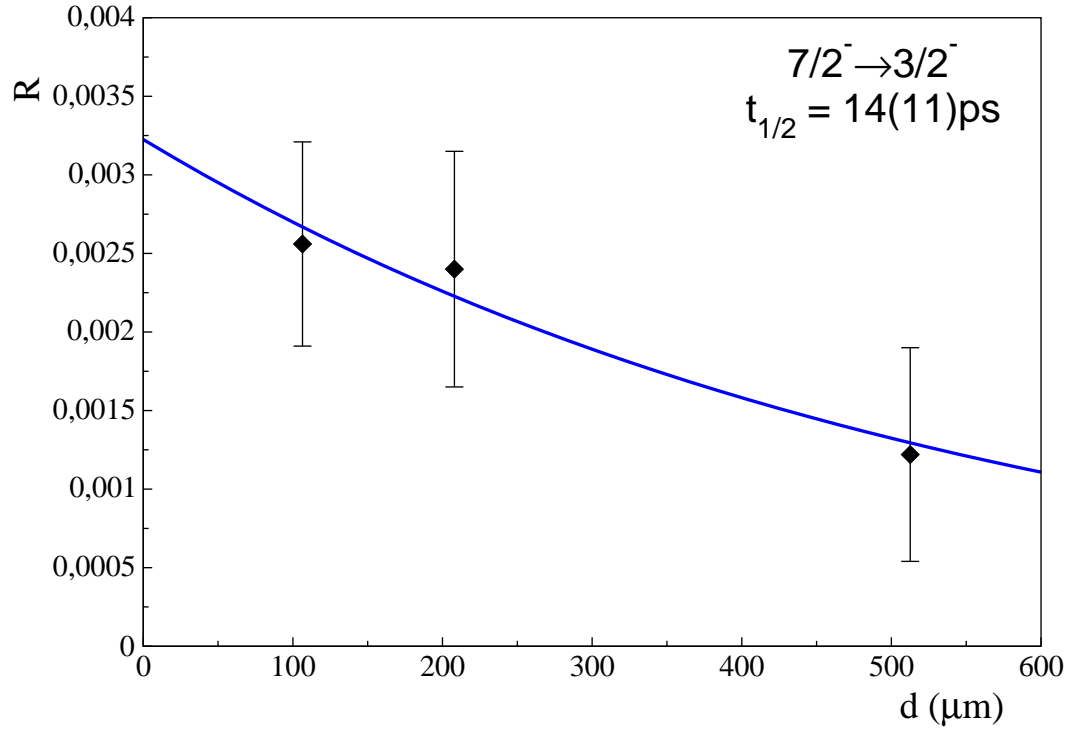

Figure 4.44: Fit for the lifetime determination for the $7/2^- \to 3/2^-$ transition with 981 keV. The new approach, where the unshifted peak is normalized to the number of ions detected in PRISMA, has been used.

Table 4.24: Half life ($t_{1/2}$), lifetime (τ) and reduced transition probability ($B(E2 \downarrow)$), determined from the $7/2^- \to 3/2^-$ transition with 981 keV energy in ^{71}Cu.

E = 981 keV $7/2^- \to 3/2^-$		
Method	$t_{1/2}$ (ps)	τ (ps)	$B(E2 \downarrow)$ (e^2fm^4)
unshifted	14(11)	20(16)	45(36)

4.8 Discussion

As it was mentioned at the beginning of this chapter, with the present study we intend to contribute to the understanding of the nuclear structure in neutron-rich nuclei in the vicinity of Z=28 and N between 40 and 50. This understanding includes as well how the collectivity evolves adding protons and neutrons to the quasi-double magic nucleus ^{68}Ni. In the discussion of the results I will resort to the Spherical Shell-Model calculations to perform the comparison of the results with nuclear structure calculations. The early Shell-model was hard to reconcile with the idea of the nuclear collectivity and nuclear deformation, the increases in tractable dimensionalities were insufficient to promote the Shell-model to the status of a general description of the nuclear structure [195]. Since the 90's there has been an impressive progress in the Shell-model approach due to the appearance of the large-scale Shell-model (LSSM) calculations [196, 197]. One good example is the fp-shell, where the middle of the $f_{7/2}$ shell, nuclei show collective properties similar to those observed in heavier nuclei, such as rotational-like bands, band termination, and backbending phenomena. In this region it is possible to describe deformed nuclei within both the mean-field and the large-scale Shell-model descriptions [198].

Shell-model calculations in the neighbourhood of ^{78}Ni have been until recently a challenge, due to the large space required. In particular, for the copper isotopic chain [199, 200]. It has been shown that the Shell-model calculations using the $f_{5/2}$, $p_{3/2}$, $p_{1/2}$ and $g_{9/2}$ neutron orbits (the fpg valence space) and realistic interactions, can reproduce rather well the level schemes of Cu isotopes as well as their magnetic moments, but underestimates the BE(2) [199,201]. To reproduce the larger quadrupole collectivity in this mass region, the inclusion of the neutron $d_{5/2}$ orbital is needed. This can be explained in terms of the quasi-SU3 approximate symmetry: The deformation can be generated by the interplay between the quadrupole force and the central field in the subspace consisting on the lowest $\Delta j = 2$ orbitals of a major shell [202]. Recently a new interaction, with the appropriated model space for neutrons, and denoted as LNPS, has been proposed [208]. This interaction is based on several sets of realistic two-body matrix elements (TBME). Its main building blocks being the following:

- The last evolution of the Kuo-Brown interaction (KB3gr) for the pf shell [203].

- The renormalized G matrix of Ref. [204] with the monopole corrections introduced in Ref. [207], for the remaining matrix elements involving the $f_{7/2}$, $p_{3/2}$, $f_{5/2}$, $p_{1/2}$, and $g_{9/2}$ neutron orbits.

- The G matrix based on the Kahana-Lee-Scott potential [206] for the matrix elements involving the $d_{5/2}$ orbit. This potential was successfully employed in the definition of the recent SDPF-U Shell-model interaction [207] for the description of neutron-rich sd-pf nuclei.

In this context, the Shell-model calculations performed by K. Sieja and collaborators [200], have considered an enlarged valence space that contains the pf-shell orbitals for protons and $f_{5/2}$, p, $g_{9/2}$ and $d_{5/2}$ orbitals for neutrons. The calculations have been performed using ANTOINE code [195], allowing for maximally 8p-8h excitations with respect to proton $f_{7/2}$ and neutron $g_{9/2}$ orbitals. The effective interaction starts with the same sets of two-body matrix elements as used in Ref. [208]. However further monopole changes to constrain the proton gap evolution from ^{68}Ni to ^{78}Ni have been introduced [199]. Two

experimental constraints have been taken into account in the monopole corrections of the interaction: the sizes of the gaps at N=40 and at N=50. While the size of the proton gap in ^{68}Ni is well established (5.8 MeV from binding energy differences), the corresponding gap in ^{78}Ni has been inferred indirectly from the recently measured $B(E2 \downarrow) : 2^+ \rightarrow 0^+$ transition rate in ^{80}Zn [209]. The calculated correlated gaps amount to 5.7 and to 5.0 MeV in ^{68}Ni and ^{78}Ni, respectively. Besides, fine changes in the multipole part of the interaction have been performed, which however leave unchanged the physics of the island of inversion studied in [208]. The effective charges used for the B(E2) calculations in the region have been: $e_n = 0.5e$ and $e_p= 1.5e$. In Table 4.25 and in Table 4.26 are shown the occupation numbers in the wave function of low-lying states in ^{71}Cu for neutrons and protons, respectively. Figure. 4.45 shows the occupation numbers in the wave function of low-lying states in ^{71}Cu for protons and neutrons via Shell-model calculations.

Table 4.25: Neutron occupation numbers in the wave function of low-lying states in ^{71}Cu.

state	$p_{3/2}$	$f_{5/2}$	$p_{1/2}$	$g_{9/2}$	$d_{5/2}$
$3/2^-$ (GS)	3.94	5.40	1.50	2.83	0.32
$7/2^-$ (1041 keV)	3.94	5.26	1.25	3.18	0.38
$7/2^-$ (1336 keV)	3.94	5.08	1.32	3.34	0.32

Table 4.26: Proton occupation numbers in the wave function of low-lying states in ^{71}Cu.

state	$f_{7/2}$	$p_{3/2}$	$f_{5/2}$	$p_{1/2}$
$3/2^-$ (GS)	7.59	0.91	0.36	0.14
$7/2^-$ (1041 keV)	7.45	0.73	0.64	0.19
$7/2^-$ (1336 keV)	7.39	0.68	0.80	0.13

The LSSM calculation foresees two low lying $7/2^-$ states in ^{71}Cu, in good agreement with our knowledge of it structure [149, 152]. As it is possible to see in Fig. 4.46, the calculated excitation energies are in fair agreement with the experimental ones. Nevertheless there are some particularities that required a extended discussion. The wave function, of the ^{71}Cu $7/2^-$ states has some particularity for the proton occupancy, There is a trend in the occupancy of the $p_{3/2}$ and $f_{5/2}$ orbitals. While the $p_{3/2}$ occupation number decreases as we go to the higher excitation energy state, the corresponding $f_{5/2}$ increases. The inclusion of the $d_{5/2}$ in the valence space for neutrons, the SU3 partner of the $f_{9/2}$, should enhance the quadrupole moment improving the description of the $B(E2 \downarrow)$ values.

Table 4.27 shows the energy and the reduced transition probability values of the $7/2^-$ excited states in ^{71}Cu obtained in the present measurement (exp), in a previous measurement performed by I. Stefanescu et al [149] and the ones obtained within the theoretical Shell-model calculations (th) of ref [200].

As it can be seen in Table 4.27 the reduced transition probability measured experimentally for both $7/2^-$ states (at 981 and 1,041 keV) is quite well reproduced within

the Shell-model calculations performed by K. Sieja [200]. The $B(E2\downarrow)$ values obtained, suggest a different collective character of both states coming from the mixing of the protons in the $p_{3/2}$ and $f_{5/2}$ orbitals and from the inclusion of the $d_{5/2}$ orbital in the neutron part of the wave function that leads to an enhancement of the quadrupole contribution of the $g_{9/2}$ and the $d_{5/2}$ orbitals not considered in previous Shell-model calculations. Nevertheless, the calculated excitation energies of both levels is inverted in the Shell-model calculations with respect to the experimental findings.

We expect that the valuable information found in the present measurement that helped to identify unambiguously the nature of both low lying states, will contribute to further development if the effective interaction necessary to have precise calculation in the vicinity of the double magic ^{78}Ni.
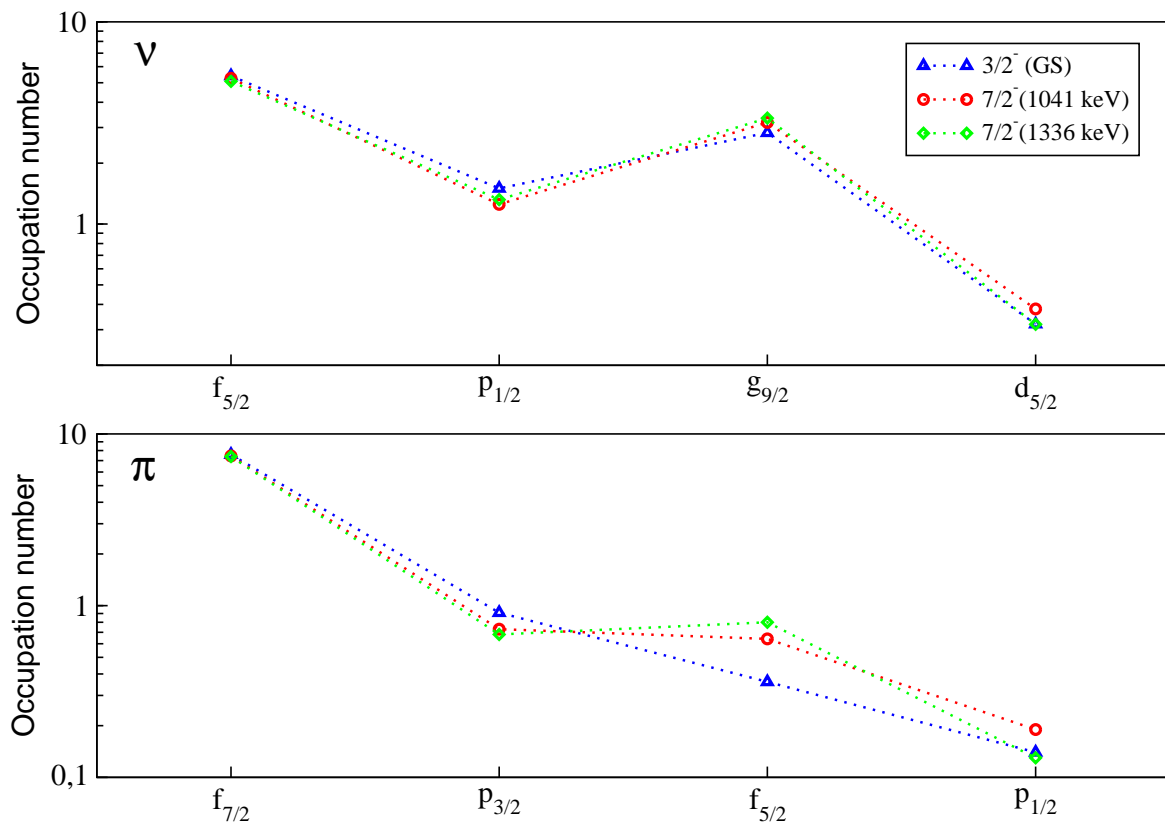

Figure 4.45: Proton and neutron occupation numbers in the wave function of low-lying states in ^{71}Cu.
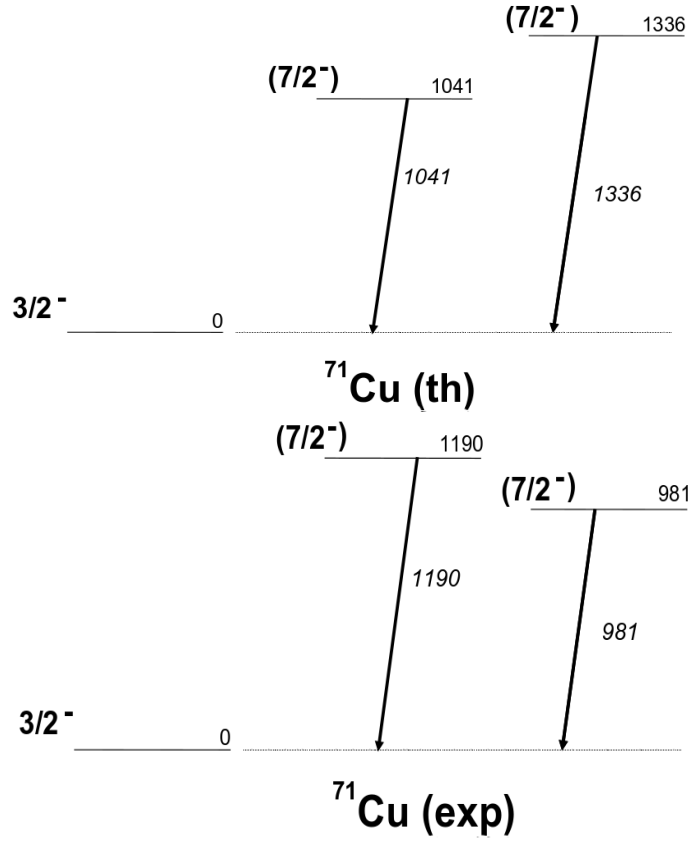
Figure 4.46: Low-lying excited levels in ^{71}Cu obtained through Shell-model calculations performed by K. Sieja et collaborators (top) [200] and in the present experiment (bottom).

Table 4.27: Energy and reduced transition probability values of the $7/2^-$ excited states in ^{71}Cu obtained in the present measurement (exp) and with the theoretical Shell-model calculations (th) of ref [200].
[1] corresponds to the experimental values measured by I. Stefanescu et al [149].

state	E (keV) th	E (keV) exp	$B(E2\downarrow)$ (e^2fm^4) exp	$B(E2\downarrow)$ (e^2fm^4) th
first $7/2^-$	1,041	1,190[1]	187(21)[1]	157.1
second $7/2^-$	1,336	981	45(36)	40.0

142

Lifetime measurement of neutron-rich nuclei in the region of the double magic ^{78}Ni with the γ-tracking AGATA demonstrator.

Conclusions

Different configurations have been studied for the Ge array of the DESPEC experiment. Our study has shown that the ones based on the technical proposal do not provide good enough specifications in terms of peak efficiency and P/T respect to what is currently obtained with present setups as for example the RISING array. Attempting to add imaging capabilities, new geometries (based on planar detectors) have been proposed. However, it has been demonstrated that they do not reach the values od efficiency needed for the Ge array of the DESPEC experiment. Therefore, a new configuration has been proposed involving AGATA aiming to profit from both, the high efficiency of AGATA and the high position resolution of planar detectors. The particular configuration studied is based on the coupling of the AGATA S2' configuration, designed to be installed in GSI along the current year, with a set of planar detectors. The study performed shows that altough no gain in efficiency is achieved, an improvement in P/T is obtained by using the imaging capabilities of the mixed array.

To this task contributes the background-suppression algorithm developed for the AGATA array. At the current status of the algorithm, the analysis performed clearly assigns the γ rays to the correct sources. The γ rays coming from sources such as beam-dump, beam-tracking detectors or primary reaction target, that contribute to the background of the measurement, can be identified using the present method and rejected by background subtraction techniques. On an event-by-event basis, this algorithm represents a contribution to the background rejection methods in development improving the peak-to-total ratio by a factor between 3 and 3.5. A further step in the algorithm development is foreseen, using the data provided by a larger AGATA detector array, including events with three or more interaction points. The algorithm has been also optimized for the proposed configuration of the Ge array for DESPEC showing a better source identification when only events having one interaction in planar and one in AGATA, PC events, are considered. Therefore, an array composed of AGATA and planar detectors presents better capabilities for imaging purposes due to the better position resolution of planar detectors.

In the path to a full development of imaging with Ge detectors, the Compton imaging algorithm developed for the Ge array of the DESPEC experiment has shown tobe able to reconstruct quite well the path of the photons inside the detector. Reconstruction efficiencies values show the good performance of the imaging algorithm. At its current status, the algorithm is able to order accurately the interaction points of the γ rays impinging the detector. On an event-by-event basis, the algorithm contributes to background rejection improving the P/T ratio.

The lifetime of the $7/2^-$ exited state at 981 keV of the ^{71}Cu isotope has been measured experimentally using the AGATA Demonstrator coupled to the PRISMA spectrometer and the plunger setup through the Recoil Distance Doppler Shift Method (RDDS). This is the

first time this setup has been used coupled together in an experimental measurement. The measured value for the reduced transition probability ($B(E2 \downarrow)$=48(18) e^2fm^4) is in good agreement with the Shell-model theoretical calculations in the very large $fpgd$ valence space using the LNPS interaction performed by K. Sieja ($B(E2 \downarrow)$=40 e^2fm^4). The $B(E2 \downarrow)$ values obtained, suggest a different collective character of the two $7/2^-$ exited states (at 981 and 1,041 keV, respectively) coming from the mixing of the protons in the $p_{3/2}$ and $f_{5/2}$ orbitals and from the increasing occupation of the $g_{9/2}$ orbital in the neutron part of the wave function that leads to an enhancement of the quadrupole contribution of the $g_{9/2}$ and the $d_{5/2}$ orbitals not considered in previous Shell-model calculations.

Bibliography

Bibliography

[1] S. Wan, et al., Eur. Phys. J. A 6 (1999) 167.

[2] J. Eberth et al., Prog. Part. Nucl. Phys. 60 (2008) 283.

[3] A. Johnson, et al., Phys. Lett. B 34 (1971) 605.

[4] R. Beetz, et al., Nucl. Instr. and Meth. A 145 (1977) 353.

[5] R. Julin, Gamma-Ray and Conversion Electron Spectroscopy of Exotic Heavy Nuclei. The euroschool Lectures on Physics with Exotic Beams, Vol I (2004).

[6] J.F. Sharpey-Schafer et al., Prog. Part. Nucl. Phys. 21 (1988) 293.

[7] P.J. Twin et al., Workshop on Nuclear Structure at High Spin, Riso, Dinamarca, 1981, p.135.

[8] P.J. Twin et al., Proc. Conf. On Instr. For Heavy Ion Nucl. Res., in: D. Schapira (Ed.) Nucl. Sci. Research Conf. Series, vol 7, Harwood, p. 231.

[9] R.M. Diamond et al., Proc. Conf. On Instr. For Heavy Ion Nucl. Res. in: D. Schapira (Ed.) Nucl. Sci. Research Conf. Series, vol 7, Harwood, p. 259.

[10] P.J. Twin, Phys. Rev. Lett. 57 (1986) 811.

[11] C. Rossi-Alvarez, Nucl. Phys. News Europe 3, (1993) 10.

[12] http://npgroup.pd.infn.it/GASP/

[13] P.J. Nolan et al., Nucl. Phys. A 520 (1990) 657.

[14] F.A. Beck et al., Procedings of the Internacional Conference on Nucl. Struct. At High Ang. Momentum, Ottawa, 1992, p. 364.

[15] J. Gerl, R.M. Lieder (Eds.). Upgrading to Euroball III, GSI Report, 1992.

[16] J. Simpson, Z. Phys. A 358 (1997) 139.

[17] http://euroball.lnl.infn.it/EBcontents/menu.html

[18] http://www-gam.lbl.gov/

[19] T.K. Alexander, J.S. Foster, Adv. Nucl. Phys. 10 (1978) 197.

[20] P. Petkov et al., Nucl. Inst. and Meth. A 431 (1999) 208.

[21] P. Petkov et al., Nucl. Inst. and Meth. A 560 (2006) 564.

[22] A. Dewald, S. Harissopulos, and P. Brentano, Z. Phys. A 334 (1989) 163.

[23] E. Farnea et al., Nucl. Instr. and Meth. A 400 (1997) 87.

[24] http://www.lnl.infn.it

[25] N. Marginean et al., Phys. Rev. C 72 (2005) 014302.

[26] D. Seweryniak, Bull. Am. Phys. Soc. 43 (1998) 1545.

[27] C.N. Davids et al., Phys. Rev. Lett. 80 (1998) 1849.

[28] F.A. Beck et al., Proc. of the Conf. on Physics from Large γ-ray Detector Arrays (Berkeley, 1994) LBL35687, CONF 940888, UC 413, p. 154.

[29] J. Eberth et al., Prog. Part. Nucl. Phys. 28 (1992) 495.

[30] J. Eberth et al., Nucl. Instr. and Meth. A 369 (1996) 135.

[31] J. Simpson et al., Acta Physica Hungarica, New Series, Heavy Ion Physics 11 (2000) 159.

[32] F. Azaiez et al., Nucl. Phys. A 654 (1999) 1003c.

[33] D. Habs et al., Prog. Part. Nucl. Phys. 38 (1997) 111.

[34] J. Eberth et al., Prog. Part. Nucl. Phys. 46 (2001) 389.

[35] W. Mittig et al, J. Phys. G: Nucl. Part. Phys. 24 (1998) 1331.

[36] http://www.ganil-spiral2.eu/leganil

[37] http://www94.web.cern.ch/ISOLDE/REX-ISOLDE/index.html

[38] D. Bazzacco. Workshop on GRETA Physics, Berkeley, LBNL-41700 CONF-980228.

[39] Zs. Podolyak et al., LNL Annual Report 1997, LNL-INFN (1998) 169.

[40] Th. Kröll et al., Nucl. Instr. and Meth. A 586 (2008) 421.

[41] http://radware.phy.ornl.gov/greta/news1.html

[42] http://www.-w2k.gsi.de/agata/

[43] J. Simpson, Journal of Physics: Conference Series 41 (2006) 72.

[44] J. Simpson, J. Nyberg, W. Korten (Eds.), AGATA Advanced Gamma Tracking Array Technical Design Report /http://npg.dl.ac.uk/agata_acc/publications_documentation/TDR_EUJRA.pdfS, 2008.

[45] N. Warr, et al., Eur. Phys. J. A 20 (2004) 65.

[46] M. Dimmock, AGATA, Detector characterization and Pulse Shape Analysis, AGATA Collaboration.

[47] R. Venturelli et al., LNL Annual Report 2003, LNL-INFN (2004) 220.

[48] D. Bazzacco et al., LNL Annual Report 2000, LNL-INFN (2001) 166.

[49] Th. Kröll and D. Bazzacco, Nucl. Instr. and Meth. A 463 (2001) 227.

[50] Th. Kröll et al., LNL Annual Report 1997, LNL-INFN (1998) 171.

[51] L. Nelson, et al., Nucl. Instr. and Meth. A 573 (2007) 153.

[52] B. Bruyneel, Ph.D. Thesis, University of Cologne (2006).

[53] http://mgs2005.in2p3.fr/Mgs.php.

[54] A. Hernandez-Prieto, Master Thesis, Universidad Complutense de Madrid, 2011.

[55] C. Domingo-Pardo et al., Nucl. Instr. and Meth. A 643 (2011) 79.

[56] J. Eberth, From Ge(Li) detectors to gamma-ray tracking arrays AGATA, AGATA Collaboration.

[57] I.Y. Lee, Nucl. Instr. and Meth. A 422 (1999) 195.

[58] http://www.nist.gov/srd/atomic.cfm.

[59] J. Van der Marel et al., Nucl. Instr. and Meth. A 437 (1999) 538.

[60] L. Milechina et al., Nucl. Instr. and Meth. A 508 (2003) 394.

[61] E. Farnea et al., Nucl. Inst. and Meth. A 621 (2010) 331.

[62] A. Lopez-Martens, Improvements to the Orsay forward tracking algorithm, AGATA Collaboration.

[63] A. Lopez-Martens et al., Nucl. Instr. and Meth. A 533 (2004) 454.

[64] S. Akkoyun et al., Nucl. Instr. and Meth. A 668 (2012) 26.

[65] http://www.gsi.de/

[66] http://www.gsi.de/fair/reports/btr.html

[67] Z. Podoliak, Acta. Phys. Pol. B 41 (2010) 493.

[68] http://personal.ph.surrey.ac.uk/ ∼ phs1zp/Home.html

[69] www-win.gsi.de/fair-eoi/PDF/TDR_PDF/TDR_Super-FRS_pdf

[70] H. Geissel et al, Nucl. Instr. and Meth. B 70 (1992) 286.

[71] cdsweb.cern.ch/record/611102/files/p7.pdf

[72] D.J. Morrissey and B.M. Sherill, In-flight Separation of Proyectile Fragments, Lect. Notes Phys. 651 113-135 (2004).

[73] T.M.J Symons et al., Phys. Rev. Lett. 42 (1979) 40.

[74] I. Tanihata et al., Phys. Lett. B 160 (1985) 380.

[75] T. Kobayashi et al., Phys. Rev. Lett. 60 (1988) 2599.

[76] H.J. Wollersheim et al., Nucl. Inst. and Meth. A 537 (2005) 637.

[77] http://www-linux.gsi.de/∼wolle/EB_at_GSI/RISING/rising.htm

[78] L. Caceres et al., Acta Phys. Pol. B 38 (2007) 1271.

[79] A. Garnsworthy et al., Acta Phys. Pol. B 38 (2007) 1256.

[80] S. Steer et al., Acta Phys. Pol. B 38 (2007) 1283.

[81] T. Saito et al., submitted to Phys. Rev. C.

[82] A. Bürger et al., Phys. Lett. B 622 (2005) 29.

[83] R. Anhold et al., Phys. Rev. Lett. 53 (1984) 234.

[84] R. Anhold, et al., Phys. Rev. A 33 (1986) 2270.

[85] R. Holzmann et al., GSI Annual Report, 1992, p. 48.

[86] www.2.ph.ed.ac.uk/∼td/AIDA/

[87] www.ires.in2p3.fr/ires/workshops/eurotrans/ITC7_S_Gorlychev.pdf

[88] B. Rubio. NUSTAR07.

[89] J. Gerl, W. Korten (Eds.), AGATA Technical Proposal, GSI, Darmstadt, 2001.

[90] M.A. Deleplanque et al., Nucl. Instr. and Meth. A 430 (1999) 292.

[91] G.J. Schmidt et al., Nucl. Instr. and Meth. A 430 (1999) 69.

[92] R.W. Tood, J.M. Nightingale, D.B. Everett, Nature 251 (1974) 132.

[93] V. Shoenfelder et al., Nucl. Instr. and Meth. A 107 (1973) 385.

[94] E.A. Wulf et al., IEEE Trans. Nucl. Sci, NS-49 (2002) 1876.

[95] R.A. Kroeger et al., IEEE Trans. Nucl. Sci, NS-49 (2002) 1887.

[96] Y. Du et al., Nucl. Instr. and Meth. A 457 (2001) 203.

[97] F. Recchia, Ph.D. Thesis, Universita degli Studi di Padova, 2008.

[98] Y. Du, Z. He, G.F. Knoll, D.K. Wehe, W. Li, Evaluation of a Compton scattering camera using 3D position-sensitive CdZnTe detectors, in: R.B. James, R.C. Schirato (Eds.), Proc. SPIE Vol. 3768, p. 228-238, Hard X-Ray, Gamma-Ray, and Neutron Detector Physics, Ralph B. James; Richard C. Schirato; Eds., Vol. 3768 of Presented at the Society of Photo-Optical Instrumentation Engineers (SPIE) Conference, 1999, pp. 228–238.

[99] A. Khaplanov et al., Nucl. Inst. and Meth. A 592 (2008) 325.

[100] C.S. William et al., IEEE Trans. Nucl. Sci. 57 (2010) 860.

[101] F. Recchia et al., Nucl. Instr. and Meth. A 604 (2009) 555.

[102] I. Piqueras et al., Nucl. Inst. and Meth. A 525 (2004) 275.

[103] I. Piqueras et al., Nucl. Inst. and Meth. A 516 (2004) 122.

[104] A. Algora. Simulations for the HISPEC/DESPEC Collaboration.

[105] A.F. Bielajew. Fundamentals of the Monte Carlo method for neutral and charged particle transport. The University of Michigan, Ann Arbor (2001).

[106] L. Lyons. Statistic for nuclear and particle physicist. Cambridge University Press.

[107] http://geant4.web.cern.ch/geant4/

[108] S. Agostinelli et al., Nucl. Inst. and Meth. A 506 (2003) 250.

[109] Evaluated Atomic Data Library, https://wci.llnl.gov/codes/tart/atomicparameters.html

[110] Evaluated Electrons Data Library, https://wci.llnl.gov/codes/tart/electrons.html

[111] Evaluated Photons Data Library, https://wci.llnl.gov/codes/tart/photons.html

[112] J. Baro et al., Nucl. Inst. and Meth. B 100 (1995) 31.

[113] S. Hurtado et al., Nucl. Inst. and Meth. A 518 (2004) 764.

[114] C. Dörr et al., Nucl. Inst. and Meth. A 513 (2003) 593.

[115] C. Domingo, MC Simulations for the PreSPEC campaign of AGATA at GSI, AGATA Week, Legnaro (2010).

[116] F.C.L. Crespi et al., Nucl. Inst. and Meth. A 570 (2007) 459.

[117] A. Ataç et al., Nucl. Phys. A 607 (2009) 554.

[118] J. Ljungvall and J. Nyberg, Nucl. Inst. and Meth. A 546 (2005) 553.

[119] F. Zocca, A. Pullia, and G. Pascovici, IEEE Trans. Nucl. Sci. NS-55 (2008) 695.

[120] M. Doncel et al., Nucl. Inst. and Meth. A 622 (2010) 614.

[121] V.T. Jordanov and G.F. Knoll, Nucl. Inst. and Meth. A 345 (1994) 337.

[122] M. Doncel et al., Nucl. Inst. and Meth. A 648 (2011) S131.

[123] M.G. Mayer, Phys. Rev. 75 (1949) 1969; O. Haxel, J.H.D. Jensen, and H.E. Suess, Phys. Rev. 75 (1949) 1766; M.G. Mayer, Phys. Rev. 78 (1950) 16.

[124] C. Thibault et al., Phys. Rev. C 12 (1975) 644.

[125] R. Klapisch et al., Phys. Rev. Lett. 31 (1973) 118.

[126] X. Campi et al., Nucl. Phys. A 251 (1975) 193.

[127] G. Audi et al., Nucl. Phys. A 729 (2003) 337.

[128] I. Hamamoto et al., Nucl. Phys. A 683 (2001) 255.

[129] T. Otsuka et al., Phys. Rev. Lett. 95 (2005) 232502.

[130] T. Otsuka et al., Prog. Theor. Phys. Supp. 146 (2002) 6.

[131] T. Otsuka et al., Phys. Rev. Lett. 87 (2001) 082502.

[132] O. Sorlin et al., Prog. Part. Nucl. Phys. 61 (2008) 602.

[133] M. Honma et al., Phys. Rev. C 69 (2004) 034335.

[134] H. Grawe et al., Eur. Phys. J. A 25 (2005) 357.

[135] O. Perru et al., Phys. Rev. Lett. 96 (2006) 232501.

[136] O. Sorlin et al., Phys. Rev. Lett. 88 (2002) 092501.

[137] R. Broda et al., Phys. Rev. Lett. 74 (1995) 868.

[138] M. Hannawald et al., Phys. Rev. Lett. 82 (1999) 1391.

[139] J. Ljungvall et al., Phys. Rev. C 81 (2010) 061301.

[140] W. Rother et al., Phys. Rev. Lett. 106 (2011) 022502.

[141] L.P. Ekstrom and J. Lyttkens-Linden, Nucl. Data Sheets 67, 579 (1992).

[142] C.J. Lister et al., Phys. Rev. Lett. 59 (1987) 1270.

[143] A.M. Oros-Peusquens and P.F. Mantica, Nucl. Phys. A 669 (2001) 81.

[144] A. Ansari and P. Ring, Phys. Rev. C 74 (2006) 054313.

[145] A.F. Lisetskiy et al., Phys. Rev. C 70 (2004) 044314.

[146] K.T. Flanagan et al., Phys. Rev. Lett 103 (2009) 142501.

[147] S. Franchoo et al., Phys. Rev. Lett 81 (1998) 3100.

[148] S. Franchoo et al., Phys. Rev. C 64 (2001) 054308.

[149] I. Stefanescu et al., Phys. Rev. Lett 100 (2008) 112502.

[150] H. Morinaga, T. Yamazaki: In-Beam Gamma-ray Spectroscopy, North-Holland Publishing Company, Amsterdam, 1976

[151] D. Mengoni et al., Phys. Rev. C 82 (2010) 024308.

[152] E. Sahin, Private Communication.

[153] R. Broda. J. Phys. G: Nucl. Part. Phys. 32 (2006) R151.

[154] L. Corradi et al., Phys. Rev. C 59 (1999) 261.

[155] R. Bass. Nuclear Reactions of Heavy Ions, Springer-Verlag, new York (1980).

[156] M.W. Guidry et al., Phys. Lett. B 163 (1985) 79.

[157] R. Grzywacz et al., Phys. Rev. Lett. 81 (1998) 766.

[158] T. Ishii et al., Phys. Rev. Lett. 81 (1998) 4100.

[159] A.O. Machiavelli et al., Nucl. Phys. A 432 (1985) 436.

[160] C.Y. Wuet al., Phys. Lett. B 188 (1987) 25.

[161] S. Juutinen et al., Phys. Lett. B 192 (1987) 307.

[162] H. Takai et al., Phys. Rev. C 38 (1988) 1247.

[163] R. Broda et al., Phys. Lett. B 251 (1990) 245.

[164] A. Winther, Nucl. Phys. A 572 (1994) 191; A 594 (1995) 203.

[165] A. Winther, program GRAZING, htpp:/www.to.infn.it/∼nanni/GRAZING.

[166] R.A. Broglia and A. Winther, Heavy Ion Reactions (Addison-Wesley, Redwood City, CA, 1991).

[167] R.A. Broglia, G. Pollarolo, and A. Winther, Nucl. Phys. A 361 (1981) 307.

[168] G. Pollarolo, R.A. Broglia, and A. Winther, Nucl. Phys. A 406 (1983) 369.

[169] L. Corradi et al., Phys. Rev C 63 (2001) 021601R.

[170] G. Pollarolo et al., Phys Rev C 62 (2000) 054611.

[171] I. Stefanescu et al., Phys. Rev. Lett. 98 (2007) 122701.

[172] K. Andgren et al., Phys. Rev. C 71 (2005) 014312.

[173] K. Andgren et al., J. Phys. G: Nucl. Part. Phys. 31 (2005) S1563.

[174] S. Harissopulos et al., Nucl. Phys. A 467 (1987) 528.

[175] A. Dewald et al., J. Phys. G: Nucl. Part. Phys. 19 (1993) L177.

[176] A. Gadea et al., Acta. Phys. Pol. B 38 (2007) 1311.

[177] J.J. Valiente-Dobón et al., Phys. Rev. Lett. 102 (2009) 242502.

[178] J. Ljungvall at el., Phys. Rev. C 81 (2010) 061301.

[179] A. Dijon et al., Phys. Rev. C 83 (2011) 064321.

[180] F. Scarlassara, Private Communication.

[181] J.F. Ziegler, J.P. Biersack, U. Littmark, The Stopping and Range of Ions in SolidsPergamon Press, New York (1985).

[182] http://personalpages.to.infn.it/ñanni/grazing/

[183] A.M. Stefanini et al., Nucl. Phys. A 701 (2002) 217c.

[184] http://www.lnl.infn.it/∼ prisma/*clara_technical*/node2.html

[185] G. Montagnoli et al., Nucl. Inst. and Meth. A 547 (2005) 455.

[186] S. Beghini et al., Nucl. Inst. and Meth. A 551 (2005) 364.

[187] T. Pissulla, Private Communication.

[188] A. Gadea et al., Nucl. Inst. and Meth. A 654 (2011) 88.

[189] A. Dewald, in Ancillary Detectors and Devices for Euroball, edited by H. Grawe (GSI and the Euroball Ancillary Group, Darmstadt, 1998), p. 70.

[190] http://www.ipnl.in2p3.fr/gammaware/doc/html/

[191] D. Mengoni et al., Eur. Phys. J. A 42 (2009) 387.

[192] http://www.nndc.bnl.gov/

[193] S. Leenhardt et al., Eur. Phys. J. A 14 (2002) 1.

[194] K.S. Krane, Introductory Nuclear Physics, John Wiley and Sons, New York Singapore, 1988.

[195] E. Caurier et al., Rev. Mod. Phys. 77 (2005) 427.

[196] E. Caurier et al., Phys. Rev. Lett. 75 (1995) 2466.

[197] G. Martinez-Pinedo et al., Phys. Rev. C 54 (1996) R2150.

[198] S.M. Lenzi et al., Phys. Rev. C 56 (1997) 1313.

[199] K. Sieja and F. Nowacki, Phys. Rev. C 81 (2010) 061303.

[200] K. Sieja and F. Nowacki, arXiv:1201.0373v1.

[201] J.M. Daugas et al., Phys. Rev. C 81 (2010) 034304.

[202] A.P. Zuker et al., Phys. Rev. C 52 (1995) 4.

[203] E. Caurier, Private Communication.

[204] M. Hjorth-Jensen, T. Kuo, and E. Osnes, Phys. Rep. 261 (1995) 125.

[205] F. Nowacki, Ph.D. Thesis, IReS Strasbourg, 1996.

[206] S. Kahana, H.C. Lee, and C.K. Scott, Phys. Rev. 180 (1969) 956.

[207] F. Nowacki and A. Poves, Phys. Rev. C 79 (2009) 014310.

[208] S.M. Lenzi, F. Nowacki, A. Poves, and K. Sieja, Phys. Rev. C 82 (2010) 054301.

[209] J. Van de Walle et al., Phys. Rev. C 79 (2009) 014309.